



The
University
Of
Sheffield.

An insight into the brain of patients with type-2
diabetes mellitus and impaired glucose
tolerance using multi-modal magnetic
resonance image processing

Maria-Eleni Dounavi

Supervised by:
Professor Iain D. Wilkinson
Dr. Chris Martin
Dr. Paul Armitage

A thesis submitted in partial fulfilment of the requirements for the
degree of Doctor of Philosophy

Academic Unit of Radiology
Department of Infection, Immunity and Cardiovascular Disease
Faculty of Medicine, Dentistry and Health
The University of Sheffield

December 2018

Abstract

The purpose of this thesis was to investigate brain anatomy and physiology of subjects with impaired glucose tolerance (IGT – 12 subjects), type-2 diabetes (T2DM - 17 subjects) and normoglycemia (16 subjects) using multi-modal magnetic resonance imaging (MRI) at 3T.

Perfusion imaging using quantitative STAR labeling of arterial regions (QUASAR) arterial spin labeling (ASL) was the core dataset. Optimization of the post-processing methodology for this sequence was performed and the outcome was used for hemodynamic analysis of the cohort. Typical perfusion-related parameters, along with novel hemodynamic features were quantified. High-resolution structural, angiographic and carotid flow scans were also acquired and processed. Functional acquisitions were repeated following a vasodilating stimulus. Differences between the groups were examined using statistical analysis and a machine-learning framework.

Hemodynamic parameters differing between the groups emerged from both baseline and post-stimulus scans for T2DM and mainly from the post-stimulus scan for IGT. It was demonstrated that quantification of not-typically determined hemodynamic features could lead to optimal group-separation. Such features captured the pattern of delayed delivery of the blood to the arterial and tissue compartments of the hyperglycemic groups. Alterations in gray and white matter, cerebral vasculature and carotid blood flow were detected for the T2DM group. The IGT cohort was structurally similar to the healthy cohort but demonstrated functional similarities to T2DM. When combining all extracted MRI metrics, features driving optimal separation between different glycemic conditions emerged mainly from the QUASAR scan. The only highly discriminant non-QUASAR feature, when comparing T2DM to healthy subjects, emerged from the cerebral angiogram.

In this thesis, it was demonstrated that MRI-derived features could lead to potentially optimal differentiation between normoglycemia and hyperglycemia. More importantly, it was shown that an impaired cerebral hemodynamic pattern exists in both IGT and T2DM and that the IGT group exhibits functional alterations similar to the T2DM group.

To my parents Alexandros and Athina and my friend, Alexandra.

Acknowledgements

First and most importantly I want to thank my supervisors Professor Iain Wilkinson, Dr. Chris Martin and Dr. Paul Armitage for believing in me and guiding me every step of the way. Their profound trust, the faith in my new ideas and their useful insight transformed me scientifically. Iain was for me an excellent tutor and supervisor. Chris provided invaluable insight on the neurovascular side of things helping me grasp the bigger picture. Paul stepped in at the end of my PhD as an additional supervisor and has helped me tremendously in such a short period of time, contributing new ideas to the project and taking the time to provide detailed feedback.

My PhD wouldn't have been possible without the existence of the NICAD network, led by Chris, which secured my funding and gave me the opportunity to present my research in conferences around the world.

I would also like to thank dear friends and colleagues who have helped me during this challenging but amazing PhD journey. Most importantly I want to thank my guardian angel Alexandra Boutopoulou for her continuous painstaking support, her invaluable advices and for refusing to stop believing in me. Also, many thanks go to Andreas Vlachos, Iain Croall, Andre Ahlgren and Dimitrios Tsarapatsanis for their help and feedback. This PhD journey wouldn't have been as fun without Karishma Chhabria and Avgoustinos Vouros; together we formed a geeky and powerful small team having its headquarters in Karishma's office.

During my PhD I was extremely lucky to be based at an office that many people would only dream of, in terms of space, cleanness, facilities and most importantly in terms of co-workers and for that I would like to thank the POLARIS group.

I am also extremely grateful to my parents Alexandros Dounavis and Athina Moshona who are always there for me, ready to support me in every possible way, happy and proud that their child decided to follow an academic path.

Finally, I want to thank my beloved sister Avgi and my dearest friends Maria, Irida and Klio for being there for me every step of the way.

Table of Contents

Abstract	iii
Acknowledgements	vii
List of figures	xiii
List of tables	xvii
Abbreviations	xix
Introduction	1
Chapter 1: Diabetes and the brain	5
1.1 The brain	5
1.1.1 Essential brain anatomy	5
1.1.2 Neurovascular coupling	6
1.1.3 Brain arterial supply.....	8
1.1.4 Oxygen and glucose path to the brain.....	9
1.2 Type-2 diabetes mellitus	10
1.2.1 T2DM background	10
1.2.2 Brain imaging findings in T2DM.....	11
1.2.3 Potential mechanism driving changes in the diabetic brain	13
Chapter 2: Magnetic Resonance Imaging theory and modalities	15
2.1 Nuclear magnetic resonance	15
2.2 MR image formation	20
2.3 EPI imaging and artifacts	24
2.4 Perfusion and CVR imaging	26
2.4.1 Arterial spin labeling	28
2.4.2 Dynamic Susceptibility Contrast MRI (DSC-MRI)	41
2.4.3 Vascular space occupancy MRI	42
2.4.4 Intravoxel incoherent motion MRI.....	43
2.5 Structural, diffusion weighted MRI and MRA	44
2.5.1 3D T1-weighted image.....	44
2.5.2 Anatomical T2-weighted imaging.....	45
2.5.3 MR Angiography	45
2.5.4 Diffusion weighted MRI.....	47
Chapter 3: Brain MR Image Processing	51
3.1 Pre-processing steps	52
3.1.1 Bias field correction	52
3.1.2 Brain extraction	54
3.1.3 Image registration	54
3.1.4 Tissue segmentation.....	56
3.2 Partial volume phenomenon and correction	59
3.3 Group-comparisons	60
3.4 Feature extraction and classification	61
3.4.1 Feature extraction	62
3.4.2 Dimensionality reduction.....	63
3.4.3 Classification techniques	65
3.4.4 Cross-validation.....	68
3.4.5 Machine learning and MR brain imaging.....	69
3.5 Theory Summary	71
Chapter 4: Retrospective cohort - MR protocol - Utilised software	73
4.1 Available cohort	74

4.2 MR Imaging Protocol	75
4.2.1 QUASAR ASL	75
4.2.2 3D- T1 weighted (MPRAGE)	76
4.2.3 FLAIR.....	76
4.2.4 PC-MRA	77
4.2.5 DWI	77
4.2.6 TOF-MRA	78
4.3 Overview of utilised software tools	78
Chapter 5: Developments in brain perfusion image processing	81
Abstract	81
5.1 Introduction	82
5.2 Post-acquisition QUASAR ASL processing strategy	85
5.2.1 Noisy scan rejection.....	85
5.2.2 Tissue relaxation and magnetization quantification.....	85
5.2.3 Arterial transit time calculation	86
5.2.4 Arterial blood volume and arterial input function calculation.....	87
5.2.5 Residue function and CBF estimation.....	90
5.2.6 Artifact detection	92
5.2.7 Partial Volume Correction	94
5.2.8 Correction for scan alignment and identification of overlapping slices	98
5.2.9 Brain-blood partition coefficient (λ).....	99
5.2.10 Simulated data.....	99
5.2.11 In-vivo data.....	101
5.2.12 Comparison with QUASIL (in-vivo data)	102
5.2.13 Performance evaluation.....	102
5.3 Results	105
5.3.1 k-radius AIF weighting.....	105
5.3.2 AIF re-evaluation	114
5.3.3 In-vivo results	116
5.4 Discussion	120
5.5 Conclusions	127
Chapter 6: Cerebral hemodynamic analysis in type-2 diabetes and impaired glucose tolerance	129
Abstract	129
6.1 Introduction	130
6.2 Methods	132
6.2.1 MR protocol.....	133
6.2.2 Partial volume correction	133
6.2.3 Quantified parameters	134
6.2.4 Vascular territory and watershed area analysis	136
6.2.5 Feature reduction and classification.....	138
6.2.6 Statistical comparisons	142
6.3 Results	142
6.3.1 Conventional analysis approach	142
6.3.2 Extended hemodynamic analysis	145
6.3.3 Classification based just on the baseline scan.....	154
6.4 Discussion	156
6.5 Conclusions	162
Chapter 7: Processing of multi-modal MR images in type-2 diabetes and impaired glucose tolerance	165
Abstract	165
7.1 Introduction	166

7.2 T1-weighted (MPRAGE) scan analysis	169
7.2.1 Methods.....	169
7.2.2 Results.....	175
7.2.3 Discussion	186
7.3 T2-weighted (FLAIR) processing	190
7.3.1 Methods.....	190
7.3.2 Results.....	192
7.3.3 Discussion	193
7.4 Phase Contrast – Magnetic Resonance Angiography (PC-MRA) analysis	194
7.4.1 Methods.....	194
7.4.2 Results.....	197
7.4.3 Discussion	204
7.5 Time-of-flight – Magnetic Resonance Angiography (TOF-MRA) analysis	206
7.5.1 Methods.....	206
7.5.2 Results.....	208
7.5.3 Discussion	214
7.6. Diffusion Weighted Image analysis.....	216
7.6.1 Methods.....	216
7.6.2 Results.....	217
7.6.3 Discussion	219
7.7 Summary	219
CHAPTER 8: MRI-derived biomarkers for hyperglycemia unraveled	223
8.1 Determination of the feature combination leading to optimal class-	
 differentiation	229
8.2 Overall thesis discussion	235
References.....	241
Appendix.....	263
Appendix1.....	263
Appendix 2.....	266

List of figures

Introduction

Figure 1: Rembrandt, The Anatomy Lesson of Dr. Nicolaes Tulp.

Chapter 1

1.1: The blood brain barrier illustration.

1.2: Coronal and axial maximum intensity projections of an MR angiogram demonstrating the brain vasculature.

Chapter 2

2.1: Magnetic moment orientation with and without the application of an external magnetic field.

2.2: MRI principle for the main 3 tissue types in the brain.

2.3: Phase and frequency encoding in 2D depiction.

2.4: Example pulse sequence diagram.

2.5: Representation of k- space trajectory for conventional and 2D single shot EPI readouts.

2.6: EPI pulse sequence diagram.

2.7: Example EPI artifacts.

2.8: Philosophy of ASL MRI.

2.9: CASL, PASL and pCASL philosophy.

2.10: Control, label and imaging planes shown schematically for four ASL implementations.

2.11: Schematic representation of a voxel (VOI) in perfusion MRI.

2.12: Perfusion system at the tissue level.

2.13: Qualitative representation of the crushed and non-crushed QUASAR signals.

2.14: QUASAR pulse sequence diagram.

2.15: Pulse diagram for PC MRA.

2.16: Diffusion weighted imaging pulse sequence.

Chapter 3

3.1: Preprocessing steps demonstrated in one coronal slice.

3.2: SVM optimally differentiating hyper-plane in 2D and 3D.

Chapter 4

4.1: Approximate anatomical coverage of the utilised MRI protocol

Chapter 5

- 5.1: AIF weighting approach.
- 5.2: Artifact detection and rejection methodology.
- 5.3: Partial volume effects in one Quasar voxel with respect to a 256*256 MPRAGE image.
- 5.4: Simulation Case 1 (homogeneous GM and WM).
- 5.5: Simulation Case 2 (hyper and hypo intense areas).
- 5.6: Simulation case 2, hyper and hypo intense GM CBF estimation.
- 5.7: Example maps for simulation Case 2 without PVC.
- 5.8: Artifact detection - Simulation case 3.
- 5.9: Simulation case 3, metrics M1-M8 with a decreasing threshold and $k=1$.
- 5.10: Simulation case 3, metrics M1-M8 with a decreasing threshold and $k=4$.
- 5.11: Simulation case 3, metrics M1-M8 with a decreasing threshold and $k=6$.
- 5.12: AIF reevaluation simulation case 1.
- 5.13: AIF reevaluation simulation case 2.
- 5.14: AIFs from 10 voxels based one subject for different degrees of AIF weighting (k).
- 5.15: Number of averaged AIFs for each of the examined voxels with an increasing k .
- 5.16: Single slice CBF maps from a representative subject as a function of PVC level and k -radius AIF weighting.
- 5.17: Example slice from an individual of a 1/T1 slice and the determined PV maps generated with the 4 tested variants.

Chapter 6

- 6.1: Example demonstration of the tissue, arterial and residue function signals.
- 6.2: Overview of the calculated hemodynamic metrics.
- 6.3: Vascular territory masks and watershed areas for all 7 QUASAR slices.
- 6.4: Philosophy of the feature ranking and selection method.
- 6.5: Hemodynamic time series curves for every group.
- 6.6: Model accuracy for every classification task obtained using LOOCV as a function of the number of features for models 1,2,4,5 and 6.

Chapter 7

- 7.1: GLM generated using FSL's dedicated tools.
- 7.2: Example results for FSL's BET tool using bias field and neck cleanup mode with a value of $f=0.1$.
- 7.3: Failure of BET in a single subject with enlarged ventricles.
- 7.4: Successful brain extraction using SPM and minor dilation and filling.
- 7.5: Segmentation results from a representative simulated slice.

- 7.6: VBM representative results with 2mm smoothing kernel.
- 7.7: Classification accuracy for the HV vs T2DM task with an increasing number of features/ voxels accompanied with a figure showing the voxels contributing towards optimal class separation.
- 7.8: Classification accuracy for the HV vs IGT task with an increasing number of features/ voxels accompanied with a figure showing the voxels contributing towards optimal class separation.
- 7.9: Classification accuracy for the T2DM vs IGT task with an increasing number of features/ voxels accompanied with a figure showing the voxels contributing towards optimal class separation.
- 7.10: Definition of the ROIs used for textural analysis.
- 7.11: PC-MRA processing steps.
- 7.12: Baseline and post-ACZ flow for the different ROIs.
- 7.13: Mean, maximum and minimum velocities for the left and right carotids and all arterial input for the three groups.
- 7.14: 1st method for angiogram segmentation for one HV.
- 7.15: Segmented MIP for one T2DM subject using the first method.
- 7.16: Segmentation with the 2nd method for one HV and one T2DM patient
- 7.17: MIP segmentation using Frangi filter with 3 different standard deviations (from left to right, $\sigma = 1, 3$ and 5) for one healthy subject.
- 7.18: MIP segmentation using Frangi filter with 3 standard deviations (from left to right, $\sigma = 1, 3$ and 5) for one T2DM patient.
- 7.19: Comparison of the MIP segmentation obtained with the 3 evaluated methods.
- 7.20: MCA territory segmentation.
- 7.21: Example $b=0$, $b=1000$ s/mm³ and ADC maps

Chapter 8

- 8.1: Spatial coverage of the utilised MR protocol.
- 8.2: Summary figure for the three examined groups and metrics of interest.
- 8.3: A pictorial representation of the machine learning analysis, combining metrics from all modalities.

List of tables

Chapter 4

4.1: Details of the retrospective cohort

Chapter 5

5.1: GM CBF, WM CBF and number of identified AIFs for 12 subjects.

Chapter 6

6.1: Details about the subject cohort analysed in chapter 6.

6.2: An overview of features extracted from 3 curves and the 5 considered ROIs.

6.3: Quantified values for CBF, aBV, ATT and CVR using the developed QUASAR ASL quantification pipeline for the scanned cohort.

6.4: Model 1, HV vs T2DM task top-10 features identified with SVM-RFE giving optimal performance, accompanied with a number indicating their occurrence (Occ.) in the top-M.

6.5: Model 1, HV vs IGT&T2DM task top-10 features identified with SVM-RFE giving optimal performance along with their occurrence in the top-M.

6.6: Model 3, HV vs T2DM task top-10 features identified with SVM-RFE giving optimal performance along with their occurrence in the top-M.

6.7: Model 3, task HV vs IGT&T2DM top-10 features identified with SVM-RFE giving optimal performance along with their occurrence in the top-M.

6.8: Model 4, IGT vs T2DM task top-10 features identified with SVM-RFE giving optimal performance along with their occurrence in the top-M.

6.9: Model 5, HV vs IGT&T2DM task top-10 features identified with SVM-RFE giving optimal performance along with their occurrence in the top-M.

6.10: Model 6, HV vs IGT&T2DM task top-10 features identified with SVM-RFE giving optimal performance

6.11: Model 7, HV vs IGT&T2DM task top-10 features identified with SVM-RFE giving optimal performance along with their occurrence in the top-M.

6.12: Comparison between the performance of models based solely on the baseline scan and models based on both pre and post-ACZ scans.

Chapter 7

- 7.1: GM and WM MAPEs for the three examined approached for N4 BFC.
- 7.2: MAPEs for GM and WM for voxels belonging in the brain mask (not necessarily in the ground truth GM cluster) and for voxels belonging in the GM cluster based on the ground truth for all examined segmentation techniques.
- 7.3: Tissue volume (normalized for total brain volume and non-normalized) for GM, WM and CSF calculated using N4 BFC and SFCM clustering.
- 7.4: GM, WM, CSF, intracranial volume and total brain volumes calculated using Freesurfer.
- 7.5: Volume of subcortical structures of interest for the three groups under consideration.
- 7.6: Cortical thickness for the left and the right hemisphere as calculated using Freesurfer
- 7.7: Number and volume of leukoaraiosis in the examined cohort.
- 7.8: Mean vessel area (mean \pm std) measured in number of voxels for the examined groups.
- 7.9: CVR for the 3 groups and examined areas evaluated as the % change between pre and post ACZ flow measurements.
- 7.10: Vasculature-descriptive metrics extracted from the MCA territory for the 3 groups.
- 7.11: ADC values for the main lobes, insula and thalamus for the examined groups.
- 7.12: ADC values in structures of interest for the examined groups.

Chapter 8

- 8.1: Accuracy (Acc) sensitivity (Sens) specificity (Spec) features and number of features (Nf) for every task and the first model.
- 8.2: Accuracy (Acc) sensitivity (Sens) specificity (Spec) features and number of features (Nf) for every task and the second model.
- 8.3: Case study results for subjects with either high volume of leukoaraioses or high ventricular volume.

Abbreviations

aBV	arterial blood volume	GMM	Gaussian Mixture Models
ACA	anterior cerebral artery	HRF	hemodynamic response function
ACZ	acetazolamide	HWL (R)	half width at half maximum left (right)
AIF (sh)	arterial input function (shape)	IGT	impaired glucose tolerance
ASL	arterial spin labeling	IVIM	intravoxel incoherent motion
ATT	arterial transit time	KURT	kurtosis
BBB	blood-brain barrier	LOOCV	leave one out cross validation
BFC	bias field correction	MCA	middle cerebral artery
BOLD	blood oxygen level dependent	MNI	Montreal neurological institute
CBF	cerebral blood flow	MPRAGE	magnetization-prepared rapid gradient-echo
CoV	coefficient of variation	MRA	Magnetic resonance angiography
CSF	cerebrospinal fluid	PASL	pulsed ASL
CT	computer tomography	PC-MRA	phase contrast MRA
CVR	cerebrovascular reactivity	PCA	posterior cerebral artery
DSC-MRI	dynamic susceptibility contrast	(p)CASL	(pseudo) continuous ASL
DTI	diffusion tensor imaging	PDF	probability density function
DWI	diffusion weighted imaging	PET	positron emission tomography
EPI	echo-planar imaging	PLD	post-labeling delay
FLAIR	fluid attenuation recovery	PVC	partial volume correction
FW	full width at half maximum		
GM	gray matter		

QUASAR	quantitative	STAR	T2DM type-2 diabetes mellitus
labeling of arterial regions			TCD Transcranial Doppler
Res residue			TE echo time
RF radiograquency			TOF-MRA time-of-flight MRA
RFE recursive feature elimination			TR repetition time
ROI region-of-interest			TTP time-to-peak
SKEW skewness			VASO vascular space occupancy
(S)FCM (spatial) fuzzy c-means			VBM voxel-based morphometry
clustering			W watershed
SNR signal-to-noise ratio			WB whole brain
SSIM structural similarity index			WM white matter
SVD singular value decomposition			$\Delta M_{(n)cr}$ (non-) crushed signal
SVM support vector machine			

Introduction

Whether to gain insight into the underlying structure and function of body organs by means of dissection has been a matter of debate for centuries. In antiquity and medieval times, the human body was considered sacred and dissection was either limited or totally prohibited. It was in Alexandria in the 4th century BC where for the first time, physicians reported their observations based on cadaver dissection. However, the practice of dissection was abandoned and subsequently prohibited mainly due to religious reasons (1). It was not until the 14th century that anatomy was reinstated in Italy. At first, dissection was used for autopsy but as the years passed, it became clear that both the scientific community and society could have a lot to gain if they invested in it (2). From being considered an unethical practice for a period of more than 1500 years, in the 15th century, dissection became extremely popular and in the 16th century anatomy theaters were built around Italy and the rest of Europe. Such was its impact in society that even renowned painters such as Leonardo da Vinci and Rembrandt were inspired by it to create some of their masterpieces (figure 1).



Figure 1: Rembrandt, The Anatomy Lesson of Dr. Nicolaes Tulp, signed and dated 'Rembrandt ft. 1632'. Canvas, 169,5 x 216,5 cm, The Hague, Mauritshuis

It was in the 16th century, in Italian cities and universities, where it became clear that empirical observations and dissection of animals was a

limiting factor in understanding the human body and disease. A proper understanding would require a window into the living human body and at that time, the only window available was human cadaver dissection.

In 1895 the emergence of X-ray imaging, discovered by Wilhelm Rontgen, gave for the first time the opportunity to study body organs in living humans. In the 1980s another breakthrough would change the way the human body was imaged. The emergence of Magnetic Resonance Imaging (MRI), attributed to Paul Lauterbur, Peter Mansfield and Raymond Damadian, allowed for non-ionizing imaging of the 3-dimensional structure of the body (3, 4).

Within a few centuries, humanity has progressed from ignorance of what is happening inside the body, to the acceptance that understanding of a disease requires an insight inside the body that only dissection could provide, and finally to medical imaging approaches based on manipulation of atomic, chemical and physical properties of tissues. In general, progression in these approaches moves from ionizing and invasive techniques to being totally non-ionizing and non-invasive. MRI is one of the core bio-imaging modalities used nowadays and along with ultrasound is the safest modality for anatomical imaging. Ultrasound imaging, however, is limited in its ability to provide an image of the brains interior since the skull shields it from acoustic waves (except in newborns). Hence, MRI is currently the only imaging modality with the ability to provide high quality brain images using a non-ionizing approach.

Although initially able to extract only structural information, nowadays MRI can also be used for functional assessment. MR images can be acquired from a wide range of body organs using a variety of specific MRI protocols.

Medical imaging techniques, in particular MRI, are increasingly used for understanding, diagnosis and assessment of a disease's severity. Another more recent field of interest is the identification of imaging biomarkers for disease prognosis. This requires that large longitudinal datasets and powerful processing methods are available in order for reliable predictions to be made. A great example is the BioBank initiative where numerous MRI scans and biometric factors are being collected from 500.000 individuals (5). The evolution of medical imaging continues, with research ongoing aimed at improving several aspects, ranging from the hardware and acquisition techniques to the highly specialized post-processing approaches. This thesis aims to be a part of

this effort, by being at the intersection of image processing and clinical research.

The purpose of this thesis is to gain a deep insight into the brain of subjects with impaired glucose tolerance (IGT – pre-diabetes) and type-2 diabetes mellitus (T2DM) patients. Diabetes currently affects 415 million people globally and 4 million in the UK (6). The prevalence of the disease and the fact that it is a risk factor for conditions such as stroke and Alzheimer’s disease renders its early diagnosis or even prognosis a necessity. It has previously been reported that the brain, amongst other organs, shows alterations of a structural and functional nature in individuals with diabetes. Uncovering the underlying brain changes could provide useful diagnostic and prognostic biomarkers for the disease.

In this study, several MRI techniques were used to evaluate cerebral structural and functional characteristics in a cohort comprised of healthy volunteers, subjects with IGT, and T2DM. Software tools were built for processing MRI images and new image analysis approaches were introduced. The developed processing pipelines have been made publically available in Matlab’s file exchange to promote reproducibility and dissemination.

The core imaging technique used in this study was arterial spin labeling (ASL) MRI, a technique used for blood perfusion assessment. In addition, high-resolution structural scans were used to shed light on anatomical changes, diffusion weighted imaging was used to evaluate the microscopic water mobility within brain tissues and angiographic scans provided information about the cerebral vasculature. Flow inside the internal carotid artery was also evaluated, providing a window into the input the brain gets from the wider cardiovascular system.

This thesis is organised as follows:

In **Chapter 1**, relevant background material is presented. A brief overview is given of basic brain anatomy, diabetes and known changes occurring in the diabetic brain.

In **Chapter 2**, an overview of MRI theory is provided. In the second part, techniques relevant to the work performed in this thesis are discussed, mainly focused on the core modality of this project, ASL.

In **Chapter 3**, brain image processing techniques and machine learning approaches utilised for data analysis are presented.

In **Chapter 4**, the available cohort, acquired imaging modalities and utilised software tools are summarised.

In **Chapter 5**, the methodology developed for processing multi inversion time-point ASL data is described, evaluated and discussed.

In **Chapter 6**, the developed ASL processing pipeline is applied to the available cohort and the resulting hemodynamic data are analysed in a novel way. Machine learning is used to extract the most significant hemodynamic feature combinations.

In **Chapter 7**, structural, diffusion-weighted and angiographic MR images are analysed and optimal processing approaches are discussed.

In **Chapter 8**, all the results from the individual MRI modalities are brought together in a single model to unravel potential disease biomarkers. The general study conclusions along with future directions are presented.

Chapter 1:

Diabetes and the brain

1.1 The brain

1.1.1 Essential brain anatomy

The brain is separated into three main structures: the cerebral cortex, the cerebellum and the brainstem. Nerve fibers forming the spinal cord conduct signals to and from the brain, and in their posterior location they form a structure known as the brainstem. This structure is associated with functions such as breathing, body temperature and blood pressure control. At the top of the brainstem lies the cerebellum, which is associated with movement coordination.

The cerebral cortex can be separated into two hemispheres and comprises four main lobes: the frontal, temporal, parietal and occipital lobe. Although these lobes are associated with distinct functions, they are highly interconnected and are interacting constantly with each other. The occipital lobes are specialized for visual information processing. Information processing for input coming from the muscles, joints, and skin is combined with information from visual and acoustic inputs within the parietal lobes. The temporal lobes are associated with higher perceptual functions such as face recognition and meaning comprehension. They accommodate areas that are unique to the human brain such as Wernicke's area, associated with speaking and comprehension. The frontal lobes accommodate the motor cortex and they are associated with 'executive functions' such as planning (7).

The brain contains billions of neurons, the essential constituents of the central nervous system. Every neuron is directly connected with around 1000-10,000 other neurons via synapses. A neuron consists of its dendrites, its soma and its axon. The bundles of axons form what is called white matter (WM) and the gray matter (GM) is formed by the soma, dendrites and axon terminals. Cerebrospinal fluid (CSF) is a fluid circulating within and around the brain, stemming from the ventricles to the subarachnoid space where it forms a protective layer surrounding the brain and the spinal cord. Other key cellular

and microstructural elements found inside the mammalian brain are glial cells, blood vessels and neural stem cells.

The brain is a highly protected organ. The principal external protection comes from the skull. On the inside, CSF provides protection since one of its functions is the absorption of vibrations. There is an additional level of protection called the blood brain barrier (BBB), which protects the brain from potential physiological threats coming via the bloodstream (figure 1.1). The BBB in a healthy individual prohibits potential pathogens from entering brain tissue from the blood stream. Tight junctions between the endothelial cells of brain capillaries form the BBB. This membrane is semi-permeable allowing substances such as oxygen, glucose, water and several molecules to cross. The BBB can be disrupted in diseases such as Alzheimer's, brain tumors, multiple sclerosis (8, 9) and type-2 diabetes (10).

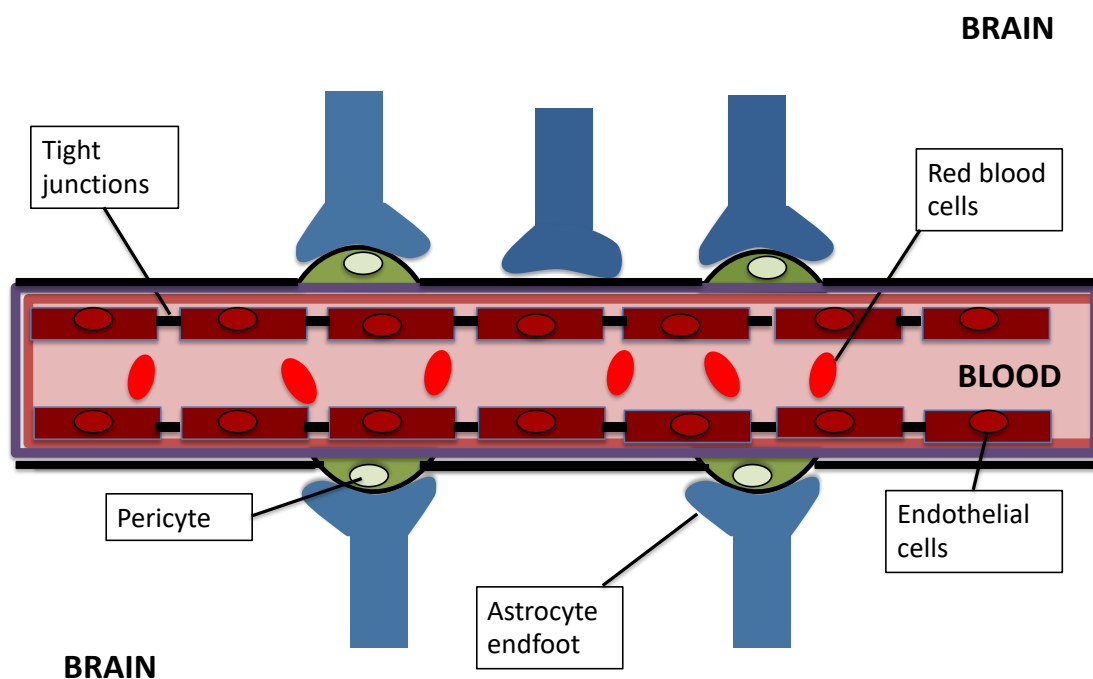


Figure 1.1: The blood brain barrier illustration.

1.1.2 Neurovascular coupling

The neurovascular unit comprises a collection of structures and cells working together to ensure that the vascular tone is adequately adapted to meet changing energy demands from activated neurons (11). This functional complex

is responsible for the maintenance of an appropriate regional blood supply in the brain.

The neurovascular unit comprises mainly three distinct levels: neurones, glial cells (astrocytes, microglia and oligodendroglia) and vascular cells (endothelial cells, pericytes and vascular smooth muscle) (12). The interface between the neuronal and vascular components is considered to be the astrocyte, which via 'endfeet' is in contact with pericytes and vascular smooth muscle. Additionally, it is in close communication with neuronal activity, playing a role in the manufacture and exchange of neurotransmitters and neuromodulators and with receptors for a range of neurotransmitter substances. Endothelial cells have the ability to produce and secrete substances regulating vascular tone such as nitric oxide (causing dilation), endothelin and thromboxane (constriction) (13).

Neurovascular coupling refers to the close interplay between the vasculature and the neurons for the maintenance of the vascular tone and its adjustment of local cerebral blood flow (CBF) when necessary. It is mediated by the neurovascular unit which enables the appropriate adjustment of cerebral blood flow to meet energy demands in metabolically activated areas. Neurovascular uncoupling is a common finding in diseases such as Alzheimer's, hypertension and stroke (14), whereby the local regulation of CBF becomes 'uncoupled' to changes in neuronal or metabolic activity. Early neurovascular uncoupling has also been reported in T2DM (15). In this T2DM study, functional MRI was used to evaluate the shape of the hemodynamic response function (HRF) to a visual stimulus. The examined subjects were cognitively asymptomatic and had no apparent lesions. The HRF differed in both the amplitude and the time-course between healthy controls and T2DM patients.

The neurovascular coupling concept suggests that increases in neuronal activation lead to increases in local blood flow. There exists also the vasculo-neural or hemo-neural hypothesis according to which the neuronal activation is adjusted based on the changes in blood flow, having glial cells and mainly astrocytes as a mediator of the process (16). Both concepts describe a two-way communication between neurons and the vasculature via glial cells (mainly

astrocytes), the endpoint being blood flow adjustment for the maintenance of homeostasis.

1.1.3 Brain arterial supply.

The brain is a greedy organ since it accounts for 2% of the total body mass but consumes 20% of the utilised oxygen and 25% of the consumed glucose (12). The needs for nutrient and oxygen supply are constant and even a short interruption in supply (ischemia) can cause significant damage to brain tissue. Long-term interruptions in blood supply have been connected with cognitive decline and vascular dementia (17). The internal carotid arteries and the vertebral arteries are the brain's main vascular supply. Inside the cranium the aforementioned arteries form a circular structure, the Circle of Willis. The carotids supply the anterior part of the brain, whereas the basilar/vertebral arteries supply the posterior part and structures such as the brain stem (18).

Cerebral anatomy in relation to the brain's blood supply and cerebrovascular disease has been recently reviewed by Chandra et al. (19). The internal carotids arise from the common carotid arteries. The right common carotid emerges from a bifurcation of the brachiocephalic trunk. The left common carotid emerges directly from the aorta. The common carotids split to internal and external at the level of the neck. The external carotids supply the facial skin. The vertebral arteries emerge from the subclavian arteries. At the level of the pons they come together to form the basilar artery. The frontal lobes are supplied by the anterior cerebral artery (ACA), the middle cerebral artery (MCA) supplies part of the frontal, temporal and parietal lobes (figure 1.2). The posterior cerebral circulation supplies the temporal and occipital lobes and is responsible for about 1/3 of perfusion. The ACA, MCA and the anterior choroidal artery (AChA) are responsible for 72% of total CBF.

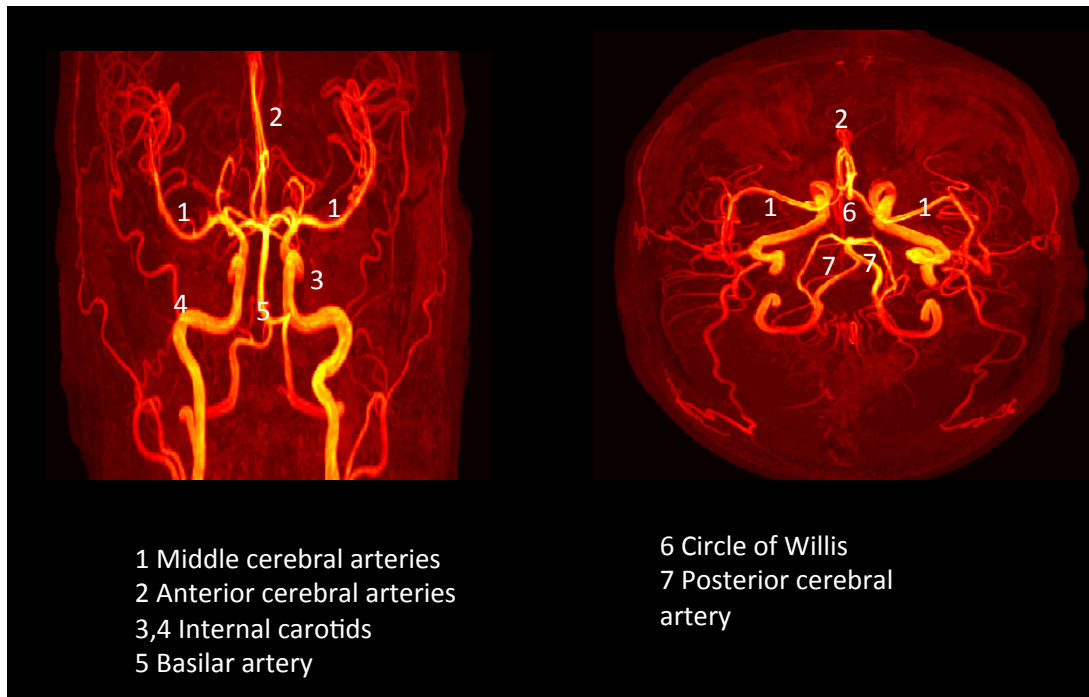


Figure 1.2: Coronal and axial maximum intensity projections of an MR angiogram demonstrating the brain vasculature.

1.1.4 Oxygen and glucose path to the brain

Oxygen and glucose are necessary for catabolic reactions taking place in the organism. The products of glucose breakdown are used for the generation of adenosine triphosphate and neurotransmitters.

Oxygen is attached to hemoglobin molecules within erythrocytes (red blood cells), forming oxyhemoglobin. Every hemoglobin molecule has four heme groups with the potential to transfer up to one oxygen molecule each, so four oxygen molecules are transported by one hemoglobin molecule. When red blood cells pass through the lungs, oxygen molecules are attached and subsequently travel through the bloodstream (20). From the arteries, they progress to the arterioles and from there they enter the capillary bed. Inside, the microvasculature oxygen and nutrient exchange occurs, with oxygen being transferred from the hemoglobin molecules into the extravascular local tissue. Oxygen has the ability to diffuse freely across the BBB (21).

Glucose is retained following a meal, it can also be stored in the body for use when required in the form of glycogen. When in the bloodstream, it travels around the body, in order to be taken up by the cells and used for energetic purposes. The brain's glucose uptake is mediated by insulin and glutamate

transporters (GLUT-1, GLUT-3) (Mergenthaler et al 2013). Glucose in the brain is used by both neurons and glial cells.

Transportation of both oxygen and glucose is based on the existence of a concentration gradient between the intravascular and extravascular compartments with the intravascular concentration being higher in both cases.

1.2 Type-2 diabetes mellitus

1.2.1 T2DM background

Diabetes mellitus is a metabolic syndrome that has two dominant forms: Diabetes mellitus type-1 (T1DM) and diabetes mellitus type-2 (T2DM). T1DM is more common in people under the age of 40 years and the most common type in childhood accounting for 10% of diabetic patients. T2DM is the most prevalent form of diabetes mellitus after the age of 40 years and it accounts for 90% of diabetic patients. T1DM, is attributed to insulin deficiency, whereas T2DM occurs due to insulin resistance (6). The main risk factors for developing T2DM are: eating habits; sedentary lifestyle; age; and family history (22).

Insulin, a hormone produced in the pancreas is responsible for the stimulation of glucose uptake by the cells. Glucose is the end product of food breakdown in the stomach, it is the basic 'fuel' of the organism and its uptake is crucial for the maintenance of homeostasis. In T2DM cells develop insulin resistance. The first response of the organism to this condition is the production of higher levels of insulin by the pancreas to compensate for the reduced insulin uptake (hyper-insulinemia). Insulin resistance results in reduced glucose uptake and glucose remains in the bloodstream resulting in hyperglycemia (23). The organism after a certain point becomes dysregulated, as the amount of energy needed by the cells in order to function properly is not met. Impaired glucose tolerance (IGT) and impaired fasting glucose are considered to be pre-diabetic conditions, whereby insulin production and glucose uptake are impaired. However, the subjects do not fulfil the clinical criteria to be categorised as diabetic. IGT is considered to be reversible with lifestyle changes (24) and anti-diabetic drug usage (25), but it has a high rate (70%) of progression to T2DM (26).

Diabetes can affect several organs such as: the eyes (retinopathy), being one of the main causes of blindness in adulthood (27); kidneys (nephropathy)

affecting 20-40% of patients with diabetes who develop diabetic nephropathy (28); and nerves (neuropathy) affecting 15-26% of individuals suffering from diabetes (29). Furthermore, it is one of the main risk factors for developing cardiovascular disease, which accounts for 52% of deaths in type-2 diabetics (30).

Usually diabetes is diagnosed following the onset of diabetic symptoms such as excessive urination, or by performing tests targeted to detect high glucose in urine or in the blood. A factor typically used to evaluate the diabetic status is the amount of circulating glycated hemoglobin (HbA1c) with a physiological level being below 6% (31). HbA1c reflects directly the amount of glucose inside the bloodstream. As described earlier, oxygen binds to hemoglobin molecules, circulates via the bloodstream and is delivered to tissues to participate in metabolic reactions. When the amount of glucose is excessive in the organism, glucose binds to hemoglobin molecules. This renders hemoglobin molecules dysfunctional in terms of O₂ delivery to tissues, since its affinity for it is increased leading to a shift in its oxygen dissociation curve (32).

1.2.2 Brain imaging findings in T2DM

The brain is not typically considered one of the organs affected by T2DM. The main reason for that is that the impact of T2DM can be detrimental for multiple organs (eyes, kidneys, nerves) creating conditions that need to be managed and closely monitored. Its effect on the brain might become prominent in the long-term and usually emerges with other complications, for example stroke and dementia.

Neuroimaging studies focused on T2DM report findings suggestive of functional and anatomical brain alterations (33, 34). Some of the most common structural abnormalities involve: Cortical and subcortical atrophies (35-38), WM hyper-intensities (35, 37, 39), hippocampal atrophy (40) and increase in CSF volume (36). A 6-year longitudinal study by Umemura, Kawamura (41) has shown that there is an association between the number of silent brain infarctions, WM lesion progression and endothelial dysfunction in T2DM.

In terms of functional abnormalities, impaired cognition has been reported in T2DM patients (35, 39). The affected cognitive skills involve

processing speed, memory and learning. Studies focused on the 'default mode network' have shown alterations in connectivity. Findings regarding cerebral perfusion have been inconsistent. Some studies report hypo-perfusion (36, 42, 43), whereas others have concluded that there is no difference between T2DM patients and healthy subjects (44, 45). A few studies (46, 47) have reported increased perfusion in T2DM. These inconsistencies are highly likely to reflect differences in the utilised perfusion imaging techniques rather than actual pathophysiological alterations. Imaging of the brain hemodynamic pattern can be conducted using a wealth of imaging techniques, each one measuring a slightly different property trying to capture the underlying perfusion pattern. Some techniques are focused on the blood velocity pattern at the level of the carotids (phase contrast- magnetic resonance angiography), whereas other try to image directly the delivery of water molecules to the brain tissue (ASL).

The ability of the cerebrovascular network to deliver the appropriate amount of nutrients and oxygen to the targeted tissues via the bloodstream can be disturbed in diabetes, rendering the brain sensitive to ischemia. This reduced perfusion is often attributed to impaired function of the endothelial cells and alteration in permeability of the BBB (36, 48) and has been found in both hyper- and hypo-glycemic conditions (10). Especially in T2DM, impaired endothelial function is found in nearly all cases and is closely connected to insulin resistance and small-vessel disease caused by prolonged exposure to hyperglycemic conditions (49-51). Hyperglycemia and insulin resistance initially cause inflammation and oxidative stress, triggering structural or functional alterations in the microvasculature, resulting in impaired endothelial function (52). One of the main functions of the endothelial cells, that becomes impaired in T2DM, is their ability to trigger vessel dilation in response to a stimulus in order to meet the increased need for blood. This property is described as Cerebrovascular Reactivity (CVR).

Findings regarding CVR, normally quantified as the % increase in blood flow following a vasodilating stimulus, have been more consistent with a lower CVR observed in T2DM patients (36, 42, 44, 53). The study by Selvarajah et al. (53) has reported a decrease in flow in both T2DM and IGT. CVR measurements are thought to capture changes in neurovascular coupling.

The consistency of the reported structural brain imaging findings might be linked to the fact that the utilised techniques are well-established, acquired with relatively high resolution and are reasonably well standardized. By contrast, perfusion imaging techniques are less well established with many different techniques in development, each one having its own advantages and disadvantages. This lack of standardization, along with the small disease effect relative to acquisition noise and limited study populations performed to date are some of the key contributors to the contradictory findings that have been obtained when perfusion imaging methodologies have been applied to T2DM patients. Another confounding factor to the inconsistent findings could be that some diabetic subjects might have developed a multitude of conditions such as hypertension (54) or peripheral neuropathy (55) which are connected with impaired perfusion.

Consequently, for diseases such as T2DM where the perfusion deficits are not prominent especially in the absence of cognitive impairment, no clear answer has emerged as to whether and how perfusion in the brain is altered. Hence, when evaluating the results of a study, one needs to examine thoroughly the characteristics of the cohort, the utilised perfusion imaging technique, its limitations, which property coupled to the underlying perfusion is measured and in which anatomical location it is measured.

1.2.3 Potential mechanism driving changes in the diabetic brain

One of the macrovascular complications of T2DM is atherosclerotic plaque formation inside major vessels (56). Additionally, hyperglycemia is connected with high blood viscosity. These effects could lead to flow alterations with reduced oxygen and nutrients reaching the tissue within a certain time-frame.

Excessive amounts of circulating glucose have a deleterious effect and are considered to affect the production and secretion of neurotransmitters such as nitric oxide, which is a vasodilatory neurotransmitter. This could lead to reduced CVR compared to healthy population.

The disruption of homeostasis due to the alterations in insulin production, increased circulating glucose and reduced glucose uptake, affects the function of the endothelial cells (57) and mainly their ability to initiate dilation or

constriction of the blood vessels (58, 59). Potential disruption of the BBB could lead to altered tissue CVR and perfusion. Under-expression of the glucose transporter GLUT-1 found in several animal studies could also drive changes in the diabetic brain (10).

Finally the amount of HbA1c circulating in the bloodstream of T2DM patients is high, suggesting that the appropriate amount of O₂ needed by the cells to function properly might not be met, since glycated hemoglobin does not deliver oxygen as efficiently as non-glycated (32). The implications of these effects can be multiple, ranging from structural to functional alterations due to changes occurring in the vasculature and the vascular supply.

Study hypothesis

Our study hypotheses were formulated based on existing findings and well-established pathophysiological mechanisms associated with diabetes. We hypothesise that cerebral hemodynamics are impaired in T2DM and in its prodromal syndrome, IGT. To examine this hypothesis we scanned a cohort comprised cognitively and neurologically asymptomatic IGT and T2DM patients and healthy volunteers. We also hypothesise that IGT and T2DM subjects present structural abnormalities in their GM and cerebral vasculature. Finally, we hypothesise that the patient cohort has an impaired carotid velocity and mean diffusivity pattern.

The described hypotheses were investigated using MR imaging modalities as the means to gain an insight into the brain of pre-diabetic and diabetic subjects. Our ultimate goal was to determine MR image-extracted metrics to be used in the future as disease biomarkers.

Chapter 2:

Magnetic Resonance Imaging theory and modalities

This thesis examines structural, functional and physiological changes in the brain of T2DM patients and subjects with IGT using a multitude of MRI techniques. The core modality investigated in this work is perfusion MR imaging using multi-time-point ASL. In the first part of this chapter, basic MRI theory is presented. In the second part, the focus is transferred to perfusion MRI and more specifically to ASL. In the final part of this chapter structural, diffusion weighted, fluid attenuation recovery (FLAIR) MRI and time-of-flight (TOF) and phase contrast (PC) magnetic resonance angiography (MRA) which were also used in this project are presented.

2.1 Nuclear magnetic resonance

Numerous imaging modalities have been developed over the last few decades for brain imaging (neuroimaging), with a view to extracting structural and functional information from acquired medical images. Structural neuroimaging can be used for identification of anatomical biomarkers, whilst functional neuroimaging enables assessment of changes occurring in the brain's physiological processes, such as alterations in hemodynamic or metabolic parameters. The three imaging modalities mainly used for cross-sectional brain imaging are: Positron Emission Tomography (PET) (60), Computed Tomography (CT) (61), and MRI. From these three modalities only MRI is completely non-ionising, making it the preferred choice when repeated scans need to be performed. The remainder of this Chapter describes basic Nuclear Magnetic Resonance theory relevant to the work presented in this thesis. PET and CT theory are not discussed, since they are out of the context of this thesis. The subsequently discussed MRI theory is based mainly on (62-65).

MRI is completely non-ionizing and does not require the introduction of a radioactive tracer, neither to acquire the signal of interest, nor to provide

contrast, thus making it a safe scanning technique. At the core of conventional MRI is the hydrogen nuclei, which consists of a single proton. Hydrogen atoms are by far the most abundant chemical species in the human organism. Protons are positively charged and spin round their symmetry axis, acting thus as a small magnet, giving rise to a magnetic moment. MRI measures the magnetization of a collection of atoms situated in a volume unit (voxel). The magnetization vector can be analysed as two constituent components: a longitudinal and a transverse vector.

When there is no external magnetic field applied, the magnetic moments of the protons are randomly oriented. When a magnetic field is applied, magnetic moments align either parallel (low energy state) or antiparallel (high energy state) to the applied field and precess around their axis with a characteristic frequency termed the Larmor frequency. There is a slight excess in the number of nuclear magnetic moments that align parallel to the applied magnetic field which is the low energy state (figure 2.1). This number can be determined by a Boltzmann distribution as in equations 2.1-2.3. The energy difference between the distinct spin states can be determined using the Zeeman equation ($\Delta E = h\gamma B_z$).

$$\frac{N_{\uparrow}}{N_{\downarrow}} = e^{-\frac{\Delta E}{k_B T}} = e^{-\frac{\hbar\gamma B_z}{k_B T}} \quad [2.1]$$

$$\frac{N_{\uparrow}}{N_{\downarrow}} \approx 1 - \frac{\hbar\gamma B_z}{k_B T} \quad [2.2] \quad n \approx \frac{N\hbar\gamma B_z}{2k_B T} \quad [2.3]$$

Where k_B is the Boltzmann constant, T is the system's temperature, ΔE is the energy difference between the distinct energy levels.

Magnetic moments precess with the same frequency, however their phase, remains random. Phase alignment can be induced using a radio frequency (RF) pulse of a certain duration and amplitude. The characteristics of the RF pulse are modulated so that the longitudinal magnetization is tipped towards the transverse plane by a factor α , which is called the 'flip angle'.

The applied RF pulse needs to have the same frequency as the Larmor frequency in order for the resonance condition to be fulfilled. Only then will the magnetization vector be effectively tipped by the flip angle. In order to create a delta-shaped function, which is an infinitely small rectangular-shaped pulse we

would require to apply in the time-domain an infinitely long sinc function. Hence, the RF pulse is not a delta-shaped function at the required Larmor frequency, but a narrow bandwidth pulse centered on the Larmor frequency (equation 2.4) created using a sinc pulse in the time-domain, thus exciting protons precessing within a certain frequency range.

$$\omega = \gamma * B_0 \quad [2.4]$$

Here, ω is the precessional frequency, γ is the gyromagnetic ratio (atom-specific) and B_0 is the applied constant external magnetic field. The value of M_0 , which determines the NMR signal, is described by equation 2.5.

$$M_0 = \frac{\gamma^2 h^2 N_s B_0}{4kT} \quad [2.5]$$

Where N_s is the number of spins. From this equation it follows that the NMR signal can be increased by either increasing the B_0 field strength or decreasing the temperature of the system.

Following application of the RF pulse, two phenomena take place in order for the system to return in equilibrium: recovery of longitudinal magnetization characterised by the T1 time-constant, a procedure involving energy transfer from the spin to the lattice; and loss of transverse magnetization governed by T2 time-constant, resulting from spin-spin interactions and loss of phase coherence in the transverse plane. This is the philosophy of the simplest MRI experiment that can be performed, which gives rise to a signal that can be measured with a coil. This resulting signal is termed the free induction decay (FID).

Regaining of the longitudinal magnetization results from re-emitting the absorbed energy back to the lattice in a process achieving thermodynamic equilibrium. The T1 relaxation time depends on two factors, the molecular tumbling rate and correlation time. The excited spins are subject to molecular motion, described as molecular tumbling, which involves vibration, rotation and translation. Free water molecules have a high tumbling rate since they move freely, whereas bound molecules have a lower tumbling rate. The second factor to be considered, correlation time (τ_c), describes the duration of the interaction of water molecules with macromolecules. Prolonged contact between the excited molecules and macromolecules will result in faster loss of the absorbed energy due to molecular interactions. Hence, water molecules have a high

tumbling rate but short correlation time, giving rise to a long T1. Molecules within soft tissues have a slower tumbling rate close to the Larmor frequency and a larger correlation time, hence T1 will be shorter. Molecules within solids have reduced tumbling rate but high correlation time, hence a long T1.

The loss of transverse magnetization can be attributed to the combined influence of two effects, one attributed to the random interactions between spins and one attributed to field inhomogeneities. The relaxation time incorporating the effects of field inhomogeneities, termed T2*, is shorter than the intrinsic T2 relaxation time. The part attributed to field inhomogeneities can be regained by applying a 180° refocusing pulse, giving rise to spin-echo techniques, where the resultant echo signal depends on T2, rather than T2*. T1 and T2 relaxation times form the basis for numerous imaging sequence designs, with T1-weighted sequences generally preferred for examination of structural information and T2-weighted sequences preferred for demonstration of pathology.

T1 and T2 relaxation times are tissue specific and are influenced by the chemical environment in which the hydrogen protons are situated (figure 2.2). The ¹H protons contributing to the NMR signal are mainly found in water molecules. Water is 50-70% of the human body and its movement can be relatively free or more restricted. Generally, more restricted or solid structures tend to have shorter relaxation times. These differences between T1 and T2 relaxation times between different tissues are the reason for the excellent soft tissue contrast in MRI.

When MRI sequences are designed, there are typically two key acquisition parameters that define the sensitivity of the sequence to T1 and T2 effects: the time between two excitations (repetition time - TR) and the time between one excitation and the readout (echo time - TE). In spin-echo imaging a 180° refocusing RF pulse is applied, refocusing spins that were initially defocused after the initial applied pulse. As the spins refocus following application of the 180° pulse, the signal measured in the transverse plane increases to a peak and then decreases again. This rise and fall in signal is known as a spin-echo. In gradient-echo sequences a defocusing gradient is applied during the FID. Subsequently a refocusing gradient of the same magnitude and opposite polarity refocuses the defocused spins generating an

echo. For example, in a spin-echo sequence, the measured signal S is associated with the following equation (2.6)

$$S = k * PD \left(1 - e^{-\frac{TR}{T1}} \right) e^{-\frac{TE}{T2}} \quad [2.6]$$

In equation 2.2, k represents an instrumental scaling factor and PD is the proton density. The term inside the brackets determines the T1-weighting and the exponential outside the brackets the T2-weighting. Hence, for a T1-weighted experiment the effect of term inside the brackets needs to be maximum, so a short TR is required, and the effect of the exponential outside the brackets needs to be a minimum, so a short TE is required. For a T2-weighted experiment, TR and TE need to be long. When TE is short and TR is long, the contributions from the T1 and T2 terms are minimised and that leaves us with a proton density image. The combination of short TR and prolonged TE is not generally used.

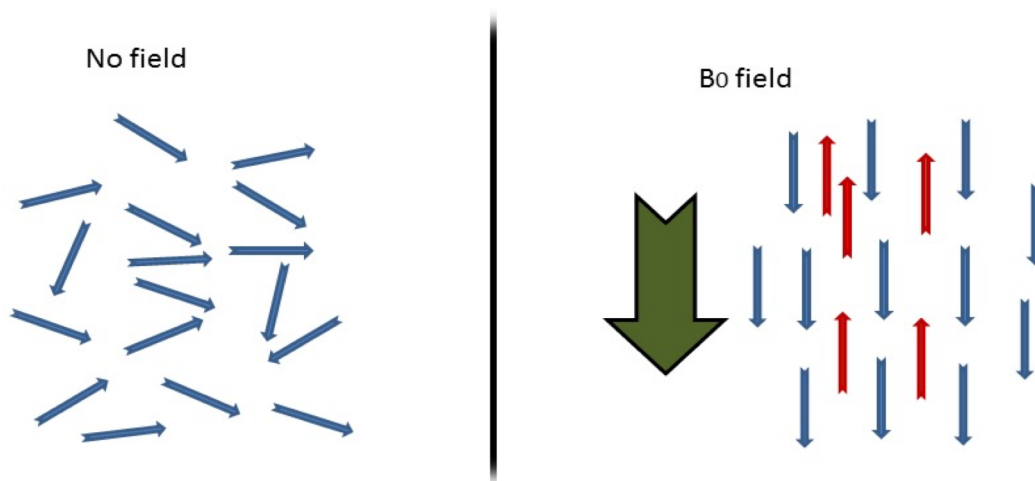


Figure 2.1: Magnetic moment orientation with and without the application of an external magnetic field. On the left, magnetic moments are randomly oriented when no field is applied. After the application of an external magnetic field B_0 (green arrow), a slight excess of magnetic moments tend to align parallel to the field (blue arrows).

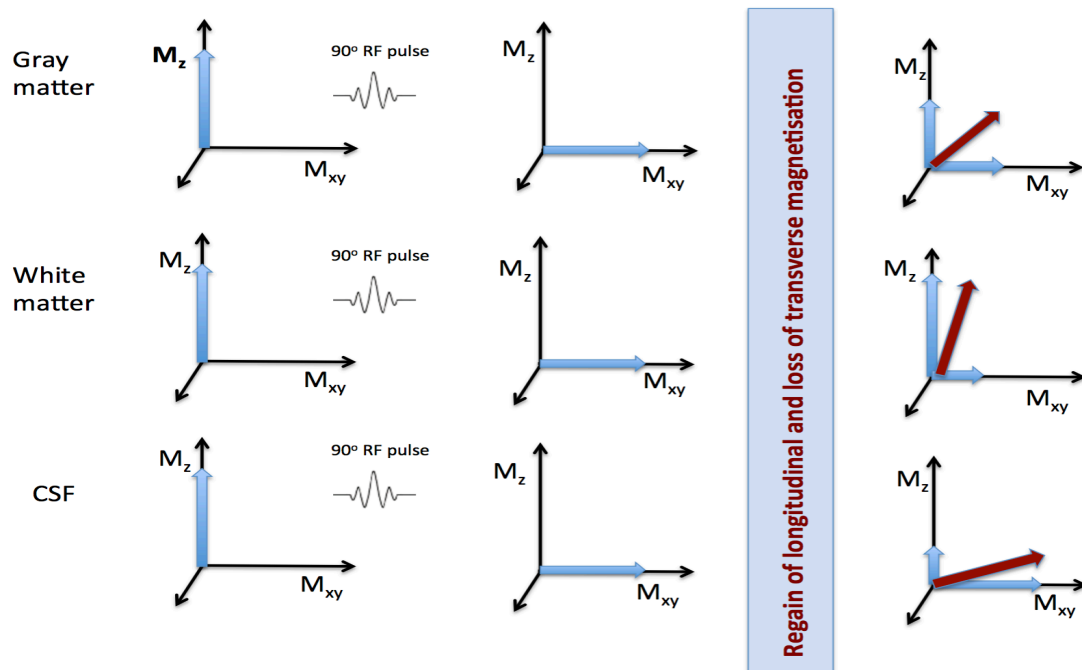


Figure 2.2: MRI principle for the main 3 tissue types in the brain. When a magnetic field is applied protons align with the field and precess with the Larmor frequency. An RF pulse is applied which causes a phase shift and aligns the phases, eliminating longitudinal magnetization (M_z), and creating a transverse magnetisation (M_{xy}). When the pulse is removed two phenomena take place: regaining of longitudinal magnetization governed by time T_1 (the convention is that this time describes the recovery of M_z to 63% of its peak value) and loss of transverse magnetization in time T_2 (which describes the time at which M_{xy} decays to 37% of its peak value).

The spin-echo sequence can be modified so that an initial RF pulse of 180° is applied prior to the 90° pulse. This leads to the definition of another commonly encountered acquisition parameter, the inversion time (TI), which is defined as the time between the initial 180° pulse and the following 90° pulse. In such a case, the opportunity is given to null signals from certain tissue types if the 90° pulse is applied at the zero-crossing time for that particular tissue type. This method is commonly used to null the signal from either CSF in the FLAIR sequence or from fat (short TI inversion recovery (STIR) sequence), but can also be used to introduce additional contrast between certain tissues.

2.2 MR image formation

In order for an image to be reconstructed from the MR signal, the information needs to be encoded spatially. This is feasible by using magnetic field gradients, which cause the magnetic field to vary with position. The

precessional frequency at each position will be dependent on the magnetic field strength at that position, as determined by the Larmor Equation. Hence, the signal strength at every image position along the gradient direction can be inferred by the strength of the signal at every frequency. The higher the applied magnetic field gradient, the greater the frequency separation is between adjacent points. At the time of writing this thesis, typical maximum gradient strengths on 1.5T and 3T clinical scanners range between 30 and 45 mT/m. The rising time of the gradients are typically in the vicinity of 0.1 - 0.3 ms and considered along with the gradient strength they give rise to the slew rate (gradient strength / rising time). Thus, typical slew rates are in the range of 150 - 200 mT/m/ms. The applied RF pulses have a typical maximum amplitude of 10 – 50 μ T and duration between 2 – 10 ms (66).

Slice selection

A linear gradient is typically used along the head-foot axis, so that the Larmor frequencies along this axis vary according to the position. Based on the desired slice thickness, the RF pulse bandwidth is modulated accordingly to excite only the limited range of frequencies corresponding to the spatial position of the slice. This gradient is termed the slice selective gradient (G_z).

In plane localization

Once the slice has been excited using the slice selective gradient and frequency selective RF pulse, the spatial position in the x-y plane needs to be encoded. This can be done by turning on and off the phase (G_y) and frequency (G_x) encoding gradients in order to induce position-specific changes in the precessional frequency and phase of the spins, which will be interpreted as spatial differences from the Fourier transform. The phase encoding gradient is briefly switched on along one axis (conventionally denoted y) following the slice selective gradient. This results in a position-dependent phase difference encoded in the magnetization across the axis on which the G_y gradient is applied. Subsequently, a frequency encoding gradient G_x is applied along the x-axis during readout of the echo signal inducing frequency differences in the spins along the axis of implementation (figure 2.3).

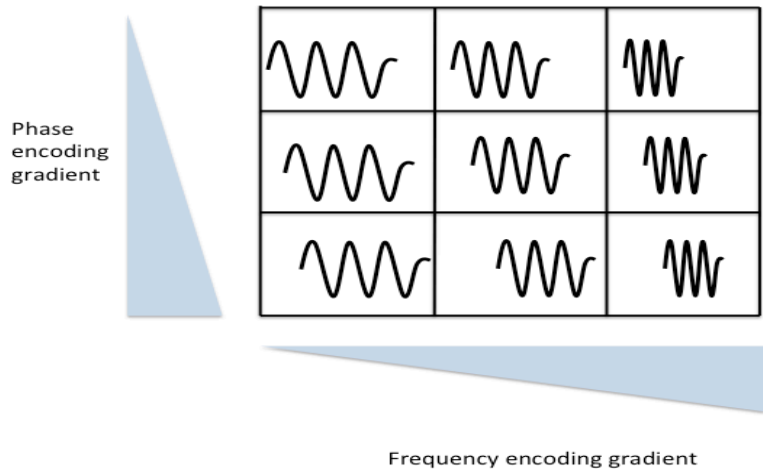


Figure 2.3: Phase and frequency encoding in 2D depiction.

In order to record multiple slices, the G_z gradient is applied for each slice location, with the central frequency of the slice selective RF pulse shifted to correspond to the desired slice position and the 2D localization procedure repeated, as described above, once the slice has been excited. The magnetic field gradients can be depicted in a pulse sequence diagram (figure 2.4) that shows the timing of the gradients relative to the applied RF pulses and signal readout. These diagrams can be particularly useful to provide a visual representation that helps to understand the intricacies of complicated pulse sequence designs.

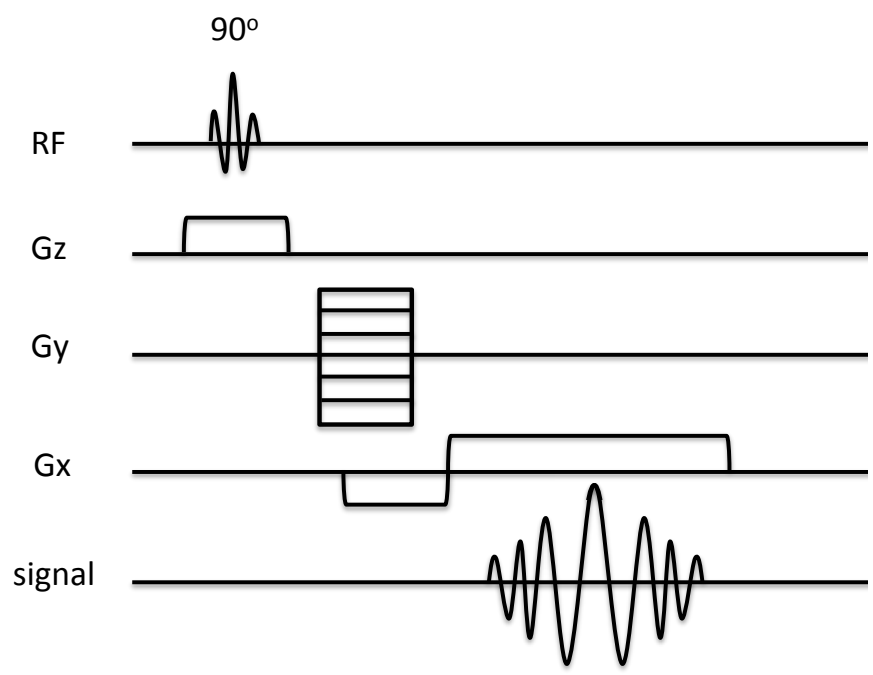


Figure 2.4: Example pulse sequence diagram. RF is the radiofrequency pulse applied to tip the magnetic moments by 90° in this case. The gradient pulse in G_z is the slice selective pulse,

exciting a certain slice, G_y is the phase encoding gradient and G_x is the frequency encoding. In G_x two equal and opposite pulses can be seen, this gradient reversal forms a gradient echo from which the signal (echo) is measured.

k-space

An RF coil records the generated MR signals, which are digitised and stored in a format organized to accommodate the recorded signals according to their spatial frequency termed the k-space. The number of samples forming k-space and its size depend on the acquisition's field-of-view (FOV) and voxel size (Δx). In particular, the distance between two k-space samples (Δk) is equal to $1 / \text{FOV}$ and the dimension of k-space ($2 \cdot k_{\text{max}}$) is $1 / \Delta x$. The horizontal axis in k-space is termed the 'frequency-encoding' axis (k_x) and the vertical axis is termed the 'phase-encoding' axis (k_y). An interesting parallel between lenses and k-space was drawn by R. Mezhich (67). In his paper, he explained how k-space can actually be described as an equivalent to a lens, which is the intermediate Fourier space between an image and its idol; an explanation facilitating understanding of the complex nature of k-space.

Every line of k-space corresponds to a certain value of the phase encoding gradient. The peak of the echo is centered along the vertical k_y axis of k-space. The higher frequency components reside in the periphery and are associated with more fine details, whereas, the low frequency components are at the centre of k-space and are associated with properties such as contrast. The sampling rate of the acquired signals determines the resulting image resolution.

In conventional imaging (gradient-echo, spin-echo imaging) the phase-encoding gradient is pulsed every TR and hence one line of k-space is filled every TR. In echo-planar imaging (EPI) the whole k-space is filled in time TR (68). Full 3-D encoding in k-space utilises the addition of a secondary phase-encoding gradient in the 3rd spatial dimension (69) instead of a slice-selective gradient. Important variants of the conventional approaches are fast gradient-echo or fast spin-echo acquisitions (70, 71) which are used extensively and provide multiple phase-encodes per TR but not in a blipped fashion as in EPI.

The conventional way to fill k-space is a line-by-line 'Cartesian' way, as illustrated in figure 2.5. The main alternative k-space trajectories include spiral,

zig-zag (utilised in EPI) and radial; each one with its own advantages and disadvantages (72, 73). Radial and spiral sampling's competitive advantage is that they are less sensitive to motion artifacts, an attribute leading to their increasing utilisation.

Conversion between k-space and the image space, is performed by using the discrete Fourier transform.

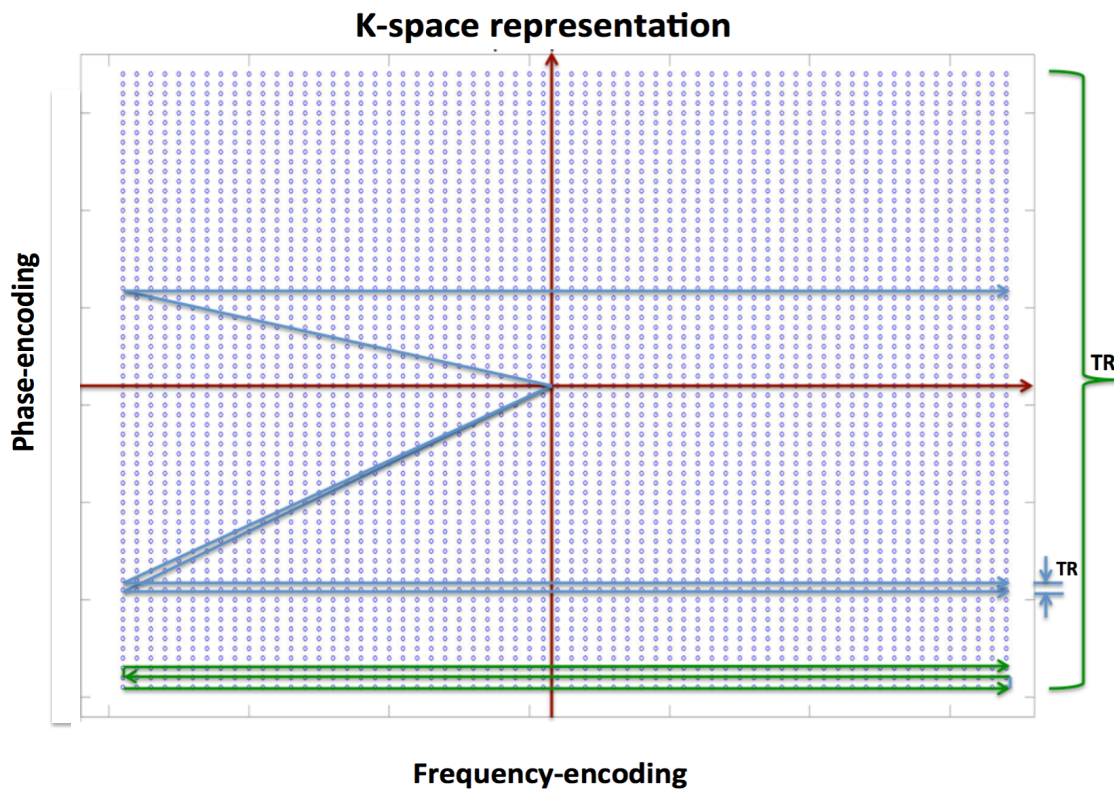


Figure 2.5: Representation of k- space trajectory for conventional and 2D single shot EPI readouts. With the green line, the EPI readout philosophy is represented. Every line is read in the frequency encoding direction, subsequently the readout is blipped and a line is read at the opposite direction. The whole of k-space is read in time TR. In conventional imaging (blue line) the phase gradient is pulsed every TR localizing the readout in a particular line in the phase encoding direction starting every time from the centre of k-space. This particular line of k-space is read in time TR.

2.3 EPI imaging and artifacts

In single-shot EPI all information needed for image reconstruction can be acquired in a “single-shot”, hence it is commonly used for rapid imaging. The pulse sequence diagram for an EPI acquisition can be found in figure 2.6. Following a slice-selective RF excitation pulse, a train of gradient pulses is

applied in the frequency encoding direction. Every echo can be encoded in the vertical (phase encoding) axis.

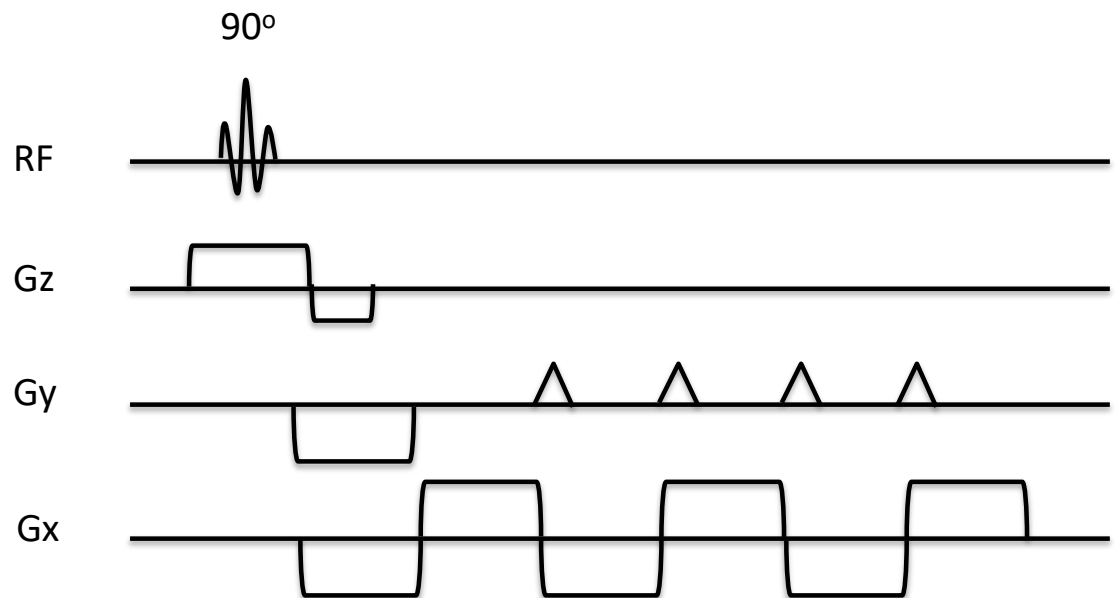


Figure 2.6: **EPI pulse sequence diagram.** Adaptation based on Haacke et al. 1999 [64].

The fast readout combined with the fact that every line in k-space is read in alternate directions, introduces a multitude of artifacts which might be present in the final image, distorting the result (69). One of the artifacts commonly found in a single-shot EPI acquisition, is termed “water-fat shift” or “chemical shift” artifact. It is attributed to the different resonance frequencies of the water and the fat and may result in distortions of the image, with a ‘ghost’ image of the fat appearing in the region of interest (figure 2.7). This effect is caused due to interpretation of different frequencies by the inverse Fourier transform as different spatial locations. As a result the fat signal might end up displaced by numerous voxels in the phase encoding direction. The higher the field applied for imaging, the higher is the frequency separation of fat and water and thus the distance between them increases (74). Techniques for the mitigation of this artifact have been developed (for example fat suppression pulses), however all of them deal with its presence at the level of the acquisition of the image (75).

Another common artifact in EPI acquisitions is the “ghost” ($N/2$ Nyquist) artifact, which appears as a ghost image in half the field of view (figure 2.7). This artifact occurs due to the very fast k-space scanning in the frequency encoding direction in alternate directions. As a result the odd and even echoes might be misaligned (76). A magnetic susceptibility artifact (figure 2.7) might be

present in the final image attributed to field inhomogeneities caused by the magnet or from the patient (69).

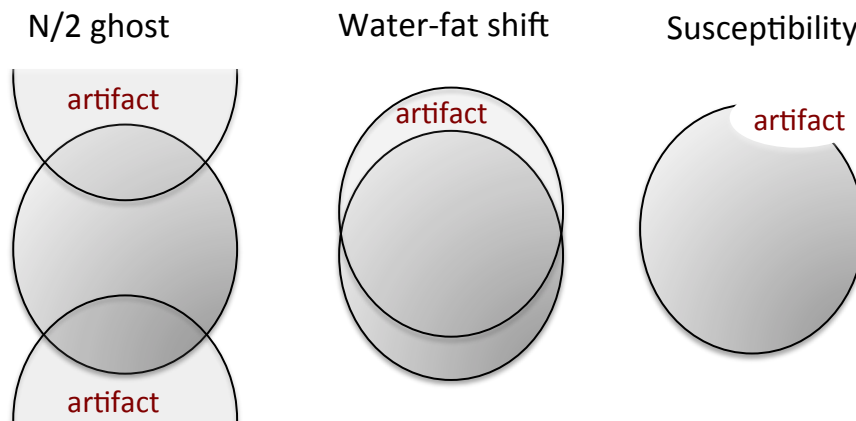


Figure 2.7: Example EPI artifacts. left: Example of a N/2 ghost present at half the field of view. Centre: example of the chemical artifact, right: example of one form that the susceptibility artifact can acquire.

2.4 Perfusion and CVR imaging

One of the functional characteristics that can be evaluated with MRI is perfusion, which is indicative of nutrients and oxygen delivery in tissues via the blood flowing in the vasculature and is connected to a tissue's viability (77). The gold standard for perfusion quantification is considered to be ^{15}O H_2O - PET (78). Other techniques used are single-photon emission computed tomography (SPECT) (79), transcranial Doppler ultrasound (TCD) (80) and MRI-based techniques.

Exogenous or endogenous contrast agents aside, the rationale behind perfusion imaging is common. A tracer is followed through the vasculature and the concentration in the tissue at a given time affects the measured MRI signal. The contrast agent when the BBB is intact in the case of dynamic susceptibility contrast (DSC)-MRI remains intravascular, hence the induced susceptibility effect is monitored. In ASL, since the hydrogen protons are monitored, the actual tissue delivery can be detected.

A vibrant area of research in the MRI field is physiological and functional imaging. As part of this effort, a multitude of MRI methods for brain perfusion imaging have been developed, namely: DSC-MRI (81), ASL-MRI (82), intravascular incoherent motion (IVIM) (83), phase contrast magnetic resonance angiography (PC-MRA) and vascular space occupancy (VASO) (84). A more

recent development, which is still at an experimental state, is the use of hyperpolarised Xenon as a contrast agent (85). Functional blood oxygen level dependent (BOLD) functional MRI (fMRI) can also be used for CVR quantification (86) but it cannot provide quantitative perfusion measurements. All these techniques capture slightly different aspects of perfusion, such as water delivery to the tissue, blood velocity and changes in arterial blood volume. DSC-MRI is a popular perfusion imaging modality owing to its simple implementation and good contrast. ASL is also a popular technique with an undisputable momentum at the moment due to: concerns about gadolinium toxicity (Gd is the main contrast mechanism in DSC-MRI), widespread introduction of 3T systems into clinical settings, commercial availability of ASL by all major scanner manufacturers and due to the numerous developments in the ASL acquisition strategies. VASO and IVIM have been occasionally implemented in clinical studies; however they are not as popular. PC-MRA does not explicitly measure perfusion, it bears similarities with TCD since both techniques measure blood velocity.

While there are several metrics of interest related to perfusion, including CBF, cerebral blood volume, arterial transit time (ATT) and oxygen extraction fraction, the physiological metric that is most commonly studied in perfusion imaging is CBF. Evaluation of CBF has been routinely used in dementia (including Alzheimer's disease) (87), brain tumours (88) and cerebrovascular disease (89) in order to account for perfusion patterns (mainly regional hyper-perfusion or hypo-perfusion) which could be associated with the condition under examination.

The ability of the brain to increase perfusion as a response to a vasodilating stimulus is indicative of the existing cerebrovascular reserve. Decreased CVR has been found in Alzheimer's (90) and has been connected with cognitive changes in T2DM (91). CVR quantification requires a vasodilating trigger, to allow for measurement of relative CBF changes compared to baseline. Typical stimuli used include: pharmacological challenge; hypercapnia; reduction of blood pressure and carotid stent placement (92, 93).

A pharmacological stress test is usually performed by injecting a potent vasodilator, such as acetazolamide (ACZ), intended to increase vasodilation, by means of vascular smooth muscle relaxation (93). The response to the

implemented stimulus is different between healthy individuals and individuals with reduced cerebral vasodilative capacity (94, 95). The response of healthy individuals to the stimulus is an increase in local perfusion of about 20-40% in all vascular territories (96). On the contrary, in individuals with impaired perfusion the response can vary between mild, no response, or even a reduction in perfusion (97). This might imply that their system has reached the maximum vasodilatory capacity previously during normal function (98, 99).

Okazawa, Yamauchi et al. (98) have questioned whether a reduction, or an increase lower than expected, in regional CBF after ACZ challenge in patients with cerebrovascular disease, is indicative of reduced ability to vasodilate. Instead, they have suggested that this phenomenon could also be explained by the fact that blood volume is not increased. Demolis et al. (100) have questioned whether ACZ can accurately cause the same effect as autoregulatory vasodilation.

Three methods have been used in the past for hypercapnia challenge: breath-hold, re-breath and gas mixture administration containing an elevated concentration of carbon dioxide (101). It has been shown in vivo that increased concentration of CO₂ results in vascular smooth muscle relaxation via a mechanism involving alteration of extracellular pH, activation of potassium channels, membrane hyperpolarization and reduction of calcium concentration inside the cells (102).

2.4.1 Arterial spin labeling

ASL is a perfusion imaging technique that doesn't require the injection or inhalation of contrast agents, as it uses water molecules as a freely diffusible tracer (82). Being an MRI technique, ASL is also completely non-ionising. Using water as the tracer has the inherent advantage of having a short half-life so it can be used multiple times (103). ASL allows multiple measurements to be made on the same person, with the only considerations being the duration of the scanning session and the comfort of the scanned individual who might move, giving rise to motion artifacts.

The rationale behind ASL is that the subtraction of images acquired with (labeled) and without (control) magnetically labeled hydrogen protons gives rise to perfusion weighed images (figure 2.8). After labeling, a short time-gap (inflow

time) is allowed for the protons to reach the tissue of interest and exchange water. The labelled protons at the time of imaging have not fully recovered; this gives rise to subtle differences between control and labelled images (104, 105). Subtraction renders this technique sensitive to motion artifacts (106).

Induction of differences in the magnetization vector between control and labelled acquisitions is common in all ASL techniques. However, the control image is not always one with non-inverted spins. For example, in some techniques the difference between the control and the labelled experiments is achieved with global inversion (control) followed by local inversion (labeled).

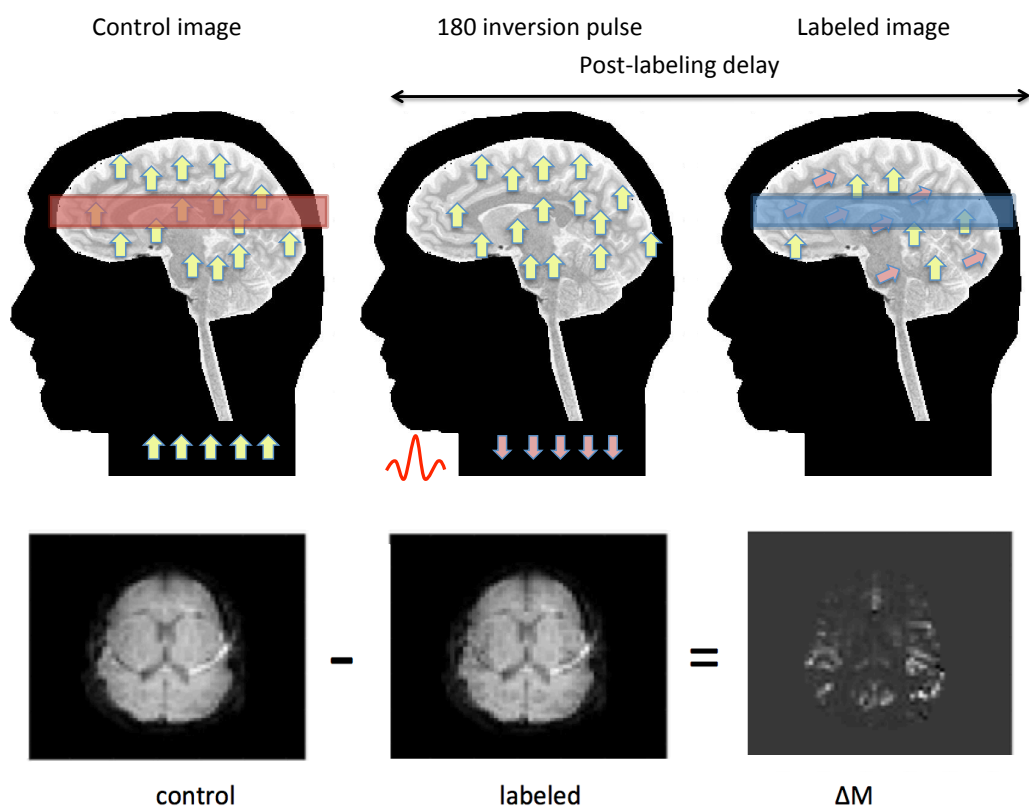


Figure 2.8: Philosophy of ASL MRI. Pairs of control and labeled images are acquired. Their subtraction yields information about perfusion.

Major disadvantages of ASL are its low signal-to-noise ratio (SNR) and low spatial and temporal resolution. In order to account for low SNR, averaging of multiple acquisitions is utilised, whereby pairs of images are acquired approximately every 4 seconds. Typical acquisition times are on the order of 5-10 minutes. Other means to increase SNR include using increased magnetic field strength or by using a phased array receiver (107). This inherently low

SNR is attributed to the fact that only 1% of tissue water is replaced every second by perfusion in GM (108). For a bolus duration of 1 - 2 seconds, the captured signal difference is at the level of 1 – 2 %, since the introduced delay between labeling and acquisition further reduces the signal due to magnetization relaxation.

In ASL, spiral or EPI sequences are typically used to ensure rapid imaging (109). Other utilised read-out schemes include: Rapid Acquisition with Relaxation Enhancement (RARE) (70), Gradient and Spin Echo (GRASE) (110) and balanced Steady-State Free Precession (bSSFP) (111). The distinctive characteristics between different ASL methods has to do with both the pulse sequences used for labeling and the readout strategy (112) .

Compared to BOLD fMRI, ASL has better spatial localization as it images the delivery in the tissue and not the susceptibility effects created by an endogenous intravascular tracer (113). Its temporal resolution though is worse than BOLD. Its major advantage is that it allows for quantitative perfusion measurement. In BOLD, a baseline acquisition and an acquisition after a task are typically performed, allowing only for qualitative assessment of the difference between the two (113). The BOLD signal relies on the local changes in concentration of oxy- and deoxy-hemoglobin and the magnetic susceptibility differences that induces, whereas ASL images the hydrogen protons within the vasculature directly.

2.4.1.1 CASL, PASL, pCASL and other ASL variants

The four major ASL categories are: pulsed ASL (PASL), continuous ASL (CASL), pseudo-continuous ASL (pCASL) (figure 2.9) and spatially non-selective ASL (114). Sometimes pCASL is presented as part of CASL, however due to its hybrid nature it can formulate a category on its own.

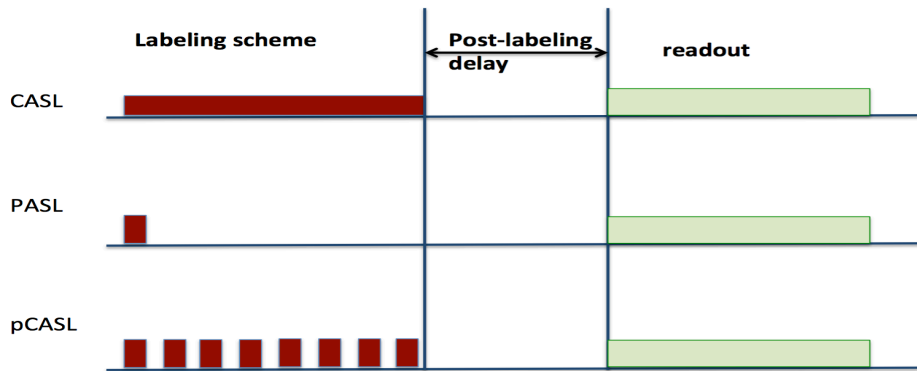


Figure 2.9: CASL, PASL and pCASL philosophy. In CASL the labeling is continuous, in PASL a short pulse is applied and in pCASL a train of short pulses instead of a continuous labeling is applied. A post-labeling delay allows for the tracer to arrive in the tissue of interest and perfuse it. Subsequently, in the readout period, the image is acquired.

CASL, uses a long RF pulse along with a slice-selective gradient, the slice being relatively thin. The spins passing through this slice are continuously inverted using flow-driven adiabatic inversion. It has a higher SNR compared to the other techniques (82). PASL uses short RF pulses to tag a blood volume in a thick slab and its competitive advantage is its high tagging efficiency (115, 116).

CASL was the first ASL technique suggested. Nowadays its usage is limited due to the hardware requirements and the high RF deposition to the scanned individual. This results from the requirement for a continuous long RF labeling pulse. Pulsed ASL on the other hand has limited hardware requirements compared to continuous ASL, lower RF deposition, better inversion efficiency but lower SNR. pCASL is a pseudo-continuous technique achieving labeling by using multiple short RF pulses. The SNR of pCASL is higher compared to PASL but the inversion efficiency is lower since the pulses used are not adiabatic (117). Four popular ASL techniques are shown schematically in figure 2.10.

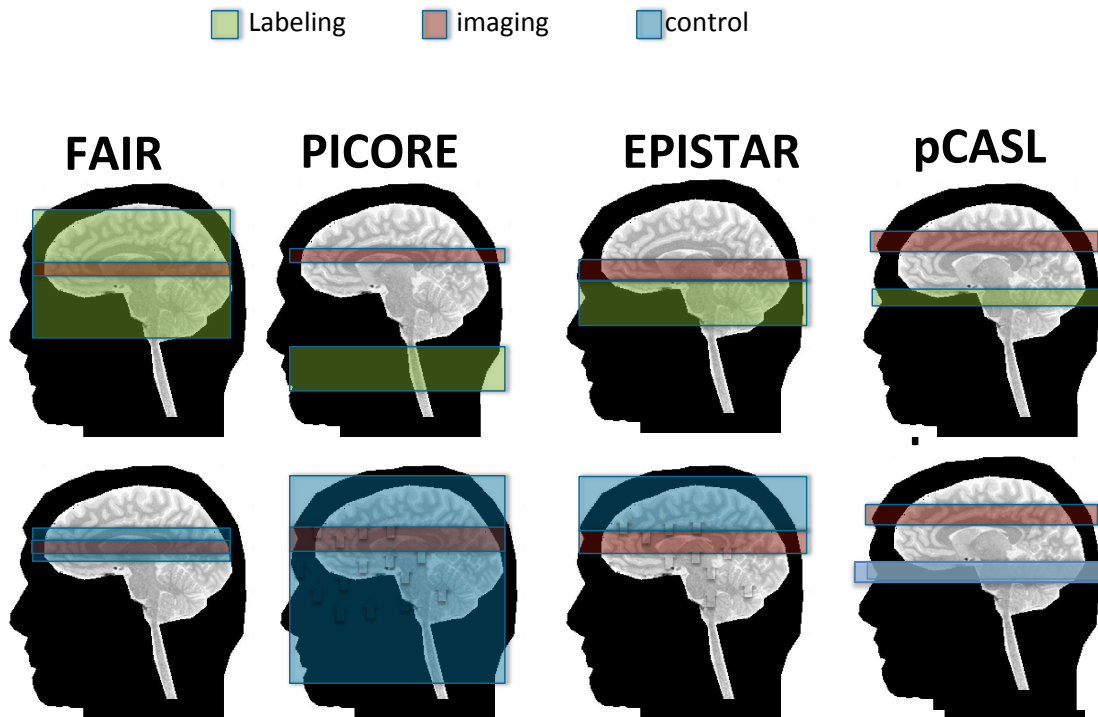


Figure 2.10: Control, label and imaging planes shown schematically for four ASL implementations. FAIR, PICORE and EPISTAR are all pulsed ASL variants. In the last column, the pCASL scheme is depicted. Green (labeling) and blue (control) regions represent the areas whereby inversion pulses are applied. The red slice represents the anatomical area which is imaged.

Spin inversion is of utmost importance in ASL since labelling is either applied in a big slab for a small time-window or in a small slab for a more extended time-frame and the labelling of moving spins needs to be effective. Non-effective spin labelling could result in erroneous perfusion estimation since the ASL contrast relies on the difference between labelled and non-labelled images. Hence an inversion efficiency of 70% would imply that around 30% of the perfusion differences could be masked out due to identical signal between the control and labelled images. As a result, an approach that reassures spin inversion will be efficient needs to be utilised. In order for the inversion to be successful (i.e. the majority of spins to be inverted efficiently) the adiabatic condition needs to be fulfilled, that is, the moving spins need to be inverted at a particular rate so that their magnetization is effectively tipped. During the adiabatic inversion the B1 field passes gradually from off-resonance to on-resonance and then beyond resonance. This is achieved by modifying its frequency and holding steady its amplitude. Application of an initial off-resonance field results in the magnetization precessing around an effective

field. The gradual increase of the frequency of the B1 field will result in the net magnetization vector following the effective field in its transition from off to on and finally beyond resonance. The adiabatic pulses utilised in PASL, are frequency and magnitude modulated hence they influence spins in different positions differently and more effectively than flow-driven adiabatic inversion does. The conventional RF pulses utilised in MRI are simply amplitude modulated and not frequency modulated as the adiabatic pulses.

Pulsed ASL utilises adiabatic pulses and this is what gives the PASL techniques higher inversion efficiency. In CASL and pCASL the adiabatic inversion can be achieved using flow-driven adiabatic inversion which is not as effective (117). This is the reason for the lower inversion efficiency of (p)CASL.

Being a hybrid technique, pCASL (118) combines some of the advantages of CASL and PASL, as it has higher SNR than PASL and higher inversion efficiency than CASL. Instead of a continuous pulse, a sequence of RF pulses with short duration along with a slice selective gradient are applied. This technique is heavily used for perfusion quantification, providing results in a good agreement with the gold standard PET (119, 120).

In 2015, scientists across Europe decided to produce a recommended ASL protocol to provide some standardization, without it being a discouragement to the development of new methods (108). They realised that the multitude of available labeling and readout schemes was having a negative impact on the translation of ASL-MRI into a standard clinically used protocol. Their recommendations suggest using pCASL as the optimal labeling scheme with one inversion time, no crusher gradients and a 3D readout scheme such as RARE or GRASE. In this 'white paper' the writers stress that using multiple inversion times renders processing more difficult, but might have the potential to provide more accurate quantification of CBF and the capacity to quantify ATT (108).

One of the major disadvantages of the aforementioned techniques in their regular implementation (one inversion time, no-crusher gradients) is that they are not insensitive to the time that it takes for the labelled bolus to reach the tissue of interest (ATT). ATT is one of the most important parameters that characterise the perfusion process and needs to be taken into account for perfusion evaluation. It has been suggested that in patients with Moya-Moya

disease, atherosclerosis (105) and steno-occlusive disease (112), CBF might be overestimated due to residual label in the vasculature. On the other hand, especially in elderly cohorts, CBF might be underestimated due to increased ATT (121, 122). Two suggested methods that account for ATT are the use of a multi-PLD technique, or to estimate ATT by dividing CBF from a non-crushed experiment with CBF from a crushed experiment (123).

Spatially non-selective ASL is a conceptually different technique, using a velocity or acceleration threshold as the criterion for imaging rather than a spatial constriction (114). The VS-ASL signal is the signal attributed to the spins, which at the time of labeling, have a velocity more than a specified threshold, but at the time of imaging, less than this threshold (124).

Indicative of the proactivity of the ASL community, is that following the publication of the consensus paper in 2015, there have been at least three review papers discussing exciting new developments (125-127). The primary areas of current research can be summarised as the development of techniques that are ATT-insensitive without SNR compromise (time-encoded ASL), territory mapping ASL, ASL fingerprinting, combined angiography and perfusion ASL and spatially non-selective ASL (125).

Since its introduction, ASL has been used to assess perfusion changes mainly in the brain (128) but also in the kidney (129), liver (130), skeletal muscle (131), bone marrow (132), placenta (133), pancreas (134), lungs (135) and myocardium (136). Conditions affecting the brain that have been investigated include: Traumatic brain injury (137), schizophrenia (138), depression (139), Parkinson's (140), Alzheimer's (141), chronic fatigue syndrome (142), multiple sclerosis (143), sickle cell disease (144) and diabetes (36). Following the ASL white paper which focused on the description of the optimal labeling and readout schemes, a guide targeted at neuroradiologists has been released by members of the consortium covering mainly the topics of acquisition parameters and clinical conditions in which ASL has identified successfully perfusion deficits (145).

2.4.1.2 Multi-TI/PLD ASL

There are numerous ways to acquire measurements with multiple post-labeling delays in order to capture differences in ATT. The first and crudest

solution is to acquire images at multiple inversion times in separate acquisitions, which is time-consuming. A second approach is to use a Look-Locker readout strategy (146) which has the ability to sample the recovering magnetization at multiple times by using low flip-angle EPI excitations (147). This allows for the retention of the whole magnetization recovery curve, however, every excitation reduces the magnitude of the signal and hence the SNR.

Time-encoded ASL with Hadamard encoding aims to create multiple sub-boli within the labeling scheme and the PLD time (148). It can be implemented using either CASL or pCASL. Sub-boli, either label or control, are interleaved within the labeling scheme based on a Hadamard matrix. The driving idea behind this scheme is to use non-identical repetitions in order to make full use of the scanning time (148-150).

2.4.1.3 Perfusion quantification

Quantification of perfusion relies on the indicator-dilution theory proposed by Zierler (151) and aims to quantify perfusion by employing a bolus tracking philosophy. Transit times of individual particles of the tracer forming the bolus are monitored and modelled as a distribution. The bolus can be either a magnetically labelled bolus (as in ASL), or an injected or inhaled contrast agent. Let the probability density function (PDF) of the transit times for every particle in the bolus be named $h(t)$ (equation 2.7). Then:

$$\int_0^{\infty} h(\tau) d\tau = 1 \quad [2.7]$$

The residual bolus in the tissue of interest is modelled as the cumulative distribution of transit times remaining in the tissue at the imaging time, thus taking the form of a residue function $R(t)$. At a time-point t , the residue signal can be calculated as follows (equation 2.8):

$$\int_0^{\infty} h(\tau) d\tau = 1 \Rightarrow \int_0^t h(\tau) d\tau + \int_t^{\infty} h(\tau) d\tau = 1 \Rightarrow H(t) + R(t) = 1 \Rightarrow \\ R(t) = 1 - H(t) \quad [2.8]$$

The volume of interest (VOI) has a single arterial input (C_{art}) and a single venous (C_{ven}) output (figure 2.11). The amount of tracer that has entered and left from this system in a time interval $[0,t]$ is as in equation 2.9.

$$tr_{in} = F \int_0^t C_{art}(\tau) d\tau \quad , \quad tr_{out} = F \int_0^t C_{ven}(\tau) d\tau \quad [2.9]$$

where F is the volume flow. The tracer inside the VOI will be $tr_{voi} = tr_{in} - tr_{out}$

From the system in figure 2.10, it follows (equations 2.10 - 2.12) that:

$$C_{ven}(t) = C_{art}(t) \otimes h(t) \quad [2.10]$$

$$tr_{voi} = F \int_0^t (C_{art}(\tau) - C_{ven}(\tau)) d\tau = F \int_0^t [C_{art}(\tau) - \int_0^\tau C_{art}(\tau) h(\tau - u) du] d\tau$$

by taking into account that $\int f(t) \delta(t - \tau) dt = f(\tau)$

$$tr_{voi} = F \int_0^t C_{art}(\tau) \int_0^\tau (\delta(\tau - u) - h(\tau - u)) du d\tau = F \int_0^t C_{art}(\tau) R(t - \tau) d\tau \quad [2.11]$$

CBF is calculated as $CBF = \frac{F}{V_{voi}}$

Hence, the venous output is: $C_{ven}(t) = CBF * C_{art}(t) \otimes R(t) \quad [2.12]$

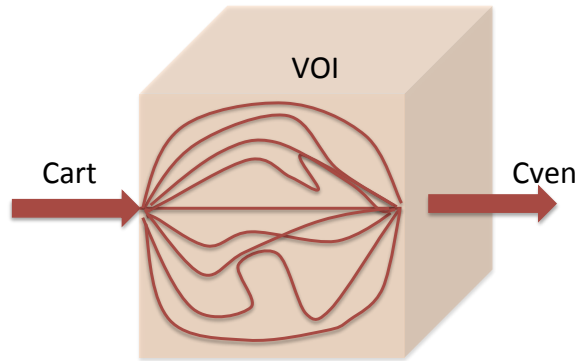


Figure 2.11: Schematic representation of a voxel (VOI) in perfusion MRI. The arterial signal (C_{art}) is the input, the venous (C_{ven}) signal is the output and inside the VOI capillary water exchange occurs. (Figure recreated based on Fieselmann et al. 2011).

For techniques that measure tissue perfusion, the tissue signal is modelled as a multiplication of the CBF by the convolution between the Arterial Input function (AIF) (or else C_{art}) and the residue function (R) multiplied by the CBF value (equation 2.13). Following the described approach, the perfusion system when an ASL acquisition whereby tissue signal is recorded is implemented can be approximated as a system with AIF as an input, $CBF * R(t)$ as an impulse response and the tissue signal $C(t)$ as the output (figure 2.12).

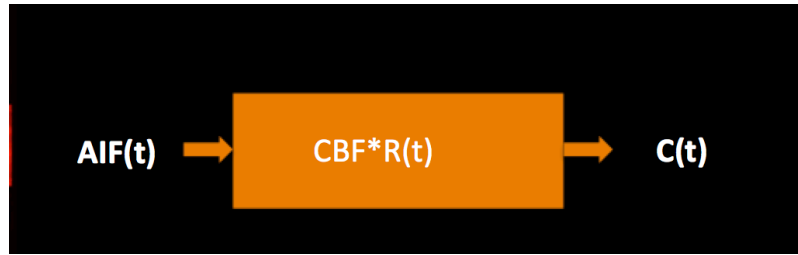


Figure 2.12: **Perfusion system at the tissue level.** AIF is the input, C(t) is the output and the transfer function of the system is CBF*R.

$$Tissue\ signal(t) = CBF * AIF(t) \otimes R(t) \quad [2.13]$$

Buxton's general kinetic model (equation 2.14) is the most heavily used model in pulsed ASL. The acquired tissue signal is denoted $\Delta M(t)$ and is modelled as follows:

$$\Delta M(t) = 2 * M_{a,0} * f * \int_0^t c(\tau) * r(t - \tau) * m(t - \tau) d\tau \quad [2.14]$$

- $M_{a,0}$ is the arterial blood equilibrium magnetization
- f is the CBF value,
- $r(t-\tau)$ is the remaining label in the vasculature after time τ ,
- $c(\tau)$ is the tissue delivery function and
- $m(t-\tau)$ is the magnetization relaxation term.

Theory suggests that the residue function decreases monotonically and has its maximum at time $t = 0$ s. However, dispersion effects, vascular anatomy and pathology, usually cause the residue function to deviate from the theoretical shape. In order to account for this effect, CBF is calculated as the maximum of the residue function. In signal processing, the impulse response (the residue function) is typically determined by taking the Laplace transform of the equation, ending up with a multiplication rather than a deconvolution. A transfer function can be calculated and by taking the inverse Laplace transform, the impulse function can be determined, if the AIF and tissue signal are known. When the signal is discrete, the Z-transform is used instead. An alternative technique for the determination of the transfer function, is to use an algebraic approach, more specifically, singular value decomposition (SVD) based techniques (152). Finally, model-based approaches can be used to model the shape of the residue function as an exponentially decaying function (153).

The AIF is one of the most important parameters that need to be determined in order to quantify perfusion, since it constitutes the input function of the system. Perfusion quantification requires that the actual shape of the AIF in the tissue of interest is known in order to be able to differentiate between a narrow AIF with a high value and a wide AIF with a lower value. The AIF can be measured either globally from a large artery, or locally, giving rise to numerous regional AIFs. A local approach is usually adopted when a cohort with pathology affecting the vasculature is examined. The most commonly used model for the AIF is a gamma-variate function (153). Other models commonly applied for the AIF are a box-car function and a gamma-variate function multiplied by a dispersion kernel (154).

2.4.1.4 QUASAR ASL

In 2006, a new model-free ASL approach for perfusion quantification was proposed (155). In this approach, the PULSAR (pulsed STAR labeling of arterial regions) labeling scheme (156), was combined with a Q-2 TIPS pulse scheme (157), which permits accurate definition of a labeling bolus. A multi-slice single-shot gradient-echo EPI readout was combined with a Look-Locker readout sampling (146). In this work, quantification of CBF by means of deconvolution was compared to fitting the acquired signal to Buxton's general kinetic linear model (158). Both approaches were used on the same dataset derived by using the newly developed quantitative STAR (signal targeting by alternating radiofrequency pulses) labeling of arterial regions (QUASAR) scheme and their efficiency was evaluated using simulations. SVD deconvolution for SNR = 10 and 15, led to CBF underestimation whereas parameter fitting to CBF overestimation.

As part of the QUASAR technique, pairs of control and labelled images were acquired for two different sets of experiments (with and without crusher gradients). The crusher gradients null the signal emerging from fast flowing spins due to residual tracer in major arteries, which is responsible for bright artifacts. Crusher gradients are particularly important as intraluminal artifacts can imply perfusion overestimation, leading in multiple cases in the need to exclude scans (89). However, they are not used in neonates due to unacceptably low SNR (159). Subtraction of these two images with and without

crusher gradients, delineates the shape of AIF. In order for the AIF to be defined in its wholeness, it needs to be normalized so as to take into account arterial Blood Volume (aBV). Hence when using QUASAR two distinct signals can be retained, one emerging from the intravascular compartment connected to aBV and one emerging from the extravascular compartment connected to CBF (figure 2.13).

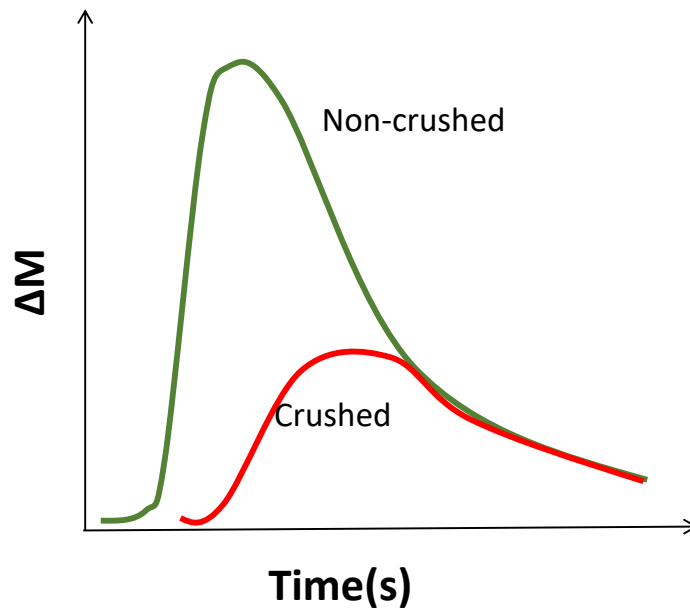


Figure 2.13: Qualitative depiction of the crushed (arterial compartment) and non-crushed (CBF compartment) signals obtained during the QUASAR acquisition.

In 2007, a short while after the technique was introduced, Petersen et al. (160) suggested a method to account for field inhomogeneities by including a low flip angle acquisition, which allows spatial mapping of the actual flip angle, rather than just assuming the nominal one. Chappell et al. (154) have proposed a correction factor for the calculated flip angle. After the introduction of QUASAR ASL, a multi-centre study took place in order to evaluate its effectiveness in perfusion quantification and its reproducibility, with very promising results (161).

The use of a Look-Locker readout, allows for retention of images at multiple inversion times, making the acquisition insensitive to ATT (162, 163). The fact that QUASAR ASL allows for quantitative CBF, aBV and ATT maps to be generated, the ability to label different vascular territories (164) and to calculate regional AIFs, render it a conceptually different technique from the commonly used single inversion time techniques. In particular, it can be useful

for studies focused on conditions, which can affect the transit time of the label from the arterial to the tissue compartment. QUASAR ASL has been used for perfusion imaging in studies investigating disease related hemodynamic changes in: multiple sclerosis (143); carotid stenosis (165); Parkinson disease (166); tumour, mainly gliomas (167, 168); Alzheimer's disease (141); and cognitive decline in middle-aged men (169). It has proven to be adept for quantification of CBF in GM, although with a tendency to underestimate it (170). QUASAR ASL has been shown to provide comparable results to PET (171) and good correlation has been found between QUASAR ASL and DSC-MRI (106).

The QUASAR pulse sequence as described in the original QUASAR publication, is shown in figure 2.14. An initial WET saturation scheme, which is typically used in spectroscopy, is applied in the imaging region (156). Subsequently, labelling takes place at the level of the carotids. The labelled acquisition comprises an 180° pulse. The control acquisition comprises two 180° pulses of half the power to induce identical magnetization transfer effects to the imaging region. Following that, a post-saturation scheme is applied. After a certain time, which in the typical QUASAR scheme is 650ms, the labelling region is saturated using a QUIPSS II scheme for a well-defined duration of the bolus. Subsequently, a small flip angle excitation (35°) is applied followed by crusher gradients where applicable (crushed acquisition). Finally, a 2D EPI readout is used. 13 such small flip angle excitations and EPI acquisitions are applied allowing for dynamic signals to be acquired.

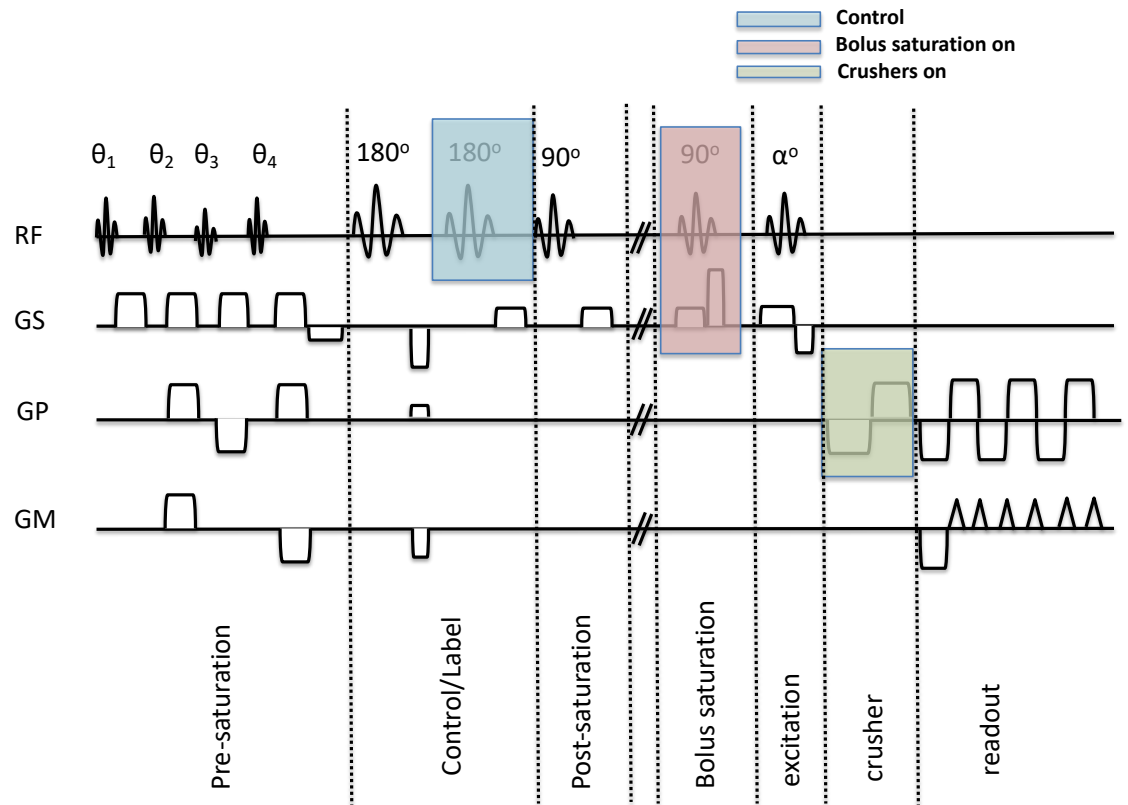


Figure 2.14: **QUASAR pulse sequence**; figure adapted based on **Petersen et al. 2006**. An initial pre-saturation WET pulse scheme is applied in the imaging area. Subsequently the labeling scheme is applied (light blue when the control scan is acquired). Post-saturation is applied in the imaging region. After a certain time a small flip angle excitation is applied and a QUIPSS II bolus saturation scheme is used for an accurate definition of the time-duration of the bolus (light pink). Crushers (light green) are turned on for the crushed acquisition. Finally an image is acquired using an EPI-readout.

2.4.2 Dynamic Susceptibility Contrast MRI (DSC-MRI)

In DSC-MRI a contrast agent (typically gadopentetate dimeglumine) is injected and passes through the vasculature. In the case of an intact BBB it remains largely intravascular within the brain and perfusion quantification relies on the induced susceptibility effects. One of the issues with this technique is that since the site of injection tends to be a vein in the arm, the injected tracer has a high degree of dispersion by the time it reaches the brain. At the time of imaging (7-10 seconds after injection), gadopentetate dimeglumine which is a paramagnetic agent, induces non-uniformities in the local magnetic field (susceptibility effects) which are imaged (172). Significant considerations regarding perfusion quantification with DSC-MRI include the definition of an accurate AIF and the second passage of the contrast agent (153).

The main drawback of using DSC-MRI is the injection of the contrast media. In 2006, a study connected Gadolinium to the development of nephrogenic systemic fibrosis, a very serious condition, in patients with abnormal kidney function (173). Following this, multiple studies investigated whether gadolinium-based contrast agents had any impact in persons without kidney dysfunction. It is now well-established that gadolinium is deposited in the brain, bones, liver and skin (174). Kanda et al. (175) have shown that there is an increase in gadolinium deposition in the brain, especially in dentate nucleus and globus pallidus in subjects without impaired renal function. In the meantime, a study group for Gadolinium toxicity found that people subjected to MRI scans with the use of gadolinium are reporting pain, skin irritation and confusion (176).

DSC-MRI has been for years the primary choice of clinicians for MR perfusion imaging due to its straightforward implementation and good contrast. Despite the quantification challenges, with an accurate AIF identified (153), it is more straightforward in interpretation, implementation and quantification compared to ASL variants (145). However, due to the increased concerns regarding gadolinium deposition, a trend toward techniques such as ASL is noted.

2.4.3 Vascular space occupancy MRI

The main idea behind vascular space occupancy (VASO) MRI is that the blood signal is nulled, resulting in an image dominated by tissue signal. Any change in the tissue signal can be attributed to changes in the inflowing blood, reducing the signal of the static tissue (177). VASO is an indirect technique to measure cerebral blood volume and it provides relative quantification, rather than absolute values. Variants of the VASO scheme have been proposed such as inflow-based VASO (iVASO) (178) and iVASO with dynamic subtraction (iVASO-DS) (179).

VASO is sensitive to both changes in arterial and venous compartments. The variant, iVASO, nulls only the signal from the blood directly beneath the imaging slice moving upwards, leading to a higher SNR and to selective sensitivity to the arterial compartment (178). In iVASO-DS, an additional control image without nulling is acquired, following a similar approach to the ASL

principle of control-label pairs (179). Good agreement of the cerebral blood volume values obtained with VASO and PET and iVASO and DSC-MRI has been reported (105).

2.4.4 Intravoxel incoherent motion MRI

Le Bihan et al. (83) developed a technique utilising motion sensitising diffusion gradients for perfusion assessment, so called intravoxel incoherent motion (IVIM). Perfusion was thus approached as a diffusion-associated process. At low b-values the signal attenuation in a diffusion weighted image is greater than expected solely from diffusion, due to the additional contribution to signal losses from water perfusing in the capillary bed. This additional signal attenuation can be modelled and used to calculate parameters associated with the perfusion contribution. Fitting the signal acquired over a range of relevant b-values to a bi-exponential model allows for separation of diffusion from microcirculatory perfusion effects. One of IVIM's interesting advantages is that both the microvasculature and the microstructure can be evaluated simultaneously (46). A direct equivalence between parameters calculated with IVIM and with conventional perfusion MRI techniques has been drawn. IVIM parameters involve blood perfusion fraction (f), diffusion coefficient (D) and pseudo-diffusion coefficient (D^*) of intravascular water, from these fD^* is the direct equivalent to CBF, f equivalent to CBV and D^* equivalent to mean transit time (180).

The technique has been used in the field of T2DM unravelling abnormal perfusion patterns in the hippocampus (46). Good agreement between IVIM and DSC-MRI in a study examining gliomas has been shown where the equivalence of fD^* to CBF was validated, but not the relationship between MTT and D^* (181). High correlation has also been found between IVIM and CBF calculated using pCASL (182, 183).

IVIM is a promising perfusion imaging technique, however the utilised fitting algorithms, range of b-values and quantification efficiency have not been thoroughly investigated (181). Compared to DSC-MRI it is non-invasive without the need to use contrast agents and measures perfusion at the level of the capillaries, on the contrary DSC-MRI depends on how leaky the BBB is and contamination from big arteries might be prominent. The technique, when

implemented for brain imaging, suffers from low SNR since the signal attributed to microcirculatory perfusion is at the level of 4%. IVIM is particularly popular for studying organs other than the brain (for example kidneys, prostate and liver) (184).

2.5 Structural, diffusion weighted MRI and MRA

Being an extremely versatile tool, MRI can provide many different ways to gain an insight of the brain's structure, function and physiology. In the following subsection a brief overview of some of the most important MR-based imaging modalities used in the present thesis is presented. The description of each technique was based mainly on Haacke and Brown (64).

2.5.1 3D T1-weighted image

As mentioned previously, to acquire a T1-weighted image the TR and TE times need to be short (with respect to underlying tissue T1 and T2) in order for the T1 effect to provide the majority of image contrast. Typical T1-weighted acquisitions are of high resolution and, depending on the vendor, they have commercial names such as magnetization-prepared rapid gradient-echo (MPRAGE) (185) and spoiled gradient echo (SPGR). MPRAGE is a purely 3D acquisition in the sense that data are not acquired slice by slice but rather the 3D encoding is achieved by using an additional phase encoding gradient in the slice encoding direction. Compared to its spin-echo counterparts, MPRAGE being a gradient-echo sequence is faster, more prone to artifacts and has a lower SAR. 3D T1-weighted images are popular in clinical settings since they are of high resolution and provide great anatomical details. Due to these attributes they are the main images used for brain volumetry. Useful biomarkers such as cortical thickness, GM, WM and CSF volume can be extracted from these images using appropriate software tools. 3D T1-weighted scans such as MPRAGE have been used in the past for studying structural changes in the diabetic brain, unraveling atrophies and regional differences in structures of interest (40).

2.5.2 Anatomical T2-weighted imaging

For T2-weighted imaging, the TR needs to be prolonged to enhance the T2 effect and reduce the T1 effect. In standard T2-weighted imaging long TR and TE (with respect to the underlying T1 and T2) times are used. Basic T2-sequences are: turbo spin echo (TSE) and FLAIR. With T1 values being on the order of 1s and T2 values being on the order of millisecond, T2 imaging is extremely useful in detecting abnormalities associated with an underlying condition. FLAIR is an inversion recovery imaging technique where the CSF signal is nulled (186). TR and TE are chosen in order to introduce heavy T2 weighting. Without the suppression of the CSF signal, typical T2 weighted images are of limited diagnostic usefulness since the tissue signal decays faster than the CSF signal (186). FLAIR is adept for depiction of white matter hyperintensities and tumors and can detect them with greater accuracy than T1-weighted sequences and T2-weighted sequences without CSF suppression (187). FLAIR has been used in diabetes studies to detect leukoaraiosis in WM with the findings being inconsistent (188).

2.5.3 MR Angiography

MRI can also be used for vasculature imaging. MRA imaging techniques are based on the fact that spins inside the vasculature are in motion. MRA acquisitions can be contrast enhanced MRA, using gadolinium as a contrast agent or non-contrast enhanced. The non-contrast enhanced methods include TOF-MRA and PC-MRA (189). Both are gradient-echo techniques with a short TR. Recently, ASL implementations have been used for quantitative MR Angiography (190).

In TOF MRA multiple RF pulses are used in the imaging region resulting in a steady state for static spins, while moving spins inside the vasculature do not experience all the RF pulses so they are left with a higher magnetization. One of the important factors to be carefully controlled when TOF-MRA is used is the applied flip angle to avoid saturation of the spins within the labeling slab; a large flip angle implies quicker saturation with a lower number of RF pulses (64).

In 2D phase contrast MRI, flow is acquired in one thick slice. The rationale is that velocity information can be encoded in the phase of the spins

using bipolar gradients. When a flow-encoding gradient is used, spins flowing in the gradient direction accumulate a phase. When a second opposite gradient is implemented then for every pixel there is an accumulated phase difference $\Delta\phi$. One of the most important parameters to be determined by the user is velocity encoding (V_{enc}), a velocity threshold introduced to de-phase fast moving spins above a certain velocity. Velocities lower than the chosen threshold are represented with a phase shift within the range from -180° to 180° . Velocities higher than the applied threshold are suppressed since they are assigned values greater than 180° , this results in mapping them to lower angles. For example a velocity exceeding V_{enc} by 25% would be mapped to 225° and this is indistinguishable from -45° . The value of V_{enc} is controlled by changing the amplitude, time separation and duration of the bipolar gradients.

A single acquisition is not sufficient to resolve phase difference due to field inhomogeneities and susceptibility effects. Hence, two sets of measurements are typically acquired, the difference being that the polarity of the gradients is inverted. These two images are subtracted (ΔM) and the result is proportional to velocity. The pulse sequence diagram for PC-MRA is shown in figure 2.15.

Velocity is proportional to the phase difference and the quantities are connected by the following relationships (equation 2.15):

$$Velocity = \Delta\phi * \frac{V_{enc}}{\pi} = \frac{\Delta\phi}{\gamma * \Delta M} \quad [2.15]$$

In PC-MRA the typical recorded images are hence a magnitude image, a complex phase difference image and a phase difference image (191).

The choice of the velocity threshold is a trade-off between a high value to avoid potential aliasing effects and a lower value since the SNR is reduced with a higher threshold and the ability to decouple slower velocities is influenced. Having calculated the velocity inside a big vessel, it is trivial to quantify the flow in the vessel by multiplying the mean velocity over the pixels with the area of the vessel.

A recent study by Yashiro et al. (192), has shown changes in the vasculature of T2DM patients using TOF-MRA analysis. PC-MRA has been

used in the past to assess flow in diabetes pointing towards reduced carotid flow (193).

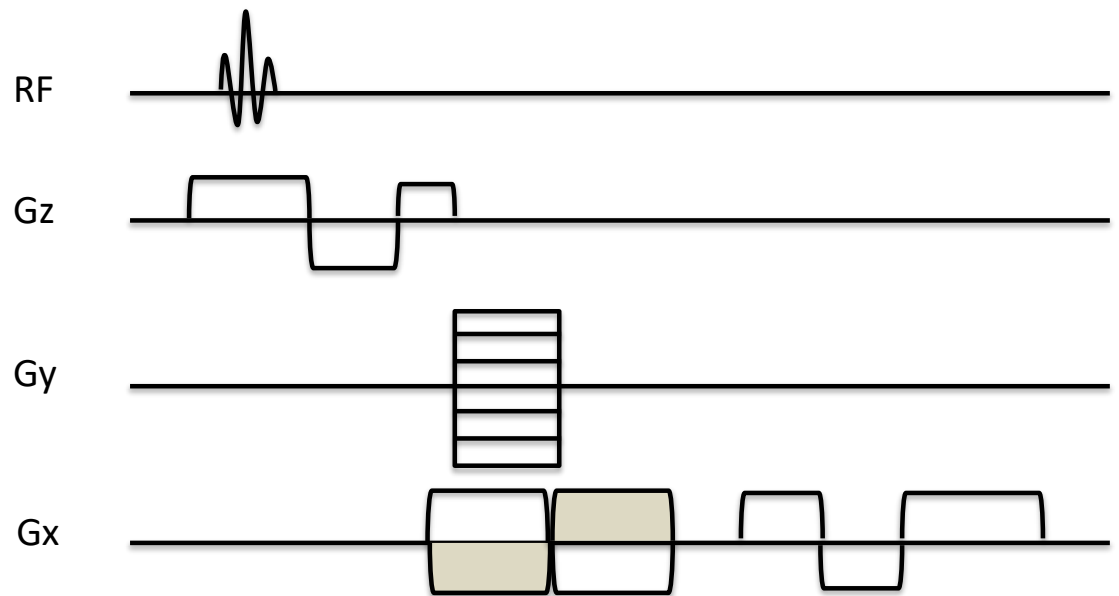


Figure 2.15: Pulse sequence diagram for PC MRA based on Haacke et al. 1999 [64].

2.5.4 Diffusion weighted MRI

Diffusion imaging focuses on the determination of the displacement of water molecules due to thermal energy. The contrast of the technique depends on the accumulated dephasing due to random spin movement. In the pulsed gradient spin-echo implementation one dephasing and one rephasing gradient are applied after the 90° RF pulse either side of a 180° pulse resulting in the dephasing of moving spins (figure 2.16) (194). In a gradient echo implementation the pair of diffusion gradients differs in polarity and follows the 90° pulse. High mean displacement results in greater signal attenuation and corresponds to darker regions on a diffusion-weighted image (195). The readout is usually a fast one such as EPI.

The sequence's sensitivity to molecular diffusion is determined by the 'b-value' which incorporates information about the amplitude, duration and separation of the applied gradients and can be calculated using the following equation 2.16, where the gradient and timing parameters are defined as in figure 2.16:

$$b = \gamma^2 G^2 \delta^2 \left(\Delta - \frac{\delta}{3} \right) [2.16]$$

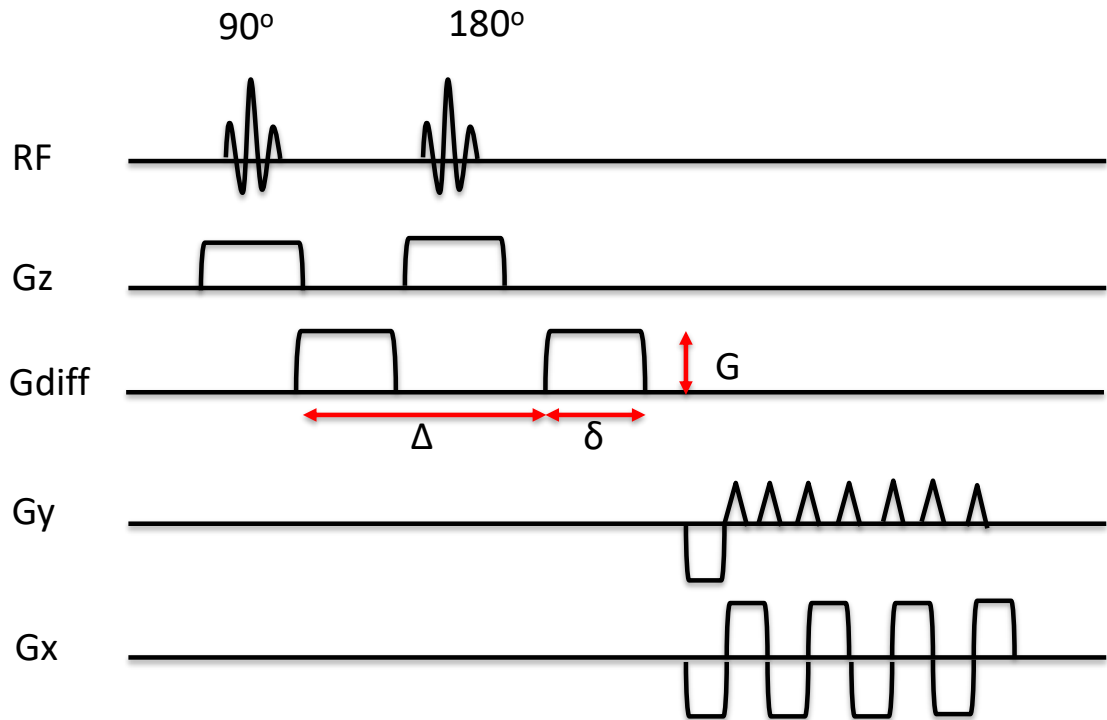


Figure 2.16: Diffusion weighted imaging pulse sequence diagram based on Haacke et al. 1999 [64].

The simplest diffusion imaging technique is diffusion weighted imaging (DWI) whereby data are acquired in three orthogonal directions to characterize the water movement in 3D. The diffusion apparent coefficient (ADC) can be quantified by measuring the signal (S) obtained from an acquisition with a non-zero b-value and a signal with $b = 0$ (S_0) which is actually a conventional T2-weighted image (equation 2.17). The signal at a certain b-value can be calculated as the geometric mean of the signal from the three orthogonal directions. The higher the b-value the stronger the diffusion weighting. However, the higher the b-value the lower the achieved SNR due to TE prolongation

$$\frac{S}{S_0} = e^{-bADC} \Rightarrow ADC = \frac{1}{b} \ln \left(\frac{S_0}{S} \right) \quad [2.17]$$

Equation 2.12 demonstrates that two b-values typically suffice to determine ADC, however, acquisition of additional b-values can allow for a more accurate estimate. Two b-values is sufficient for the calculation of ADC when using a monoexponential model where ADC can be calculated from the slope of the $b=f(S)$ plot which is a straight line, as in equation 2.12. However,

inclusion of more b-values can allow for more complex models to be fitted to the data than the simple monexponential model. At present, the vast majority of clinical diffusion imaging sequences in the neuroimaging domain use two b-values of approximately 0 and 1000 s / mm².

More advanced diffusion imaging modalities allowing for the complete characterization of the displacement of water molecules include diffusion tensor imaging (DTI), diffusion kurtosis imaging (DKI), diffusion spectrum imaging (DSI), q-ball imaging (195). The basic difference of these techniques from a DWI acquisition has to do with the fact that acquisitions are performed for a bigger set of b values and gradient orientations. Diffusion kurtosis imaging differs from DWI in that it avoids assuming a Gaussian distribution as a pattern for the water diffusivity (196). DSI and Q-ball imaging are capable to resolve small differences in the directionality of the tracts within a voxel (197).

Neuroimaging studies have reported increases in mean diffusivity (198) and decreases in fractional anisotropy (199) in patients with T2DM.

In the present study, QUASAR ASL was used to evaluate cerebral hemodynamics in IGT and T2DM. An MPRAGE and a FLAIR scan were acquired to detect structural changes in the brain. TOF and PC-MRA scans were acquired to investigate the cerebral vasculature and finally a DWI scan was acquired to detect alterations in water movement.

Chapter 3:

Brain MR Image Processing

The output from every medical imaging modality is a clinical image providing structural, physiological or functional information. The varying intensity levels present in the image are associated with the structural or physiological parameter under consideration. Through image analysis, regions or properties affected by a potential disease, and existing patterns indicative of the pathological condition, can be unveiled. In terms of image processing, the image comprises of entities termed pixels (2D) or voxels (3D). The number of pixels comprising an image depends on its field of view and sample array size. The intensity of each pixel is associated with the parameter that the specific technique is measuring. Image resolution in MRI can vary from small voxels (i.e. 0.125mm^3) to voxels of several mm depending on the implementation and the desirable SNR. Functional imaging techniques are often constrained by SNR and have larger voxel sizes than structural imaging methods.

While it is often desirable to make imaging “measurements” on a single individual, as in traditional diagnostic imaging, research studies frequently perform group comparisons to try and identify general differences in measured parameters between specific cohorts (or groups) of patients. To enable these group comparisons, several pre-processing steps have been developed. Motion correction and registration of the image to a standard template coordinate system by applying a geometrical transformation are examples of such pre-processing steps which might be implemented. Temporal filtering and spatial smoothing can be used in order to filter out frequencies that might not be of interest, or frequencies irregularly high (101, 200). These pre-processing steps are widely used to ensure that images from different subjects are comparable.

Numerous software tools have been developed with a focus on processing of brain images. Some of the most popular ones used in neuroimaging research are: Statistical Parametric Mapping - SPM (201); FMRIB’s Software Library - FSL (202); FreeSurfer (203) and Analysis of functional neuroimages - AFNI (204).

In this chapter image processing techniques utilised in the present thesis are discussed in the context of the existing research and bibliography. These techniques range from regular pre-processing to advanced methods based on machine learning. Focus is put on segmentation using fuzzy c-means clustering (FCM), voxel-based morphometry (VBM), linear support vector machine (SVM) classifiers and feature ranking with SVM – RFE (recursive feature elimination).

3.1 Pre-processing steps

An example slice from an individual is shown in figure 3.1 before and after bias field correction, brain extraction and tissue segmentation.

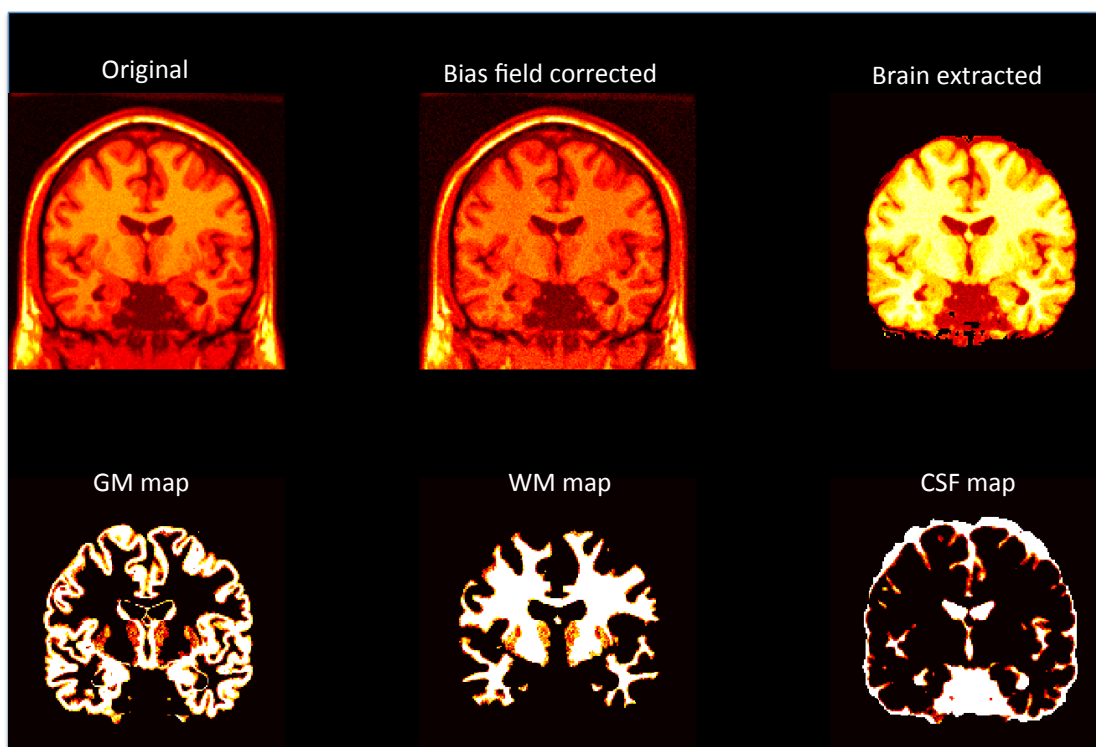


Figure 3.1: Preprocessing steps demonstrated in one coronal slice. The original/acquired image, is bias field corrected, the brain is extracted and subsequently segmented.

3.1.1 Bias field correction

Bias field correction (BFC) attempts to account for signal variation introduced by field inhomogeneities during the image acquisition process. These inhomogeneities cannot be attributed to a single factor. One of the potential sources is the RF coil(s) used for MRI signal transmission and reception, which does not have a perfectly uniform field (205). The bias field is not always visually obvious; but it can greatly influence the subsequent

analysis. Its presence might imply intensity changes in the same tissue type across the image, independent of underlying pathology, and it usually increases the variance within individual tissue classes, thereby reducing sensitivity to detecting abnormal tissue. Several methods have been developed for BFC. Two broad categories exist: correction at the level of acquisition by adjustments in the hardware and approaches relying on the acquired image and in some cases prior knowledge. The latter approaches can correct for bias introduced both by the scanner and by the scanned object (206).

The typical model used to describe the acquired image is given in equation 3.1, where the acquired image (I) is modelled as the original uncorrupted image ($I_{original}$) with a multiplicative slow varying field (B) and additive noise (n). Other suggested models are as on equations 3.2 & 3.3 (206, 207).

$$I = B * I_{original} + n \quad [3.1]$$

$$I(x) = (I_{original} + n) * B \quad [3.2]$$

$$\log I = \log(I_{original}) + \log B + \log(n) \quad [3.3]$$

All cases tend to assume that n is approximately Gaussian. When B is determined, it is removed from the image and the resulting image is described as bias field corrected.

Currently, the most popular and robust bias field correction algorithm is N4ITK (208), which is based on the N3 (non-parametric non-uniformity normalization) algorithm (209). This algorithm uses the first model for BFC and determines via an iterative procedure the bias field. The idea is that the histogram of the acquired image is a convolution of the histogram of the true image and the histogram of the bias field. The algorithm utilises deconvolution to determine the bias field. A deconvolution step is followed by an updated estimation of the bias field. The procedure ends when the difference of the standard deviation between two subsequent bias field estimations falls below a pre-defined threshold (210). Differences between the N4 and N3 algorithm are centered on the estimators used for the calculation of the bias field and equation used for iterative estimation, with the N4 using in every iteration the residual bias field from the previous iteration and not the total bias field. For

more details the reader is referred to Larsen et al. (210) and Tustison et al. (208).

3.1.2 Brain extraction

Extraction of the brain, otherwise known as ‘skull-stripping’ is of great importance as remaining non-brain tissue (i.e. skull, skin, eyes) might distort the results of the subsequent analysis. Manual extraction is an extremely time-consuming task even for experienced radiologists. Hence, automated skull stripping is regularly used and the resulting brain mask can be inspected for potential failures.

Available brain extraction methods can be classified into several distinct categories: morphological algorithms, intensity-based, deformable surface approaches and atlas-based models (211). The morphological approaches aim to use thresholding and/or edge detection for an initial stripping followed by morphological operations such as erosion or dilation. Intensity based approaches are usually based on the image intensity histogram and changes in local intensity gradient to separate tissue and non-tissue entities. Deformable surface models rely on an initial closed curve that dynamically evolves using energy metrics until it fits the surface limit. Atlas-based methods utilise prior information from generated atlases in order to exclude the skull, following registration of the subject’s brain into the atlas space. Hybrid and more sophisticated methods have been developed as well, with the recent trend being to use deep neural networks (212) for the task.

The major neuroimaging research software tools have all incorporated brain extraction methods into their pipelines. FSL’s BET (213) uses deformable surface models and SPM’s algorithm relies on an atlas-based model used for tissue segmentation (214). AFNI’s (204) 3dSkullStrip utilises a modified BET technique and Freesurfer’s tool (215), combines a watershed algorithm with deformable surface models and an atlas.

3.1.3 Image registration

Image registration is concerned with the determination of an appropriate geometrical transformation that maps the pixels of one image (moving image) to a reference image. The major linear geometrical operations are translation,

rotation, scaling and shearing (216). Rigid transformation comprises translation, and rotation, whereas affine transformation comprises all four linear geometrical operations. The optimum transformation is identified as that which minimises (or maximises) a defined similarity metric between the two images, such as normalized cross-correlation, normalized mutual information, etc. Once the optimum transformation has been found, the moving image is warped using the resulting transformation so that it is in spatial registration (or as close as possible) to the reference image. Linear registration can be used when there are no major differences between the two images.

A linear registration takes the form of $\mathbf{y} = \mathbf{Ax}$ where \mathbf{y} is the resulting image, \mathbf{x} is the moving image and \mathbf{A} is the transformation matrix. The transformation matrix can be represented as a matrix multiplication of the individual translation, rotation, scaling and shear matrices.

While linear registration may be sufficient for intra-subject motion correction, the consensus in medical imaging is that linear registration is not sufficient for successful inter-subject anatomical structure alignment. A study published in 2009 examined in great depth 14 non-linear registration algorithms and came up with certain recommendations (217). The best two algorithms were the SyN (218) and the ART (219). Another popular non-linear method, aimed at preserving topological information and utilised by SPM, is diffeomorphic registration, which approaches registration as a problem of an image flowing to match another image (220). This algorithm came fourth in the evaluation of non-linear registration algorithms.

Registration is used for motion correction, to match images of different resolutions, images from different subjects, different imaging modalities, or to register images to an already existing atlas (normalization). It is important to use a robust registration approach, although care must be taken as the original image values are usually modified in the procedure due to interpolation. Additionally, it is important to evaluate the registration result to reassure that the automated process has been successful and that there are no gross misalignments between the registered image and the target. Potential imperfect registration might imply that the extracted metrics do not reflect the actual values from the region under consideration.

Spatial normalization utilises image registration in order to align the subjects image space with a reference image space such as the Montreal Neurological Institute (MNI) (221) or the Talairach-Tournoux (222) coordinates system. Registration into a “standard” reference space is commonly used in neuroimaging, as it allows for easy correspondence of spatial information between studies and for utilisation of developed atlases.

3.1.4 Tissue segmentation

Medical image segmentation can be described as the task of assigning each voxel to a distinct category/class. Specifically, for a healthy brain, the most typical considered classes are GM, WM and CSF. Segmentation results from this procedure are typically used for volumetric quantification. Complex segmentations are also possible, where the brain is separated into detailed anatomical sub-regions. Segmentation is frequently performed so that measurements can be obtained from the region, or tissue of interest. These can be physiological and functional parameters, which can be calculated by registering the segmented region of interest (usually emerging from a structural scan) onto quantitative images (e.g. emerging from functional acquisitions).

The main segmentation approaches are: manual, region-based, threshold-based, classification-based and clustering-based (223). Region-based approaches for segmentation are very similar to brain extraction region-based approaches, in that starting from a certain region, they expand an initial curve or seed point until a termination criterion (usually energy-related) is met. Threshold-based approaches are among the most popular for image segmentation. Thresholding can be local, adaptive or global. The optimal threshold in all cases can be determined using techniques such as Otsu thresholding and entropy-based criteria (223).

Classification based segmentation approaches relying on SVM classifiers (224), deep neural networks (225) and k- nearest neighbors (226) have also been use for tissue segmentation.

Tissue segmentation can be approached as a problem of clustering using algorithms such as K-means (227) and FCM clustering (228). Clustering for tissue segmentation can have two forms: soft (whereby a voxel does not

need to belong to one class exclusively, as in FCM and mixture models); or hard (where a voxel belongs only to one class, as in k-means).

The first category of soft clustering-based approaches involves mixture models. Usually the segmentation problem is addressed by fitting Gaussian shaped curves to the histogram of the image, or of a region, and assigning to every voxel a probability of belonging to a certain class. FSL's FAST tool utilises an expectation maximization algorithm combined with Gaussian Mixture Models (GMM). SPM's segmentation routine also makes use of GMM along with prior probability maps. Mixture models have the disadvantage of making assumptions about the underlying intensity distribution, i.e. the data conforms to a Gaussian distribution with a certain number of tissue classes. Utilising prior probability atlases introduces an additional bias to the segmentation task, so their use needs to be weighed carefully against the potential for increased robustness.

FCM clustering originally proposed by Dunn (229) and adapted by Bezdek et al. (228) is a classification technique of great interest for image segmentation and is based on the fuzzy logic theory (230). In fuzzy logic, a function termed the "membership function" determines the degree of belonging to a specific cluster. The concept of fuzziness intends to describe variables with vague edges, in an attempt to avoid a binary logic of belonging or not belonging. This property renders FCM a promising technique for tissue segmentation and partial volume estimation (231).

The philosophy underlying FCM is that a pixel does not belong explicitly to a class, but has a degree of membership in all clusters with a value in the interval [0 1], with 1 suggesting strong membership in a cluster. Calculation of the membership level is an iterative process. Initially, an informed estimate is made about the centroid locations of every cluster. Subsequently, equation 3.4 is minimized. Minimization occurs when pixels with values close to the centroid acquire a high membership function for this particular cluster. The membership value and the centroid of every cluster are updated until convergence is achieved (equation 3.5) (228, 232).

$$J = \sum_{j=1}^N \sum_{i=1}^c u_{ij}^m \left| |x_j - v_i| \right|^2 \quad [3.4]$$

Where, c is the number of clusters, u_{ij} is the membership value, x_j is the pixel under consideration, m is the degree of fuzziness and v_i is the centroid of a cluster.

$$u_{ij} = \frac{1}{\sum_{k=1}^c \left(\frac{\|x_j - v_i\|}{\|x_j - v_k\|} \right)^{\frac{2}{m-1}}}, \quad \text{where } v_i = \frac{(\sum_{j=1}^N u_{ij}^m x_j)}{\sum_{j=1}^N u_{ij}^m} \quad [3.5]$$

In its original implementation, FCM does not take into account the local neighborhood of a pixel. Techniques to circumvent this limitation have been suggested, mostly focused on modifying the membership function to incorporate spatial information, thus making the classification dependent on the information from the local neighborhood. Focusing on medical image segmentation, one such algorithm performing spatial fuzzy c-means (SFCM) clustering was proposed by Chuang et al. (232). The algorithm incorporates information from a 5*5 window in the classification task and modifies accordingly the membership function (equation 3.6).

$$u'_{ij} = \frac{u_{ij}^p h_{ij}^q}{\sum_{k=1}^c u_{kj}^p h_{kj}^q}, \quad \text{where } h_{ij} = \sum_{k \in \text{win}(x_j)} u_{ik} \quad [3.6]$$

Where $\text{win}(x_j)$ is a $k*k$ size window centered at pixel j .

Ahmed et al. (233) introduced a technique to incorporate BFC to FCM (not accounting for spatial information). In some studies an effort was made to incorporate in the fuzzy classification both spatial information and BFC by modifying the membership function accordingly (234, 235). Recently all FCM based algorithms for MR image segmentation have been compared (236) and the best performance was demonstrated by SFCM.

WMH segmentation

Segmentation of hyper-intense WM regions is a non-trivial problem. Several software tools have been developed, however, none of them is considered a gold standard. The difficulty arises from the fact that WMH regions can have an unpredictable appearance; they can consist of very small localized regions, large diffuse areas, or a combination of both (237). Their distinct

intensity profile makes them recognizable with a bare eye, however automated detection has generally proved to be suboptimal. Currently, the most reliable and commonly used approach is to use an automated tool with subsequent manual correction for regions that have been missed, or were mistakenly labeled as abnormal. Some of the automated tools are: Lesion segmentation toolbox (238) and BIANCA (FSL) (239).

3.2 Partial volume phenomenon and correction

The lower the resolution of an image the bigger the volume of the voxel or area of the pixel for a given field of view. This means that there is a higher probability of a pixel/voxel containing information from more than one tissue type. This problem is dubbed the 'partial volume effect' (PVE). Another factor associated with PVE is the imperfect point spread function of the imaging system, which is more important in PET imaging. In higher resolution images, it is less of a problem, however, in perfusion imaging, and especially in ASL, it can lead to underestimation of GM CBF. Asllani et al. (240) have shown that in an ASL experiment, the GM CBF value can be underestimated by up to 50% and have proposed a method to account for PVE based on linear regression. This method introduces a degree of smoothing to the data, as it assumes relatively stable perfusion values in a kernel. Chappell et al. (241) have shown that an alternative to this method for multiple inversion time-point ASL, could be to fit the signal with kinetic curve equations based on Buxton's model for every tissue type. This technique has also been used in single-PLD ASL (242). Both approaches use a high-resolution anatomical image to generate fractional volume maps.

Ahlgren et al. (243) have implemented a different approach for partial volume correction (PVC), using only the information obtained from the QUASAR ASL sequence, without reliance on a high-resolution anatomical image. Tissue maps were generated by fitting Gaussian distributions to the low resolution ASL-derived images for every tissue type (244). The saturation recovery signal was modelled as a linear combination of the saturation recovery from the tissue types (GM, WM and CSF).

3.3 Group-comparisons

In cross-sectional and longitudinal studies, comparisons are made between different scans of different individuals, or of the same person, in order to unravel patterns of localized or global differences. Various approaches exist to perform comparisons between different scans. One approach is to use manual or semi-automated segmentation of regions of interest (ROI), usually focusing on areas known to be affected by the examined condition and any differences can be identified by statistical comparisons. Another option is to use morphometric approaches, which avoid making assumptions about the extent, location and number of ROIs.

The most heavily used morphometric technique is VBM, which is designed to detect regions in the brain (typically GM) that differ in volume between groups, by applying group comparisons at a voxel level (245). The pipeline behind VBM has been implemented in both FSL and SPM with both implementations being highly similar. In its regular implementation, the initial step of the pipeline is brain extraction. Subsequently all brains need to be normalized to a common space to facilitate group-wise comparisons. It is a common approach for a study-specific template to be constructed at this stage from some, or all scans. This template is used as a registration target for the next step where all segmented PV maps, are registered to the common space. At this stage an optional processing step described as 'modulation' which preserves volumetric information can be applied. The GM and WM segments are subsequently smoothed using a Gaussian filter (with kernels ranging from 6mm to 18mm FWHM) to render the intensity more normally distributed, in order to facilitate parametric statistical tests. The endpoint result of the pipeline is therefore a series of images in a common space, where the information in each voxel effectively describes the density of tissue for each subject.

Subsequently, statistical tests between equivalent voxels determine whether these voxels differ significantly between the groups. Usually, these comparisons take place using the partial volume maps. Comparisons are typically based on the general linear model and study-specific designs are generated and implemented. The applied statistical tests depend on the cohort, time-points and states. Due to the thousands of comparisons equivalent to the

number of non-zero voxels it is of utmost importance to correct for multiple comparisons and account for the false positive rate.

The VBM implementation in SPM and FSL is almost identical, but differences arise in the specific pre-processing tools, which are used to achieve the same conceptual steps.

Alternative suggested morphometric approaches involve deformation-based morphometry (focused on the position of the structures), tensor-based morphometry (focused on the shape of structures) (246) and pattern-based morphometry (247).

Morphometric techniques, such as VBM, are mass-univariate (comparisons are conducted at a single voxel level) and cannot capture a spatially distributed pattern, nor can they be used as a stand-alone model for individual prediction (248). These concerns are addressed by using machine learning approaches. Such approaches have been used extensively in dementia classification and more specifically in Alzheimer's using mainly structural scans (249).

When using machine learning, the scans need to be registered to a common space. The whole image can be used as an input to a classification algorithm along with the respective classes in order to determine optimally differentiating regions. Due to the high resolution of the structural scans, the classification task involves thousands of features (each voxel can be one feature) so the dimensionality of the problem needs to be greatly reduced. An approach is to down-sample the considered image and utilise methods for dimensionality reduction. Of utmost importance when detection of regions of difference is of interest, is to retain the original features, hence a feature preserving technique ought to be used (250, 251).

The important difference of such approaches compared to VBM is that they can be used for classification of a single individual and not just in the context of group-wise comparisons once a model is constructed (250). Additionally these techniques are multivariate (248).

3.4 Feature extraction and classification

In the era of big data, processing using machine learning, or more recently deep learning, is a particularly appealing approach. The difference

between machine learning and deep learning, is that deep learning is purely neural network - based with numerous hidden layers (hence the term 'deep'), whereas, in machine learning there is no such hidden deep neuronal structure. In the context of medical imaging, numerous characteristics can be extracted from one, or multiple, modalities and multiple regions. Every such characteristic is considered to be a *feature*. Every subject is characterised by a collection of features; comprising its feature vector. The task of *classification* is essentially the task of classifying the feature vector, referred sometimes as 'pattern' into one of the categories, or else 'classes', under consideration. The extracted features can be used as an input to a classifier, with a view to classifying individuals into specific categories based on extracted features.

The two main categories of learning are supervised (for example classification and regression) and unsupervised (e.g. clustering). In supervised machine learning both input data and their corresponding classes are used as input to the algorithm for training purposes. Classification techniques are used for categorical outputs, whereas regression techniques are used for continuous outputs. In unsupervised techniques, the algorithm finds intrinsic data patterns. Learning techniques are not confined to supervised or unsupervised; but learning can also be semi-supervised or reinforced.

3.4.1 Feature extraction

Multiple features can be extracted from an image. For example, features that characterise the shape of structures include their circularity, area, or perimeter. Textural analysis is a term reserved to describe the investigation of changes in the gray level pattern of an image. Textural features involve amongst others statistical features of first or higher order and spectral features. This type of features has been used for analysis of gray level patterns in conditions such as brain tumors, epilepsy and multiple sclerosis (252). First order statistical features are the mean, standard deviation, skewness and kurtosis. The gray-level co-occurrence matrix (253) is a popular approach for textural feature determination. The features derived from this matrix are second-order statistical features such as entropy, energy and contrast.

Transform-based features can be determined using transformations analysing the frequency content of the image. Such methods can utilise

amongst others: Fourier, wavelet and Gabor transforms (254). The Fourier transform is capable of disentangling the spatial frequencies present in an image by using a number of superimposed sinusoidals. Wavelet transforms are less restricted than Fourier, since the basis functions used for the frequency content analysis are not confined to sinusoidals (252). Gabor filters are sinusoidal waves modulated by a Gaussian. Their interesting property is that they approximate the way the human visual system works. By implementing several modifications, they can be rotationally invariant (255).

Following calculation of features of interest with one or more of the described methodologies, all extracted features are positioned in a feature vector.

3.4.2 Dimensionality reduction

An important step prior to classification, particularly when the dimensionality of the problem is higher than the number of available observations, is dimensionality reduction. Especially in the medical field, the number of features can greatly outweigh the number of available observations, giving rise to the 'curse of dimensionality'. Dealing with this 'curse' mandates that an appropriate feature selection, or reduction, technique is used to reduce the number of features used in the classification task. This step is of great importance since it is crucial in order to avoid overfitting. Classification algorithms, trained on a large number of features, might present a superficially high performance for the training set (overfitting), however, when the classifier is used on a testing set, the performance might be very poor (256). Overfitting results from the classifier having learned the idiosyncrasies of the available training dataset and when presented with a new one it cannot generalise. The smaller the available dataset, the more likely it is for the classifier to identify patterns with poor generalisability.

Feature selection techniques choose a subset of the available features, whereas feature reduction techniques might reduce dimensionality by using linear combinations of the features. A multitude of feature reduction and selection techniques have been developed and under the main branches numerous subcategories have emerged (256).

Examples of popular dimensionality reduction algorithms include principal component analysis (PCA) and linear discriminant analysis (LDA), both these algorithms do not examine non-linear feature relationships. An alternative approach, capable of unravelling non-linear relationships between the features, is a feature ranking technique which can be used for feature selection known as SVM-RFE (257).

SVM-RFE which was used in the present thesis, was introduced as a feature ranking method by Guyon et al. (257). The philosophy behind the technique is that the weights of a SVM classifier are used as a criterion to rank the features. Following feature ranking, a subset of the features can be retained for further analysis leading to dimensionality reduction. An important advantage of SVM-RFE is that the features are maintained in their original form, following feature reduction, allowing for further analysis. The pseudo-code for its execution is as follows (257, 258):

- 1) Train a classifier and retain the weights of every feature.
- 2) Select a subset of features (higher weights).
- 3) Proceed with a backwards elimination approach eliminating one, or multiple, features per iteration.
- 4) Repeat until all features are removed.
- 5) Rank the features based on the sequence of their removal.

In their paper introducing SVM-RFE, Guyon et al. (257) decided to analyse the top-7 features with the highest weights in a study about colon cancer. One of the top-scoring features for distinguishing colon cancer patients from normal volunteers had to do with a parasitic protozoon, trypanosoma. Initially, they thought this was a failure of their method; however, they actually found out that people infected by trypanosoma develop resistance to colon cancer, thus demonstrating the robustness of the developed technique and the potential new insight it can offer. Especially for classification tasks in the medical field, such a method allowing for retention of the top features in their original form and their further analysis could be of great importance and could provide us with candidate disease biomarkers.

3.4.3 Classification techniques

A binary classifier utilises a decision function $D(x)$ which if positive the pattern is assigned to the +1 class, if negative, the pattern is assigned to the -1 class. There are two main classifier types, those that rely on Bayesian theory and those that attempt to optimize a cost function by determining a decision boundary (259). Classification based on Bayesian inference usually assumes a PDF of a certain type (typically Gaussian) and seeks to optimize the parameters of the function to better describe the data (i.e. mean and covariance matrix). The within class PDF needs to be known or estimated before the classification task. Estimation of the PDF can be performed using maximum likelihood estimation or by using mixture models combined with an expectation-maximization algorithm (259).

Classifiers based on a decision surface rather than on PDF estimation seek to deduce the optimally differentiating surface separating the classes in the N-dimensional space. These classifiers can result in better classification when the available data-points are limited. Examples of these algorithms include the perceptron, the least-squares classifier and SVMs (259).

3.4.3.1 Support Vector Machines (SVM)

One of the most popular classification algorithms is the SVM classifier, which is adept for two outcomes of a particular state but can be expanded to more than one outcome categories. SVMs introduced by Cortes and Vapnik (260) are particularly stable, well-studied, with open-access and easy to implement software (libraries are available in Matlab, Python, etc.) and more importantly they work well with relatively small data sizes, which doesn't tend to be the case with neural network based methods. For these reasons, they were the preferred classifier in this project.

SVM attempts to separate the data by determining an optimally separating hyper-plane (maximum margin) (260). The dimensionality of the problem is determined by the number of available features. In a toy problem where 2 or 3 features are available, the problem is equivalent to finding the optimally separating hyper-plane in 2D or 3D where the axis is determined by the feature value (figure 3.2). For problems defined in a higher dimensional space it is mathematically trivial to expand the methodology, but difficult to

visualize and depict the hyper-plane. In this case, all instances are placed in the N-D space, with N determined by the dimensionality of the feature vector and the SVM algorithm determines a N-D hyper-plane. SVM is one of the classifiers that is considered to be relatively robust regarding overfitting.

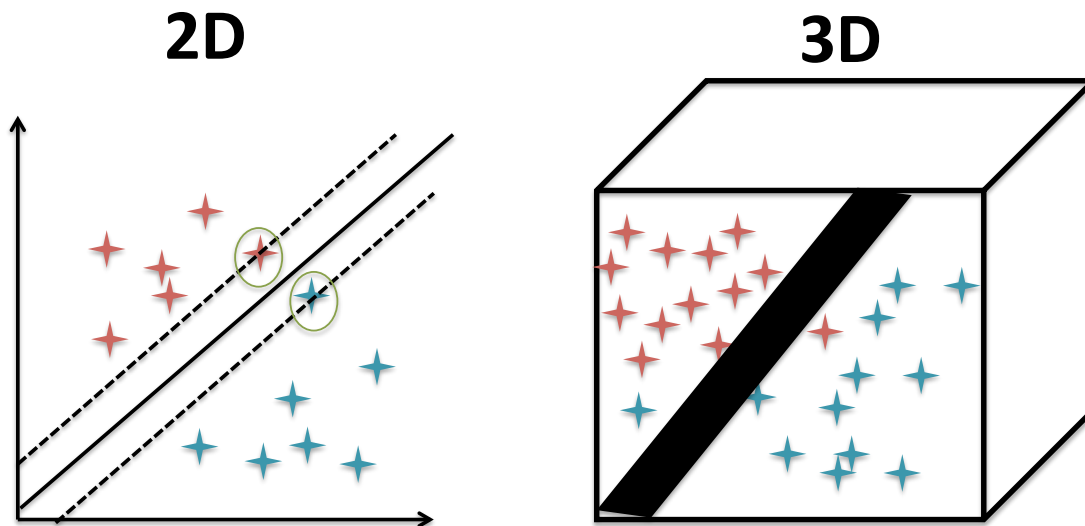


Figure 3.2: SVM optimally differentiating hyper-plane in 2D and 3D.

Non-linear SVM operates by projecting the feature vector in a higher dimension using a kernel function. Kernel functions can be: polynomial, radial basis function and sigmoid. The linear SVM is a particular case of polynomial SVM whereby there is no projection to a higher dimension using a kernel function.

In the rest of this section the mathematical concepts underpinning SVM are briefly discussed, following the lectures of Professor Patrick Winston (261) and tutorials from (262-264).

A linear classifier has the form of $\mathbf{w}^T \mathbf{x} + b = 0$ where \mathbf{x} is the feature vector, \mathbf{w} are the weights associated with each feature and b corresponds to a bias. Numerous planes can separate the data into two classes and SVMs search for the hyper-plane that maximizes this margin.

In SVM, the optimally separating hyper-plane is defined by $\mathbf{w}^T \mathbf{x} + b = 0$ and the maximum margin is defined by two hyper-planes: $\mathbf{w}^T \mathbf{x} + b = 1$ and $\mathbf{w}^T \mathbf{x} + b = -1$. The distance between the two hyper-planes defining the margin is $2 / \|\mathbf{w}\|$. This distance arises by considering the distance between a point and a hyper-plane. For the sake of simplicity in the distance calculation we will consider the 2D case where we calculate the distance between a point and the

hyper-plane, which for the 2D paradigm is a line. Let a point on the line consisting the hyper-plane (i.e. $w_1x_1 + w_2x_2 + b = 0$) be $C(x_{1o}, y_{1o})$ and a line of the form $\mathbf{w}^T\mathbf{x} + b = 1$ (one of the two lines defining the maximum margin), which could be written as $w_1x_1 + w_2x_2 + b - 1 = 0$. Then for point C, it follows that $w_1x_{1o} + w_2x_{2o} + b = 0$

The distance between them is given by equation 3.7.

$$d = \frac{|w_1x_{1o} + w_2x_{2o} + b - 1|}{\sqrt{w_1^2 + w_2^2}} = \frac{|0 - 1|}{\sqrt{w_1^2 + w_2^2}} = \frac{1}{\|\mathbf{w}\|} \quad [3.7]$$

It follows that the distance between a point situated on one of the lines defining the maximum margin and the hyper-plane (being a line in this 2D example) is $1 / \|\mathbf{w}\|$. As mentioned previously the goal of SVM is to maximize this margin; it follows that $1 / \|\mathbf{w}\|$ needs to be maximized so $\|\mathbf{w}\|$ needs to be minimized, having in mind that all observations need to be situated outside this margin.

The classifier should have the following behavior based on whether the class y of every instance is 1 or -1 which could be summarised in the following expression (equation 3.8):

$$y * (\mathbf{w}^T\mathbf{x} + b) \geq 1 \quad [3.8]$$

So when $\mathbf{w}^T\mathbf{x} + b > 1$ then $y = 1$ and when $\mathbf{w}^T\mathbf{x} + b < -1$ then $y = -1$

The optimization task seeks to maximize $1 / \|\mathbf{w}\|$ (or minimize $\|\mathbf{w}\|$) so the distance between the hyper-planes is maximized according to constraints. Minimizing $\|\mathbf{w}\|$ is actually the same as minimizing $0.5 * \|\mathbf{w}\|^2$. One of the advantages of formulating the problem as such, is that the function to be minimized is convex, meaning that the minimum will be global. Problems involving a cost function minimization with equality and / or inequality constraints can be solved using Lagrange multipliers. The basic idea is that the gradient of the function to be optimized is equal to the gradient of the constraint multiplied by a_i - the Lagrangian multipliers.

So, the problem becomes an optimization problem with the following constraint (equation 3.9) where the equality holds only for the points situated on the margin.

$$\min_{\mathbf{w}, b} \frac{1}{2} \|\mathbf{w}\|^2 \text{ subject to } y(\mathbf{w}^T\mathbf{x} + b) - 1 \geq 0 \quad [3.9]$$

This is the so-called ‘primal’ problem when the optimization is focused on finding the weights. The Lagrangian for this problem is:

$$L = \frac{1}{2} \|w\|^2 - \sum a_i [y_i (wx_i + b) - 1] \quad [3.10]$$

In order to find the extremes of L, the partial derivatives with respect to w and b are calculated as follows:

$$\frac{\partial L}{\partial w} = 0 \Rightarrow w - \sum a_i x_i y_i = 0 \Rightarrow w = \sum a_i x_i y_i \quad [3.11]$$

$$\frac{\partial L}{\partial b} = 0 \Rightarrow \sum a_i y_i = 0 \quad [3.12]$$

By substituting 3.11 and 3.12 into 3.10, the problem becomes

$$\max L_a = \sum_{k=1}^m a_i - \frac{1}{2} \sum_{k=1}^m \sum_{j=1}^m a_k a_j y_k y_j \langle x_k, x_j \rangle \quad [3.13]$$

Subject to the following constraints: $a_i \geq 0$ and $\sum_{i=1}^m a_i y_i = 0$.

This is the so-called dual problem, since the focus has been shifted from the weights (primal problem) to the Lagrangian multipliers (dual). In equation 3.13, α_i are the Lagrangian multipliers. The majority of them are zeros and those with non-zero values are the support vectors.

The final decision function for SVMs is $D(x) = w^T x + b$ with

$$w = \sum_i a_i y_i x_i \quad [3.14]$$

In other words, having calculated the Lagrangian multipliers, in order to decide the class of a pattern we only need to calculate its inner product from some of the vectors, those with positive a_i values or in other words: *the support vectors*.

For non-linear SVM classifiers equation 3.13 is slightly different, in the sense that instead of the product of the two vectors, the product is $\langle \varphi(x), \varphi(x_j) \rangle$ where $k(x_i, x_j) = \langle \varphi(x), \varphi(x_j) \rangle$ is the kernel function mapping the vectors into a higher dimension.

3.4.4 Cross-validation

In order for the classification results to be generalisable, the available data points are normally separated into a training and a testing set. When large datasets are available the algorithm is usually trained on a percentage of them

(ranging between 60-80%) and tested on the rest. The performance is usually reduced when the test data are presented to the classification algorithm. The disadvantage of these hold-out techniques is that not all available data-points are used for training. This problem is particularly important when small datasets are considered and using all of the available sample is highly desirable. Cross-validation aims to use all available samples and evaluate the model's performance through repeated resampling (265).

Numerous techniques exist for cross-validation and these can be exhaustive or non-exhaustive. An example of exhaustive cross-validation is "leave-p-out" cross-validation whereby p observations are used for testing and the classifier is trained on the remaining ones; subsequently it is tested on the remaining p . This approach runs for every possible partitioning of the data hence it can be computationally expensive depending on the available features and data-points. A special case of leave-p-out cross validation is leave-one-out cross-validation (LOOCV) whereby a single observation is left out in every iteration. For every iteration, the mean square error in classification of the testing sample (s) is measured. The performance of the classifier is calculated as the mean performance over all iterations (265).

An example of a non-exhaustive method is k-fold cross-validation where the data points are separated in k-folds and in every iteration, one fold is kept for testing and the rest for training. In all cases, the average performance is reported and is indicative of the generalisability of the model. This method is less computationally expensive than exhaustive methods examining all possible partitions. It has been shown that using LOOCV reduces bias, however k-fold has been shown to have less variance (266).

It needs to be noted that as the sample size decreases the 'curse of dimensionality' might lead to underestimation of the generalisation error when cross-validation is used (267).

3.4.5 Machine learning and MR brain imaging

Classification based on features extracted from MRI images is used at an increasing rate in studies investigating conditions such as: mild cognitive impairment and Alzheimer's, (246, 249, 268), brain tumors (269), Parkinson's (270), mental disorders (271) and mild traumatic brain injury (272).

Structural MRI is by far the most thoroughly examined modality when attempting to detect patterns of difference between examined groups and perform classification of subjects into a certain class. The majority of studies looking into patient classification using structural MR images, seek to identify regions leading to optimal class-separation, hence the initial feature vector comprises all the image voxels. When machine learning approaches are used to detect differences at a voxel-wise level, it is essential that the images are registered to a common space as is the case with voxel-based morphometry since every voxel is examined individually in terms of its classification power.

Only a few studies have evaluated features from MRI modalities outside of structural imaging, such as resting state fMRI, DSC-MRI and diffusion imaging (249, 269). In terms of ASL only two studies have incorporated single-PLD ASL-derived metrics and these were limited to values extracted from the CBF maps (273, 274). One of the most popular classifiers used in such studies is SVM due to its competitive advantages such as good generalisation, stability and most importantly good performance in small datasets. A review from 2012 nicely summarises the use of SVM classifiers in neurological and psychiatric disorders for classification, prediction of conversion to un-healthy state and response to treatment (275).

In Alzheimer's disease, classification and feature selection based on structural MRI images is highly popular and multiple algorithms have been explored (249, 268). The popularity of such methods led to a global challenge for classification of Alzheimer's using information from T1-weighted structural MRI scans (CADDementia 2015 challenge - <https://caddementia.grand-challenge.org/>).

Currently there is no published study looking into classification of T2DM patients using MRI data. This could be due to multiple reasons. First of all, diabetes is not considered to be a neurological disease, but rather a disease with several neurological complications, which are not present in every patient. In Alzheimer's disease, structural and functional changes are prominent and consistently seen in the brain. For this reason, structural scans with high resolution are heavily used for feature extraction and classification. In T2DM though, the pattern is more subtle and depending on the disease stage, neurological complications might not be present. The disease's indistinct

pattern is a hindering factor to using such techniques, since it is difficult to capture the disease's spectrum in the typically small samples used for training. Additionally, diabetes patients can present with a wide range of microvascular complications, which can have their own distinct neurological pattern such as retinopathy and neuropathy. Diabetes might be well controlled or non-well controlled, the subjects might or might not be on insulin. All these factors contribute to complicating the classification process, since the disease's spectrum is broad and the structural abnormalities may or may not exist.

With the majority of research to-date being focused on using structural scans for brain MRI based classification, it does not come as a surprise that the neuroimaging field in T2DM is not rife with papers attempting classification of T2DM vs healthy controls.

3.5 Theory Summary

In this, and the previous chapters, the theoretical background of the MR imaging modalities used in this study was presented, along with the brain image processing and machine learning approaches chosen to analyse the available datasets. The condition under investigation, T2DM, and the relevant neuroimaging findings have also been presented. ASL was discussed in detail and QUASAR ASL, the core modality in this project used for perfusion imaging, was introduced. The described brain image processing techniques ranged from brain extraction, segmentation and registration to VBM. Finally, the triplet of feature extraction, feature selection and classification was introduced and the theory of the classifier used in this project, SVM, was discussed.

Chapter 4:

Retrospective cohort - MR protocol - Utilised software

The aim of this PhD thesis was to provide a deep insight into the changes occurring in the brain of type-2 diabetes patients and in subjects with pre-diabetes. The key imaging modality was QUASAR ASL, used for perfusion quantification. At the same anatomical level where QUASAR was acquired, T1- and T2-weighted scans were conducted to shed light onto structural abnormalities. DW images were acquired as a means to detect potential changes in the diffusivity of water molecules. A TOF-MRA scan was acquired to delineate the whole cerebral vasculature of the subjects and finally PC-MRA was used to determine the velocity of the inflowing blood at the level of the carotids. The approximate spatial coverage of the considered MRI techniques is as in figure 4.1.

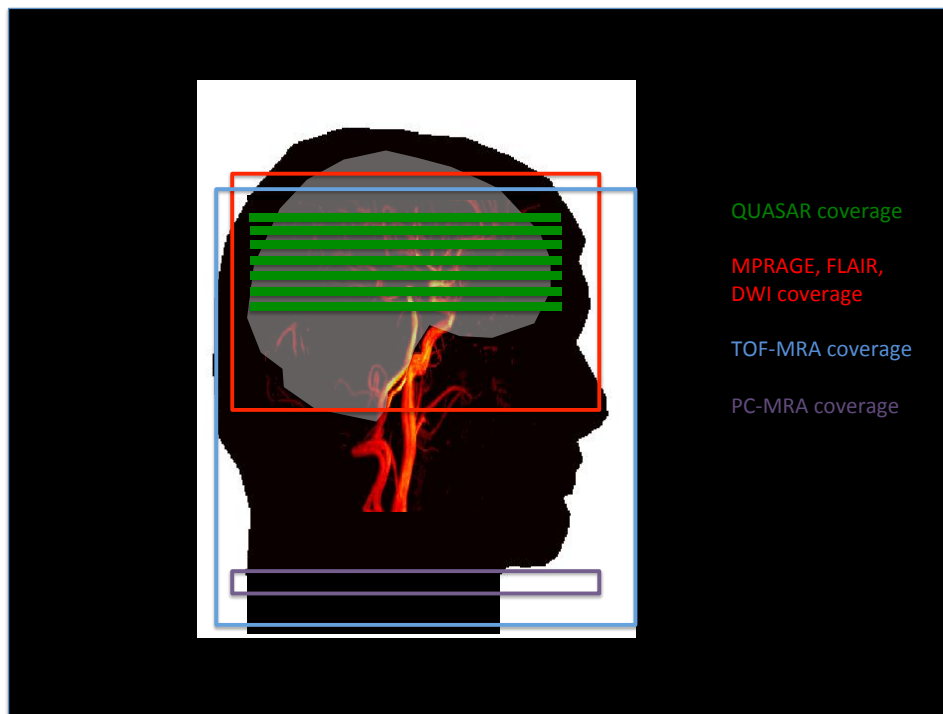


Figure 4.1: Approximate anatomical coverage of the utilised MRI protocol

4.1 Available cohort

Data from 45 subjects (table 4.1) were collected in 2011 as part of the “Magnetic Resonance characterisation of Cerebrovascular Disease in type-2 Diabetes” study. The participants belonged to one of the following groups: healthy individuals; individuals with IGT; and T2DM patients who were neurologically asymptomatic. Individuals having suffered stroke or other acute neurological conditions were excluded from the study. Ethical approval was obtained by the NHS South Sheffield Research Ethics Committee (REC reference number 06/Q2305/57). All subjects provided written, informed consent. The analysis, storage and management of the data was in line with this ethical approval. Data were kept at all times in STH and University of Sheffield premises and equipment, all files were anonymised before processing.

Table 4.1: Details of the retrospective cohort

	HV	IGT	T2DM
N	16	12	17
Age (y)	50.0±12.0	54.8±5.3	55.6±12.5
sex	8♀ 8♂	5♀ 7♂	8♀ 9♂
BMI (kg/m²)	26.0±34.7	32.3±3.2	31.3±3.7
Hypertension (subjects)	4	6	7
Diabetes duration (y)	N/A	N/A	10.0±4.4
HbA1c (%)	-	-	9.5±1.8
Microvascular complications	-	-	5 neuropathy 3 retinopathy 1 nephropathy
insulin	-	-	4
Smoking history	3 ex-smokers	3 ex- 3 current	7 ex – 2 current

The sample size for the present study was quite small, hence conclusions drawn from the subsequent analysis should be interpreted with caution. This is

a preliminary study which will be used as a pilot study to examine subtle changes occurring in subjects with pre-diabetes and T2DM without neurological or cardiovascular complications. The groups were age matched ($p = 0.2$), however the HV group was on average younger (but not significantly). Additionally, the age range was quite large, hence some of the effects that might be observed could be attributed to age differences. The ultimate goal of this study is to use the pilot results in a larger study population to examine whether the observed effects generalise to the T2DM and pre-diabetes population.

4.2 MR Imaging Protocol

Imaging was performed at 3T (Achieva 3T, software version 2.1.3.5, Philips, Healthcare, Best, NL). Radiofrequency transmission utilised the in-built body resonator for all subjects. Radiofrequency reception used an 8-channel localised head coil enabling sensitivity encoding (SENSE) methodology when appropriate. The magnet gradient system (dual mode Quasar, Philips) had a maximum peak amplitude of 80 mT/ m with a slew rate of 100 mT/ m/ ms. The superconducting magnet had a 0% liquid helium cryogen boil-off rate. Data acquisition was conducted in 2010, five years prior to the commencement of the PhD resulting in the present thesis.

Details of the sequences acquired in the imaging protocol, the reasons why they were acquired (i.e. key project contribution) and the methods used to analyse those images are provided below:

4.2.1 QUASAR ASL

Key project contribution: Evaluation of multiple perfusion-related parameters.

Following pilot scans for localization of intracranial anatomy, five QUASAR ASL scans were acquired for every individual, one before and four after they were subjected to an ACZ pharmacological stress test. After the first QUASAR scan the participants were intravenously administered with 1g of ACZ (Diamox Sodium parenteral, Wyeth laboratories, Maidenhead, UK) through a cannulated antecubital vein while they remained in the scanner over 10 minutes. Following this step, 4 further consecutive QUASAR scans without a

time-gap between them were acquired to evaluate the response of the subjects to the hemodynamic vasodilating stimulus.

The characteristics of the QUASAR acquisition were as follows: TR/TE/ Δ TI/TI1=4000/23/300/40ms, 13 inversion time-points (40 - 3640ms) Matrix = 64x64, 7 slices, in-plane resolution=240x240 (mm²), flip angle (FA) = 35/11.7°, SENSE factor = 2.5, inversion slab=150mm. 84 averages were acquired (48 with V_{enc} = 4cm/s, 24 without crusher gradients and 12 low flip angle acquisitions), all implemented in a single sequence (interleaved). The duration of every scan was 5min 36s. The gap between slices was 2mm and the thickness of every slice was 6mm. The readout was conducted using single-shot Look-Locker EPI (147).

Analysed with: Software developed in-house using the Matlab platform (described in detail in **chapter 5**) and the QUASIL ASL tool (154) from FSL. QUASAR data from the cohort were analysed in detail in **chapter 6**.

4.2.2 3D- T1 weighted (MPRAGE)

Key project contribution: Evaluation of brain structure, atrophy and volumetric changes.

A high-resolution 3D magnetization prepared rapid gradient echo (MPRAGE) scan was acquired with the following characteristics: TR/TE = 7.2/3.2ms, FOV= 218.5x240x162 mm³, Matrix = 288x288x180, scan duration 5min 52s and a FA=8°.

Analysed with: Software developed in-house using the Matlab platform, FSL (276, 277), SPM (214) and Freesurfer (203). Detailed description and analysis results are presented in **chapter 7**.

4.2.3 FLAIR

Key project contribution: White matter hyperintensities detection and quantification of their number and volume.

The parameters for the FLAIR acquisition were as follows: TR/TE=11s/120ms, inversion time=2.8s, FOV=230x172.5x141.5mm³, matrix=512x512, scan duration 4min 24s, slice thickness=5mm, gap =1.5mm, 22 slices and FA=90°.

Analysed with: Brain lesion toolbox (238) and textural analysis. Detailed results can be found in **chapter 7**.

4.2.4 PC-MRA

Key project contribution: Measurement of flow and velocity at the level of the carotids.

The parameters for this acquisition were as follows: TR/TE=8/4.39ms, FOV=220x178.75 mm², matrix size=256x256, scan duration 1min 53s, slice thickness=5mm, max number of cardiac phases=40, FA=10° and Venc=120cm/s along the slice encoding direction. One scan was acquired before and one after ACZ injection. The acquisition was optimised for the right carotid.

Analysed with: Software developed in-house using the Matlab platform. Description of the software and analysis results can be found in **chapter 7**.

4.2.5 DWI

Key project contribution: Local and global quantification of the apparent diffusion coefficient.

The scanning parameters for the DWI scan were: TR/TE=2667.41/88ms, FOV=230x230mm², matrix=256x256, slices=22, scan duration 50.7s, slice gap=1mm, slice thickness=5mm, FA=90°, at b-values of 0 and 1000 s/mm², number of diffusion orients: 3.

Analysed with: Software developed in-house using the Matlab platform. Results can be found in **chapter 7**.

4.2.6 TOF-MRA

Key project contribution: Evaluation of the cerebral vasculature.

The parameters of the TOF-MRA scan were set as follows TR/TE=25/3.45ms, FOV=210x199.5x111mm³, matrix size= 512x512, slices=222, slice thickness=1mm, scan duration 6min 55s and FA=20°.

Analysed with: Software developed in-house using the Matlab platform. Details about the software tools and analysis results are in **chapter 7**.

4.3 Overview of utilised software tools

Processing took place using a MacPro under OS X (Apple, Inc., Cupertino, California, US). Images were exported from the scanner in .PAR/.REC format (Philips Healthcare, Best, NL).

Software tools were built on the Matlab 2016a platform (The MathWorks, Inc., Natick, Massachusetts, US) for all the aforementioned modalities. Wherever applicable the results were compared with those obtained with other post-processing tools. The Matlab toolboxes used in this thesis were: fuzzy logic toolbox, image processing toolbox, statistics and mathematics toolbox and LibSVM (278). Additional downloaded functions from third parties found on the Matlab file exchange were: fuzzy c-means clustering (279) used for image segmentation, SVM-RFE (280) used for feature ranking, registration toolbox (281) used for all registration steps implemented in Matlab and Frangi's vesselness filter (282) used for segmentation of the acquired angiogram.

ITK SNAP (283) was used to generate an affine transformation to be used for normalization to the Montreal Neurological Institute (MNI) space. The MNI map used was the 2mm smoothed map (91x109x91 voxels) based on 152 individuals. The transform was implemented using the convert3D tool provided as part of the ITK-SNAP toolkit.

Software tools utilised throughout the thesis apart from Matlab were: advanced normalization toolbox (ANTs) (208, 218) for registration and bias field correction purposes, ITK-SNAP for registration and FSL, Freesurfer and SPM for analysis of the MPRAGE scan. A more detailed description of the specific tools used from FSL, Freesurfer and SPM can be found in the associated

chapters where they are explained as part of the methodology. For statistical comparisons either Matlab or SPSS (IBM Corp. Released 2017. IBM SPSS Statistics for Mac, v. 25, Armonk, NY: IBM Corp) were used.

Chapter 5:

Developments in brain perfusion image processing

Abstract

Cerebral perfusion evaluation using QUASAR ASL has had limited clinical uptake due to the technique's low SNR, image artifacts and non-trivial quantification of blood flow. The aim of this part of the study was to improve the QUASAR processing pipeline by introducing three modifications: weighted AIF assignment, AIF re-evaluation and artifact detection. Additionally, we evaluated approaches for PVC using linear regression based on both high and low-resolution T1-weighted data. Changes were evaluated using the model-free QUASAR ASL variant whereby determination of the CBF relies on deconvolution of the tissue and arterial signals rather than on fitting the signals to well-defined curves.

In this Chapter, a k-radius AIF weighting method is introduced, where AIFs are assigned to every voxel based on a weighted average of neighboring AIFs within a sphere of radius k. The AIF re-evaluation step relies on an initial CBF calculation used to determine and exclude from the AIF assignment step voxels with unrealistic CBF values. A technique based on edge detection on the ASL difference images was built for artifact detection. Simulated and in-vivo data (twelve healthy subjects) were used to evaluate the methods. CBF from the in-vivo data was compared to values obtained using available QUASAR processing software. Additionally, CBF values were calculated by creating pseudo-single time-point pulsed ASL experiments for every time-point to evaluate inter-subject variability in the timing of the perfusion peak.

Simulations indicated that k-radius AIF weighting results in accurate GM CBF estimates with lower mean absolute percentage errors for voxels with high GM content, especially in the presence of hyper/hypo intense regions which are typically present in pathology (e.g. stroke). The QUASAR artifact detection algorithm effectively identified a water-fat shift artifact in simulated and in-vivo data. PV maps generated based on a combination of PV estimates from high

and low-resolution data demonstrated good performance in terms of variance and structural similarity to QUASAR-T1 maps. The CBF values obtained for the examined subjects were physiologically realistic when using the developed pipeline, which also demonstrated a lower inter-subject coefficient of variation in GM CBF estimation when compared to existing analysis software. Variation in the timing of the perfusion peak was observed in this healthy cohort, suggesting that due to transit time variability, in general, multi-PLD approaches might be beneficial for accurate perfusion quantification.

The novel model-free QUASAR processing pipeline described in this chapter produced realistic perfusion values with reduced variance and provided an effective mechanism for artifact detection. These improvements can be targeted toward enhancing the applicability of the QUASAR method to clinical studies.

5.1 Introduction

Cerebral perfusion relates to nutrient and oxygen delivery to brain tissue by the bloodstream and can be measured using a medical imaging technique such as ASL MRI (82). Multiple ASL variants have been devised and can be grouped in different categories using criteria such as the labeling technique, the read-out method and the PLD. In 2015 the ISMRM Perfusion Study Group recommended the use of a particular ASL implementation, that of pCASL (284) with a single PLD, along with the preferred readout schemes (108). The advantages of this method included relatively high SNR, simplicity in implementation and sequence availability.

One disadvantage of the proposed pCASL scheme is its sensitivity to ATT variations. ATT is an important factor to be considered when CBF is quantified, since in aging or neurodegenerative conditions, an increase in ATT can result in erroneous perfusion estimates when single-PLD approaches are used (121, 122). A promising multi-PLD approach termed time-encoded ASL is based on adding multiple labeling/control sub-boli within the previously 'empty' PLD of pCASL. The distribution of these boli is based on a Hadamard-encoded matrix (150, 285). One of the early multi-time-point ASL techniques that overcame the single-PLD limitation by acquiring images at multiple inversion times (TI) is QUASAR ASL. This pulsed ASL technique, combines vascular

signal crusher gradients with a Look-Locker EPI read-out strategy (146, 155). Its reproducibility has been validated in a multi-center study (161).

The Look-Locker read-out involves small flip angle excitations allowing for rapid read-out in multiple time-points (147). Sampling of the recovering magnetization at multiple time-points (13 for the regular QUASAR implementation) allows for signals rather than single data-points to be acquired. Hence the term 'signal' in the rest of the chapter, when used, will refer to the evolution of the measurement under consideration (e.g. tissue signal) during the acquired 13 time-points at a voxel-wise level. Vascular crushing is achieved by applying gradients of the same magnitude and inverse polarity to suppress signal from fast moving spins exceeding a certain velocity threshold.

Perfusion evaluation using QUASAR ASL can be a cumbersome task due to the technique's relatively low SNR and non-trivial quantification. The goal of this part of the thesis was to improve the QUASAR model-free processing pipeline by introducing and evaluating a number of modifications. Several parts within the pipeline lend themselves to optimization. We have focused on the AIF assignment strategy, detection of a water-shift artifact and partial volume correction. A strategic choice was made to avoid techniques that might introduce bias in the processing by means of model fitting and introduction of normality assumptions, since the pipeline is to be used in a non-healthy cohort.

One of the advantages of QUASAR is that based on the difference signal between non-crushed and crushed acquisitions, multiple local AIFs can be identified. AIFs are typically determined in voxels with aBV exceeding 1.2%. Alternative approaches for AIF determination are their statistical reduction using factor analysis of dynamic studies (FADS) (163) and de-noising by fitting the arterial signal to a gamma-variate function (154). The common characteristic of these methods is that a single input function is assigned to every voxel by means of its closest neighboring AIF. A weighted approach accounting for noisy AIFs and the possibility of multiple inputs from more than one source has not yet been evaluated. Such an approach could be of great importance where, for example, disease-related topological changes in blood supply, for example Moya-Moya disease (286), may exist.

Caveats associated with QUASAR ASL often relate to low SNR (a generalised ASL issue), a relatively large voxel size leading to PVE (240) and

acquisition-related artifacts. One such artifact that has been alluded to in several studies has been described as resulting from a 'water-fat' interface shift (106, 168). This effect can be cancelled during control-labeled subtraction; however, potential imperfect anatomical alignment between the experiments may result in non-physiological hyper- or hypo- intense regions in calculated CBF maps. Currently the mitigation technique to avoid potential impact of this is to exclude hyper-intense voxels from the analysis following CBF quantification. However, this approach does not ensure artifactual voxels are not used to determine AIFs and they may hence influence CBF values in neighboring voxels.

Choosing a technique for PVC for the QUASAR data requires a decision over whether the PV estimates will be extracted from a high resolution T1-weighted scan or directly from ASL data. The first approach requires segmentation of a high-resolution T1 scan, down-sampling and registration to the ASL data (240, 241). Considerations pertinent to this approach are the imperfect registration and the difference in point spread functions between the different scans (242). An alternative approach, FRASIER (FRActional Signal mapping from InvErsion Recovery), seeks to determine the tissue content of every voxel based on the QUASAR data. This is feasible by expressing the signal in every voxel as a linear combination of the signals arising from three different compartments- GM, WM and CSF (243, 244). The advantage of this technique is that it does not require registration; however it utilises low SNR data and hence it is susceptible to noise. When opting for a technique based on a high resolution scan, two of the most popular approaches are linear regression (240) and an approach based on spatially adaptive priors used in a Bayesian context (241).

The developed pipeline described in detail in this chapter was constructed with a view to improving the model-free CBF quantification procedure. This new pipeline was validated using both simulated and in-vivo data and was compared with existing processing software.

5.2 Post-acquisition QUASAR ASL processing strategy

5.2.1 Noisy scan rejection

The acquired ASL data can be separated into six groups: high FA crushed control (24); high FA crushed labelled (24); high FA non-crushed control (12); high FA non-crushed labelled (12); low FA control (6); and low FA labelled (6). For every acquisition in each group, 13 time-points were acquired. In order to account for excessive motion, an algorithm for rejection of pairs of control-labelled images evidencing excessive motion was implemented following Knutsson et al. (163). Labelled images were subtracted from their controls and a mean image was generated. An artifact level was calculated for every pair of images by measuring the absolute difference from the mean image and summing up the values for every voxel. If the result exceeded the mean artifact level by more than one standard deviation, then the pair of images was rejected. Average images were generated for every acquisition, for every slice and every time-point.

For the generation of brain masks, every slice's histogram was thresholded using Otsu thresholding (287) and minor morphological operations (dilation, image filling) were carried out. The mask was manually corrected when not visually optimal. Following brain masking, a registration step was added to the processing pipeline to account for subject motion between the numerous QUASAR acquisitions. Every 2D image was registered using rigid registration to the first non-crushed control acquisition of each experiment using the Matlab registration function part of the Image Processing Toolbox. This procedure took place for every time-point. New average images were generated after registration and were used for the subsequent analysis.

5.2.2 Tissue relaxation and magnetization quantification

Effective values for tissue relaxation time, $T1t$ ($T1t_{\text{eff}}$) and tissue equilibrium magnetization, $M0t$ ($M0t_{\text{eff}}$) were calculated by means of fitting to a saturation recovery curve (equation 5.1). The fitting procedure takes place for both the low ($\varphi_{n,\text{low}}$) and high ($\varphi_{n,\text{high}}$) flip angle data (155).

$$S(t) = M0t_{eff} \left(1 - A * e^{-\frac{t}{T1t,eff}} \right) \quad [5.1]$$

The method used for the fitting was mean square error fit. The effective values are lower than the actual T1t and M0t, an effect attributed to signal reduction due to the application of small flip angle excitations as part of the Look-Locker EPI acquisition. The connection between the effective and actual values is as in equations 5.2 & 5.3.

$$M0t_{eff} = \lim_{n \rightarrow \infty} M_z[n] = M0t * \frac{\left(1 - e^{-\frac{\Delta TI}{T1t}} \right)}{1 - \cos(\varphi) e^{-\frac{\Delta TI}{T1t}}} \quad [5.2]$$

$$\frac{1}{T1t_{eff}} = \frac{1}{T1t} - \frac{\ln(\cos(\varphi))}{\Delta TI} \quad [5.3]$$

Where φ is the actual flip angle and ΔTI is the time between excitations.

The true relaxation time of the tissue is not dependent on the applied flip angle, hence an angle correction factor (g) incorporating the effects of field inhomogeneities can be calculated by minimizing the expression in equation 5.4 (160) which is based on minimizing the difference between the true relaxation times calculated for both applied flip angles based on equation 5.3.

$$\frac{1}{T1t_{efflow}} - \frac{1}{T1t_{effhigh}} + \ln \left(\frac{\cos(\varphi_{nlow} * g)}{\cos(\varphi_{nhigh} * g)} \right) \quad [5.4]$$

In order to minimize this expression, g values from 0 to 1 with a step of 0.01 were evaluated and the one minimizing the equation was selected. When there was more than one such value, the average was taken into account. Having determined the angle correction factor at a voxel-wise level, it was feasible to calculate the actual values (accounting for the actual and not the nominal flip angle) for T1t and M0t by using equations 5.2 & 5.3.

5.2.3 Arterial transit time calculation

Arterial transit time can be evaluated by measuring the time interval

during which the tracer traveled from the site of the arterial input to the microvasculature. This calculation is feasible by identifying the arrival time of the signal in the tissue (τ_m) and subtracting from it the time of arrival in the arterial input (τ_α). The arterial and tissue signals were defined at a voxel-wise level based on the 13 inversion time-points. One suggested method to quantify τ_m and τ_α is to identify the rising edge of the signals by using Canny edge detection (155). The method applies convolution of the initial signal (tissue or arterial) with a Gaussian function to account for the noisy high frequency components. Subsequently Canny filter, which is capable of localizing the position of edges with great accuracy is used (288).

In the present thesis localization of the rising edge of the tissue and arterial signals was conducted as follows: The signals were linearly interpolated. The peaks of the signals were identified and moving backwards in time the time-point at which the 30% of the maximum value of the signal was reached was determined. This procedure was implemented for every image voxel and voxel-wise estimates of τ_m and τ_α were extracted. Arterial Transit Time (ATT) was calculated using: $ATT = \tau_m - \tau_\alpha$.

5.2.4 Arterial blood volume and arterial input function calculation

Arterial blood volume is modelled as the area underneath the curve formed by the subtraction of the crushed (ΔM_{cr}) from the non-crushed (ΔM_{ncr}) signal, multiplied with an exponential factor to account for T1t relaxation of the blood and divided by the theoretical bolus area (equation 5.5).

$$aBV = \frac{\int_{-\infty}^{\infty} (\Delta M_{ncr}(t) - \Delta M_{cr}(t)) e^{\frac{t}{T1a}} dt}{2 * M0a * \tau_b * a * \cos^n \varphi} \quad [5.5],$$

- **T1_a** Longitudinal arterial blood relaxation time
- **τ_b** temporal length of the bolus
- **α** inversion efficiency and

$$n = \frac{\text{floor}(\tau_m - \tau_\alpha)}{\Delta TI} \quad [5.6]$$

The term $\cos^n\phi$ is used to account for incomplete renewal of the arterial blood between different acquisitions (289) and n is calculated based on equation 5.6. $M0_\alpha$ can either be measured in a voxel filled with blood usually in the sagittal sinus (290), or it can be mapped as follows: $M0_\alpha = M0t / \lambda$, where λ is the blood-brain partition coefficient.

Given the arterial blood volume (aBV), voxels with aBV of more than 1.2% (as suggested by Petersen et al. (155)) can be used as candidate voxels to calculate regional AIFs by using equation 5.7. In published QUASAR papers, an AIF is assigned to every tissue voxel by means of its closest rAIF voxel. If more than one AIF is at the same distance then their average is used (155).

$$AIF(t) = \frac{(\Delta M_{ncr}(t) - \Delta M_{cr}(t))e^{\frac{t}{T1a}}}{aBV} * e^{-\frac{t+(\tau_m-\tau_a)}{T1a}} \quad [5.7]$$

Another suggested approach relying on a model-based post-processing identifies candidate voxels using the same 1.2% threshold by fitting the arterial signal with a gamma variate function and choosing the voxels for which the peak amplitude of the fitted signal scaled by $M0_\alpha$ exceeds 1.2% (154) or by using a statistical method (FADS) for reduction of the available AIFs (106).

k-radius AIF weighting

Typically, the closest AIF (or average if more than one) is assigned to every voxel. In this chapter, a novel method for AIF assignment termed, 'k-radius AIF weighting', is introduced. The rationale behind this method is that AIFs are assigned to every voxel using a weighted average of a varying number of neighboring candidate AIFs situated within a certain radius of the voxel of interest (figure 5.1). The distances (radii) considered for each AIF component were as follows: the reference distance (d) was that of the closest neighboring AIF(s) ($k = 1$) following the conventional QUASAR AIF assignment approach. For increasing k , the considered radius was calculated as in equation 5.8. Hence for $k = 1$, this approach is the same as for the regular QUASAR processing.

$$rad(k) = d + (k - 1) * 1.5 \quad [5.8]$$

where $k = 1 \dots N$ and $rad(N)$ is the maximum radius considered which in the following simulations was $N=6$. The weight (w) assigned to each of the

component AIFs was given by $w_k = 1 / \text{rad}(k)^3$, and thus depended on their distance from the voxel of interest within the sphere of radius $\text{rad}(k)$. The AIF assigned to each voxel was a weighted average of the neighbor component AIFs (equation 5.9). All distances were calculated between the voxel centers and $\text{rad}(k)$ distance was measured in voxels rather than in mm.

$$AIF(t) = \frac{\sum_{k=1}^N (w_k * \sum_{j=1}^{M(k)} AIF_j)}{\sum_{k=1}^N (w_k * M(k))} \quad [5.9]$$

Where $M(k)$ is the number of identified AIFs at each considered radius, k .

The resulting CBF was then quantified using a model-free approach (155). The deconvolution method used was singular value decomposition with an oscillatory index of 0.15 (oSVD) and was based on the implementation by Ahlgren et al. (291).

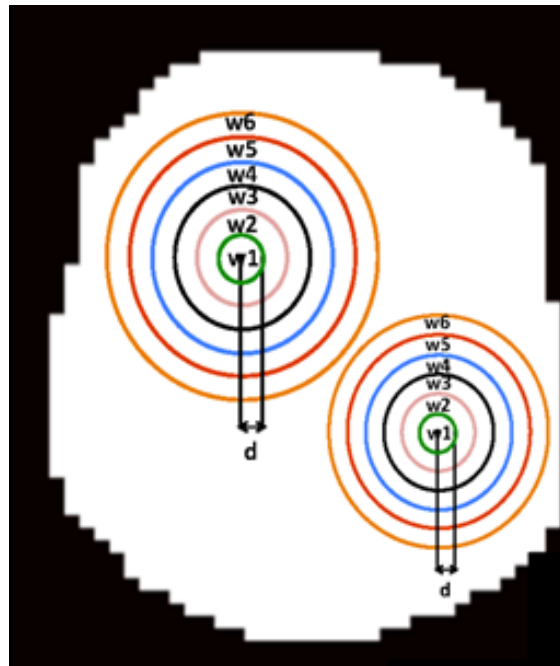


Figure 5.1: AIF weighting approach. The candidate AIFs situated within a sphere of a certain radius k are assigned a weight based on their distance from a voxel of interest. The procedure takes place in 3D but 2D slices are shown for simplicity.

AIF re-evaluation

Following CBF quantification it was noticed in some cases that several voxels had non-physiological CBF values, either extremely small positive (CBF < 5 ml/ 100g/ min) or negative, or excessively large (CBF > 150 ml/ 100g/ min). To account for the fact that these potentially noisy voxels might have been used as voxels for AIF determination, an ‘AIF re-evaluation’ step was added to the

pipeline. During this step, the voxels with non-physiological values that were used as for AIF determination were identified and the whole AIF assignment and CBF quantification step was re-run without them. This procedure was run a single time to avoid excessive regularization but has the potential to be applied numerous times.

Following re-evaluation, voxels exceeding the chosen CBF thresholds were masked out in the end of the procedure. It is worth mentioning that mean normal values for GM CBF and WM CBF are considered 60 ml/ 100g/ min and 20 ml/ 100g/ min respectively (241). Currently there is no mitigation technique for this effect. The typical approach is to threshold the final calculated CBF map with a threshold between 120-150 ml/ 100g/ min; this approach does not address the fact that even for the typical QUASAR quantification with $k = 1$, these noisy AIFs might have been used for AIF assignment thus impacting directly the whole area around them. Potential inclusion of voxels with artifactually high CBF values in perfusion quantification would imply over-estimation of both GM and WM CBF values. Especially in a small cohort such as the one utilized in the present study this effect could directly impact on the drawn conclusion following estimation of perfusion in every considered group. Hence, it is of utmost importance to account for these artefactual voxels as early as possible in the analysis pipeline to reassure that they do not influence neither their local neighborhood nor the final estimated CBF values.

5.2.5 Residue function and CBF estimation

The residue function (\mathbf{R}) and from this the CBF (\mathbf{f}) can be calculated by means of deconvolution. SVD is an algebraic solution to the deconvolution problem, which can be used since the signal is discrete, so the deconvolution problem is reduced to a matrix problem (equation 5.10). In matrix formation, $\Delta\mathbf{M}$ (which when both crushed and non-crushed data are acquired is typically the crushed acquisition - $\Delta\mathbf{M}_{cr}$) and the residue function acquire the form of vectors having as elements their values for every time-point.

$$\Delta\mathbf{M} = \mathbf{f} * \mathbf{AIF} * \mathbf{R} \quad [5.10]$$

With the **AIF** matrix comprising weighted elements as in equation 5.11, in order to reduce noise (292).

$$a_{i,j} = \begin{cases} \frac{1}{6} * (\Delta TI(AIF(t_{i-j-1}) + 4AIF(t_{i-j}) + AIF(t_{i-j+1}))), & 0 \leq j \leq i \\ 0, & \text{otherwise} \end{cases} \quad [5.11]$$

A block-circulant matrix can be constructed for every voxel to account for potential lag of the arterial signal compared to the tissue signal and can be used for circular SVD deconvolution. The square matrix dimensions ($L * L$) must be at least double the size of the initial **AIF** matrix (in order to meet the criteria of the Nyquist limit). The elements of the new matrix (**B**) are equal to the elements of the initial AIF matrix for $j < i$; for $j > i$ the matrix lines are shifted one position to the right each time, resulting in a new matrix **B** (292). In order to calculate the residue function, the inverse of the **B** matrix needs to be found. If the **B** matrix is non-singular, there exists an SVD decomposition of the matrix ($\mathbf{B} = \mathbf{U} * \mathbf{S} * \mathbf{V}^T$). If the matrix is singular, then the SVD algorithm returns the closest decomposition possible in a least-square sense (293). In SVD it is a common approach to threshold the diagonal elements of the **W** matrix ($\mathbf{W} = \mathbf{1}/\mathbf{S}$) to account for high frequency noise. This truncation is thought to underestimate the calculated CBF result (153). The scaled residue function can be calculated as follows (equation 5.12):

$$\mathbf{R} = \mathbf{V} * \mathbf{W} * \mathbf{U}^T * \Delta \mathbf{M}_{zp} \quad [5.12]$$

where $\Delta \mathbf{M}_{zp}$ is the ΔM signal zero-padded to length L .

Circular deconvolution can be modified to account for the excessive oscillations, attributed to high frequency noise by using an oscillatory index (OI) (equation 5.13) (292).

$$OI = \frac{1}{L} * \frac{1}{\max(R)} * \sum_{k=2}^{L-1} |R(k) - 2R(k-1) + R(k-2)| \quad [5.13]$$

For the present implementation, a block-circulant matrix was constructed for every voxel. The matrix had double the size of the **AIF** matrix moving from an initial size of $13 * 13$ (for the 13 time-points comprising the AIF discrete signal)

to a size of 26*26. The tissue signal was zero-padded at a length of N=26. To account for excessive oscillations, a threshold was used for the eigenvalues of the diagonal matrix (S) emerging from the SVD decomposition. The starting value for the threshold was 20% of the maximum eigenvalue. Any value lower than that was zeroed. The OI was calculated again after zeroing; if it was higher than $OI = 0.15$ then the threshold value was increased by 1%. This step was repeated until the calculated OI had a value below the permitted 0.15.

5.2.6 Artifact detection

In several QUASAR ASL images the presence of an artifact was noticed as in figure 5.2A. A similar artifact has been reported in the literature as a 'chemical water-fat' shift artifact (106). The existence of such an artifact can be attributed to absence of fat suppression pulses in the QUASAR pulse sequence. Potential inclusion of such pulses would require a longer and more complicated preparation scheme with an increased inversion time, which would end up in further attenuation of the signal and SNR reduction. Additionally, a separate background suppression scheme as instructed by the ASL consortium is not applied in QUASAR, however, the applied low flip angles compensate for this effect.

By examining the QUASAR .PAR/REC files there appears to be a displacement between the water and the fat of 12-13 pixels in the phase encoding direction. In QUASAR ASL background suppression and fat suppression pulses are not used, to reduce the complexity of the acquisitions. The absence of such pulses is a potential confound to the artifact. A method described in QUASAR literature to compensate for its presence, is to exclude from the analysis voxels with values more than three times the average value of CBF (106, 168). However, this approach does not correct for the fact that some of these voxels might have been used for the calculation of regional AIFs.

A new approach is presented in this chapter to compensate for the artifact. An algorithm was built to localize its position (figure 5.2). Initially, the crushed data were subtracted from the non-crushed data, giving rise to images whereby the arterial signal is brightened. The gradient magnitude image which highlights the regions with a sudden change in the intensity pattern of the resultant difference image was calculated and multiplied with the initial ΔM_{ncr}

ΔM_{cr} image to amplify the effect of the edges. The result was squared for further effect amplification. This manipulation resulted in the artifactual voxels being brighter than the non-artifactual ones (figure 5.2A). As a result, a threshold could be used in the image to separate the artifact (figure 5.2B). This approach was run for every time-point, hence the application of the algorithm resulted in 13 separate masks (one per time-point).

It was noticed that some of the voxels were not influenced by the artifact in every time-point so the masks differed. The developed technique used a weighting approach allowing a maximum of three time-points to be influenced by the artifact. Weighting also accounted for the arterial bolus arrival (voxels exceeding the defined threshold at the 2nd and 3rd time-points when the intravascular signal will be at its peak had to be identified in at least 7 time-points as being artifactual) and attenuation of the labeling effect (at the 13th time-point the inverted magnetization is expected to be fully recovered so all voxels exceeding the threshold at this time-point were considered artefactual even if they were not picked by the algorithm in earlier time-points). The resultant masks for every time-point, were weighted and summed up giving rise to an image as in figure 5.2C (middle). Voxels with a lower resultant weight were more likely to be artifactual. For their exclusion, a threshold was applied yielding an inclusive mask to define non-artifactual voxels. This mask was applied to every time-point and to both crushed and non-crushed data. The optimal threshold used was based on the results obtained by simulations (see section 5.2.10 case 3). Optimal thresholds ranged from a value of 3 (more relaxed criterion) to a value of 9 (stricter criterion).

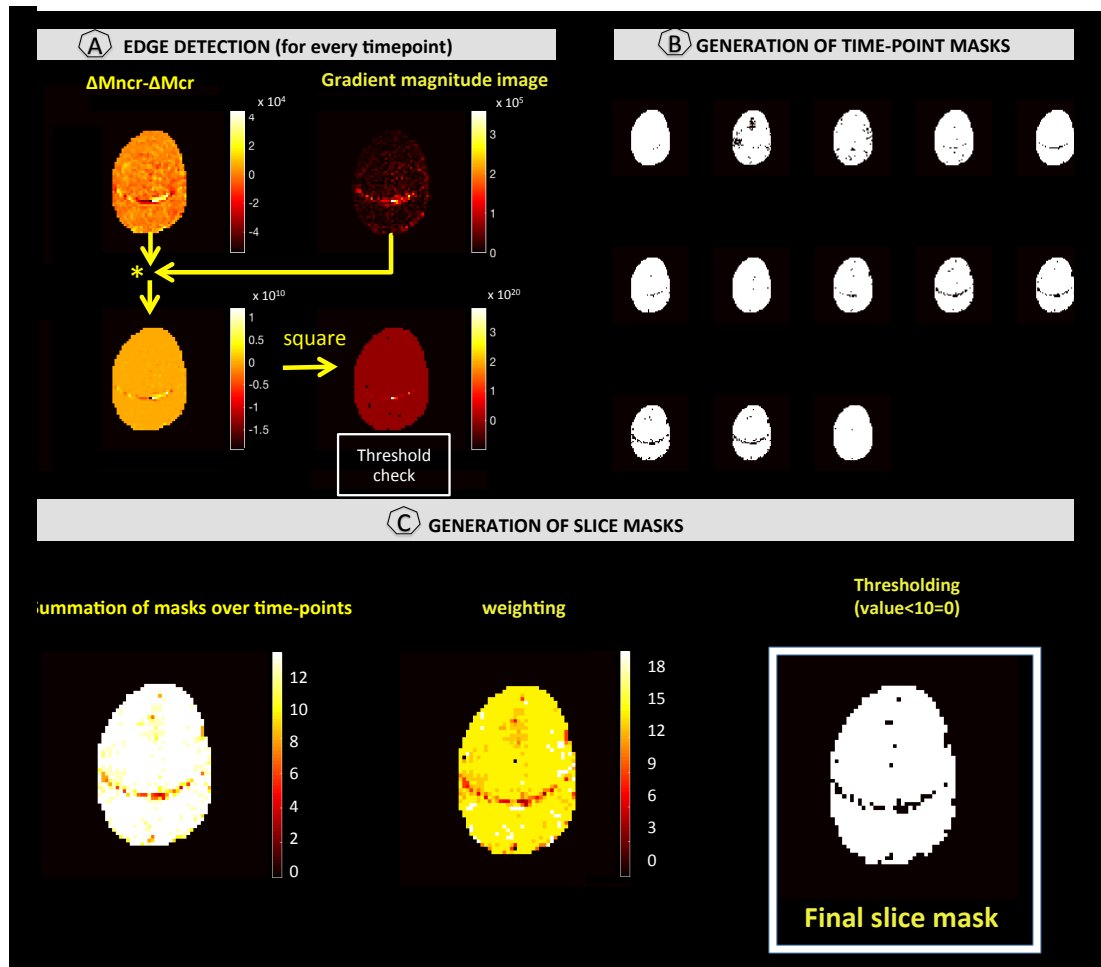
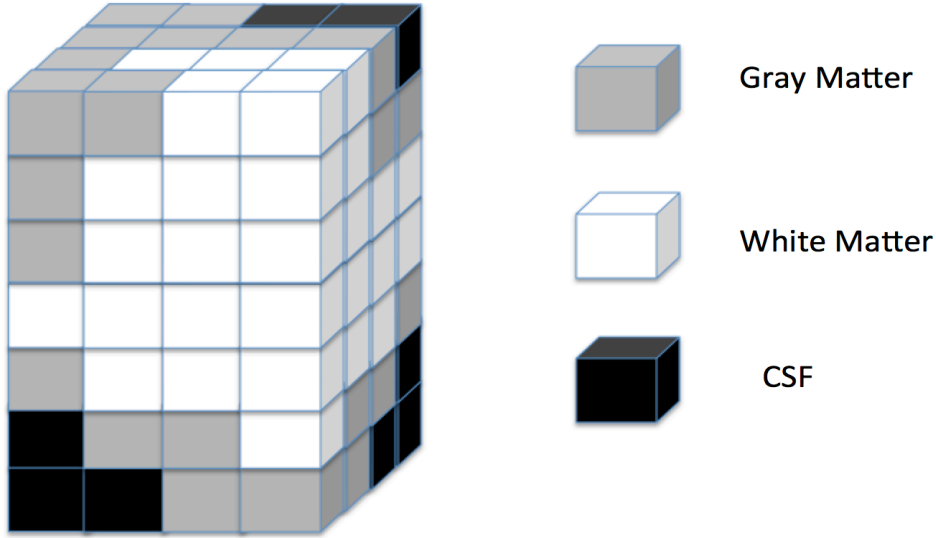


Figure 5.2: Artifact detection and rejection methodology. (A) The artifact is apparent in the $D = \Delta M_{ncr} - \Delta M_{cr}$ difference image. D is multiplied by its gradient magnitude and then squared. A threshold identifies voxels with excessive values. (B) This procedure runs for all 13 time-points in every slice. Artifactual voxels in every iteration are assigned a value of 0. (C) After all 13 time-points are considered for each slice, the masks are summed. A voxel which never exceeds the threshold, is allocated a value of 13; a voxel identified as artifactual each time has a value of zero. At this point a weighting is implemented followed by thresholding.

5.2.7 Partial Volume Correction

The main cause of partial volume effects in ASL is the large voxel size used to account for the inherently low SNR of the technique. The extent of the problem can be grasped if one compares the voxel of a high-resolution T1 scan and an ASL voxel (QUASAR in this case) (figure 5.3). An ASL voxel is highly unlikely to contain only one tissue type and more likely to contain a combination of GM/WM, GM/CSF, or GM/WM/CSF. If the issue is left unaddressed then GM CBF might be greatly underestimated. In this study, the primary utilised PVC technique was the Asllani, Borogovac (240). In its regular implementation, this approach makes use of PV estimates extracted from a high resolution T1-scan to correct for PVE.



*Figure 5.3: Partial volume effects in one Quasar voxel with respect to a 256*256 structural image. A QUASAR voxel can fit 112 voxels emerging from a high-resolution structural scan. For simplicity voxels emerging from the structural are depicted free of PVE.*

The linear regression method works as follows: The ΔM_{cr} signal can be modelled as having only two components: a component attributed to GM and a component attributed to WM, omitting inclusion of the arterial vascular signal. The contribution of CSF was considered as negligible (241, 243). PVC was implemented to the CBF maps (equation 5.14). In its original implementation the method was implemented in the ΔM data, however it has been shown that it can be directly implemented in the final CBF images (243).

$$CBF_{\text{voxel}} = PV_{GM} * CBF_{GM} + PV_{WM} * CBF_{WM} \quad [5.14]$$

In PVC with linear regression, tissue specific CBF is considered to be stable in a certain pixel window. In matrix formation the expression takes the form:

$$CBF_{\text{nei_voxel}} = PV_{\text{nei_tissue}} * CBF_{\text{tissue}} \quad [5.15]$$

Where $CBF_{\text{nei_voxel}}$ is a vector comprised the CBF values in the defined kernel, the $PV_{\text{nei_tissue}}$ matrix has a size of $2 * \text{nei}$ (nei is the number of neighbouring voxels, 2 tissue types) and comprises the tissue specific PV values for every voxel and CBF_{tissue} is a vector containing CBF_{GM} and CBF_{WM} , stable quantities inside this kernel. PV values range from 0 to 1 and indicate the

volume of the voxel covered by a certain tissue type (1 for 100%). By determining the pseudo-inverse matrix of $\mathbf{PV}_{\text{nei_tissue}}$ it is feasible to calculate CBF in the two different tissue types over the neighborhood for which the CBF values for the two tissue types are considered as stable (equation 5.16).

$$\text{CBF}_{\text{tissue}} = (\mathbf{PV}_{\text{nei_tissue}}^T \mathbf{PV}_{\text{nei_tissue}})^{-1} \mathbf{PV}_{\text{nei_tissue}}^T * \text{CBF}_{\text{nei_voxel}} \quad [5.16]$$

Ahlgren et al. (243) have compared PVC results based on PV estimates extracted from the ASL data (FRASIER) and PV estimates from a 3D T1-weighted scan. They have shown that the partial volume corrected GM CBF map generated based on the high-resolution scan tends to be less homogeneous, a factor they attributed to mis-registration between the high and the low-resolution scan.

In this chapter, we have looked into both techniques for PV estimate extraction and also evaluated two ‘hybrid’ methods combining both the high and the low resolution extracted PV estimates. PVC was implemented directly on the CBF maps (240, 243). Overall, four variants were evaluated for the determination of the final PV maps.

For **variant 1**, partial volume maps were generated from the MPRAGE image using SFCM clustering (232). This unsupervised algorithm does not require priors and does not make assumptions about the distribution of the T_1 relaxation times. For PVC based on MPRAGE-derived estimates, the adopted PVC pipeline comprised:

1. N4 bias field correction of MPRAGE images.
2. Identification of overlapping QUASAR and MPRAGE slices, as described in Section 5.2.8 (approximately 7 MPRAGE slices extracted in the transaxial plane overlap with each QUASAR slice).
3. SFCM clustering (5x5 window) in the stack of T1-weighted data with the same anatomical coverage as the QUASAR slices.
4. For every QUASAR slice, averaging of the respective MPRAGE, GM and WM PV maps.
5. Down-sampling of the averaged PV and MPRAGE-T1 maps to the QUASAR spatial resolution.

6. 2D registration of the resultant low resolution MPRAGE-T1 to the QUASAR anatomical-1/T1 maps using affine transformation with a normalized cross-correlation cost function.
7. Registration of the PV maps to the QUASAR anatomical-T1 maps, using the previously generated affine transformation matrix (variant 1).

For the generation of PV maps using the ASL data (**variant 2**) the FRASIER method (243) was used. In this method Gaussian distributions are fitted to the QUASAR-derived T1 image histogram and the T1 of GM and WM are extracted. In the suggested implementation, due to the difficulty to detect the CSF peak in the histogram, a fixed value is used ($T1_{CSF} = 4.3s$). Subsequently the signal in every voxel is expressed as a linear combination of the signal attributed to a certain tissue type and the tissue content. Hence, the tissue content of every voxel can be determined by solving a least square estimation problem (243, 294).

More specifically, the recorded ASL signal attributed to all components can be written as:

$$S(t) = \sum_i [f_{s,i} M_{ss,i} (1 - Ae^{-\frac{t}{T1_{eff,i}}})] \quad [5.17]$$

where

$$M_{ss,i} = \frac{1 - e^{-\frac{\Delta T1}{T1_i}}}{1 - \cos\varphi e^{-\frac{\Delta T1}{T1_i}}} \quad [5.18]$$

In matrix formation $\mathbf{S} = \mathbf{X} * \mathbf{F}_s$ where \mathbf{F}_s is the CBF vector for every tissue and \mathbf{X} is the signal without it being scaled with the CBF for every tissue. It is, hence, feasible to solve for the fractional values as follows using the pseudo-inverse: $\mathbf{F}_s = (\mathbf{X}^T \mathbf{X})^{-1} \mathbf{X}^T \mathbf{S}$.

The third and fourth evaluated PVC variants in this study were hybrid methods combining FRASIER and MPRAGE-derived estimates. In the first of these two, the FRASIER estimates were used as a reference image for more accurate registration of the down-sampled MPRAGE estimates due to their similarity in contrast and measured information (**variant 3**). In the second, a mean PV estimate between variant 2 and variant 3 was constructed (**variant 4**).

In all approaches, the concept of the pseudo-inverse matrix instead of the inverse was used. The pseudo-inverse is typically used to calculate the best solution of a linear system of equations, in a least square sense, in cases where the system lacks a solution or when the optimal between multiple solutions needs to be determined (by choosing the one with the minimum Euclidean norm) (295).

5.2.8 Correction for scan alignment and identification of overlapping slices

The angulation between the slices and the reference axes of the scanner was different between the QUASAR and the MPRAGE scans for every subject. This misalignment was a result of the QUASAR labelling and acquisition strategy. Labelling took place based on the maximum intensity projection of the acquired cerebral angiogram so that it would be perpendicular to the flow.

In order to account for that, the MPRAGE image was rotated into the same orientation as the QUASAR scan as a rotation to the reference coordinates would require a rotation of the QUASAR scan as well. The latter comprises of 7 slices with gaps between them, so interpolation would introduce significant re-sampling errors. As a result of rotation, the initial MPRAGE axial resolution changed from 288*180 pixels to a patient-specific value. The resulting images were resampled to 256*256 in-plane resolution to facilitate the PVC step. Downsampling to the 64*64 QUASAR in-plane resolution was applied by averaging over 4*4 voxel regions.

The requirement for automated processing, requires that the equivalent anatomical slices to the low-resolution QUASAR slices are identified by an algorithm without manual intervention. The developed algorithm chose the slices for which the difference in the z-axis (head-foot) values between the two scans with respect to the initial coordinates was minimized. Subsequently based on these slices, the algorithm identified the overlapping QUASAR and MPRAGE slices based on the thickness of QUASAR slices. The anatomical slices overlapping spatially with the QUASAR slices were subsequently averaged. The similarity between the average slices and the R (1/T1t) QUASAR maps was visually assessed. In case the slices were not visually identical an offset was added or subtracted from the MPRAGE off-centre distance.

5.2.9 Brain-blood partition coefficient (λ)

Having calculated fractional volume maps, it was possible to account for the different values of the brain blood partition coefficient for GM and WM. The PV values in every voxel needed to be scaled for the amount of WM and GM present to avoid underestimation of the λ value due to the presence of CSF. The blood-brain partition coefficient was calculated by equation 5.19.

$$\lambda_{voxel} = \frac{PV_{GM}}{PV_{GM} + PV_{WM}} * \lambda_{GM} + \frac{PV_{WM}}{PV_{GM} + PV_{WM}} * \lambda_{WM} \quad [5.19]$$

5.2.10 Simulated data

Every voxel can be approximated as a simplified system having an AIF as an input and the measured magnetization difference signal (ΔM) as an output. The system's response is defined as $R(t) = r(t) * m(t)$, where $r(t)$ is the residue function and $m(t)$ is the magnetization relaxation function. This system can be described using the general kinetic model (equation 5.20).

$$\Delta M(t) = 2M0_b a * CBF * AIF(t) \otimes r(t) * m(t) \quad [5.20]$$

With AIF(t), $r(t)$ and $m(t)$ as described by equations 5.21-5.22.

$$AIF(t) = \begin{cases} \alpha e^{-\frac{t}{T1b}} & , \quad \Delta t < t < \Delta t + \tau \\ 0 & , \quad \text{elsewhere} \end{cases} \quad [5.21]$$

$$r(t) = e^{-CBF \frac{t}{\lambda}} \quad m(t) = e^{-\frac{t}{T1_{eff}}} \quad [5.22]$$

By substituting AIF(t), $r(t)$ and $m(t)$ in equation 5.20 and solving the convolution integral, the crushed simulated signal is modeled as:

$$\Delta M_{cr}(t) = \begin{cases} 0 & , \quad t < \tau_{arr} \\ \frac{2aM0_b CBF e^{-t * R_{app}} (e^{-\tau_{arr} \Delta R} - e^{-t \Delta R})}{\Delta R} & , \quad \tau_{arr} < t < \tau_{arr} + \tau_b \\ \frac{2aM0_b CBF e^{-t * R_{app}} (e^{-\tau_{arr} \Delta R} - e^{-(\tau_b + \tau_{arr}) \Delta R})}{\Delta R} & , \quad t > \tau_{arr} + \tau_b \end{cases} \quad [5.23]$$

Where $M0_b$ is the blood equilibrium magnetization, α is the inversion efficiency, $R_{app} = \frac{1}{T1t} + \frac{CBF}{\lambda}$, $\Delta R = \frac{1}{T1b} - R_{app}$, $T1t$ and $T1b$ are the $T1$ of the tissue and blood respectively, λ is the blood-brain partition coefficient, τ_{arr} is the bolus arrival time and τ_b is the bolus duration. Values used in the simulations were: $\lambda_{GM} = 0.98$, $\lambda_{WM} = 0.82$, $CBF_{GM} = 60$ ml/ 100g/ min, $CBF_{WM} = 20$ ml/ 100g/ min, $T1_{GM} = 1.3s$, $T1_{WM} = 0.83s$, $T1_{CSF} = 4s$, $T1_b = 1.65s$, $\tau_b = 0.65s$, $\alpha = 0.95$, $\tau_{arr} = 0.6s$ and $\Delta TI = 300ms$ (241, 296).

$M0_a$ and aBV maps were generated from the in-vivo data (equations 5.1 and 5.5). Masks for the whole brain, gray matter, white matter (WM) and cerebrospinal fluid (CSF) were generated from the same individual, based on segmentation of its MPRAGE scan (variant 1; 5.2.7 section).

The non-crushed signal (ΔM_{ncr}) was simulated as the summation of the crushed signal considered to emerge solely from GM, WM and CSF and the arterial signal (ΔM_{art}) (equations 5.24-5.25).

$$\Delta M_{art}(t) = 2 * M0_a * AIF(t) * aBV \quad [5.24]$$

$$\Delta M_{ncr}(t) = \Delta M_{cr}(t) + \Delta M_{art}(t) \quad [5.25]$$

Simulation cases

In order to validate the new pipeline, simulations were run for the following cases based on the data generated as described above:

- a) Case 1 - homogeneous GM (60 ml/ 100g/ min) and WM (21 ml/ 100g/ min) flow regions were simulated and the pipeline was assessed for $k = 1, \dots, 6$. 21 was used instead of 20 for WM since this value is divided by 6000 during the simulation steps.
- b) Case 2 – GM hyper-intense (90 ml/ 100g/ min) and hypo-intense (10 ml/ 100g/ min) regions were added (to Case 1) at one slice to simulate regions with abnormal perfusion. As in Case 1, the pipeline was assessed for $k = 1, \dots, 6$.
- c) Case 3 – the described artifact (as outlined in section 5.2.6, above) was added in both ΔM_{cr} and ΔM_{ncr} simulated datasets with a single-pixel

offset between the crushed and non-crushed images. A random artifact pixel-value was assigned to every voxel in the interval between the maximum intensity value in the dataset and double this value. In this case the pipeline was assessed for $k = 1, 4 \text{ \& } 6$ and for each value of k . In order to determine the optimal threshold to be used as part of the newly introduced artifact detection algorithm, 7 thresholds values were tested. These thresholds were: $\text{thr1} = 10^{20}$, $\text{thr2} = 5 \cdot 10^{19}$, $\text{thr3} = 10^{19}$, $\text{thr4} = 5 \cdot 10^{18}$, $\text{thr5} = 10^{18}$, $\text{thr6} = 5 \cdot 10^{17}$ and $\text{thr7} = 10^{17}$. The chosen values were based on the maximum intensity values, which are at the level of 10^6 . Subsequent processing of the image using the developed algorithm (filtering, square, multiplication) leads voxels not influenced by the artifact having values at the level of up to 10^{14} . Any value above these thresholds was considered artifactual.

For Cases 1 and 2, three regression kernels for PVC were evaluated: one involving the four direct neighbors (minimum smoothing, $\text{PVC} = 5$ voxels); a $3 \times 3 \times 1$ voxel kernel ($\text{PVC} = 9$) and a $5 \times 5 \times 1$ voxel kernel ($\text{PVC} = 25$). In Case 3, only $\text{PVC} = 5$ (i.e. minimum smoothing) was considered. For all simulations, Gaussian noise was added to the ΔM_{cr} and ΔM_{ncr} signal to produce simulated data with a $\text{SNR} = 20$ dB (161). PV maps generated from a single individual were used. The AIF re-evaluation step was evaluated for simulation cases 1 and 2.

5.2.11 In-vivo data

The in-vivo analysis was run for 12 subjects (mean age 47.8 ± 17.4) out of the 16 available HV in the present study, with AIF re-evaluation, artifact detection where applicable (2 cases) and $\text{PVC} = 5$ for all examined k -values. The broad range of ages in our cohort could result in a quite variable AIF shape and potentially to more re-evaluated AIFs. Due to the small sample size, the effect of age was not examined in the present thesis, however, it could be an interesting further extension to this study.

5.2.12 Comparison with QUASIL (in-vivo data)

Due to the lack of a gold standard pipeline for quantification of CBF in QUASAR ASL, the results were compared with a publicly available tool (QUASIL) provided as part of the FSL software package (154). FSL-based tools, require input images in a Nifti format, so Nifti QUASAR images were generated based on the .PAR/.REC images using dcm2niix (297). Based on its published description, QUASIL fits the local AIF signals using gamma variate functions and rejects from potential AIFs those curves that deviate from this specific shape. It has two modes, model-free and model-based, whereby the data are fitted to hemodynamic curves based on the Buxton model for CBF determination in order to avoid deconvolution. For comparison purposed the same PVC strategy was applied to the QUASIL derived CBF maps.

5.2.13 Performance evaluation

Simulated data

To evaluate the performance of the developed methodologies, and to optimize values for weighting of neighboring AIFs, thresholds for the artifact detection step and PVC kernel size, eight metrics were used:

- M1 - the estimated GM CBF value.
- M2 - the estimated WM CBF value.
- M3 - the voxel-wise mean absolute percentage error (MAPE) (equation 5.27) for the calculated CBF map.
- M4 - the voxel-wise MAPE for voxels with GM > 50%, for the final CBF map.
- M5 - the voxel-wise MAPE for voxels with GM > 80%, for the final CBF map.
- M6 - the voxel-wise MAPE for voxels with GM > 50%, for the GM CBF map calculated based on PVC.
- M7 - the voxel-wise MAPE for voxels with GM > 80%, for the GM CBF map calculated based on PVC.

- M8 - the voxel-wise MAPE for voxels with WM > 50%, for the WM CBF map calculated based on PVC.

$$MAPE = 100 * \frac{1}{N} \sum_{i=1}^N \frac{|M_t - M_e|}{M_t} \quad [5.27]$$

where M_t is the true value, M_e is the estimated value and N the total number of instances.

Metric M3 was calculated for the non-PVC CBF maps; all other metrics were calculated for both non-PVC and PVC-corrected CBF maps. For metrics M1 and M2 and the non-PVC scenario GM and WM CBF were calculated as the mean value in voxels with GM or WM content higher than 50% respectively.

Focus was put on GM as ASL is known to be adept for GM perfusion estimation. The signal in WM by the time of imaging due to the higher transit time is attenuated. Only a few ASL techniques such as the ones utilising background suppression are known to be adept for WM CBF quantification (108).

Pipeline evaluation – in vivo data

AIF re-evaluation

For all subjects the analysis was run with and without AIF re-evaluation in order to record the number of re-evaluated AIFs and the impact on the final GM CBF value.

Comparison with QUASIL

The analysis was run with both the model-free and the model-based QUASIL modes and the same PVC strategy as previously described was implemented. The coefficient of variation for each technique was calculated as $CoV = 100 * \sigma / \mu$, where σ is the standard deviation and μ is the mean.

Partial volume correction

The metric used for evaluation of the PVC variants was the structural similarity index (SSIM) (equation 5.28), calculated between the QUASAR T1-maps and the generated GM PV maps. This metric was chosen to evaluate the ability of the segmentation algorithms to preserve anatomical information.

$$SSIM(\xi, \eta) = \frac{(2\mu_\xi\mu_\eta + C_1)(2\sigma_{\xi\eta} + C_2)}{(\mu_\xi^2 + \mu_\eta^2 + C_1)(\sigma_\xi^2 + \sigma_\eta^2 + C_2)} \quad [5.28]$$

where ξ and η are two different images, μ refers to the mean and σ to the standard deviation. $C_1 = (0.01*DR)^2$ and $C_2 = (0.03*DR)^2$, where DR is the dynamic range calculated as the ratio between the maximum and the minimum. The SSIM for the different variants were compared using two-sample t-tests.

5.3 Results

5.3.1 k-radius AIF weighting

Simulation case 1 - homogeneous GM and WM regions

Results for the first simulation case are shown in figure 5.4. No – PVC leads to lower estimated GM CBF values ($k = 1 - 45.7 \pm 0.09$ ml/ 100g/ min; $k = 6 - 44.04 \pm 0.08$ ml/ 100g/ min) and higher WM CBF values ($k = 1 - 24.56 \pm 0.03$; $k = 6 - 23.7 \pm 0.01$ ml/ 100g/ min). Calculated values for all PVC kernels can be found in figure 5.4 A,B. The performance of the developed pipeline was stable between repetitions with low standard deviation. Based on figure 5.4 (A), PVC = 5 with $k = 2, 3$ and PVC = 9 with $k = 1, 2$ consistently produce values closer to the simulated ones. This first set of results suggests that values are stable for an increasing weighting AIF kernel and PVC = 5, 9 are optimal.

Figure 5.4 (E) suggests that errors in metrics M3, M4 and M5 reflecting voxel-wise CBF estimates are lower for an increasing k (except for $k = 2$). No-PVC is connected with higher errors in GM estimation in voxels with high content of GM (figure 5.4 F, G) and lower error in voxels with high content of WM compared to instances where PVC was applied (figure 5.4 H). MAPEs are lower for a high PVC kernel (increased smoothing) when examining voxel-wise GM CBF values and higher when examining WM CBF values. Focusing on GM (figure 5.4 F, G), higher k -weighting is associated with slight reduction in errors with the only exception for $k = 2$ where an increase in the MAPE is observed. A good balance between voxel-wise MAPEs and global estimates is achieved with PVC = 5 with $k = 3, 4$ and PVC = 9 with $k = 3$.

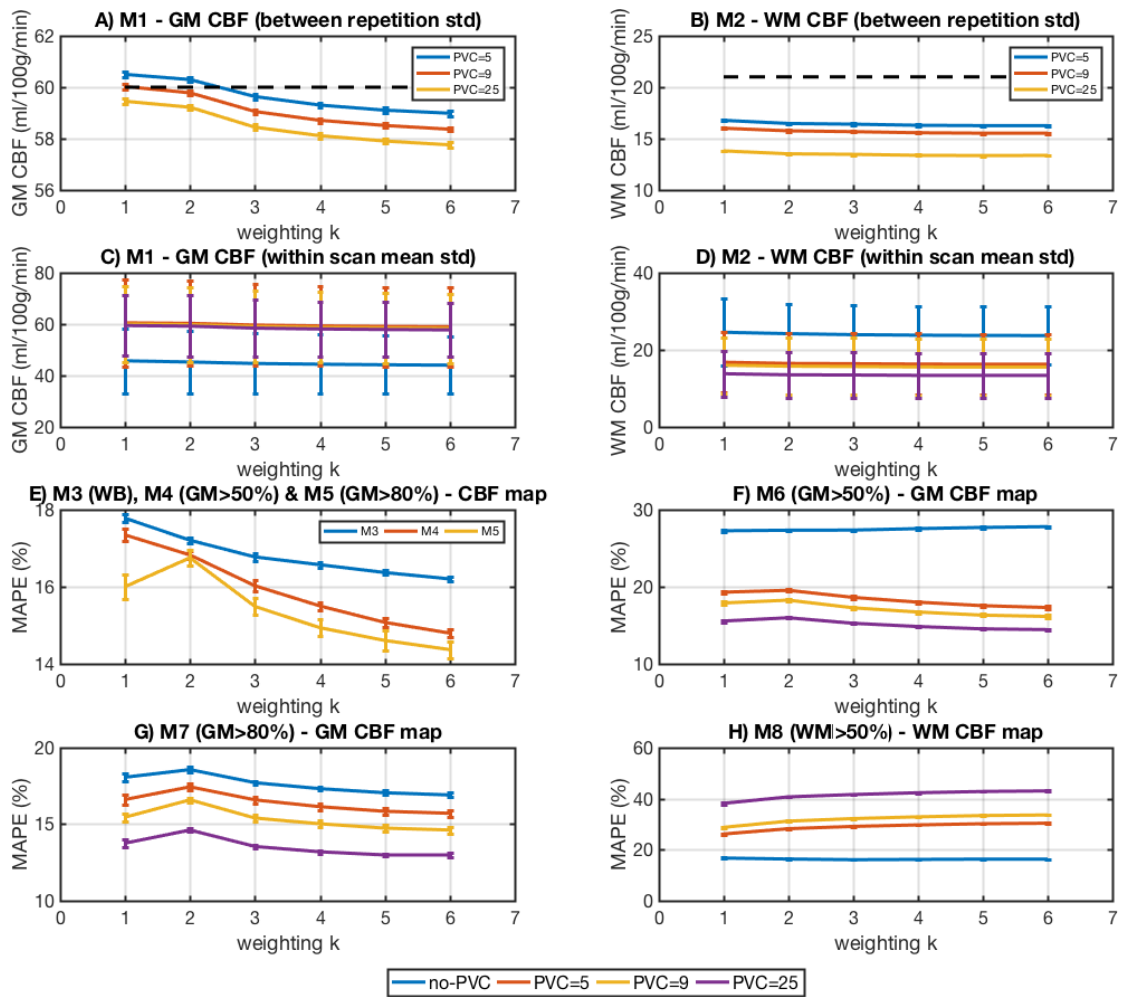


Figure 5.4: Simulation Case 1 (homogeneous GM and WM). Mean GM (A) and WM (B) whole brain CBF values calculated using PVC (mean value in voxels with GM > 50% or WM > 50% for the non-PVC scenario) are shown. Values are accompanied by error-bars reflecting the standard deviation for the 10 repetitions. Along with these, voxel-wise mean estimates for GM (C) and WM (D) CBF accompanied by standard deviation bars reflecting the within scan mean standard deviation. The dashed lines represent the simulated ground truth. E) voxel-wise MAPEs in CBF for the whole brain (blue), voxels with GM > 50% (orange) and voxels with GM > 80% (yellow), F) voxel-wise MAPE for the GM CBF maps for voxels with GM > 50%, G) voxel-wise MAPE for voxels with GM > 80% and H) voxel-wise MAPE for voxels with WM > 50% when considering the WM map.

Simulation Case 2 – GM hyper- and hypo-intense regions

Results for simulation case 2 are presented in two figures. The first figure (5.5) demonstrates the impact of increased weighting and different PVC kernel sizes in the calculated GM and WM CBF values. No-PVC leads to underestimation of GM CBF and overestimation of WM CBF (similar to case 1). From the examined PVC kernels PVC = 5 with $k = 1, 2$ and PVC = 9 with $k = 1$ lead to values closer to the simulated ones for normal GM and WM. When GM hyper and hypo-intense regions were examined (figure 5.6), PVC = 5 and 9 estimated values closer to the simulated ones. Especially for the hypo-intense GM region, PVC = 5 was optimal; PVC = 9 was optimal for the hyper-intense region.

The voxel-wise MAPEs with and without PVC were similar to the ones obtained for case 1 for the examined PVC and k -value combinations. Higher k -weighting results in lower MAPEs and larger PVC kernels were associated with reduced error in the mean voxel-wise calculated value when examining the GM CBF map. Example maps for a single slice where hyper- and hypo-intense GM regions were simulated are shown for an increasing k in figure 5.7. Accurate identification of the hyper-intense region is noticed for $k > 3$. Optimal combinations are the ones with lower MAPEs and accurate GM CBF estimates such as: PVC = 5 with $k = 3, 4$ and PVC = 9 with $k = 3$.

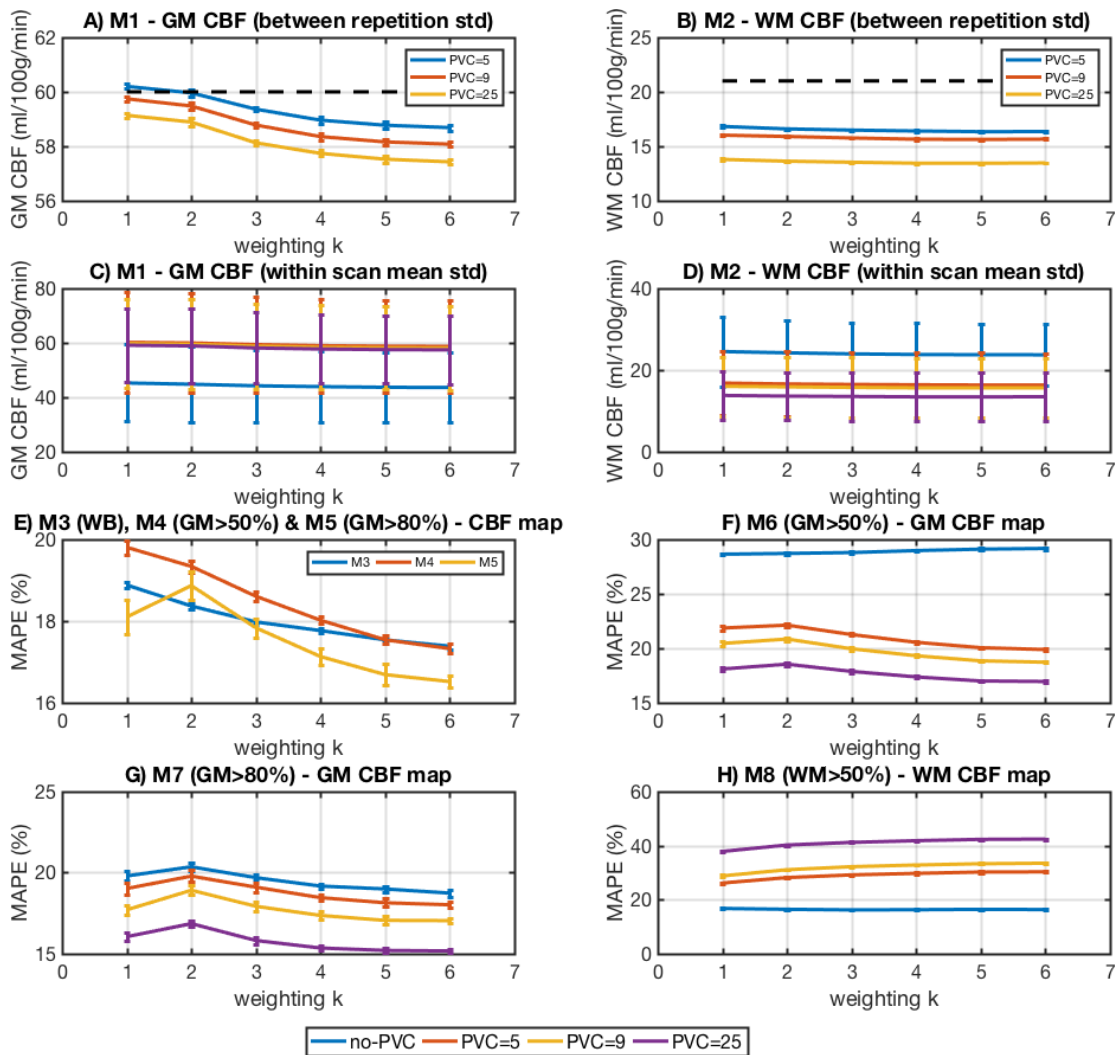


Figure 5.5: Simulation Case 2 (hyper and hypo intense areas). Mean GM (A) and WM (B) whole brain CBF values calculated using PVC (mean value in voxels with GM > 50% or WM > 50% for the non-PVC scenario) are shown. Values are accompanied by error-bars reflecting the standard deviation for the 10 repetitions. Along with these, voxel-wise mean estimates for GM (C) and WM (D) CBF accompanied by standard deviation bars reflecting the within scan mean standard deviation. The dashed lines represent the simulated ground truth. E) voxel-wise MAPEs in CBF for the whole brain (blue), voxels with GM > 50% (orange) and voxels with GM > 80% (yellow), F) voxel-wise MAPE for the GM CBF maps for voxels with GM > 50%, G) voxel-wise MAPE for voxels with GM > 80% and H) voxel-wise MAPE for voxels with WM > 50% when considering the WM map.

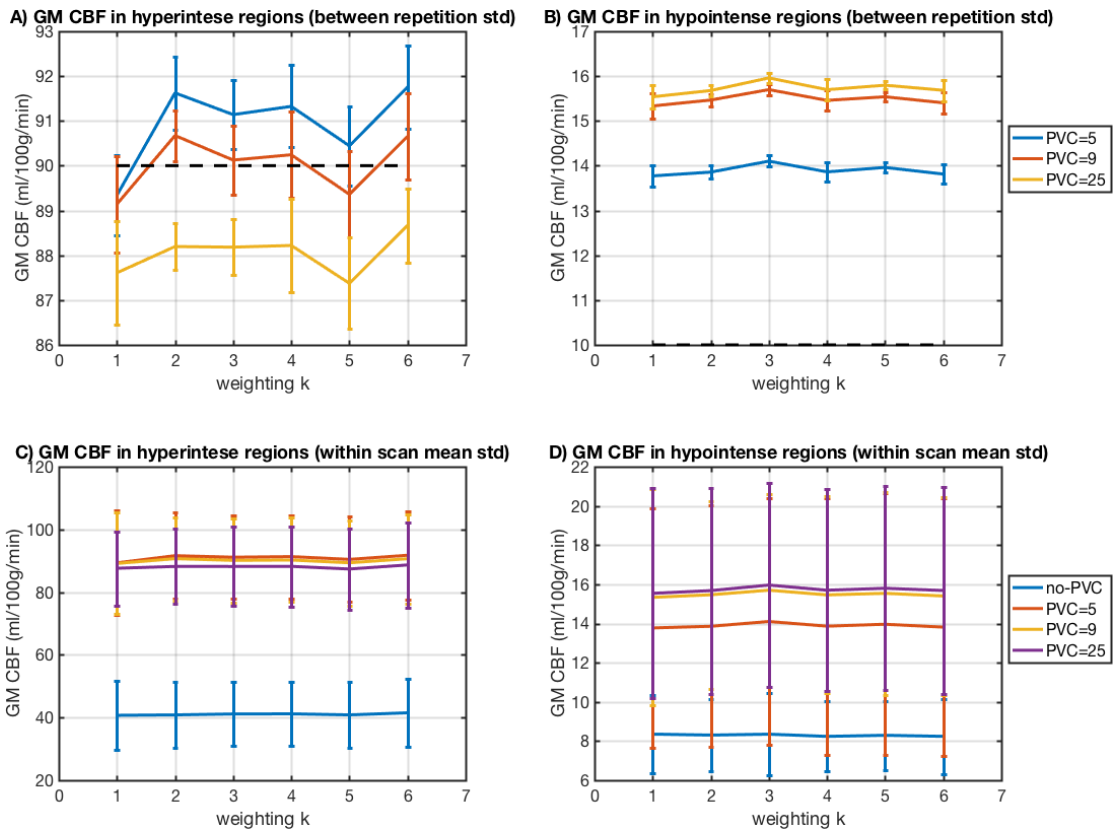


Figure 5.6: Simulation case 2, hyper and hypo intense GM CBF estimation. Mean GM CBF within the hyperintense (A) and hypointense (B) GM regions CBF values calculated using PVC (mean value in voxels with GM > 50% or WM > 50% for the non-PVC scenario) are shown. Values are accompanied by error-bars reflecting the standard deviation for the 10 repetitions. Along with these, voxel-wise mean estimates for GM hyper-intense (C) and hypo-intense (D) GM CBF accompanied by standard deviation bars reflecting the within scan mean standard deviation. The dashed lines represent the simulated ground truth.

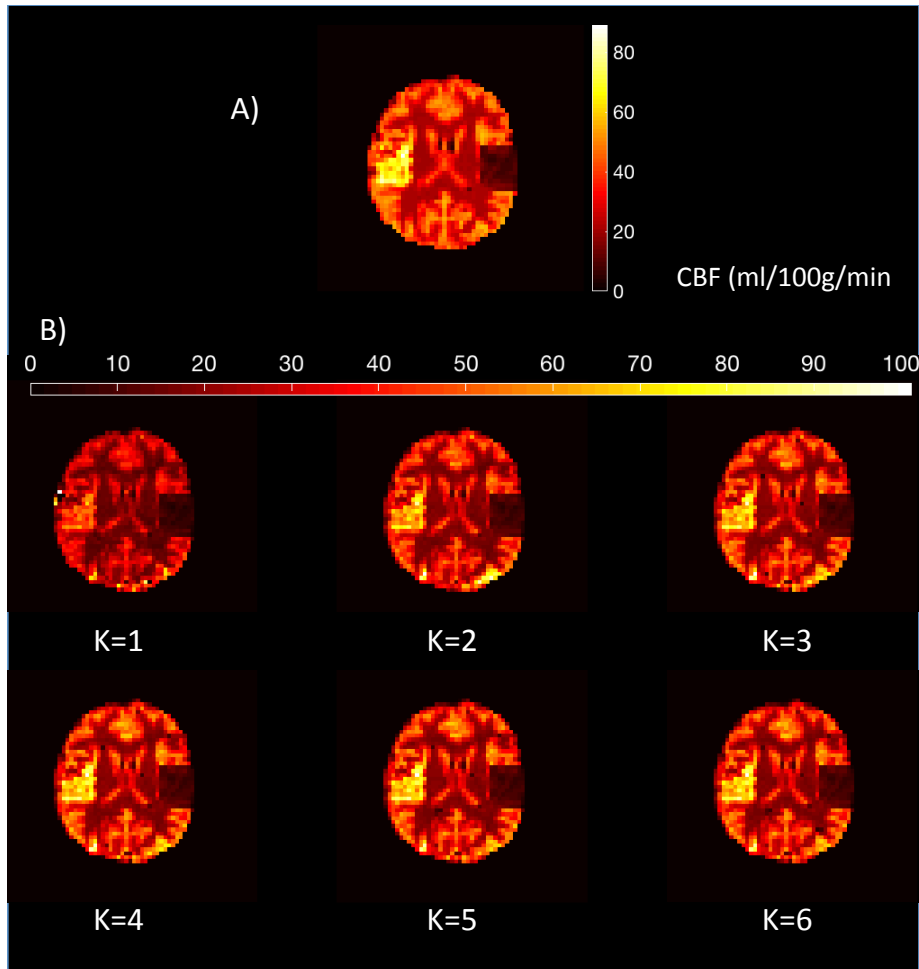


Figure 5.7: **Example maps for simulation Case 2 without PVC.** A) The initial simulated CBF map with a hyper- and a hypo-intense region. B) Calculated CBF maps with increasing k-radius.

Simulation Case 3 -artifact detection

Simulation results for the identified artifactual voxels with a decreasing threshold are shown in figure 5.8. For $k = 1$ (figure 5.9) $PVC = 5$ is optimal for a decreasing threshold when GM CBF is considered. $PVC = 5$ and 9 are optimal when WM is taken into account. When focusing on voxel-wise CBF values without PVC (M3, M4 & M5) a decreasing threshold leads to lower voxel-wise MAPEs. Errors in the GM CBF maps are lower with a large PVC kernel and the general tendency is for them to increase with a decreasing threshold after a certain limit (thr_4) for the detection of the artifact under consideration. A similar pattern is noticed for both $k = 4$ (figure 5.10) and $k = 6$ (figure 5.11). Errors in WM CBF and voxel-wise estimates are decreasing with a decreasing threshold.

Optimal combinations based on case 3 are: $k = 1$ with $PVC = 5, 9$ and $thr3$ & $thr4$; $k = 1$ with $PVC = 25$ and $thr1, thr2$; $k = 4$ with $PVC = 25$ and $thr1, thr2$; $k = 4$ with $PVC = 5, 9$ and $thr3, thr4$; $k = 6$ with $PVC = 25$ and $thr4$; $k = 6$ with $PVC = 5$ and $thr5$.

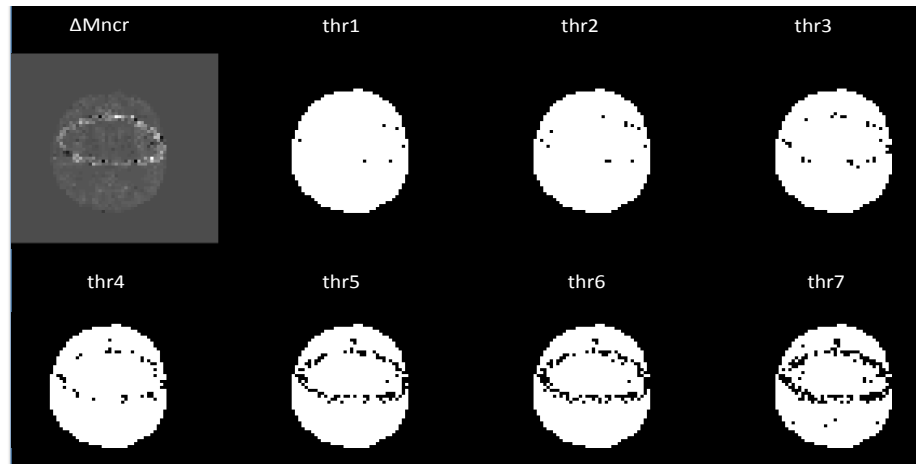


Figure 5.8: Artifact detection - Simulation case 3. A) Simulated ΔM_{ncr} image with a typical artifact plus binary masks with decreasing threshold cutoff levels. B, C, D) MAPEs for error metrics (M2, M3, M4 & M5) and calculated GM CBF with decreasing thresholds for kernel size $k = 1$ (B), $k = 4$ (C) and $k = 6$ (D). **Where: $thr1 = 10^{20}$, $thr2 = 5 \cdot 10^{19}$, $thr3 = 10^{19}$, $thr4 = 5 \cdot 10^{18}$, $thr5 = 10^{18}$, $thr6 = 5 \cdot 10^{17}$ and $thr7 = 10^{17}$.**

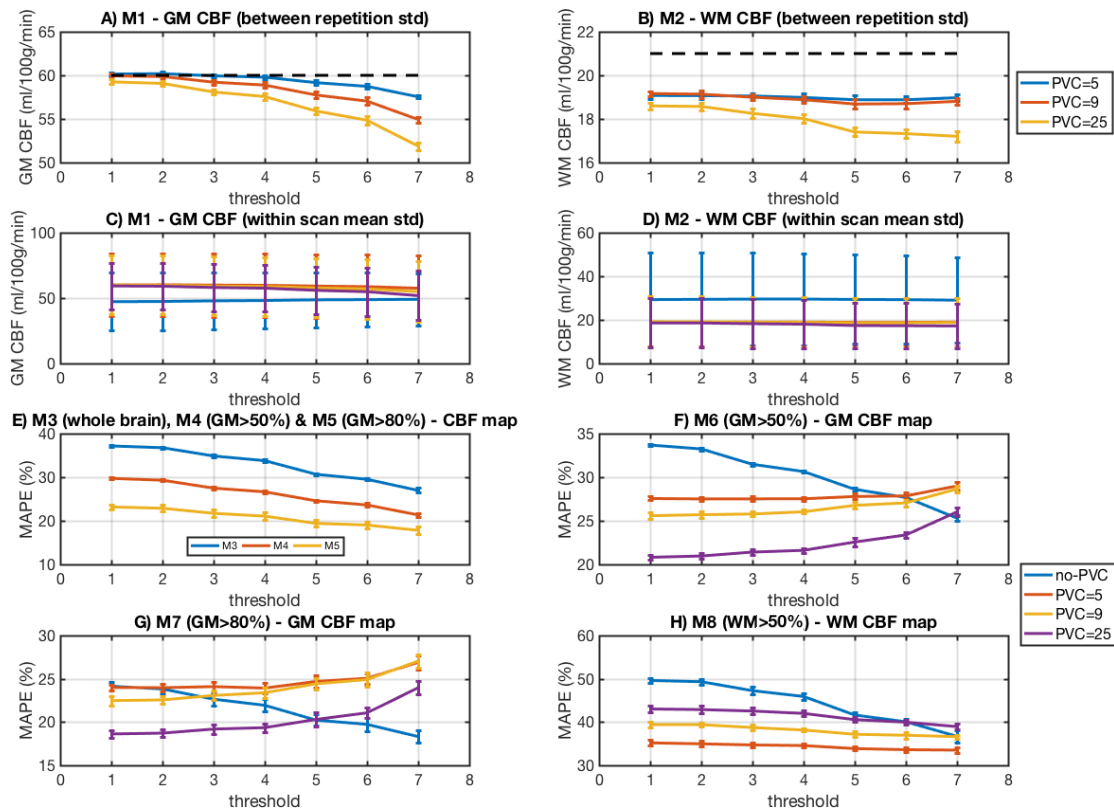


Figure 5.9: Simulation case 3, metrics M1-M8 with a decreasing threshold and $k=1$.

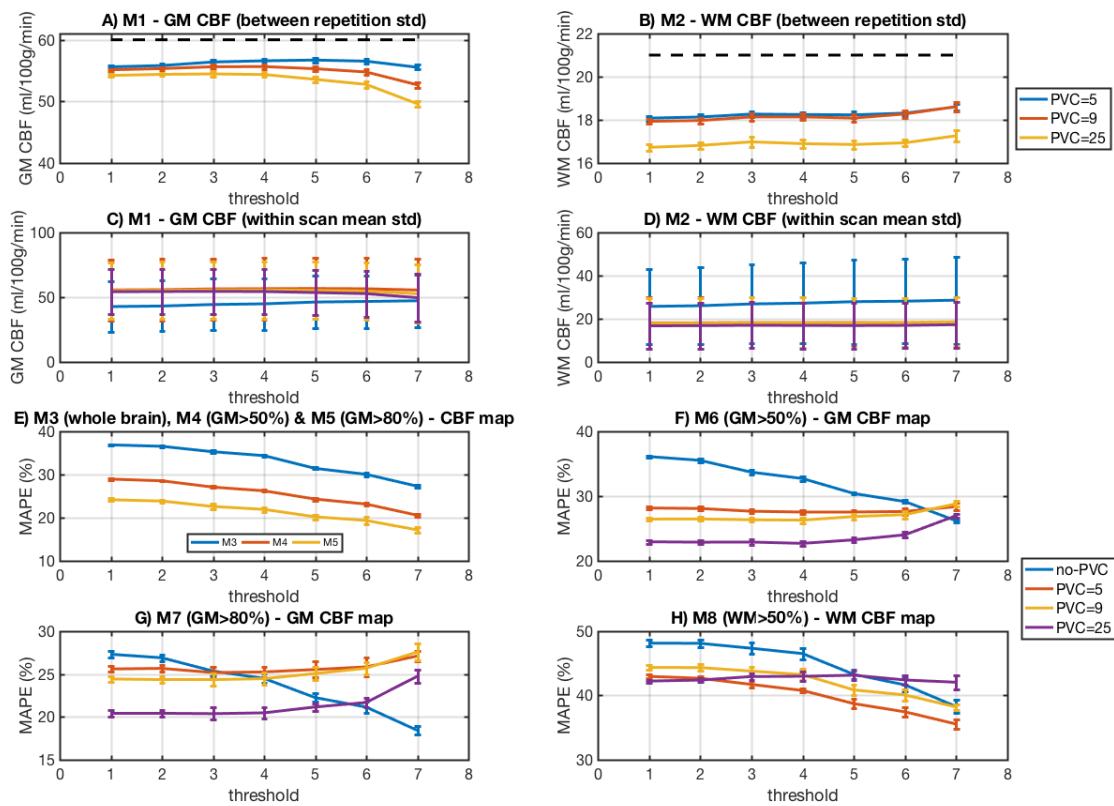


Figure 5.10: Simulation case 3, metrics M1-M8 with a decreasing threshold and $k=4$.

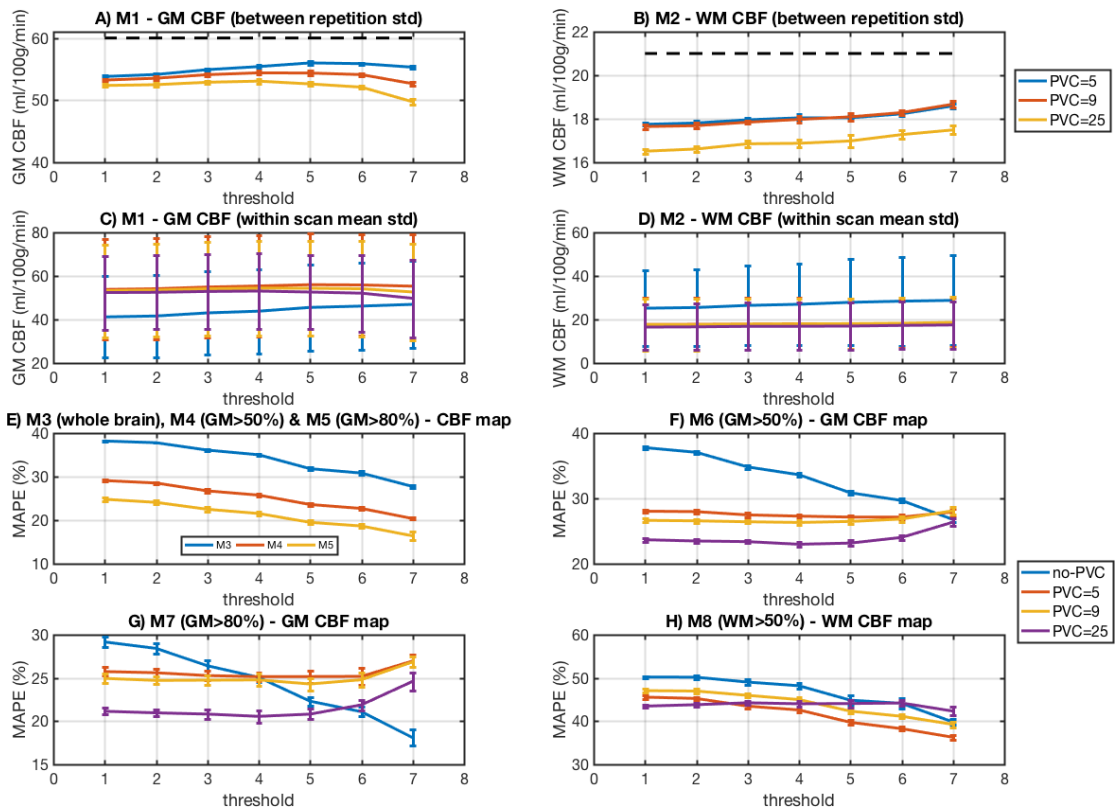


Figure 5.11: Simulation case 3, metrics M1-M8 with a decreasing threshold and k=6.

- An increasing k-radius AIF weighting results in lower errors in the voxel-wise CBF estimates (M3, M4 and M5 metrics).
- The GM and WM CBF values (M1, M2) are relatively stable with an increasing k following PVC.
- No-PVC is associated with underestimation of the GM CBF (M1) and overestimation of WM CBF (M2).
- PVC = 5 with k = 3, 4 and PVC = 9 with k = 3 were optimal when accurate estimation of the GM CBF value (M1) was of interest.
- In the presence of hyper and hypo-intense regions (case 2) PVC = 5 results in better CBF estimates for the affected hypo-intense areas and PVC = 9 for hyper-intense areas.
- Voxel-wise MAPEs in GM CBF for voxels with high GM content (M6 & M7) decreased with an increasing k.
- When an artifact was present (case 3) the developed algorithm effectively identified it with a decreasing threshold.
- MAPEs were reduced for the voxel-wise CBF estimates (M3, M4 & M5) and a decreasing threshold.

- After a certain threshold (thr5) MAPEs tend to increase (M6, M7) especially with a large PVC kernel and GM CBF values are underestimated.

5.3.2 AIF re-evaluation

Results for AIF re-evaluation can be found in figures 5.12 & 5.13. For all metrics the results were highly similar so values are shown for M1, M3, M5, and CBF within hyper- and hypo-intense regions (simulation case 2). The mean number of re-evaluated regional AIFs per k-value was: 7.9 ± 0.7 ($k = 1$), 79.1 ± 0.3 ($k = 2$), 50.9 ± 1.2 ($k = 3$), 30.7 ± 1.3 ($k = 4$), 19.2 ± 1.3 ($k = 5$) and 18 ± 1.2 ($k = 6$).

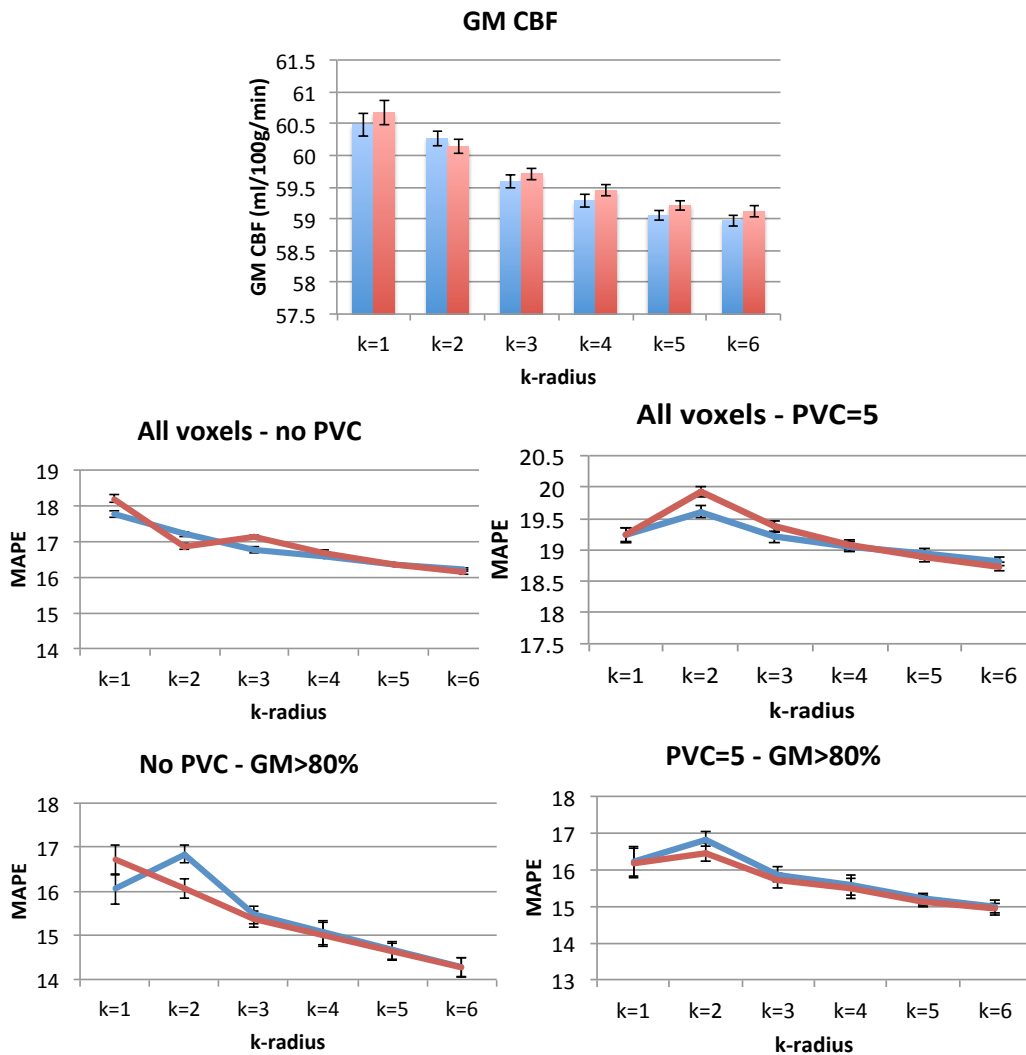


Figure 5.12: AIF reevaluation simulation case 1. Blue is used for AIF re-evaluation and red for no re-evaluation.

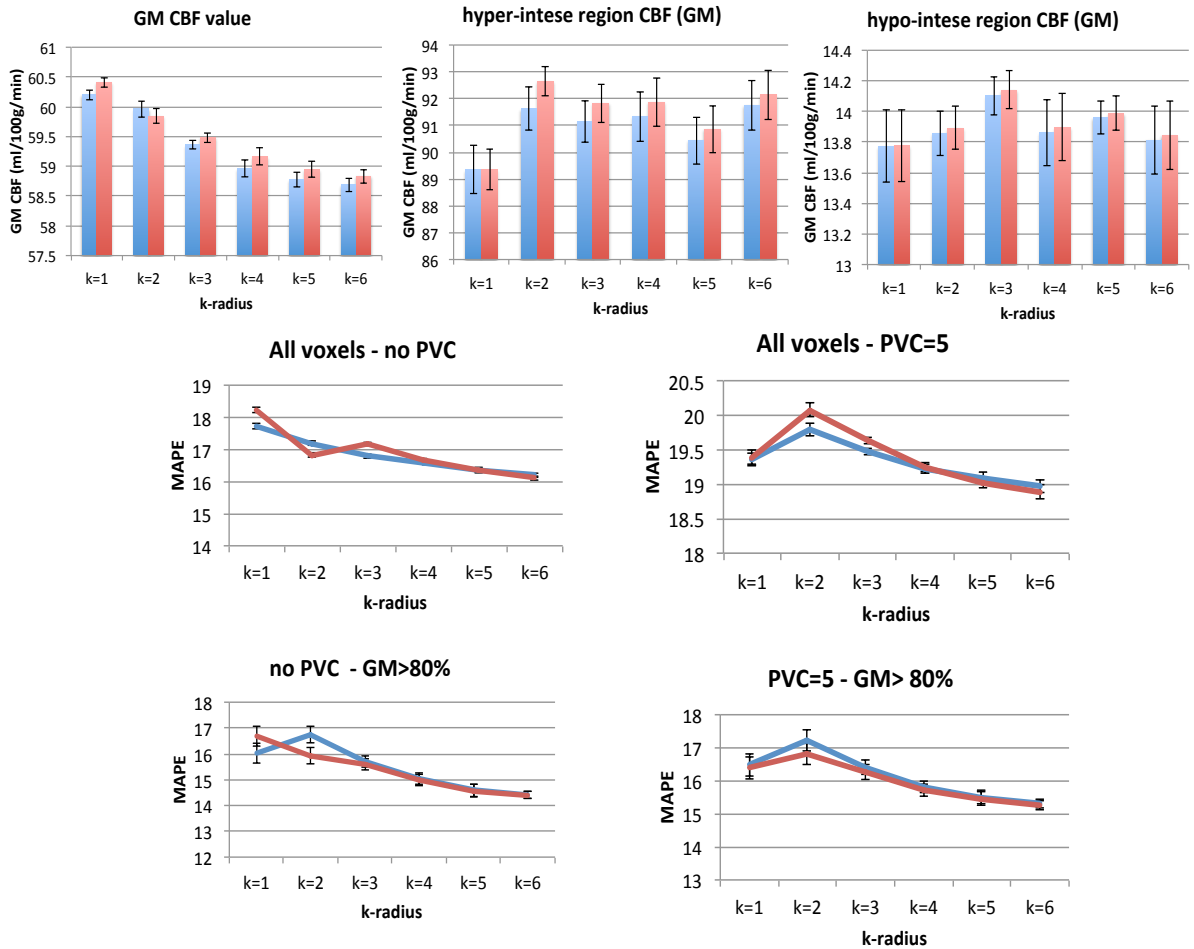


Figure 5.13: **AIF reevaluation simulation case 2.** Blue is used for the AIF re-evaluation step and red for no AIF re-evaluation.

Overall, AIF re-evaluation did not have a big impact in the calculated MAPEs especially for $k = 3, 4$ and 5 which were identified in previous steps as optimal. A slight difference is noticed for case 2 and the calculated GM CBF values. No re-evaluation is connected with slight overestimation inside hyper-intense and hypo-intense GM areas.

Based on the simulation findings, when accurate GM and WM CBF whole brain values and voxel-wise CBF estimates are of interest, the optimal implementation is k-radius AIF weighting with $k = 3, 4$ or 5 and AIF re-evaluation with $PVC = 5$. In case an artifact is present, the implementation of the developed algorithm with a threshold in the range 10^{18} - 10^{19} results in effective artifact detection and can be used along with the developed pipeline with a combination such as $k = 4$ and $PVC = 5$.

5.3.3 In-vivo results

Calculated CBF for GM and WM for the examined healthy subjects along with the number of AIFs for varying k-radii can be found in table 5.1. QUASIL model-based and model-free results are also given in the same table. The PVC kernel used in this analysis was $PVC = 5$. In 10/12 subjects, the described chemical-shift artifact was not visually detected in the difference images. The lowest CoV in the calculated GM CBF with the developed pipeline was observed for $k = 1$ (CoV = 7.3%) and the highest for $k = 5$ (CoV = 10.4%). For QUASIL model-free analysis the CoV was 16.9% and for the model-based analysis, the CoV was 19.5% (CoVs are reported for 10/12 subjects). Within this group the mean number of neighboring AIFs identified for every voxel ranged from 1.3 ± 0.1 (for $k = 1$) to 92.2 ± 31.9 (for $k = 6$). The GM CBF values demonstrated stability with increasing number of considered AIFs, a finding consistent with the simulation results. Example AIFs obtained from different voxels using the 6 k-values can demonstrate varying effects of k on the resultant input functions (figure 5.14).

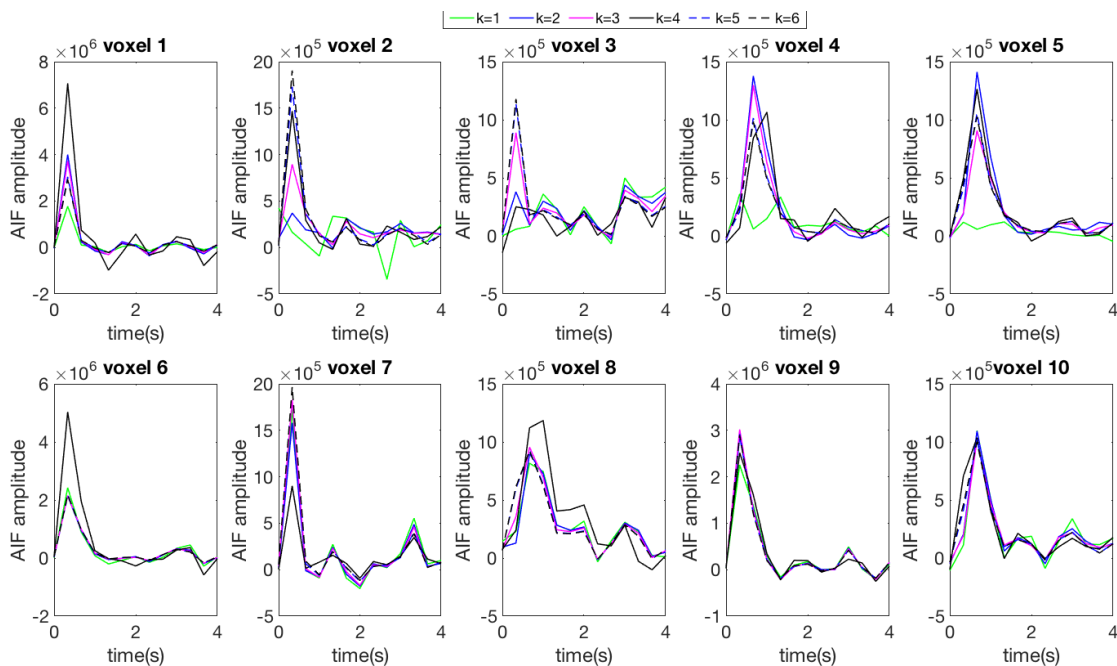


Figure 5.14: AIFs from 10 voxels based on one subject for different degrees of AIF weighting (k). Examples in the first row indicate that choice of k impacts on AIF shape whereas examples in the second row demonstrate negligible impact.

For the 5 chosen voxels in the first row in figure 5.14, the value of k impacts the shape and amplitude of the voxel AIF, for the other 5 voxels the

impact of k appears to be negligible. There is no clear pattern of difference in the number of recruited AIFs between the first and the second set of examined voxels for each k that could explain in a systematic way the reason for seeing noisy AIFs for lower k -values in the first set (figure 5.15). To visually evaluate the effect of different combinations of k -values and PVC kernels on the resultant CBF, maps are shown for one representative individual in figure 5.16.

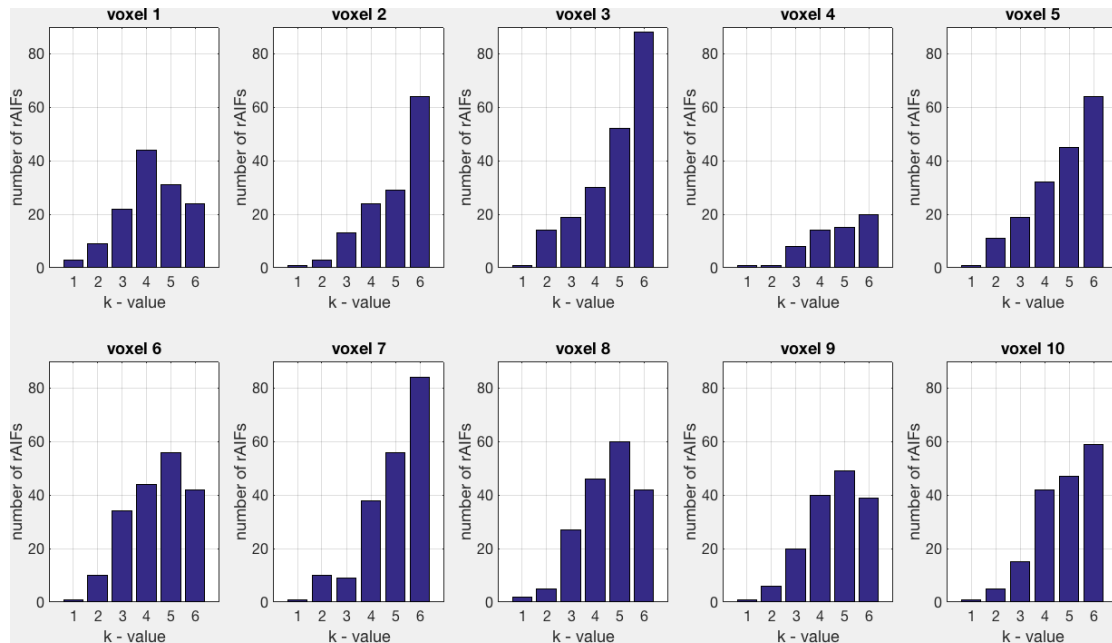


Figure 5.15: Number of averaged AIFs for each of the examined voxels with an increasing k .

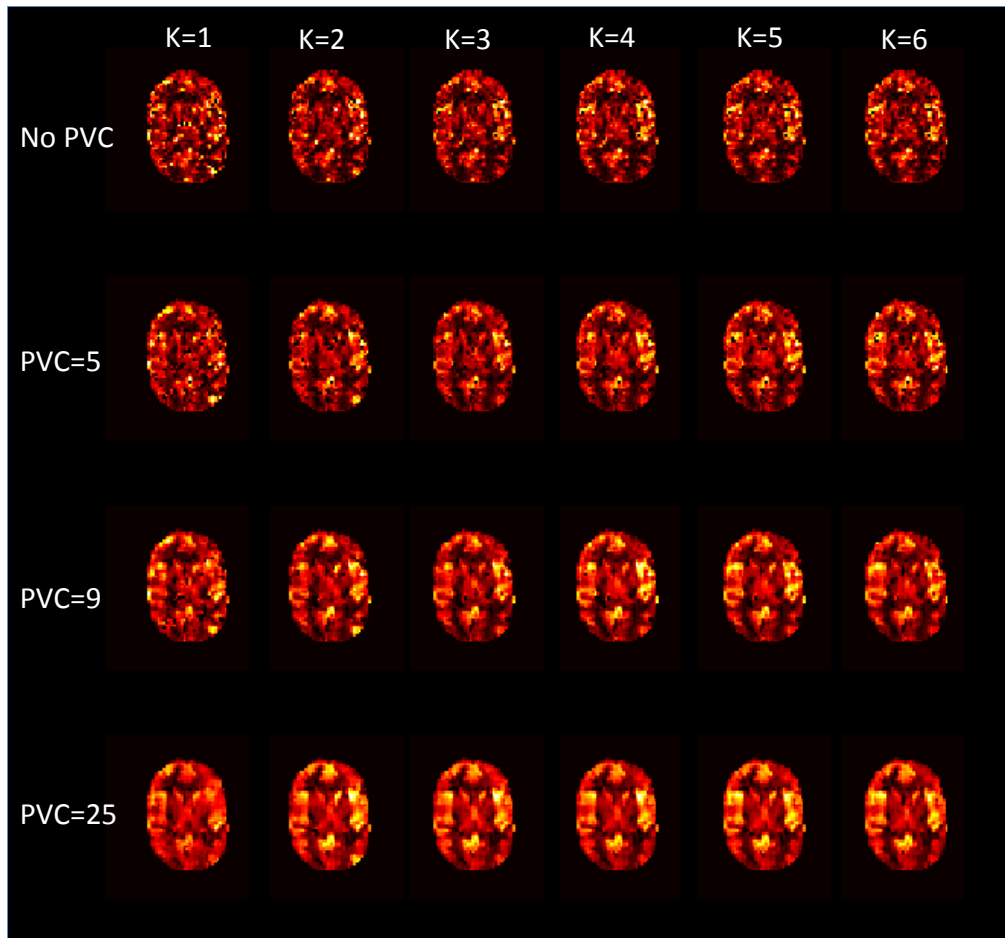


Figure 5.16: Single slice CBF maps from a representative subject as a function of PVC level and k-radius AIF weighting. As the PVC kernel size increases the blurring effect is more prominent. As the k-radius increases de-noising of the image occurs without introducing prominent smoothing/blurring.

Two individuals were influenced by the presence of the multi-parametric artifact. The mean CBF values were calculated before and after artifact correction (Table 5.1). Correction led to the mean exclusion of 553 ± 141 voxels i.e. a 6.8 ± 1.4 % reduction.

For the AIF re-evaluation step, the mean CBF without re-evaluation was 54.7 ± 5.5 ml/ 100g/ min as opposed to 54.5 ± 4.7 ml/ 100g/ min with AIF re-evaluation. The number of identified AIFs without re-evaluation was 1915.2 ± 585.2 and with AIF re-evaluation 1719.8 ± 570.5 , leading to a mean of 195.3 ± 60.6 excluded AIFs. The mean number of excluded voxels due to extremely low CBF values (<5 ml/ 100g/ min) was 187.3 ± 60.9 and a mean of 8.1 ± 4.5 voxels were excluded because their value was very high (150 ml/ 100g/ min).

Partial volume correction

The SSIM was calculated for all PVC variants. When compared to the T1-QUASAR maps, the mean SSIM for variant 1 (PV maps generated based on the MPRAGE scan down-sampled and registered to the QUASAR-T1) was 0.18 ± 0.05 . PVC using the FRASIER method (variant 2) resulted in a SSIM of 0.11 ± 0.09 . When using the FRASIER maps as an intermediate registration target for the MPRAGE derived GM PV maps (variant 3) the SSIM was 0.17 ± 0.06 and for variant 4 (mean of variant 1 and 2) SSIM was 0.15 ± 0.08 . The SSIM value was significantly higher for variant 1 compared to variant 2 ($p = 0.02$). GM and WM CBF were quantified for all subjects with all the PV map generation methods for PVC = 5 kernel and $k = 4$ to measure the CoV for the GM CBF value. For the first variant the CoV was 10.1%, for the second CoV = 10.3%, for the third CoV = 9.1% and for the fourth CoV = 8.7%.

Example maps for the PV techniques are shown in figure 5.17.

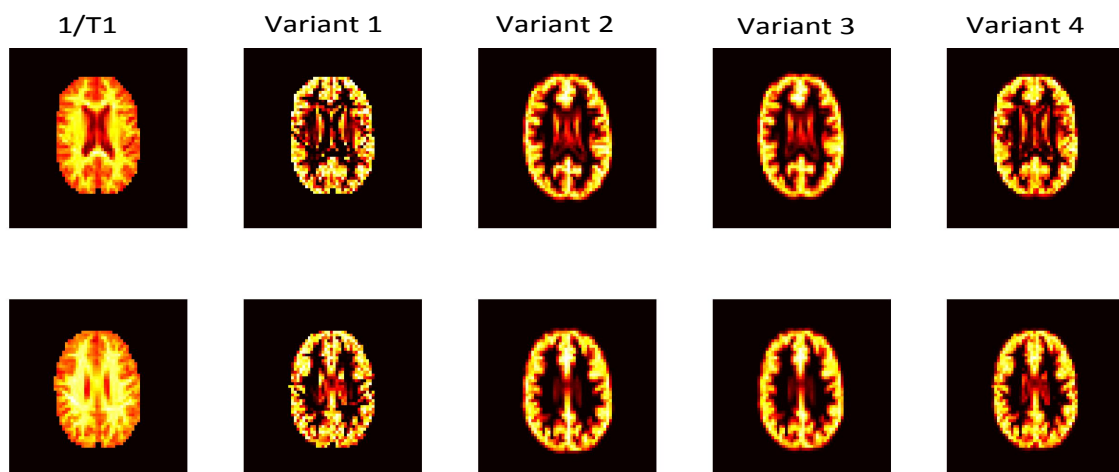


Figure 5.17: Example slice from an individual of a 1/T1 slice and the determined PV maps generated with the 4 tested variants.

Overall based on the in-vivo data an increase in the k-values did not lead to big differences in the calculated GM and WM CBF values. Artifact detection led to a slight reduction in calculated CBF. The CoV was lower with the developed technique compared to the QUASIL software. PV maps generated with methods based on a high resolution MPRAGE scan had higher structural similarity with the QUASAR-T1 maps compared to the FRASIER PV maps.

Table 5.1: GM CBF, WM CBF and number of identified AIFs for 12 subjects. 2 out of the 12 subjects were influenced by a multi-parametric artifact. For these two subjects results are shown before and after artifact correction. The values shown are for an increasing k-radius and the results obtained using QUASIL model-free and model-based analysis.

Artifact-free								
	k=1	k=2	k=3	k=4	k=5	k=6	QUASIL free	QUASIL model
GM CBF (ml/100g/min)	54.4±4.0	54.4±4.7	54.2±5.2	54.3±5.5	54.4±5.6	55.6±5.6	58.7±9.9	61.1±11.9
WM CBF (ml/100g/min)	24.1±1.9	22.8±2.2	22.7±2.4	22.6±2.5	22.7±2.7	22.7±2.7	25.4±3.4	29.9±3.7
AIFs	1.3±0.1	7.4±1.0	23.1±5.4	44.3±12.8	66.7±21.3	92.2±31.9	N/A	N/A
Influenced by the artifact before correction								
GM CBF (ml/100g/min)	55.3±0.1	55.4±0.6	55.7±0.8	55.9±0.7	55.8±0.8	57.2±0.6	60.6±0.3	66.5±6.0
WM CBF (ml/100g/min)	25.7±0.5	25.5±0.1	25.2±0.4	25.3±0.5	25.2±0.6	25.2±0.6	26.7±0.4	31.3±1.3
AIFs	1.3±0.1	7.3±1.0	22.1±1.9	42.4±5.5	64.3±9.0	90.7±14.6	N/A	N/A
Influenced by the artifact after correction								
GM CBF (ml/100g/min)	53.8±0.1	54.0±0.1	54.2±0.2	54.2±0.2	54.0±0.8	54.5±0.7	N/A	N/A
WM CBF (ml/100g/min)	25.3±0.5	25.1±0.1	24.9±0.2	25±0.3	25.0±0.2	25.1±0.4	N/A	N/A
AIFs	1.1±0.0	5.8±0.1	15.8±0.6	28.3±1.5	41.7±2.3	57.0±4.4	N/A	N/A

5.4 Discussion

In this chapter, several modifications were introduced to the QUASAR processing pipeline. Optimization of the model-free post-processing version may hold great importance especially when the protocol is applied in clinical cohorts where assumptions about the shape of hemodynamic signals (introduced when using a model-based approach) might be violated due to the presence of pathophysiology. The introduced changes revolved around the AIF assignment and the mitigation of a common water-fat shift artifact. Additionally, four variants for PV map determination were evaluated. The pipeline was developed and evaluated specifically for QUASAR ASL. However, parts within the pipeline can also have application in other ASL implementations where the chemical-shift artifact is present or in multi-PLD protocols where AIFs are calculated at a local level.

k-radius AIF weighting improves perfusion quantification

Accurate AIF determination is essential in perfusion imaging since it directly impacts blood flow quantification (153). The introduction of k-radius AIF weighting aims at reaching a 'golden mean' between assigning a single, local input or an AIF based on a surrounding region (e.g. due to vascular territories or global brain blood supply). AIF weighting, leads to AIF de-noising by means of weighted spatial smoothing, rather than model-fitting. Considering more than one local AIF has the additional benefit of accounting for perfusion resulting from more than one local source. This effect is prominent in, for example, watershed areas within the brain parenchyma that are supplied by more than one arterial input. AIF weighting takes into account the hemodynamic characteristics in a sphere centered on the voxel of interest. The findings indicate that implementation of this approach can yield more reliable voxel-wise perfusion estimates compared to $k = 1$ which reflects the conventional QUASAR post-processing. This effect was captured by both the quantitative and qualitative analysis and is clearly depicted in figure 5.7, whereby the hyper and hypo-intense regions are clearly identified with k-values greater than 3.

It was demonstrated that using k-radius AIF weighting can improve perfusion quantification, both in the presence of hyper- or hypo-intense regions and in normal cases. A consistent finding in simulation Cases 1 (homogeneous GM and WM CBF) and 2 (hyper and hypo-intense areas) was that increased AIF weighting led to reduced MAPE in voxel-wise CBF values (M3). This finding should be taken into account when ROI-specific CBF values are to be extracted or voxel-wise comparisons are conducted. On the other hand, a high k-value might result in slight GM CBF underestimation.

The developed isotropic k-radius AIF weighting approach does not account for the complex topology of different vascular territories. An AIF weighting approach restricted within vascular territories (or within the two hemispheres) would be an interesting future development. This would require mapping of the vascular territories, for example, using TASL (an implementation based on QUASAR) (164) or ASL techniques without explicit territorial labeling combined with pre-defined vascular territory maps with which to restrict the AIF assignment step.

A small PVC kernel size results in lower errors

Along with the degree of weighting, we evaluated PVC with linear regression using different kernel sizes. The use of either $PVC = 9$ or $PVC = 25$ is common, due to superior noise suppression. Additionally, small kernel sizes are not typically evaluated since the matrix inversion problem involved in the quantification of GM and WM CBF is ill-defined when a small number of voxels is used. In the present implementation though, when this was the case, the utilized algorithm did not return the actual inverted matrix but a least square approximation. Our findings suggest that a kernel of 4 neighbors ($PVC = 5$) is sufficient to solve the regression equation in a stable manner and results in minor smoothing. This regression kernel demonstrated high accuracy in CBF quantification within hyper- and hypo-intense regions. In addition, final estimated GM CBF was closer to the simulated value with the lower kernel size; this was concomitant with minor increases in the other variance-related parameters (MAPEs). For simulation Cases 1 and 2, MAPEs in voxels with lower GM content tended to be higher with an increasing PVC kernel.

The optimal choice of k-values and PVC kernel size is dependent upon subsequent analysis. If the mean GM CBF is of primary interest, then the optimal k-PVC combinations are: $k = 1, 2$ with $PVC = 9$ and $k = 3, 4$ with $PVC = 5$. For an ROI-based approach, a combination giving the minimal error at a voxel-wise level (M3, M4 and M5) would be a better choice. Where hypo- or hyper-perfused regions are expected, a combination, which does not smooth out these regions and provides results closest to ground-truth values is likely to be beneficial such as $k = 3, 4, 5$ and $PVC = 5$. The simulation results for case 2 (figure 5.16) imply that $k > 3$ delineates the hyper- and hypo-perfused regions from normal areas in a more robust manner. This suggests that spatial smoothing introduced with k-radius weighting does not smooth out abnormally perfused regions, an unwanted effect observed when large PVC kernels are implemented for noise reduction. Hence, a small PVC kernel accompanied by spatial smoothing at the level of the AIF assignment step might be a viable alternative to big linear regression kernels.

k-radius AIF assignment with AIF re-evaluation was optimal

AIF re-evaluation introduced as a step here to account for potentially noisy AIFs had little impact on the final calculated CBF values in both the simulations and in-vivo data. Simulations indicate that the error in CBF estimates is slightly lower when re-evaluation is not used. This step could be omitted, however, it is reassuring that AIFs resulting in spurious CBF values are not used in the k-radius AIF weighting step and hence do not impact in any way on their local neighborhood.

Of interest is that a mean of 195.3 AIFs (the mean number of identified AIFs was 1915.2) gave rise to non-physiological CBF values and the majority of them are below 5 ml/ 100g/ min. This effect could be attributed to the fact that for CBF quantification the crushed signal is used. Hence, in voxels containing large arterial compartments we would expect that the arterial signal will be nulled, hence the recorded crushed signal would be particularly low. However, the aBV rarely goes beyond 20% in any voxel, so we would expect a tissue signal from these voxels to arise as well. Suppression of the arterial signal due to the crushers, hence, is not sufficient to explain the unphysiologically low CBF values. It needs to be emphasised that these voxels are not excluded from subsequent analysis; they are just excluded as candidate AIFs in the AIF reassignment step.

In the future an approach incorporating AIF re-evaluation as a regularisation step, implemented iteratively until all AIFs provide CBF values within the desired limits could be evaluated.

A water-fat shift artifact was effectively detected

The artifact detection algorithm is capable of identifying erroneous voxels in both simulated and in-vivo data. The artifact was successfully identified in two subjects and elimination led to reduction in GM and WM CBF. Simulations suggested that voxel exclusion up to a certain point results in a closer approximation to the underlying perfusion values. However, exclusion of a large number of voxels (i.e. using thr7) may result in higher errors in voxels with GM > 50%. Hence, a recommended threshold to be used with the developed algorithm ranges between 10^{18} and 10^{19} .

Ideally, artifact mitigation should be a pre-reconstruction technique. Following reconstruction, if the artifact is not successfully removed during motion correction, only a post-processing technique can be applied. It needs to be highlighted that the developed artifact detection algorithm does not correct for the artifact; it detects influenced voxels and it relies on the user whether to include these voxels in the analysis or not.

Partial volume correction using the MPRAGE-derived estimates was optimal

In terms of the evaluated PVC variants, it was demonstrated previously that FRASIER performs well in relatively high SNR scenarios (243). When applied to the in-vivo data in this study it demonstrated the resulting GM, WM and CSF PV maps were realistic; there were cases though where it failed to determine accurately GM and WM, especially in the presence of enlarged ventricles. In such cases the generated PV maps were substantially different from the maps calculated based on the high-resolution T1-weighted scan, which are usually taken as the gold standard. On the other hand, when using the MPRAGE approach, in some cases, the registration was suboptimal.

Accurate registration of the PV maps to the low resolution T1t maps is crucial since if there is a small degree of rotation or imperfect translation, the PV maps will not overlap with their respective voxels. A combination of these two PV generation methods might be beneficial, since the FRASIER map provides a good target for direct registration of the down-sampled PV maps. Taking into account the SSIM and CoV, the hybrid methods evaluated here improved on CoV and demonstrated a higher structural similarity to the QUASAR-T1 maps, when compared to FRASIER-derived estimates. In the present thesis we chose for subsequent processing variant 1, since the generated GM PV maps demonstrated a higher SSIM to the QUASAR-T1 image. Variant 3 which used the FRASIER maps as a registration target had a lower SSIM but also a lower CoV compared to variant 2 and could be used alternatively when the between modality registration fails as an intermediate registration target.

The developed model-free pipeline provides realistic perfusion estimates.

In a previous study where QUASAR was used (296), mean GM and WM CBF were 55.5 ± 9.5 and 21.8 ± 7.7 ml/ 100g/ min, respectively, when using stable spline deconvolution, whereas the values were 34.9 ± 5.2 and 17.3 ± 5.5 ml/ 100g/ min when standard SVD deconvolution was applied. In the QUASAR reproducibility study, the mean GM CBF was 47.4 ± 7.5 ml/ 100g/ min (161). Finally, in another report (243) where linear regression was used for PVC, the mean value for GM CBF was 60.6 ± 1.5 ml/ 100g/ min. Hence, our findings are in line with previously reported values for GM CBF. In the majority of studies using QUASAR (155, 162, 163, 165, 166, 171), no correction was implemented for PVE and only in a few of them ROIs in areas thought to be minimally influenced by PVE were used (143, 159). In studies using QUASAR where PVC was not used the calculated GM CBF ranged between 34-47 ml/ 100g/ min (143, 155).

It is worth mentioning that, throughout this thesis, a decision was made to avoid introduction of assumptions into the processing pipeline wherever possible. In the present QUASAR ASL processing optimisation, we tried to avoid excessive smoothing, fitting, and use of prior information. The inherent advantage of QUASAR is that it is a model-free technique allowing CBF quantification without assuming an explicit model for the hemodynamic signals and imposing it upon the data. Assumptions about the shape of the arterial input function, the tissue signal or the residue function would contradict this inherent advantage of the technique. On the other hand, the analysis and the results might be more robust and less noisy by fitting data with suggested model functions. For example, QUASIL uses priors and spatially adaptive priors. Additionally, there is the option to avoid SVD deconvolution by fitting the data to the general kinetic model (154). Ahlgren et al. (291) have suggested non-linear stochastic regularization for the deconvolution step and Castellaro et al. (296) have used stable splines. These literature suggestions were aimed at introducing regularisation steps for the residue and the arterial signal assuming a certain shape based on physiological models. Such approaches lead to beneficial noise suppression, however, they tend to introduce bias in the form of prior information based on healthy subjects. We have shown with this analysis

that accurate perfusion quantification is possible with the model-free QUASAR pipeline and we have contributed four modifications towards its optimisation.

The net impact on the quantified values for all introduced modifications as judged by the final GM CBF and MAPEs is not high, however, an improvement is noticed with all introduced modifications. The absolute errors are reduced at a voxel-wise level and the values, especially considering the simulation steps, are close to the ground truth ones.

Comparison with QUASIL

When QUASIL was used (model-free and model-based), the mean GM CBF was higher than that obtained with the developed pipeline. The difference in mean GM CBF value compared to the model-free QUASIL approach may be attributed to the difference in AIF assignment. In QUASIL, local AIFs are fitted to a gamma variate function and assigned using a closest neighbour criterion (154). Lower GM CBF calculated from a model-free, as opposed to a model-based approach, is a consistent finding usually attributed to the use of SVD deconvolution in the former method. WM CBF values calculated with the model-based approach are higher compared to both the k-radius AIF weighting method and model-free QUASIL, giving a mean value of 30ml/ 100g/ min when that expected is 20ml/ 100g/ min. For the two subjects influenced by the multi-parametric artifact, QUASIL GM and WM CBF were high compared to the calculated mean for the subjects not influenced by the artifact, suggesting that CBF quantification is influenced by its presence.

It is worth noting that the coefficient of variation for the GM CBF measured with the suggested pipeline is lower than that obtained using the QUASIL tool, a result suggestive of a more stable performance, which carries potential importance in clinical research studies. When comparing the algorithmic execution times, a model-based QUASIL run requires 46s. With our pipeline implemented with $k = 4$ the execution time was 180s, when supplying directly the PV maps and 300s when generating PV maps within the pipeline.

There are several limitations to this study. Firstly, the developed pipeline was tested in a limited cohort and it needs to be validated using a larger study population. Secondly, a discrete number of radii were considered for the AIF weighting step and alternative approaches could be tested to determine the

optimal approach, such as, AIF assignment being confined within specific vascular territories. Thirdly, in this study, SVD deconvolution was used for the determination of the residue function. SVD is known to underestimate perfusion values and alternative mathematical approaches could be used to determine the transfer function of the system on a voxel-wise basis. Finally, the artifact detection and rejection algorithm relies on the principle that hyper-intense regions at specific time-points are artifactual rather than reflecting true perfusion, an assumption that could be violated resulting in the rejection of non-artifactual voxels.

5.5 Conclusions

QUASAR ASL is one of the first methods suggested by the ASL community having the potential to image perfusion dynamically in a non-invasive manner. This technique was first suggested in 2006 (155). Since then, the only modification to the acquisition process has been the introduction of a small flip angle acquisition in order to map the nominal flip angle at a voxel-wise level (160). Petersen et al. have been working over the past years on TURBO-QUASAR, however, it is still subject to optimization and a full-length paper on the technique has not yet been published (298). On the other hand, QUASAR post-processing optimization has been a vivid area of interest for some years, with the latest paper been published by Castellaro et al. suggesting stable spline deconvolution (296). At about the same time, the ASL white paper suggested pCASL as an optimal implementation (108). Since then, spatially non-selective ASL and time-encoded ASL have emerged as very promising alternatives, with promising insensitivity to transit time delays. These last techniques have not yet been thoroughly validated and are quite experimental (126).

The QUASAR post-processing optimization has mainly focused on four aspects: AIF assignment, deconvolution – residue determination, partial volume correction and modelling of the signals. In this chapter, we contributed towards optimization of the AIF assignment step, PVC step and in addition to these, we presented an algorithm for artifact detection. Using simulations and in-vivo data, we demonstrated an improvement in the quantification procedure and determined optimal values and approaches to be used in the subsequent

processing. More importantly, we have made our pipeline publicly available to be used and tested by the ASL community. This is the 3rd tool available for QUASAR- based ASL quantification. The first is the program written in IDL by Esben Petersen which is of a 'black box' kind, and the other is the QUASIL tool available as part of the FSL toolbox.

Aside from more challenging post-processing, QUASAR has the very important advantage of being ATT insensitive. Additionally, the entire hemodynamic signals used for perfusion estimation and not a single time-point are acquired at a voxel-wise level. Hence, a robust, open access pipeline, making use of the acquired signals without introducing excessive smoothing, regularisation or prior assumptions and which demonstrates a stable performance, could be a useful tool for clinical studies. This pipeline, with values optimised as described in this chapter, was used in the subsequent hemodynamic analysis (Chapter 6).

Chapter 6:

Cerebral hemodynamic analysis in type-2 diabetes and impaired glucose tolerance

Abstract

Perfusion impairment in T2DM is suspected due to potential neurovascular unit dysfunction leading to impaired delivery of energy to the tissue. Neuroimaging findings, however, have not been consistent. The aim of this part of the thesis was to evaluate cerebral hemodynamics in IGT and T2DM using, for the first time, an arterial transit time insensitive ASL technique, namely, QUASAR ASL.

Data from 16 HV, 12 subjects with IGT and 16 T2DM patients were processed. Two analysis approaches were utilised, the first one involved calculation of commonly quantified QUASAR metrics accompanied by a conventional statistical analysis. The second approach involved quantification of novel hemodynamic features extracted from the QUASAR signals, which were subsequently analysed using a machine learning framework to detect optimally-differentiating features between the groups. Overall, seven multi-parametric models were evaluated, each containing a different combination of hemodynamic features. Due to the large number of features and the small dataset, dimensionality reduction was implemented. Binary classification tasks were conducted using linear SVM.

Commonly quantified perfusion parameters such as CBF, CVR and ATT differed between the groups suggesting hemodynamic differences. Baseline CBF in IGT and T2DM was increased, potentially indicating the presence of an early compensatory mechanism to account for reduced oxygen delivery to the tissue. A multitude of newly quantified hemodynamic features also differed between the groups. The applied extended hemodynamic analysis combined with a machine learning framework, resulted in high classification performance for all binary classification tasks examining HV vs hyperglycemic states, suggesting: a) a distinct hemodynamic pattern in the hyperglycemic groups compared to HV and b) that QUASAR ASL can provide important hemodynamic

information not typically captured by single time-point ASL, which may be pertinent to the correct classification of healthy vs. non-healthy brains.

To evaluate the additional benefit of conducting an extended hemodynamic analysis, we compared the discriminatory capacity of the novel feature combinations to the commonly quantified QUASAR parameters and found that for all considered classification tasks, the classification performance increased with the newly considered metrics. The feature combination with the best performance was the one involving metrics extracted from non-processed QUASAR signals, followed by the one combining non-processed signals and typical QUASAR measurements. Interestingly IGT had a distinct hemodynamic pattern compared to HV, which was prominent after the administration of a vasodilating stimulus and bore similarities with the T2DM group.

6.1 Introduction

Several techniques have been devised in recent years for cerebral perfusion quantification. In the field of T2DM some studies have reported hypoperfusion (36, 42, 43), whereas others have concluded that there are no differences between T2DM patients and healthy subjects (44, 45). A few studies (46, 47) have reported increased baseline perfusion in T2DM with van Bussel et al. focusing on the hippocampus. This inconsistency in findings is highly likely to reflect differences in the utilised perfusion imaging techniques. Findings regarding CVR have been more consistent with a lower value observed in T2DM patients (36, 42, 44, 53). The study by Selvarajah et al. (53) has reported a decrease in brain blood flow in both T2DM and IGT.

In these studies, flow has been examined with one of the following techniques: PC-MRA, TCD, BOLD fMRI, DSC-MRI, PET, ASL-MRI. When using PC-MRA the acquisition typically takes place at the level of the carotids and the acquired quantity is a blood velocity measurement. Transcranial Doppler also measures blood velocity rather than pure tissue perfusion. Techniques capturing a pattern close to the underlying perfusion based on MRI are BOLD fMRI, DSC-MRI and ASL MRI. BOLD fMRI captures changes in the amount of oxygenated and deoxygenated hemoglobin in response to a stimulus, which are coupled to neuronal activation (299). DSC and ASL MRI follow a tracer within the vasculature. DSC follows a gadolinium contrast agent that in normal

circumstances remains intravascular and creates a susceptibility gradient. Perfusion is captured during the first passage of the tracer. In cases of BBB disruption though, leakage of the tracer can lead to quantification errors (153). In ASL, the labeled hydrogen protons get delivered to the tissue, so perfusion measurements relying on ASL can be thought as more direct measurements of perfusion compared to the other techniques. In the study reported in this chapter we have used a multi-TI ASL technique to investigate in depth cerebral hemodynamics in T2DM utilising the assumption-free, model-free, processing pipeline explained and validated in detail in the previous chapter.

Such a technique accounting for ATT variations could be appropriate for perfusion quantification in cohorts of non-healthy subjects. QUASAR ASL is an implementation insensitive to ATT delays (155) since it samples the recovering magnetisation at multiple time-points. Due to the acquisition of dynamic signals at a voxel-wise level, QUASAR can provide rich hemodynamic information along with quantitative CBF maps. Such a technique has not yet been used to investigate cerebral perfusion in T2DM.

QUASAR ASL has the potential to provide multiple hemodynamic parameters that can be investigated using a machine learning approach to extract the most significant feature combination leading to optimal class-differentiation. Machine learning approaches are becoming increasingly popular in neuroimaging and have been extensively used for MR biomarker identification in Alzheimer's disease (246, 249, 268) and brain tumors (269). Structural MRI scans are usually the modality of choice; only a few studies have evaluated features derived from alternative MR acquisitions such as BOLD, pCASL and DTI (249, 274). In the field of diabetes, machine learning techniques have been used for identification of novel biomarkers though not relying on features extracted from MR images (300).

Typically, when machine learning approaches are applied to MR images, the focus is on the intensity of a voxel or of an ROI. Metrics directly connected to the intensity, statistical metrics and less frequently textural metrics are extracted. In this study, we shift the processing focus from the 3D intensity images reflecting CBF, ATT and aBV to the dynamic ASL signals acquired at a voxel-wise level. To our knowledge, this is the first study examining multi-TI ASL derived features using a machine learning analysis approach. Additionally,

classification of normoglycemia vs hyperglycemia based on perfusion MR features has not been investigated in the past.

In the present chapter, we utilised QUASAR ASL, which accounts for ATT delays to evaluate cerebral hemodynamics in IGT and T2DM. Multiple perfusion-related parameters were quantified in order to retain a descriptive hemodynamic pattern for every individual. The dimensionality of the problem was reduced by feature selection and the resulting pattern was used for supervised classification. The hypothesis under examination was that cerebral hemodynamics are altered in T2DM and its prodromal condition IGT. We attempted to take advantage of the potential of QUASAR ASL to provide rich hemodynamic information not confined to the calculation of CBF maps. We investigated the impact of the additional hemodynamic parameters in optimal class differentiation by quantifying the classification accuracy using only CBF, CVR, aBV and ATT measurements on the one hand, and using all the suggested additional hemodynamic parameters on the other. Overall classification was performed for 7 different feature combinations and 4 tasks (HV vs T2DM, HV vs T2DM & IGT, HV vs IGT and IGT vs T2DM) in order to conclude the optimally differentiating pattern. Finally, the data were analysed using the pseudo-single-PLD approach described in the previous chapter.

6.2 Methods

Data from 16 healthy volunteers (HV), 12 people with IGT and 17 patients with T2DM were acquired on a 3T Philips Achieva scanner. Scans from 2 subjects with IGT and 1 subject with T2DM were discarded due to poor image quality (cohort details in table 6.1). Image quality was deemed poor if following registration and noisy scan rejection, the resultant mean crushed and non-crushed images demonstrated strong motion artifacts that would influence the subsequent processing. The quality was assessed visually by a single individual (M.E.D).

Table 6.1: Details about the subject cohort analysed in the present chapter.

	HV	IGT	T2DM
N	16	10	16
Age (y)	50.0±12.0	54.1±5.5	54.9±11.8
sex	8♀ 8♂	5♀ 5♂	8♀ 8♂
BMI (kg/m²)	26.0±34.7	31.6±3.4	31.1±3.9
Hypertension (subjects)	4	5	6
Diabetes duration (y)	N/A	N/A	9.9±4.6
HbA1c (%)	-	-	9.4±1.9
Microvascular complications	-	-	5 neuropathy 2 retinopathy 1 nephropathy
insulin			4
Smoking history	3 ex-smokers	3 ex- 3 current	7 ex – 2 current

6.2.1 MR protocol

- 1) A T1-weighted MPRAGE scan.
- 2) Four QUASAR ASL acquisitions. The first QUASAR scan was acquired at baseline and the next three were acquired consecutively 15 minutes after ACZ injection.

For more details regarding the MR protocol, please refer to Chapter 4.

6.2.2 Partial volume correction

The high resolution anatomical scan was corrected for bias field using N4 (208). Subsequently the scan was segmented using SFCM (232). Overlapping QUASAR and MPRAGE slices were determined and the PV maps were averaged over the overlapping slices. Subsequently the PV maps were down-sampled to the QUASAR resolution and registered to the T1-QUASAR maps. PVC was implemented using linear regression (240) with a kernel

involving the four direct neighbours of a voxel, which was found to be optimal in Chapter 5.

6.2.3 Quantified parameters

Typically, CBF is calculated as the maximum of the residue function, and ATT as the difference between the rising time of the tissue curve and the AIF. Arterial blood volume is associated with the area under the curve of the non-crushed – crushed difference signal (155). Hence, this is the current hemodynamic information used in QUASAR ASL studies to investigate perfusion abnormalities. Other metrics, characteristic of the curves, and hence the acquired signals, are currently not considered in the QUASAR implementation and quantification. Such metrics were evaluated in the present chapter to investigate whether potential hemodynamic information not captured by ATT, aBV and CBF can be extracted.

As described in Chapters 2 and 5, every voxel can be modelled as a system having an AIF as the input, the tissue signal as the output and the residue function is the system's transfer function (figure 6.1). The AIF describes the distribution of the 'tracer' in the arterial compartment, the tissue curve the distribution in the output. The residue curve is associated with the tracer retention by the tissue and represents the amount of labeled spins remaining inside the system at the time of imaging (151). The tissue signal is considered to be the acquired crushed signal (ΔM_{cr}) and the arterial signal can be calculated by subtracting the tissue signal from the mixed arterial & tissue signal (ΔM_{ncr}); the residue signal is determined via deconvolution. These three signals have the potential to shed light onto the hemodynamic pattern in every region allowing for the extraction of multiple perfusion-related parameters.

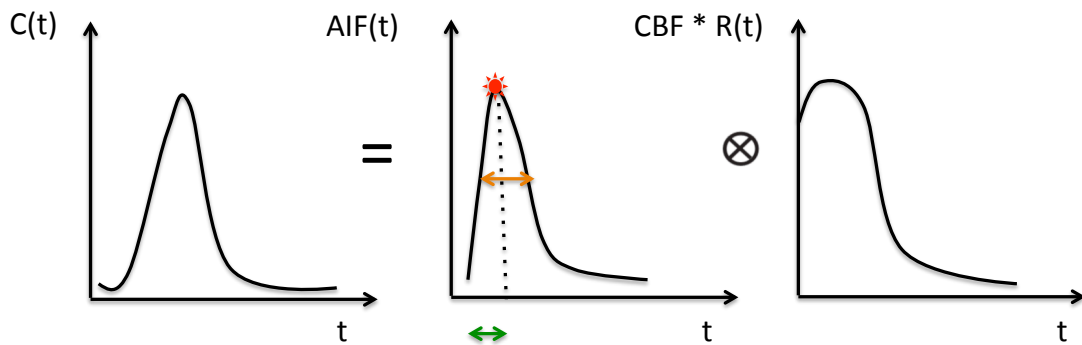


Figure 6.1: Example demonstration of the tissue, arterial and residue function signals. Overlapping the AIF are example metrics not currently considered such as the time-to-peak (green), full width half maximum (orange) and the peak (red). Modified based on Ahlgren et al. 2011 (301).

A multitude of hemodynamic features were quantified at a local and global level. These metrics were: the time-to-peak (TTP), peak height, full width at half maximum (FW), half width at half maximum of the left (HWL) and the right (HWR) part of the signal peak, skewness (SKEW) and kurtosis (KURT). The metrics were recorded for: a) the assigned weighted AIFs (AIF), b) the AIFs before assignment and weighting (AIF_{SH}), c) the residue function (R), d) the tissue signal (ΔM_{cr}) and e) the mixed tissue & arterial signal (ΔM_{ncr}). In addition to this, CBF, ATT and aBV, as normally quantified with QUASAR, were determined. It should be noted that the GM CBF value calculated with QUASAR differed from the peak of the residue function since PVC was incorporated in the pipeline. So, the peak of the residue is actually the non-PVC corrected CBF value within that voxel. Additionally, GM and WM CBF were calculated using PVC; CVR was determined as the percentage change of the GM CBF following ACZ injection.

All described metrics were extracted from the following regions of interest (ROIs): the whole brain (WB), anterior, medial and posterior cerebral artery (ACA, MCA, PCA) vascular territories and watershed (W) areas. A mask created by Mutsaerts et al. (121) was used for the vascular territory analysis. The mask was registered to the low-resolution GM partial volume maps using affine registration with normalized cross correlation. The watershed area mask was generated based on the vascular territory mask. A summary of the identified hemodynamic curves, the metrics extracted by them and the ROIs can be found in figure 6.2.

The response time to ACZ is known to vary between individuals (93). To address this issue, four scans were acquired following injection; the scan used to evaluate the response to the stimulus was the one with the highest residue function peak (reflecting CBF). All described features were acquired from the baseline and post-ACZ scans.

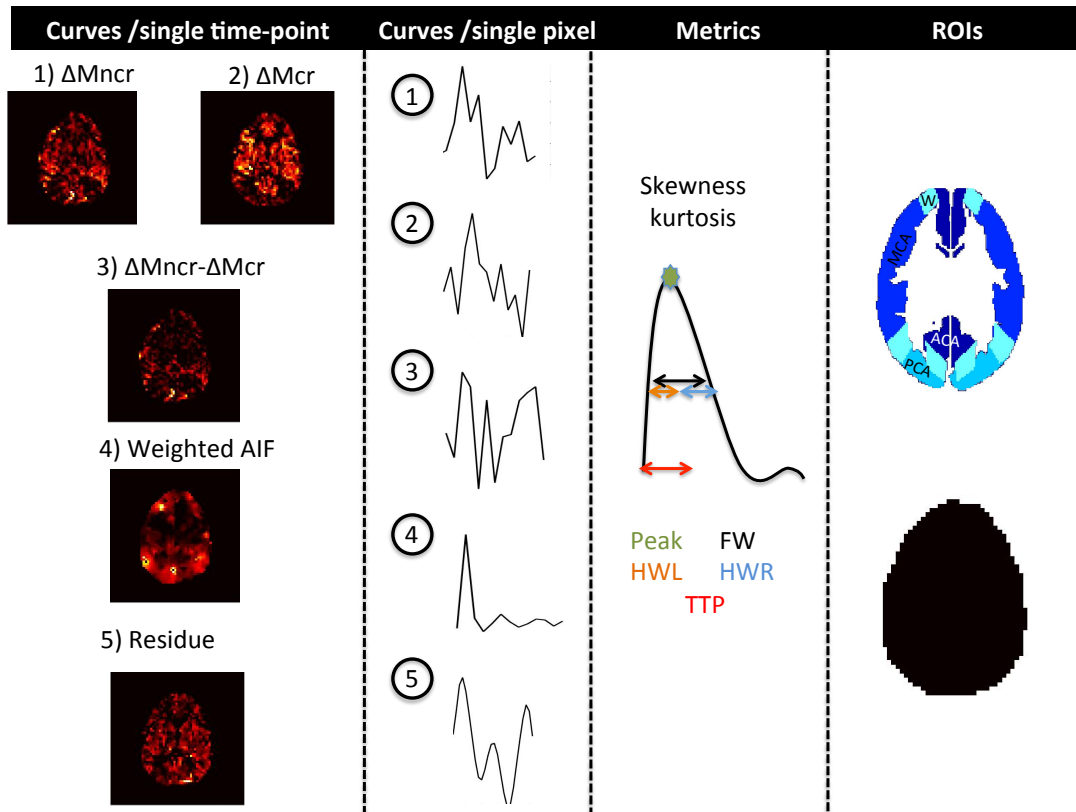


Figure 6.2: **Overview of the calculated hemodynamic metrics.** A single slice for a single time-point is shown for the 5 considered signals. In the second column we see the signal for a single voxel and all time-points, following that there is a representation of the extracted metrics from a curve and finally the considered ROIs.

6.2.4 Vascular territory and watershed area analysis

Maps published by Mutsaerts et al. (121) involved nine separations of the vascular territories. In the present analysis the three subdivisions for ACA, MCA and PCA were merged and the territory masks were registered as previously described. The watershed area masks were defined based on the vascular territory maps as in figure 6.3. An overview of the calculated metrics, each named according to the vascular territory and the measured parameter is shown in table 6.2. In this table, metrics are shown for the three (AIF, R, ΔM_{cr}) out of a total of five considered QUASAR-derived time-signals (AIF, R, ΔM_{ncr} , ΔM_{cr} and AIF_{SH}). The omitted ones are the non-crushed signal, referred to as

ΔM_{ncr} and the AIFs before assignment (AIF_{SH}). Overall 351 hemodynamic features were extracted from the QUASAR signals and used in the subsequent analysis. The number of features is very high especially when considering the available cohort, hence a number of models examining different feature combination was evaluated. Additionally, state-of-the-art feature reduction techniques and cross-validation were used to reduce the risk of overfitting and noise-modelling.

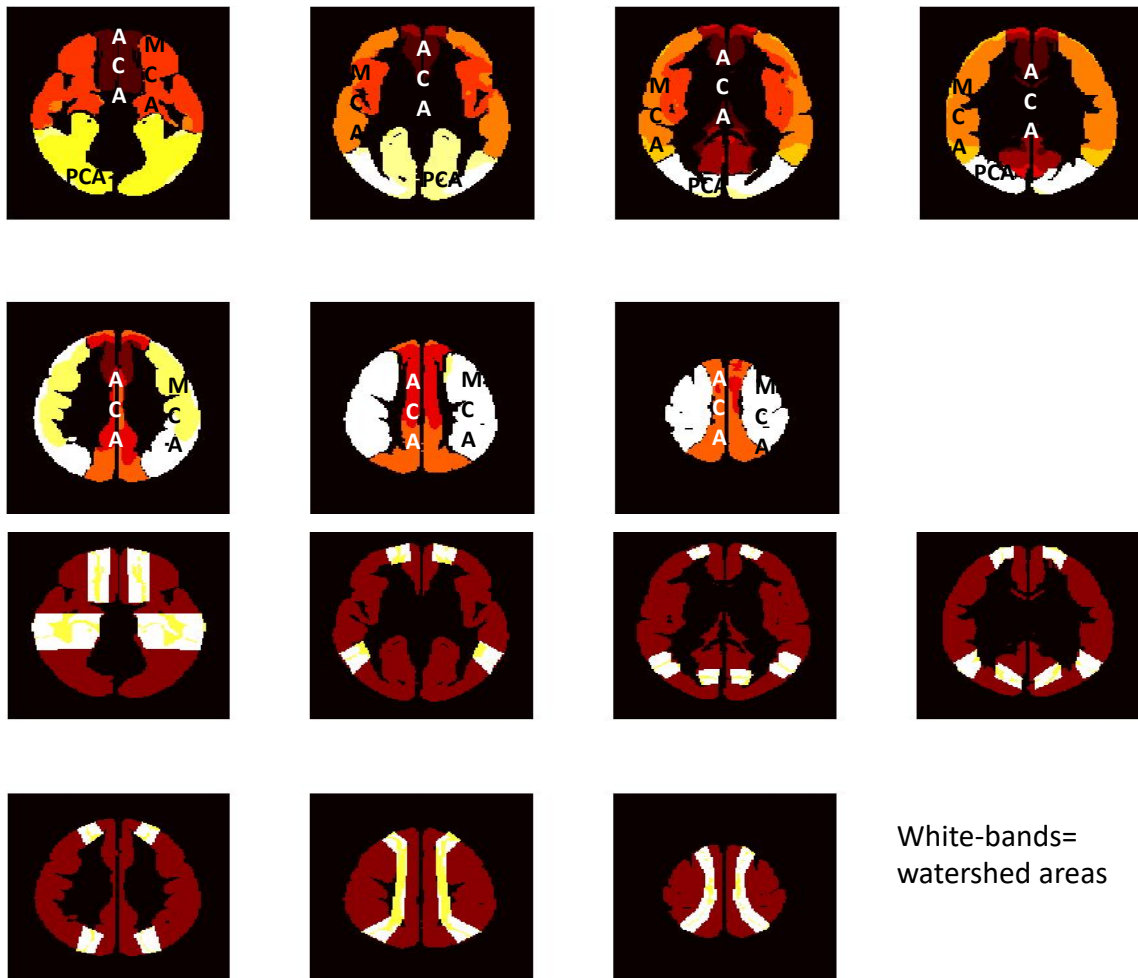


Figure 6.3: Vascular territory masks based on Mutsaerts et al (121) and watershed areas for all 7 QUASAR slices.

Table 6.2: An overview of features extracted from 3 curves and the 5 considered ROIs. Each feature is named according to the vascular territory (anterior cerebral artery-ACA, middle cerebral artery-MCA, posterior cerebral artery – PCA and watershed areas) and hemodynamic parameter.

Metric\ROI	WB	ACA	MCA	PCA	watershed
CBF	WB CBF	ACA CBF	MCA CBF	PCA CBF	W CBF
ATT	WB ATT	ACA ATT	MCA ATT	PCA ATT	W ATT

aBV	WB aBV	ACA aBV	MCA aBV	PCA aBV	W aBV
AIF FW	WB FWAIF	ACA FW AIF	MCA FW AIF	PCA FW AIF	W FW AIF
AIF HWR	WB HWR AIF	ACA HWR AIF	MCA HWR AIF	PCA HWR AIF	W HWR AIF
AIF HWL	WB HWL AIF	ACA HWL AIF	MCA HWL AIF	PCA HWL AIF	W HWL AIF
AIF TTP	WB TTP AIF	ACA TTP AIF	MCA TTP AIF	PCA TTP AIF	W TTP AIF
AIF skewness	WB SKEW AIF	ACA SKEW AIF	MCA SKEW AIF	PCA SKEW AIF	W SKEW AIF
AIF kurtosis	WB KURT AIF	ACA KURT AIF	MCA KURT AIF	PCA KURT AIF	W KURT AIF
AIF peak	WB PEAK AIF	ACA PEAK AIF	MCA PEAK AIF	PCA PEAK AIF	W PEAK AIF
ΔM_{cr} FW	WB FW ΔM_{cr}	ACA FW ΔM_{cr}	MCA FW ΔM_{cr}	PCA FW ΔM_{cr}	W FW TIS ΔM_{cr}
ΔM_{cr} HWR	WB HWR ΔM_{cr}	ACA HWR ΔM_{cr}	MCA HWR ΔM_{cr}	PCA HWR ΔM_{cr}	W HWR ΔM_{cr}
ΔM_{cr} HWL	WB HWL ΔM_{cr}	ACA HWL ΔM_{cr}	MCA HWL ΔM_{cr}	PCA HWL ΔM_{cr}	W HWL ΔM_{cr}
ΔM_{cr} TTP	WB TTP ΔM_{cr}	ACA TTP ΔM_{cr}	MCA TTP ΔM_{cr}	PCA TTP ΔM_{cr}	W TTP ΔM_{cr}
ΔM_{cr} skewness	WB SKEW ΔM_{cr}	ACA SKEW ΔM_{cr}	MCA SKEW ΔM_{cr}	PCA SKEW ΔM_{cr}	W SKEW ΔM_{cr}
ΔM_{cr} kurtosis	WB KURT ΔM_{cr}	ACA KURT ΔM_{cr}	MCA KURT ΔM_{cr}	PCA KURT ΔM_{cr}	W KURT ΔM_{cr}
ΔM_{cr} peak	WB PEAK ΔM_{cr}	ACA PEAK ΔM_{cr}	MCA PEAK ΔM_{cr}	PCA PEAK ΔM_{cr}	W PEAK ΔM_{cr}
R FW	WB FW R	ACA FW R	MCA FW R	PCA FW R	W FW R
R HWR	WB HWR R	ACA HWR R	MC AHWR R	PCA HWR R	W HWR R
R HWL	WB HWL R	ACA HWL R	MCA HWL R	PCA HWL R	W HWL R
R TTP	WB TTP R	ACA TTP R	MCA TTP R	PCA TTP R	W TTP R
R skewness	WB SKEW R	ACA SKEW R	MCA SKEW R	PCA SKEW R	W SKEW R
R kurtosis	WB KURT R	ACA KURT R	MCA KURT R	PCA KURT R	W KURT R
R peak	WB PEAK R	ACA PEAK R	MCA PEAK R	PCA PEAK R	W PEAK R

6.2.5 Feature reduction and classification

The primary purpose of implementing a machine learning approach was to determine which feature combination provides for a better class-differentiation. Due to the large number of features and the limited amount of data with regards to the current dataset it is good practice to reduce dimensionality in order to

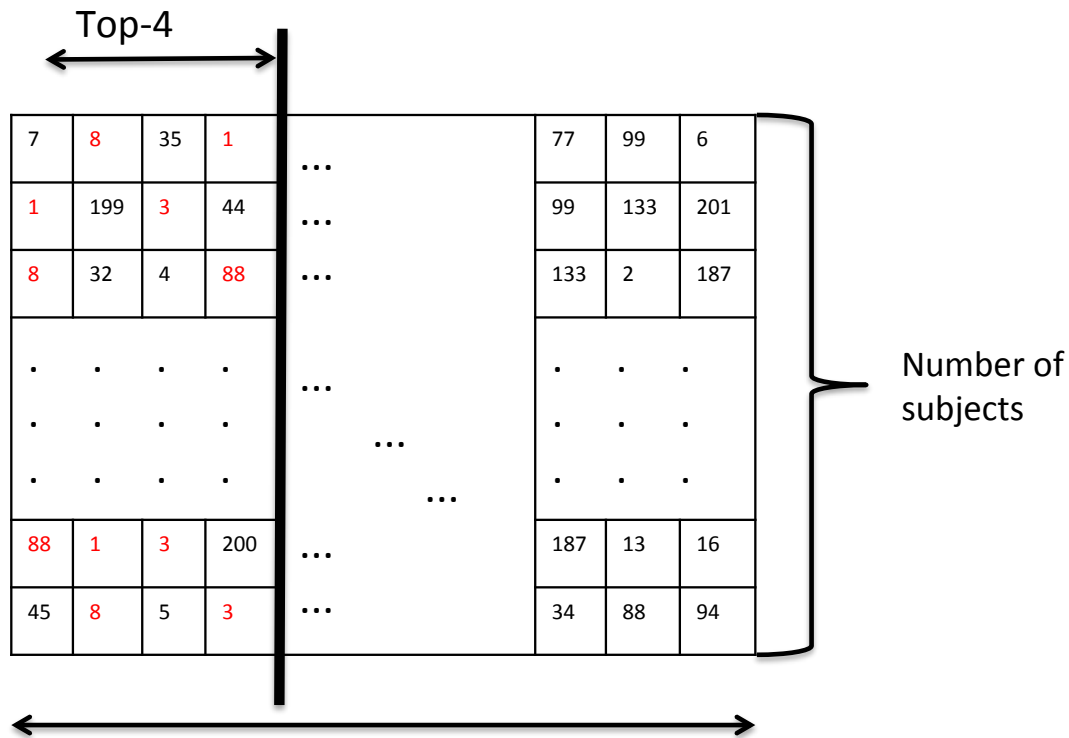
avoid overfitting. A framework proposed by Zacharaki et al. (269) was utilised, with minor modifications. The investigated binary classification tasks were:

- a) HV vs T2DM,
- b) HV vs IGT&T2DM,
- c) HV vs IGT and
- d) IGT vs T2DM.

For every task, t-tests were run to retain only the features that were significantly different between the groups; the significance threshold was $p < 0.05$. Subsequently the retained features were normalized (0 mean, 1 variance) and used as an input to the SVM-RFE algorithm (257, 258). SVM-RFE is a subset selection method, which allows for the reduction of the problem's dimensionality. This algorithm leaves one feature out in every iteration and trains an SVM classifier with the remaining ones. Ranking of the features is obtained using the weights assigned to every feature during the classification task. The Matlab implementation by Yan and Zhang (280) was utilised. It needs to be noted that utilisation of t-tests is highly likely to yield a number of false positives resulting from the multiple comparisons between the groups. However, the utilised feature dimensionality reduction technique based on the SVM classifiers deals with redundant features with overlapping information by reducing their associated weights. Hence, it is not necessary to account for multiple comparisons since the outcome of t-tests is utilised in a dimensionality reduction framework based on SVMs.

SVM-RFE was run N times (N is the number of considered subjects in the task), leaving one subject out in every iteration ending up with N separate rankings for all features which were stored in a table having dimensions [N , number of features]. The top-ranked features from every iteration were retained and used for the subsequent classification task (figure 6.4). In order to determine the classifier's performance with an increasing number of features and identify the ones comprising the optimally differentiating combination, we tested several values regarding the number of the retained top-ranked features ranging from $M = 1$ to 50. If, for any of the classification tasks, the number of significantly different features between the groups was lower than 50 then the actual number of different features was used as a limit. The classification

accuracy of linear SVM was evaluated for an increasing M. Following this, the optimal M was determined. The number of features associated with this M was recorded. Additionally, the number of times every feature occurred in the top-M (measured as explained in figure 6.4) was recorded and is presented in the results section inside parentheses.



Features ranked based on SVM-RFE
(features with higher weight have a higher rank)

Figure 6.4: **Philosophy of the feature ranking and selection method.** The SVM-RFE algorithm is trained leaving out one subject every time and a ranking occurs for every iteration of this procedure, which is stored in a table. Subsequently, a decision is made on the top features to be retained. In a simplified experiment with 5 subjects (5 shown rows), retention of the top-1 features would end up with 5 features being considered (unique features in the first column). If the top-2 features were considered, 7 features would be chosen (8 and 1 occur three and two times respectively and so on for an increasing number of top-M retained features).

Classification was run using Matlab functions supplied as part of the statistics and machine learning toolbox and linear SVM was chosen. The feature combinations evaluated in the classification tasks were:

- 1) Hemodynamic features extracted from the ΔM_{cr} , ΔM_{ncr} , AIF_{SH} curves. This feature combination is completely independent from the analysis, as these are the original QUASAR curves. The only processing prior to the

determination of these signals is the registration of the scans, averaging and noisy scan removal (**model 1**).

- 2) Hemodynamic features extracted from the curves comprising the linear perfusion system (ΔM_{cr} , AIF, residue). Both the AIF and residue curves depend on the post-processing. The AIF depends on the AIF assignment technique and the residue function on the post-processing and deconvolution techniques (**model 2**).
- 3) Hemodynamic features extracted from all five hemodynamic curves (ΔM_{cr} , ΔM_{ncr} , AIF_{SH}, AIF, residue) (**model 3**).
- 4) CBF, ATT and aBV maps. These are the typically quantified perfusion parameters when the technique is used and are analysis-dependent (**model 4**).
- 5) Combination of models 1 & 4 (**model 5**).
- 6) Combination of models 2 & 4 (**model 6**).
- 7) Combination of models 3 & 4 (**model 7**).

The first three models were built purely to evaluate the ability of the hemodynamic curves to provide features leading to an optimal class differentiation. With model 4 we wanted to evaluate and present in quantitative terms the potential benefit from an analysis approach not confined to the typical QUASAR-derived features by evaluating the classification performance based solely on these. Hence, we evaluated the accuracy using typically quantified QUASAR ASL metrics (CBF, ATT, aBV and CVR) from the considered ROIs. We compared the performance of the linear SVM classifier using these, as opposed to the performance obtained using a detailed hemodynamic analysis as described here. In models 5, 6 and 7 we combined the typically quantified QUASAR metrics with the detailed hemodynamic features extracted from the first three combinations. For all classification tasks, age, was added in the feature vector. In addition to these, the classification was run for models 1, 4 and 5 only with the baseline data to evaluate the classification accuracy and derived patterns assuming the acquisition did not include post-ACZ scans.

This combination of t-tests, SVM-RFE and linear SVM was used in order to preserve the original features, which cannot be retained if methods such as principal component analysis are selected. Hence, it is feasible working

backwards to identify the specific features comprising the optimally differentiating pattern, potentially leading to biomarker identification.

In order to evaluate the classification performance and the generalisability of the models leave-one-out cross-validation (LOOCV) was used. Cross-validation is an important step in statistical and machine learning analysis associated with the predictable power of a model. In small datasets, where the ability to separate the available data in training and testing does not exist, cross validation is used to evaluate the generalisability of the developed model instead.

All classification steps were run in Matlab. An SVM model was generated using the `fitsvm` function, which was used as an input to the `crossval` function by specifying that the desired cross validation scheme is LOOCV. Finally, `kfoldloss` was used to assess the generalisability of the model and the prediction accuracy. Furthermore, in order to provide reassurance of the reproducibility of our results, the random number generator in Matlab was set to 'default' in every iteration. The alternative approach is to run the classification procedure numerous times and record the mean value. Recorded values were: accuracy (percentage of correctly classified samples), specificity (percentage of correct true positives) and sensitivity (percentage of correct true negatives). A model was considered to be optimal by judging the following attributes: a) classification accuracy and b) number of features contributing towards optimal accuracy. The desirable behaviour of a model is to provide the highest possible accuracy with the lowest possible number of features to avoid overfitting.

6.2.6 Statistical comparisons

Comparisons between the groups were conducted using one-way analysis of variance (ANOVA), or its non-parametric equivalent (Kruskal-Wallis), when the normality and equality of variance assumptions were violated.

6.3 Results

6.3.1 Conventional analysis approach

The mean hemodynamic curves comprising the linear perfusion system at a voxel-wise level (AIF, residue, tissue) calculated for every subject group

along with a semi-transparent region corresponding to the standard deviation are plotted in figure 6.5.

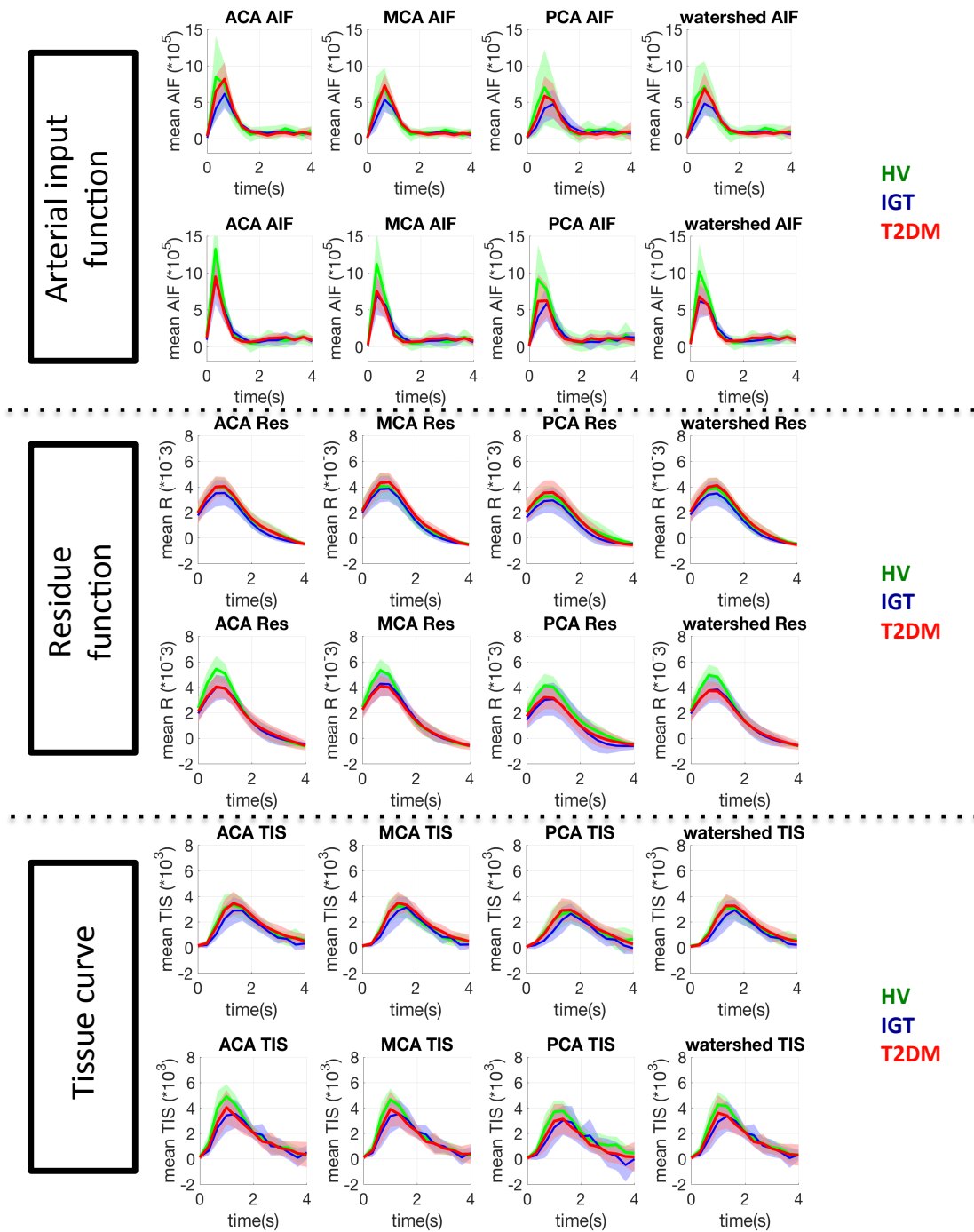


Figure 6.5: Hemodynamic time series curves for every group. From top to bottom AIF, the residue function and the tissue curve are shown for the 3 groups for 4 ROIs (ACA, MCA, PCA, watershed areas) pre and post-ACZ injection.

Results for the whole brain ATT, aBV, GM and WM CBF pre and post- ACZ, CVR and the volume of GM, WM and CBF inside the brain volume covered with the ASL protocol are shown in table 6.3.

Table 6.3: Quantified values for CBF, aBV, ATT and CVR using the developed QUASAR ASL quantification pipeline for the scanned cohort.

	HV (16)	IGT (10)	T2DM (16)	p-value
Age (years)	50.0±12.0	54.1±5.5	54.5±11.8	0.47
GM CBF baseline (ml/100g/min)	55±5.9	55.7±4.7	60.8±4.2	0.01
GM CBF post- ACZ (ml/100g/min)	63.6±5.9	59.8±3.6	61.2±4.8	0.17
WM CBF baseline (ml/100g/min)	23±2.4	23.3±2.1	24.6±1.6	0.15
WM CBF post- ACZ (ml/100g/min)	24.8±1.7	24.8±2.1	24.7±2	0.98
CVR (%)	16.4±13.1	7.7±6.5	0.8±5.7	< 0.001
ATT baseline (s)	0.62±0.04	0.61±0.05	0.65±0.05	0.13
ATT post-ACZ (s)	0.55±0.07	0.62±0.07	0.59±0.08	0.08
aBV baseline (%)	1.1±0.4	1.3±0.3	1.1±0.3	0.05
aBV post-ACZ (%)	0.9±0.3	1.1±0.4	1±0.2	0.19

Significant differences were detected for GM CBF baseline ($F(2,39) = 5.807$, $p = 0.01$), CVR ($\chi^2(2) = 16.826$, $p < 0.01$) and aBV baseline ($\chi^2(2) = 5.832$, $p = 0.05$). When examining specific ROIs, the only significant difference

was for ACA ATT post-ACZ ($F(2,39) = 3.89, p = 0.03$). The absence of differences between the groups in CBF within the examined vascular territories and watershed areas (when in the meantime differences were identified for GM CBF and CVR) could be attributed to the fact that the CBF values within the examined vascular territories were not PV corrected and hence reflect the total GM and WM CBF. Following multiple comparison correction with FDR the only remaining significant difference was for CVR ($p=0.004$).

Metrics differing between the groups based on conventional QUASAR analysis were: baseline GM CBF, CVR, baseline aBV and ACA ATT post-ACZ.

6.3.2 Extended hemodynamic analysis

In this section, results based on the newly quantified hemodynamic features are presented. Every model is examined separately. Results are also presented solely for the baseline perfusion data. For every model, accuracy, specificity and sensitivity values are reported for the best performing (highest accuracy) feature combination. Additional recorded data involve: a) the number of features (NF) giving optimal performance; b) the top-M features, where M differs from NF as described in figure 6.4; c) the top features (maximum = 10); d) the number of SVM-RFE iterations for which the feature under consideration was identified in the top-M. The number of subjects included in a task defines the maximum occurrence for a feature. For the HV vs T2DM task maximum occurrence was 32; for the HV vs IGT&T2DM 42; for HV vs IGT 26 and for IGT vs T2DM 26.

First feature combination

Overall number of quantified features: **211**.

For the HV vs T2DM task, 59 features were significantly different following t-tests. The maximum accuracy was 96.9% (sensitivity = 100%, specificity = 93.8%) achieved with 27 features identified in the top-12 of the SVM-RFE matrix. 10 out of the 27 features (the ones with maximum occurrence) are shown in table 6.4.

Table 6.4: **Model 1, HV vs T2DM task top-10 features identified with SVM-RFE giving optimal performance, accompanied with a number indicating their occurrence (Occ.) in the top-M.**

Feature	Occ. (times)	Feature	Occ. (times)
ACA TTP AIF _{SH} post-ACZ	32	ACA KURT AIF _{SH} baseline	31
ACA SKEW AIF _{SH} baseline	32	ACA TTP ΔM_{ncr} post-ACZ	28
ACA HWL AIF _{SH} post-ACZ	32	ACA SKEW ΔM_{cr} post-ACZ	27
PCA HWR ΔM_{cr} post-ACZ	32	W KURT ΔM_{cr} baseline	27
PCA FW ΔM_{cr} post-ACZ	32	WB HWL AIF _{SH} post-ACZ	25

For the HV vs IGT&T2DM task, 85 features were significantly different. Maximum accuracy of 92.9% was achieved (sensitivity = 93.8%, specificity = 87.5%) with 14 features identified in the top-4 of the SVM-RFE matrix (table 6.5).

Table 6.5: **Model 1, HV vs IGT&T2DM task top-10 features identified with SVM-RFE giving optimal performance along with their occurrence in the top-M.**

Feature	Occ. (times)	Feature	Occ. (times)
PCA HWR ΔM_{cr} post-ACZ	42	PCA HWL AIF _{SH} baseline	15
MCA SKEW ΔM_{cr} post-ACZ	35	ACA SKEW AIF _{SH} baseline	7
ACA SKEW ΔM_{cr} post-ACZ	18	ACA HWL AIF _{SH} post-ACZ	6
W KURT ΔM_{cr} baseline	18	W KURT AIF _{SH} baseline	4
ACA KURT AIF _{SH} baseline	17	ACA TTP ΔM_{ncr} post-ACZ	3

For the HV vs IGT task 85 features differed significantly between the groups. Maximum accuracy of 100% was achieved with 5 features that made it to the top-3 of the SVM-RFE matrix; these were: PCA HWL AIF_{SH} post-ACZ (26), PCA TTP AIF_{SH} post-ACZ (26), W KURT ΔM_{cr} post-ACZ (17), PCA HWL ΔM_{ncr} post-ACZ (8) and ACA TTP ΔM_{ncr} post-ACZ (1). For the IGT vs T2DM task, 6 features differed significantly and the accuracy was 65.4% (specificity = 40%, sensitivity = 81.3%) with 4 features (top-1 in the SVM-RFE matrix); These

were W HWR ΔM_{cr} baseline (14), MCA TTP AIF_{SH} baseline (8), ACA KURT ΔM_{ncr} post-ACZ (2), PCA HWL ΔM_{ncr} post-ACZ (2).

Second feature combination

Overall number of quantified features: **211**.

For the HV vs T2DM task, 71 features differed significantly. Maximum accuracy was achieved with 7 features (top-3 in the SVM-RFE matrix) and was 84.4% (sensitivity = 87.5%, specificity = 81.3%); these were: WB TTP R post-ACZ (32), WB HWL R post-ACZ (32), ACA HWL R post-ACZ (25), PCA TTP R post-ACZ (4), ACA TTP R post-ACZ (1), MCA HWL R post-ACZ (1) and W KURT ΔM_{cr} baseline (1). For the HV vs IGT&T2DM task 85 features differed significantly. Maximum accuracy was 83.3% (sensitivity = 88.5%, specificity = 68.8%) achieved with 5 features (W KURT AIF baseline (2), WB HWL R post-ACZ (37), MCA SKEW ΔM_{cr} post-ACZ (1), WB TTP R post-ACZ (1), PCA HWR ΔM_{cr} post-ACZ (1)) that made it to the top-1 of the SVM-RFE matrix.

For the HV vs IGT task 86 features were significantly different, maximum accuracy was 92.3% (sensitivity = 80%, specificity = 100%) with 7 features that made it to the top-3 (SVM-RFE matrix); these were: PCA TTP R post-ACZ (26), PCA HWL R post-ACZ (26), PCA HWR AIF post-ACZ (13), PCA FW AIF post-ACZ (10), W KURT ΔM_{cr} post-ACZ (1) and PCA HWL AIF post-ACZ (1) and WB TTP AIF post-AZC (1). For the IGT vs T2DM task, 10 features differed significantly between the groups. Maximum accuracy was 69% (sensitivity = 87.5%, specificity = 50%) achieved with 5 features that made it to the top-1 of the SVM-RFE matrix. These were: MCA HWL R baseline (17), MCA HWL AIF baseline (4), W HWR ΔM_{cr} baseline (2), ACA PEAK AIF baseline (2) and WB HWL AIF baseline (1).

Third feature combination

Overall number of quantified features: **351**.

For the HV vs T2DM task, the significantly different features were 116. The maximum accuracy was 93.8% (sensitivity = 87.5%, specificity = 100%) achieved with 9 features that made it to the top-3 of the SVM-RFE matrix (table 6.6).

Table 6.6: Model 3, HV vs T2DM task top-10 features identified with SVM-RFE giving optimal performance along with their occurrence in the top-M.

Feature	Occ. (times)	Feature	Occ. (times)
WB HWL R post-ACZ	32	PCA TTP R post-ACZ	3
WB TTP R post-ACZ	28	W KURT AIF _{SH} baseline	2
ACA SKEW AIF _{SH} baseline	18	PCA HWL R post-ACZ	1
ACA TTP AIF _{SH} post-ACZ	7	W KURT ΔM_{cr} baseline	1
ACA HWL R post-ACZ	4		

For the HV vs IGT&T2DM task 153 features differed, the maximum achieved accuracy was 88.1% (sensitivity = 92.3%, specificity = 81.3%) achieved with 42 features (table 6.7) that made it at least for one iteration of the SVM-RFE to the top-19 features.

Table 6.7: Model 3, task HV vs IGT&T2DM top-10 features identified with SVM-RFE giving optimal performance along with their occurrence in the top-M.

Feature	Occ. (times)	Feature	Occ. (times)
WB HWL R post-ACZ	42	ACA HWL ΔM_{ncr} post-ACZ	42
WB TTP R post-ACZ	42	PCA TTP R baseline	41
ACA TTP ΔM_{ncr} post-ACZ	42	PCA HWL R post-ACZ	41
PCA HWL AIF _{SH} post-ACZ	42	PCA HWR ΔM_{cr} post-ACZ	41
W KURT ΔM_{cr} baseline	42	W KURT AIF _{SH} baseline	39

For the HV vs IGT task 148 features differed; for 2 features that made it to the top-1 (SVM-RFE matrix) the accuracy was 92.3% (70% sensitivity, 100% specificity). These features were: PCA HWL AIF_{SH} post-ACZ (21) and PCA TTP R post-ACZ (5). For the IGT vs T2DM task 15 features differed significantly, maximum accuracy was 69.2% (sensitivity = 75%, specificity = 50%) achieved with 11 features that made it to the top-4 (SVM-RFE matrix). These were as in table 6.8.

Table 6.8: Model 4, IGT vs T2DM task, top-10 features identified with SVM-RFE giving optimal performance along with their occurrence in the top-M.

Feature	Occ. (times)	Feature	Occ. (times)
W HWR ΔM_{cr} baseline	21	MCA TTP AIF _{SH} baseline	9
ACA KURT ΔM_{ncr} post-ACZ	20	PCA HWL ΔM_{ncr} post-ACZ	6
W PEAK R baseline	14	MCA HWL AIF _{SH} baseline	4
MCA HWL R baseline	13	MCA KURT ΔM_{ncr} post-ACZ	2
ACA PEAK AIF baseline	12	MCA HWL AIF baseline	2

Fourth feature combination

Overall number of quantified features: **34**.

For the HV vs T2DM task, 3 features were different following t-tests, the maximum accuracy was 81.3% (sensitivity = 87.5%, specificity = 75%) achieved with 1 feature (CVR - 32). For the HV vs IGT&T2DM task 7 features were significantly different, maximum accuracy of 81.0% (sensitivity = 92.3%, specificity = 62.5%) was achieved with minimum four features (top-3 in the SVM-RFE matrix): CVR (42), GM CBF baseline (32), ACA ATT post-ACZ (41) and PCA CBF post-ACZ (11).

For the HV vs IGT task, 6 features were significantly different, maximum accuracy was 73.1% (sensitivity = 50%, specificity = 81.3%) with 6 features (WB ATT post-ACZ (2), ACA ATT post-ACZ (26), PCA aBV post-ACZ (25), ACA CBF post-ACZ (2), W CBF post-ACZ (22) and MCA ATT post-ACZ (1)) identified in the top-3 of the SVM-RFE matrix. For the IGT vs T2DM task, 4 features were significantly different and the accuracy was 73.1% (sensitivity = 81.3%, specificity = 70%) with all 4 features (GM CBF baseline, CVR, W CBF baseline, ACA aBV baseline).

Fifth feature combination

Overall number of quantified features: **244**.

For the HV vs T2DM, 62 features were different, maximum accuracy was 90.6% (sensitivity = 93.8%, specificity = 87.5%) with 6 features identified to the top-3 of the SVM-RFE matrix (PCA HWR ΔM_{cr} post-ACZ (3), ACA TTP AIF_{SH} post-ACZ (30), ACA SKEW AIF_{SH} baseline (1), ACA HWL AIF_{SH} post-ACZ (27)

GM CBF baseline (3), CVR (32)). For the HV vs IGT&T2DM task 92 features differed, the maximum accuracy was 92.9% (sensitivity = 96.2%, specificity = 87.5%) achieved with 11 (table 6.9) features that made it to the top-3 of the SVM-RFE matrix.

Table 6.9: Model 5, HV vs IGT&T2DM task top-10 features identified with SVM-RFE giving optimal performance along with their occurrence in the top-M.

Feature	Occ.(times)	Feature	Occ. (times)
CVR	36	PCA HWL AIF _{SH} post-ACZ	2
MCA SKEW ΔM_{cr} post-ACZ	31	ACA TTP ΔM_{ncr} post-ACZ	2
ACA HWL AIF _{SH} post-ACZ	23	GM CBF baseline	2
PCA HWR ΔM_{cr} post-ACZ	20	W KURT ΔM_{cr} baseline	1
ACA SKEW AIF _{SH} baseline	7	ACA TTP AIF _{SH} post-ACZ	1

For the HV vs IGT task 91 features differed significantly, accuracy was 100% with 5 features that made it to the top-3 in the SVM-RFE matrix (W KURT ΔM_{cr} post-ACZ (17), PCA TTP AIF_{SH} post-ACZ (26), PCA HWL AIF_{SH} post-ACZ (26), PCA HWL ΔM_{ncr} post-ACZ (8) and ACA TTP ΔM_{ncr} post-ACZ (1)). For the IGT vs T2DM task 10 features differed, the accuracy of 80.7% (sensitivity = 87.5%, specificity = 70%) was achieved with 7 features that were identified to the top-1 of the SVM-RFE matrix (GM CF baseline (10), CVR (9), ACA ABV baseline (2), PCA HWL ΔM_{ncr} post-ACZ (2), W HWR ΔM_{cr} baseline (1), ACA KURT ΔM_{ncr} post-ACZ (1) MCA KURT ΔM_{ncr} post-ACZ (1)).

Sixth feature combination

Overall number of quantified features: **244**.

For the HV vs T2DM task 74 features were significantly different. The highest accuracy was 93.8% (sensitivity = 93.8%, specificity = 93.8%) achieved with three features that made it to the top-2 of the SVM-RFE matrix (WB HWL R post-ACZ (31), WB TTP R post-ACZ (26) and CVR (7)). For the HV vs IGT&T2DM task, 92 features differed significantly, the maximum accuracy was

83.3% (sensitivity = 88.5%, specificity = 75%) achieved with 23 features (table 6.10) that made it to the top-13 (SVM-RFE matrix).

Table 6.10: Model 6, HV vs IGT&T2DM task top-10 features identified with SVM-RFE giving optimal performance

Feature	Occurrence (times)	Feature	Occurrence (times)
CVR	42	PCA HWR ΔM_{cr} post-ACZ	42
WB HWL R post-ACZ	42	ACA SKEW ΔM_{cr} post-ACZ	42
MCA SKEW ΔM_{cr} post-ACZ	42	MCA SKEW ΔM_{cr} post-ACZ	42
		W KURT AIF baseline	40
WB TTP R post-ACZ	42	W KURT ΔM_{cr} baseline	38

92 features were significantly different between the groups for the HV vs IGT task. 92.3% (sensitivity = 80%, specificity = 100%) was the maximum accuracy achieved with 6 features that made it to the top-3 in the SVM-RFE matrix; these were: PCA TTP R post-ACZ (26), PCA HWL R post-ACZ (26), PCA HWR AIF post-ACZ (14), PCA FW AIF post-ACZ (10), PCA HWL AIF post-ACZ (1) and W KURT ΔM_{cr} post-ACZ (1). For the IGT vs T2DM task 14 features differed significantly. Maximum achieved accuracy was 65.4% (sensitivity = 75%, specificity = 50%) with 11 features that made it to the top-5 of the SVM-RFE matrix.

Seventh feature combination

Overall number of quantified features: **384**.

For the HV vs T2DM task, the number of significantly different features identified with t-tests was 119. Following SVM-RFE implementation the maximum achieved accuracy was 84.4% (sensitivity = 93.8%, specificity = 75%) achieved with a minimum of 3 features, these features made it to the top-1 in the SVM-RFE matrix and were as follows: WB HWL R post-ACZ (29), WM TTP R post-ACZ (2) and ACA TTP AIF_{SH} post-ACZ (1).

For the HV vs IGT&T2DM task, the significantly different features identified with t-tests were 160. The maximum achieved accuracy was 88.1%

(sensitivity = 88.5%, specificity = 87.5%) achieved with a minimum of 22 features that made it at least once to the top-7 in the SVM-RFE matrix. The identified top-10 features can be found in table 6.11.

Table 6.11: Model 7, HV vs IGT&T2DM task top-10 features identified with SVM-RFE giving optimal performance along with their occurrence in the top-M.

Feature	Occ. (times)	Feature	Occ. (times)
WB HWL R post-ACZ	42	ACA TTP ΔM_{ncr} post-ACZ	24
CVR	35	PCA HWL R post-ACZ	21
ACA HWL ΔM_{ncr} post-ACZ	34	PCA HWR ΔM_{cr} post-ACZ	13
WB TTP R post-ACZ	32	W KURT AIF baseline	11
W KURT ΔM_{cr} baseline	31	PCA TTP R post-ACZ	11

For the HV vs IGT task, the significantly different features identified with t-tests were 154. The maximum accuracy was 92.3% (sensitivity 70%; specificity 100%) achieved with 2 features (PCA TTPR post-ACZ (5) and PCA HWL AIF_{SH} post-ACZ (21)) that made it to the top-1 of the SVM-RFE matrix. For the IGT vs T2DM task, the significantly different features identified with t-tests were 19. The maximum recorded accuracy was 80.7% (sensitivity = 81.3%, specificity = 80%) for 6 features (MCA HWL R baseline (1), W HWR ΔM_{cr} baseline (1), PCA HWL ΔM_{ncr} post-ACZ (2), GM CBF baseline (17), CVR (4), ACA aBV baseline (1)), all made it to the top-1 (SVM-RFE matrix) at least once.

A summary of the model performance, the identified number of features and the number of significant features per task, can be found in the Appendix 1 in table A6.1. In table A6.2, the accuracy, sensitivity, specificity, NF and the top-5 features are shown for the best two performing models per task. Finally, in figure 6.6 the classification accuracy as a function of the number of features incorporated in the task is plotted for models 1,2,4,5 and 6.

Overall models 1 and 5 had the optimal performance for the HV vs T2DM, HV vs IGT&T2DM and HV vs IGT tasks. For the IGT vs T2DM task, models 5 and 7 were the optimal. Perfect classification (100%) was achieved for the HV vs IGT task. Classification was also very high for the HV vs T2DM task (96.9%). The performance for IGT and T2DM separation was lower compared to other tasks.

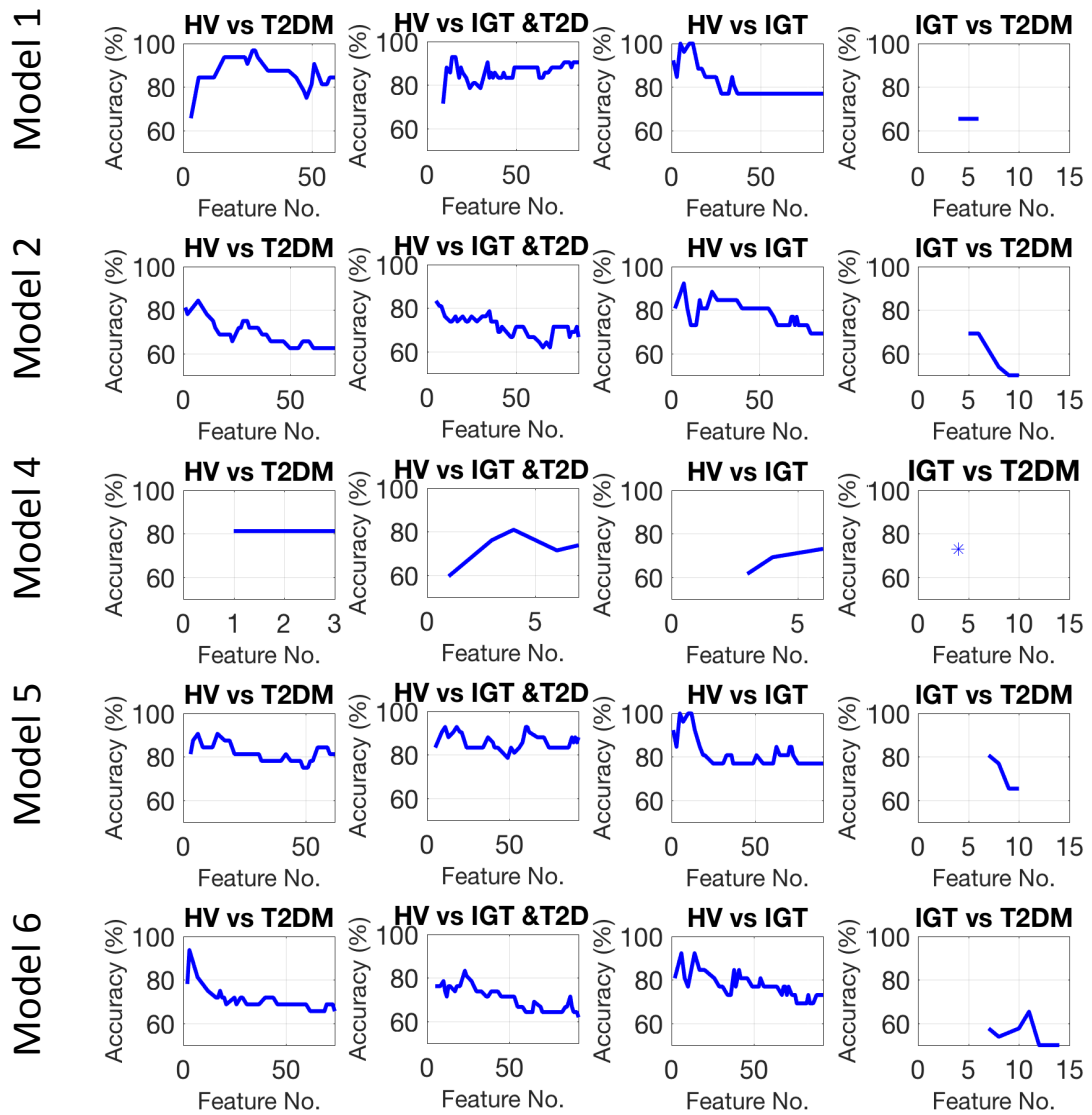


Figure 6.6: Model accuracy for every classification task obtained using LOOCV as a function of the number of features for models 1,2,4,5 and 6.

6.3.3 Classification based just on the baseline scan

Model 1

106 features were identified, for the HV vs T2DM task, 11 differed significantly, the calculated 75% accuracy (sensitivity = 62.5%, specificity = 68.8%) was achieved with one feature: ACA SKEW AIF_{SH}. For the HV vs IGT&T2DM task, 23 features were different; the achieved accuracy was 81.0% (sensitivity = 92.3%, specificity = 62.5%), achieved with 6 features (PCA KURT ΔM_{cr} (4), W KURT ΔM_{cr} (12), ACA SKEW AIF_{SH} (31), W KURT AIF_{SH} (26), ACA KURT ΔM_{ncr} (9) and W KURT ΔM_{ncr} (2)) that made it to the top-2 in the SVM-RFE matrix. For the HV vs IGT task, 24 features were different, the achieved accuracy was 61.5% (sensitivity = 40%, specificity = 62.5%) achieved with 10 features (top-5: W HWR ΔM_{cr} (16), WB TTP ΔM_{ncr} (14), WB HWL ΔM_{ncr} (6), W FW ΔM_{cr} (5) and MCA TTP ΔM_{ncr} (4)) that made it to the top-2 in the SVM-RFE matrix. For the IGT vs T2DM task, 3 features differed significantly and the maximum accuracy with all 3 (W HWR ΔM_{cr} , MCA TTP AIF_{SH}, MCA HWL AIF_{SH}, all with an occurrence of 26) was 69.2% (sensitivity = 81.3%, specificity = 50%).

Model 4

17 features were identified. For the HV vs T2DM task, 2 features differed significantly, 71.9% was the maximum accuracy (sensitivity = 62.5%, specificity = 62.5%) achieved with minimum 1 feature (GM CBF). For the HV vs IGT&T2DM task 1 features differed, maximum accuracy was 64.3% (sensitivity = 88.5%, specificity = 18.8%) with 1 feature (GM CBF). For the HV vs IGT task, no features differed significantly between the groups. For the IGT vs T2DM task, 3 features were significantly different; maximum accuracy was 76.9% (sensitivity = 75%, specificity = 80%) with all three features (GM CBF, W CBF, ACA aBV).

Model 5

122 features were identified. For the HV vs T2DM task 13 features differed; maximum performance was 75% (sensitivity = 75%, specificity = 75%) with 2 features (ACA SKEW AIF_{SH} (29), GM CBF (3)) that made it to the top-1. For the HV vs IGT&T2DM task 24 features differed significantly, maximum

accuracy of 78.6% (sensitivity = 88.5%, specificity = 62.5%) was achieved with 7 features (top-5: W KURT AIF_{SH} (15), ACA SKEW AIF_{SH} (32), ACA KURT ΔM_{ncr} (18), W KURT ΔM_{cr} (9), PCA KURT ΔM_{cr} (6)) that made it to the top-2 in the SVM-RFE matrix. For the HV vs IGT task 24 features differed, maximum accuracy was 61.5% (sensitivity = 70%, specificity = 86.4%) with 10 features; the same as for model 1. For the IGT vs T2DM task 24 features differed significantly, maximum accuracy was 61.5% (sensitivity = 40%, specificity = 62.5%) achieved with 4 features (top-1) these were W HWR ΔM_{cr} (6), GM CBF (18), W CBF (1), ACA aBV (1). In table 6.12 a summary can be found facilitating comparisons between the performance based on features derived from the baseline scans and for both baseline and post-ACZ for all 4 tasks and the 3 models.

Table 6.12: Comparison between the performance of models based solely on the baseline scan and models based on both pre and post-ACZ scans. NF1 refers to the initial number of significantly different features following t-tests. NF2 refers to the number of features contributing towards optimal class-differentiation following SVM-RFE and training of the SVM classifier. Acc. Is the recorded classification accuracy.

Model	NF1	Acc. (%)	NF2	Only baseline			Baseline & post-ACZ		
Healthy volunteers vs type-2 diabetes									
1	11	75	1	59	96.9	27			
4	2	71.9	1	3	81.3	1			
5	13	75	2	62	90.6	6			
Healthy volunteers vs type-2 diabetes & impaired glucose tolerance									
1	23	81	6	85	92.9	14			
4	1	64.3	1	7	81.0	4			
5	24	78.6	7	92	92.9	11			
Healthy volunteers vs impaired glucose tolerance									
1	24	61.5	10	85	100	5			
4	0	N/A	0	6	73.1	6			
5	24	61.5	10	91	100	5			
Impaired glucose tolerance vs type-2 diabetes									
1	3	69.2	3	6	65.4	4			
4	3	76.9	3	4	73.1	4			

5	6	76.9	4	10	80.7	7
---	---	------	---	----	------	---

For every task the performance was increased when using both baseline and post-ACZ features. This is particularly noticeable for the HV vs IGT task. The results indicate that an additional perfusion acquisition following induced vasodilation can provide invaluable information on hemodynamic alterations and contribute towards optimal class-separation.

Optimal features emerged from all vascular territories and mainly captured the pattern of delayed and dispersed bolus delivery (e.g. HWL, TTP, KURT). From the typically quantified QUASAR metrics, CVR was the one identified most often as part of the optimal patterns. The majority of important features emerged from the post-ACZ acquisition.

6.4 Discussion

Increased GM CBF and reduced CVR were detected in hyperglycemia

Our findings suggest that baseline CBF is increased in T2DM compared to HV, and IGT demonstrates a similar pattern to T2DM. This has been found in only a few studies and could suggest the existence of a potential compensatory mechanism to account for impaired oxygen delivery to the tissue. Vasodilation as a response to tissue hypoxia has been found in diabetes (302). Glycated hemoglobin (HbA1c), which is higher than normal in both IGT and T2DM has an increased heme-oxygen affinity. The oxygen dissociation curve of this hemoglobin species is shifted compared to normal and this underlies tissue hypoxia (303). Insufficient oxygen and glucose retention by the tissue due to insulin resistance could result in the observed compensatory mechanism causing dilation with increased amounts of blood flowing to the tissue. Following vasodilation a big increase in the GM CBF value was observed for healthy individuals. This change captured by CVR was lower in IGT and even lower in T2DM compared to HV.

Increased baseline CBF and reduced CVR in T2DM suggest that maximum vasodilation has been reached at baseline since pharmacologically

induced vasodilation, which is supposed to mimic the physiological one, does not lead to the anticipated blood flow increase. Our findings, regarding the response to a vasodilating stimulus, are in line with transcranial Doppler, internal carotid blood flow and BOLD studies reporting reduced responses (15, 42, 53). These techniques are substantially different from ASL since the first two are focused on the velocity of red blood cells and the second does not quantify baseline and post-stimulus values but rather the observed change. There is no published study currently examining cerebral perfusion in T2DM using a multi-TI/PLD ASL approach. The single-PLD approaches have detected a lower or similar baseline CBF value in T2DM compared to HV and a lower CVR (15, 36).

The increased baseline CBF finding could also be connected with the findings of van Bussel et al. (304); in their study examining the default mode network they found a better more efficient organization of the network in T2DM and pre-diabetes. This finding, similarly to the increased baseline perfusion observed here, might indicate an early compensatory mechanism, in a cognitively asymptomatic population, preceding cognitive decline. In their study, as in ours, the population was neurologically normal.

Brain perfusion in T2DM is hypothesised to be impaired as a result of endothelial dysfunction and BBB disruption (10, 51). The inconsistency of perfusion imaging findings in diabetes could be attributed both to cohort idiosyncrasies (usually the studies involve small cohorts) and to the utilised imaging techniques. When considering the adopted perfusion imaging approaches, both sequence parameters and post-processing approaches can vary and have the potential to impact the observed perfusion values and affect the resulting conclusion.

One of the factors that can vary, especially in single-PLD ASL MRI studies is the PLD value per se. In Moya-Moya patients it has been shown that a single-PLD approach underestimates perfusion compared to multi-PLD implementations, which also demonstrate a better agreement with PET measurements (305). Increased ATT does not necessarily lead to perfusion underestimation (the perfusion peak is missed) as it can lead to overestimation due to slower magnetization relaxation inside the blood (125). A technique insensitive to transit time changes such as the one used in this study is unlikely

to miss the perfusion peak and could potentially shed light upon the underlying perfusion pattern. In addition to this, time-resolved ASL and in particular QUASAR ASL has the potential to provide rich information that can be used to unravel abnormal cerebral perfusion patterns. Its competitive advantage is the retention of hemodynamic signals allowing for a detailed hemodynamic analysis.

It is important to emphasise that our results are corrected for potential atrophy due to the use of a partial volume correction method, thus reflecting the actual perfusion value in the existing cortical GM.

Usually in brain perfusion studies, CBF and CVR are quantified and in more rare cases arterial or mean transit time are also determined. A more detailed hemodynamic analysis is not typically conducted.

Extended hemodynamic analysis of ASL signals provides additional insight into hemodynamic impairment.

Per model analysis

It was shown that the hemodynamic curves representing the pattern of delivery of water to the tissue are different between healthy individuals and subjects with diabetes and pre-diabetes. By carefully examining figure 6.5 it can be seen that baseline T2DM curves have a higher peak and are wider than the HV ones. Following ACZ injection, the anticipated increase is observed in the peak value in all curves for HV, a lower increase in IGT and an even lower increase in T2DM for all examined ROIs. IGT curves at baseline are more similar to HV curves and the post-ACZ curves are more similar to the diabetes curves. This observation could suggest that a compensatory mechanism has not yet been established for IGT. This pattern, which can be characterised in a qualitative manner by observing figure 6.5, has also been captured by our more detailed hemodynamic analysis. The evaluated models combined hemodynamic features extracted from processed and unprocessed QUASAR data.

It should be noted that the AIF_{SH} , ΔM_{cr} and ΔM_{ncr} signals are based on originally acquired signals and not on any subsequent processing, which can have an impact on the observed differences. These signals comprised model 1 for which a very high accuracy in the examined classification tasks was

achieved. This finding is of great importance, since, if a significant pattern was not captured by the original unprocessed ASL signals, a potential high performance after processing could imply that this was the effect of modelling.

The second evaluated model comprised metrics extracted solely from the three hemodynamic curves comprising the linear perfusion model (AIF \rightarrow residue $\rightarrow \Delta M_{cr}$). The third examined model comprised features from all 5 hemodynamic curves. Along with the detailed hemodynamic features extracted for the first time from the QUASAR signals, typically quantified QUASAR metrics were also determined. ATT, aBV and CBF are also extracted from the hemodynamic curves. CBF is quantified as the peak of the residue function, ATT is the difference in the rising times of the AIF and ΔM_{cr} signals and aBV is the area under the arterial signal curve scaled by several parameters related to the theoretical bolus area. These typically quantified QUASAR features constituted the fourth evaluated model. When model 4 was used, the performance for all tasks was reduced with only one exception, task 4, where it was one of the three best models. In models 5, 6 and 7, model 4 was combined with different combinations of hemodynamic curves.

Per task analysis

For the HV vs T2DM task, we observed that the best models were model 1 and model 6. Model 1 had a very high performance achieved with a large number of features. Models 3, 5 and 6 also achieved a high performance though with a smaller number of features. Interestingly enough, model 6 had a high performance with only 3 features. When only the QUASAR-derived features were used, the model's accuracy (model 4) was 81.3%, lower than the accuracy of models 1, 5 and 6 indicating that the consideration of additional hemodynamic features is beneficial for accurate class-differentiation. Most importantly, the features leading to optimal separation between HV and T2DM based on the top-performing models emerged mainly from the ACA and PCA territories, the whole brain and from GM.

For the HV vs IGT & T2DM task, high accuracy (lower than the HV vs T2DM task) was achieved with model 1 and model 5. This task investigated whether the IGT and T2DM groups, if put together, could be accurately

separated from HV. The high performance suggests that IGT and T2DM could be potentially considered as one distinct group.

For the HV vs IGT task, when the QUASAR-derived features alone were considered, the accuracy was 73.1%. When models 1 and 5 were used, the classification accuracy was perfect (100%) and more importantly, achieved with a low number of features indicating that the considered extended analysis captures better the difference between HV and IGT than a conventional QUASAR analysis. These features were the same for both models. They stem from the PCA and ACA territories and watershed areas and were all extracted from the post-ACZ curves indicating that the main difference between the groups was not at baseline but following the vasodilating stimulus. They are all capturing the time it takes for the tracer to reach the peak in the PCA and ACA territories and the pattern of dispersion in watershed areas.

The classification accuracy when conducting analysis of the baseline scan for the HV vs IGT task was far lower (61.5%) compared to the recorded 100% when features from both pre- and post-ACZ acquisitions were used. This observation is of great importance, since it suggests that at baseline the perfusion differences between IGT and HV are less prominent compared to the post-ACZ ones. Based on hemodynamic features examining the response to a vasodilating stimulus, classification of HV vs IGT was perfect, suggesting that a distinct hemodynamic pattern for IGT is absent at rest but has already developed for tasks requiring increased blood flow. Hence, when investigating early hemodynamic impairment, recording the response to a stimulus could be of additional prognostic or diagnostic benefit.

For the IGT vs T2DM task, all models had a relatively lower performance compared to the previous tasks. Model 1, which was optimal for the other tasks, provided a low accuracy of 65.4%. Models 7 and 5 had a higher accuracy (80.7%), based mainly on typically quantified QUASAR features. The number of significantly different features between the groups also is of great interest since on its own it is indicative of an existing pattern. For the first three tasks when considering the top performing models examining normoglycemia vs hyperglycemia, the number of identified features ranged between 59 and 92 depending on the task and model. For the fourth task this number ranged between 4 and 10.

Overall top-scoring features extracted from the hemodynamic curves for the first three tasks involved TTP, skewness and HWL, which are indicative of the delays in the delivery of the tracer to the tissue and kurtosis and HWR which capture the dispersion profile of the delivered bolus.

The performance of the model is not the only metric that one should focus on. We should not forget that the utilised sample size is small so a large number of features comparable to the sample size could imply that the classification performance is a result of overfitting. In tasks and models where the number of features giving high classification was small (i.e. models 3, 5, 6, HV vs T2DM task; models 1, 3, 5, HV vs IGT task) confidence can increase about the generalisability of the result. LOOCV, which was used as a safeguard for overfitting, is a robust method which is used to address such issues, however it is known to provide optimistic values with regards to the generalisability error (267).

It should be emphasised that the goal of this part of the study was not to build a robust classifier to be used as a 'stand-alone' model. Rather, based on our data and by acknowledging the limitations posed by our sample size, we attempted to capture a pattern describing the differences between our groups, using methods adept for small datasets. The generalisability of the model was assessed using cross-validation. We demonstrated a certain tendency captured by QUASAR ASL. This tendency was particularly strong for HV vs T2DM and HV vs IGT tasks, where the accuracy was high and the number of utilised features by the classifier very low.

A detailed hemodynamic analysis, as described in this chapter, is not typically conducted. The majority of ASL protocols do not actually allow for such an analysis, since they are single time-point or they do not utilise vascular crushers. However, this work has shown that considering multiple metrics, which can capture the whole shape of the hemodynamic curves, holds great potential to better characterise the underlying perfusion pattern and thus distinguish subtle differences between normal from abnormal. This hemodynamic analysis could be used in other diseases affecting brain perfusion, whether severe or subtle, in order to monitor hemodynamic alterations over time, or between groups.

It is important to note that this pipeline utilised a model-free post-processing approach, whereby inferences about hemodynamic curves and curve-fitting are avoided. This makes the technique less robust to noise, but avoids using models based on assumptions that could be violated, particularly due to existing pathological alterations. Even in this implementation, not all priors could be avoided. A value of 91% inversion efficiency was assumed, based on published QUASAR measurements (154). Also, a single value for the relaxation time of the blood was used ($T1b = 1.65s$) for every subject. However, it is known that $T1b$ varies with the value of the hematocrit (306), it is also known to be different between normoglycemia and hyperglycemia (307). At the time when the subjects were scanned, their hematocrit was not recorded. Another factor to be taken into account with regards to the acquisition is that for all subjects the velocity threshold when the crusher gradients were on, was 4cm/s. For subjects with atherosclerosis and delayed perfusion, there is a chance that the intravascular signal will not be crushed properly due to its low velocity compared to healthy volunteers.

6.5 Conclusions

In this chapter, we investigated in depth cerebral hemodynamics in IGT and T2DM using a conventional and an extended hemodynamic analysis approach. Conventional perfusion analysis captured several differences of interest, such as increased baseline GM CBF, reduced CVR and differences in ATT between groups. As part of the applied extended hemodynamic analysis, hundreds of features capturing the underlying perfusion pattern were extracted from QUASAR data.

We examined the performance of models comprising different hemodynamic feature combinations in the following classification tasks: HV vs T2DM, HV vs insulin resistance, HV vs IGT and IGT vs T2DM. Numerous metrics differed between the groups and we used t-tests to determine the significantly different features. Subsequently, we utilised a machine learning pipeline to determine optimally differentiating feature combinations by evaluating 7 possible models, each model containing a different feature combination. Due to the small dataset, overfitting was a major concern that was somewhat addressed by LOOCV. However, claims about model building and

biomarker identification cannot be made with a high degree of confidence. We determined feature combinations derived from hemodynamic curves that differ between our groups and have shown that, for the given dataset, these features can capture class-differences. Of particular interest are the features with high occurrence, especially in tasks where the optimal feature number leading to high accuracy was low.

The best models were the ones involving the unprocessed QUASAR curves (initial crushed, non-crushed signal and their subtraction). This is an indication that there is indeed a difference captured by the technique and it is not the by-product of the processing pipeline. One of our models comprised the typically quantified QUASAR features. This model demonstrated a lower accuracy compared to models incorporating the newly quantified metrics. Additionally, we have shown that the features with the highest impact in the correct classification of the subjects were not the typically quantified QUASAR features, which were only occasionally top-ranked features, being outperformed by newly evaluated curve-descriptive metrics.

The significance of our findings extends in several directions. First and most importantly, we found a distinct hemodynamic pattern for both T2DM and IGT compared to HV. T2DM differed both pre- and post-ACZ from HV whereas, interestingly, IGT at baseline had a similar pattern to HV, while post-ACZ it was dissimilar to HV. Class-separation between HV and IGT was optimal, as opposed to IGT and T2DM separation, suggesting the existence of more hemodynamic similarities between IGT and T2DM rather than between IGT and HV. Secondly, we identified metrics that can capture better the hemodynamic pattern compared to the typically quantified QUASAR metrics. Thirdly, we have shown that there is an additive advantage of having a post-stimulus acquisition and combining the metrics of both acquisitions in a single model. Finally, we have shown that QUASAR ASL, which is currently under-used as an ASL modality given its advantage of acquiring multiple signals, can capture subtle hemodynamic patterns and could potentially provide us with hemodynamic disease biomarkers.

Chapter 7:

Processing of multi-modal MR images in type-2 diabetes and impaired glucose tolerance

Abstract

Retinopathy, neuropathy and nephropathy are some of the most common complications of T2DM. In addition, patients are at a higher risk of developing Alzheimer's or having a stroke compared to the healthy population. The disease can influence both the macro and microvasculature. Studies have shown that the degree of mild cognitive impairment compared to aged-matched healthy volunteers is higher in diabetes. The disease's impact on the vasculature, complications such as stroke and its connection with cognition, are some of the main drivers for examining the diabetic brain.

MRI can provide an invaluable window into alterations occurring at both a functional and a structural level. In this chapter, we shift the focus from perfusion changes in the brain to structural and physiological changes, the latter ones connected with the velocity of the inflowing blood at the carotid level and the diffusivity of water molecules. Several techniques and pre-processing tools were evaluated and optimal suggestions are presented for brain extraction, bias field correction and segmentation; three of the most important pre-processing steps in brain MR image analysis. By using state-of-the-art techniques for structural MRI analysis we have quantified the volume of numerous structures of interest (e.g. amygdala, hippocampus), GM, WM, cerebrospinal fluid and cortical thickness. Using voxel-based morphometry, we sought to determine regions of difference between the groups without defining specific ROIs. FLAIR T2-scans were used to quantify the white matter hyper-intensity burden in our cohort using available software. PC-MRA images were used to quantify velocity of the inflowing blood at the level of the carotids. A detailed analysis of the blood velocity pattern was implemented in Matlab using an in-house developed semi-automated tool allowing for arterial vessel determination. The apparent

diffusion coefficient was quantified for structures of interest using DWI. Finally, using in-house software, the coronal maximum intensity projection of 3D TOF-MRA scans was analysed and several vasculature-descriptive metrics such as the vessel length, density and number of branching points were quantified.

The results for the T2DM patients relative to the healthy volunteers point towards: a) increased number of leukoaraiosis; b) lower carotid flow velocity at baseline and post-ACZ, c) lower number of branching points in the vasculature and d) GM differences in structures such as the thalamus, hippocampus and amygdala. The examined IGT subjects had similarities with the HV population structurally, however, they demonstrated a similar pattern to the T2DM group when carotid flow velocity was examined.

The results point towards global and localised functional and structural differences between T2DM and HV, with the pre-diabetes group demonstrating structural characteristics similar to the HV group and functional ones similar to the T2DM group.

7.1 Introduction

The ability to learn and remember, along with the speed of information processing, are the main cognitive domains influenced during late-life in patients with T2DM (308). Global and local GM atrophy patterns, volume reduction in structures such as the hippocampus, white matter lesions, lacunes and silent brain infarcts are considered end-point changes, possibly preceded by functional alterations (34). Such changes have been thoroughly investigated using high resolution T1-weighted and T2-weighted MRI scans (mainly FLAIR) and are connected with small vessel disease and cognitive decline (309). Findings, based on a large study conducted to investigate structural changes in the diabetic brain as a result of the followed treatment protocol, ACCORD-MIND (310), suggest that global and local atrophies are connected with diabetes duration and that lower GM volume is connected with cognitive decline (311). It was found that intensive glucose control was connected with reduction in the loss of GM (312). MR imaging has also been used to examine structural alterations associated with the integrity of the WM tracts, and changes focused on diffusion-related parameters, blood velocity and perfusion (33, 34).

Being a multi-purpose imaging technique, MRI allows for the extraction of information capturing a variety of structural and functional aspects of the examined organ - in our case the brain. As briefly discussed in Chapter 2, numerous MRI modalities have been devised that enable the detection of abnormalities in the brain structure, diffusion, perfusion, blood velocity and vasculature. For some modalities, it might be sufficient to visually inspect the resulting image and detect obvious alterations. For instance, when examining a T2-FLAIR scan, a neuro-radiologist can spot relatively quickly and accurately the presence of white matter hyper-intensities. When examining cerebral angiograms, prominent collateral circulation, stenosis or occlusions can be detected by carefully examining the image.

However, when the investigated changes are not eye-catching, a simple visual assessment of the scan might result in missing crucial information. For example, when a subtle global atrophy pattern exists, only an automated technique is capable of successfully capturing this information. A 3D high-resolution structural image might consist of more than 200 slices; a radiologist will have to inspect them one-by-one to segment structures of interest and detect potential abnormalities. This laborious task usually requires going back and forth in the image to validate the manual selections and is typically conducted on MPRAGE and T2-FLAIR scans. In MR Angiography, utilisation of the maximum intensity projection is quite common for detection of potential abnormalities (313).

Manual region definition is considered the gold standard for anatomical segmentation and is not confined to high resolution T1-weighted and FLAIR scans, but is also used for modalities such as PC-MRA. Numerous studies have reported high inter- and intra - observer variability when examining manual segmentations of T1 and T2-weighted scans (314, 315). Due to this variability and the time requirements for the task, significant scientific effort has been made over the last decades in developing algorithms to perform such tasks automatically. The development of automated tools for segmentation and ROI selection has the potential to facilitate, and greatly accelerate, image interpretation, while being at the same time easy to use. These tools can also boost reproducibility and potentially provide metrics that can be used for disease stage evaluation.

Processing of a high resolution anatomical scan might involve detailed cortical parcellation and ROI analysis usually centered on areas of interest such as the hippocampus (46) or other subcortical structures. Another popular approach is VBM, whereby comparison at a voxel-wise level between groups is conducted following image normalization to a common space (245). However, conventional VBM approaches are mass-univariate (248). Multivariate approaches, typically based on machine learning and regression models, are particularly popular in studies examining brain tumors and Alzheimer's dementia (249, 250). In the field of T2DM, machine learning based MRI analysis methods have not yet been tested. The analysis of the structural scan in the present study was conducted using well-established methods.

Along with the structural images used to assess atrophy patterns and cortical abnormalities, in this chapter we processed FLAIR, PC-MRA, DWI and TOF-MRA images. FLAIR images are usually analysed either manually or by using existing WM lesion segmentation tools. Here, we used one of the most popular tools for WMH segmentation, namely the lesion segmentation toolbox (238). Blood velocity was studied using PC-MRA. Findings based on the PC-MRA technique are usually presented as flow values. In T2DM and IGT, it has been found that flow and velocity at the level of the carotids is decreased. This finding is corroborated by PC-MRA and TCD studies (36, 42, 44, 53). In the present study, we conducted a detailed velocity pattern analysis based on the PC-MRA data.

Angiogram processing usually involves the construction of maximum intensity projections, which are visually inspected to detect obvious stenosis or occlusions. Automated tools for vessel segmentation are at an experimental stage (313, 316) and neuroimaging software tools have not yet incorporated angiogram analysis software. Only one study published recently has looked into angiogram-derived metrics in T2DM, which reported a lower number of branching points (192).

Our aim in the present chapter was to process the following MR modalities: High resolution T1-weighted (MPRAGE), FLAIR, DWI, PC-MRA, TOF-MRA and extract useful metrics that could be evaluated as potential disease biomarkers. For processing of the DWI, PC-MRA and TOF-MRA scans, in-house Matlab scripts were developed. The MPRAGE images were analysed

using cortical parcellation, voxel-based morphometry and a machine-learning based technique.

This chapter describes preliminary evaluation of every modality described above (as a series of sub-chapters) as an initial study of abnormalities occurring in IGT and T2DM. The goal is to gain an insight into changes of structural and physiological nature that could fuel future work especially when considered in tandem with the hemodynamic findings reported in the previous chapter.

7.2 T1-weighted (MPRAGE) scan analysis

7.2.1 Methods

7.2.1.1 Brain extraction

Two approaches were assessed for brain extraction. The first evaluated tool was FSL's BET (213). Several values were tested for the intensity threshold (f), separating brain from non-brain tissue, starting from the values suggested by Popescu et al. (317). The second approach used SPM's tissue segmentation tool. The outputs of the segmentation are tissue specific maps. In order to construct a brain mask based on the segmentation results, the generated GM, WM and CSF masks were summed up to acquire the contour of the brain tissue. The masks generated with both approaches were visually evaluated for the presence of holes; the masked brains were subsequently checked for detection of areas where part of the cortex was masked out. In such cases, morphological operations were performed locally (dilation, erosion and image filling) to correct for imperfections in the generated mask.

7.2.1.2 Bias field correction and brain segmentation

Three tools were evaluated for bias field correction and brain tissue segmentation. The first tool was FSL's FAST (318) and the second, SPM's new segment algorithm (214). Both SPM and FSL segmentation routines have BFC strategies incorporated in their pipeline and rely on GMMs for tissue segmentation. The main difference is that SPM incorporates spatial priors, whereas FSL uses Markov random fields theory to incorporate spatial

information. For the third approach, the ANT's N4 algorithm (208) was utilised for the BFC step and SFCMC (232), was used for tissue segmentation.

BFC can be applied on the masked or the non-masked images. To determine the optimal choice, the N4 algorithm was implemented using three different approaches. The algorithm was run having as an input: a) the whole image, b) a masked version of the image and c) the whole image along with the respective mask.

As described in section 3.1.4, SFCM operates in a local window, which in the default implementation is a 5x5 isotropic window (232). To identify the optimal neighbourhood size for the spatial extent of the clustering, we tested a weighted 5x5 window, no window (equivalent to simple FCM without accounting for similarities in a local neighbourhood) and isotropic 3x3, 7x7 and 9x9 windows. The MAPE was calculated for voxels within the brain mask and for voxels with ground truth GM value greater than zero.

The tissue classification problem was defined as a three-class problem, the classes being: GM, WM and CSF.

The efficacy of the aforementioned algorithms was evaluated by using simulated data from the McGill's brainweb database (<http://brainweb.bic.mni.mcgill.ca/brainweb/>). For the downloaded simulated data (involving T1-weighted and segmented GM, WM, CSF maps), the specific chosen parameters of 1mm³ isotropic voxel and 25% bias field were based on brains of healthy subjects and on manual tissue segmentation. The brainweb digital phantom is typically used to evaluate segmentation techniques (319). Metrics used to determine the accuracy of the segmentation techniques were the MAPE at a voxel wise level for GM and WM maps.

7.2.1.3 Voxel-based morphometry

Voxel-based morphometry allows for detection of brain regions that differ between groups by avoiding specific ROI determination, since it proceeds to group-wise comparisons at a voxel level. The pipeline behind VBM in FSL and SPM is highly similar. Both these techniques are mass-univariate (comparisons are conducted at a single voxel level).

In this study, FSL's pipeline was used, since fewer prior assumptions compared to SPM are utilized in the analysis. We deviated slightly from the

pipeline instructions, so that we could use the brain extracted and BFC images generated during the previous steps. The first applied pre-processing step outside the VBM FSL pipeline was bias field correction using N4. Subsequently, the images were brain extracted as per method two described in the previous section (7.2.1.1).

Following brain extraction, the FSL VBM (276) pipeline was implemented. FSL creates a GM study template using the same number of subjects from every group. This template is subsequently mirrored and a final mean GM template is created and used as a registration target. There are two transformation options for the generation of the template, linear or non-linear; in the present study the non-linear option was used and the results were visually inspected using FSLeyes. Subsequently, this template was used as a registration target for normalization of the individual GM PV maps to a common space (MNI).

Group-wise comparisons were conducted for the registered GM partial volume maps. The registered maps are typically smoothed to render them more normally distributed so that statistical comparisons can take place without violation of the normality assumption. In the present study two Gaussian kernels were evaluated: a) $\sigma=2$ and b) $\sigma=3$. The implementation of two kernels served as a means to evaluate whether the extent of the observed effects was larger with increasing smoothing.

The constructed GLM model comprised analysis of variance (ANOVA) (3 groups HV, IGT, T2DM) tests with age and sex as covariates. These covariates were mean centered, by subtracting the study population mean from every subject. Registration to the generated study-specific template involves a Jacobian modulation step, hence correction for global differences of the brain size is a redundant step. The generated model was as in figure 7.1 and was constructed using detailed published instructions, part of the FSL VBM (276) and FSL GLM (320) guides.

The regions of difference were detected using the resulting thresholded p-value maps and the labeled Harvard-Oxford cortical and subcortical atlases with 2mm thickness and 25% threshold provided as part of the FSL software. Regions of difference were detected using a dedicated Matlab script.

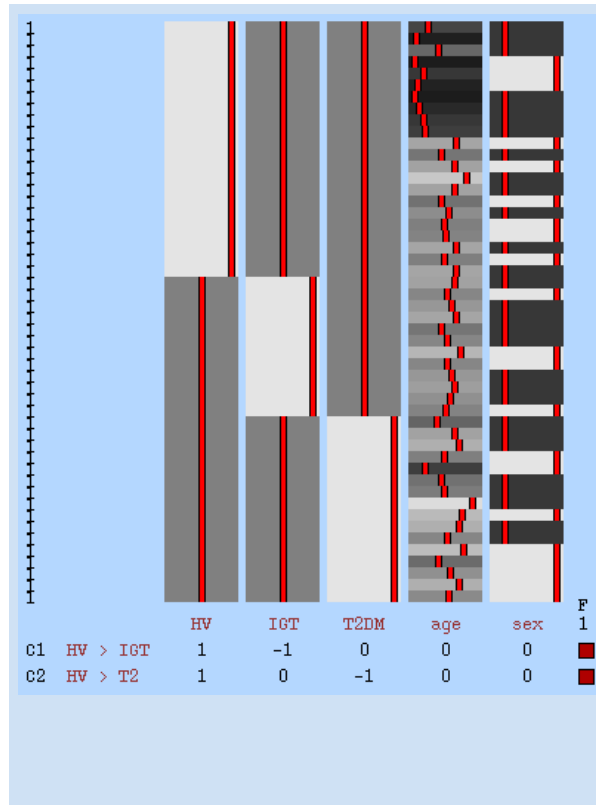


Figure 7.1: **GLM generated using FSL's dedicated tools.** Two covariates were used for the three groups.

VBM was run with the TFCE option on (321) and 5000 permutations accounting for multiple comparisons, a combination which has demonstrated optimal performance according to the FSL documentation (276). The analysis was run for 16 HV, 12 IGT subjects and 16 patients with T2DM (1 discarded due to poor image quality). New age mean for the T2DM group was 54.4 ± 11.8 years.

7.2.1.4 Freesurfer analysis

Freesurfer operates in a conceptually different way compared to the rest of the popular neuroimaging software. The 3D brain volume is transformed to a 2D cortical surface. This surface consists of triangles (described by vertices and edges), as opposed to the standard Cartesian image representation in 3D. This surface is subsequently inflated, turning into a sphere. The idea is that this sphere will be similar amongst subjects, so it can be used for registration to and from an atlas-sphere by aligning the gyri and sulci. Subsequently, this sphere is used for cortical parcellation based on an existing atlas (203, 322). The

execution time of “recon-all”, the command used for detailed structural analysis is, on average, 17 hours depending on the available processing power. The preprocessing steps implemented in this 17h window involve amongst others: motion correction, normalization to the MNI space, intensity normalization, neck and skull stripping, segmentation, tessellation and sphere inflation and cortical parcellation (323) and are described in detail in the Freesurfer online guide (<https://surfer.nmr.mgh.harvard.edu/fswiki/recon-all>). One of the most important outcomes of the analysis, unique to the Freesurfer pipeline, is the cortical thickness measure. Additionally, PV maps are generated and regional volumes of cortical and subcortical structures of interest are quantified.

Here, we report the values for cortical thickness, GM, WM, CSF, total intracranial volume, normalized values for GM, WM and CSF, the volume of structures of interest and more specifically the thalamus (RL), amygdala (RL), hippocampus (RL), brainstem, caudate, putamen and pallidum. Values were extracted from the “aseg.stats” file, one of the main outputs of the Freesurfer analysis. Additionally, generated masks for every structure were used to calculate volume structures. To account for gross differences in the head and brain size between the subjects, GM, WM and ventricular volume were divided by the total intracranial volume, as calculated during the Freesurfer analysis. The same step was followed for all the subcortical structures.

7.2.1.5 Machine learning approach

Utilising machine learning-based approaches for detection of patterns of difference has the benefit of being multivariate compared to morphometric approaches (248). In this chapter, we used a pipeline similar to the one described in Chapter 6. Comparisons were conducted for GM PV maps. The T1 MPRAGE scans were normalized to the MNI space using an affine transformation, implemented in ITK-SNAP. These images were first segmented to their native space using SFCM; the transformation matrix generated in the previous step was used for their registration to the MNI using for this registration the c3d software. The registered PV maps were smoothed using a Gaussian filter to render them more normally distributed ($\sigma=1.5$).

The registered GM and WM maps were down-sampled giving rise to images comprising 23x28x23 voxels (250). T-tests were implemented to keep

only the significantly different voxels. Subsequently, SVM-RFE was implemented to evaluate the weight of every voxel in the correct classification of the subjects. This pipeline is a simplified version of (250). In their study, direct neighboring voxels to the voxels with the higher weights identified as part of the feature ranking step were also incorporated in the analysis (even if they did not differ significantly between the groups), addressing one of SVM's disadvantages, which is that it does not incorporate spatial information in the classification task.

7.2.1.6 Statistical comparisons

The groups were compared initially using binary comparisons, either by t-tests or using the non-parametric equivalent (Wilcoxon rank sum test) when normality assumptions were violated. Binary comparisons were conducted in Matlab. For 3-group comparisons one-way ANOVA, or its non-parametric equivalent, the Kruskal Wallis test, was used when ANOVA assumptions were violated. These comparisons were conducted using SPSS. The Benjamini-Hochberg false discovery rate (FDR) methodology (324) was used to correct for multiple comparisons using a dedicated Matlab function.

7.2.2 Results

7.2.2.1 Brain extraction

Brain extraction results using FSL's BET tool were not consistent. The skull was removed along with portions of GM an effect that could impact the subsequent registration process and VBM analysis (figure 7.2). Different threshold values were tested but there was not a single value providing consistently good results. The results shown in figure 7.2 are for $f = 0.1$ which is a very low threshold (maximum: $f = 0.5$, minimum: $f = 0$) for the separation of brain and non-brain tissue.

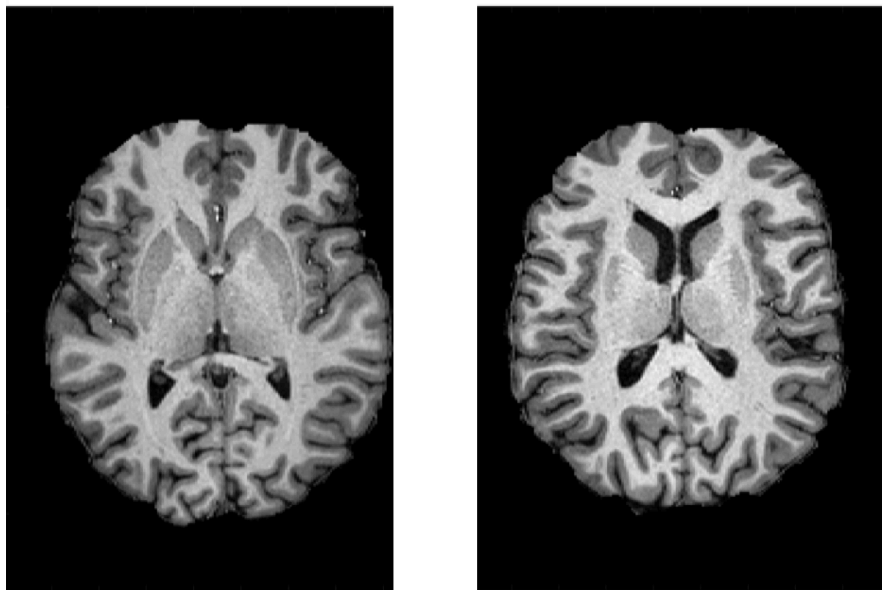


Figure 7.2: Example results for FSL's BET tool using bias field and neck cleanup mode with a value of $f=0.1$. The algorithm cuts part of GM in the frontal part, an issue which would influence the subsequent registration process and CBF calculation.

The effects were worse when non-healthy individuals were evaluated. Especially for diabetic subjects with enlarged ventricles, part of the brain filled with CSF was masked out and classified as background. This could greatly impact subsequent analysis especially in a batch mode as is usually the case in VBM. In figure 7.3 a representative case is shown from one such individual for whom BET failed. The approach based on SPM's segmentation tool was chosen for the subsequent analysis since it demonstrated more stable performance (figure 7.4; same individual as in figure 7.3).

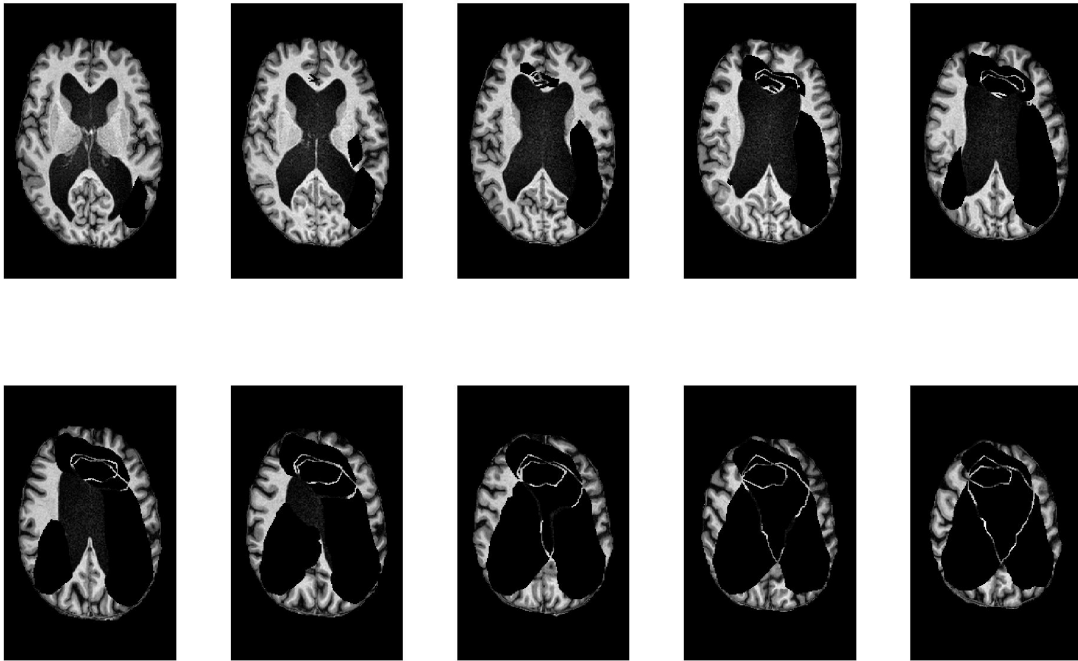


Figure 7.3: Failure of BET in a single subject with enlarged ventricles.

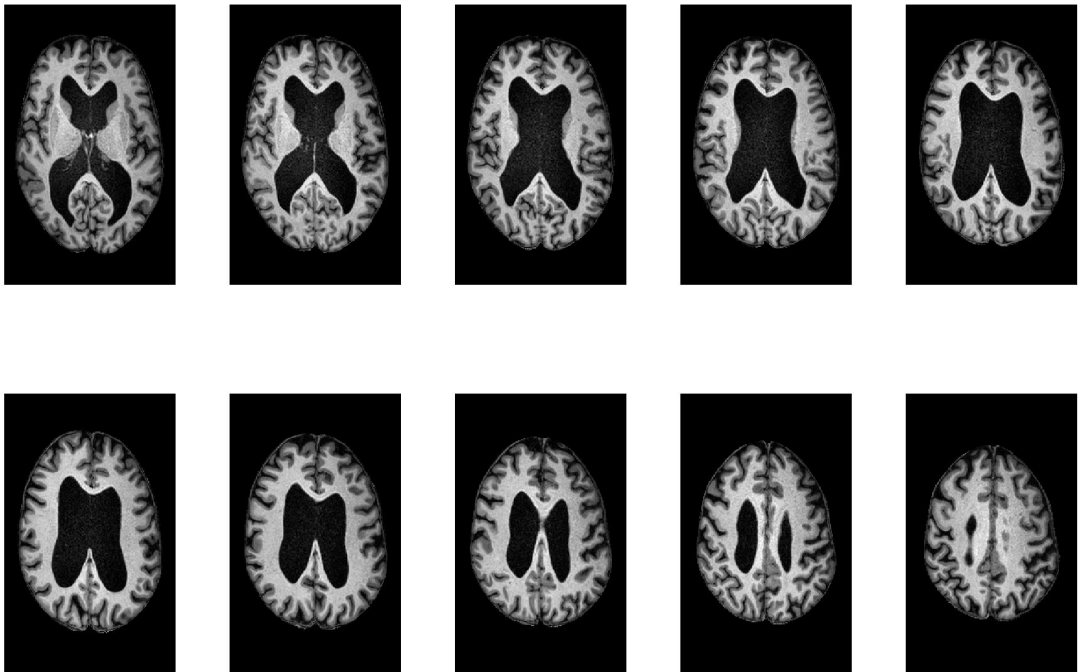


Figure 7.4: Successful brain extraction using SPM and minor dilation and filling.

7.2.2.2 Bias field correction and tissue segmentation

N4 bias field correction was implemented in three different ways to identify the optimal implementation with regards to the input data in the algorithm. These were: unmasked brain, masked brain and unmasked brain along with the mask. The results were as in table 7.1.

Table 7.1: GM and WM MAPEs for the three examined approaches for N4 BFC.

	N4 unmasked	N4 masked	N4 with mask
MAPE GM	23.56%	26.00%	43.36%
MAPE WM	13.37%	15.79%	19.70%

Mean absolute percentage errors for the segmentation process were calculated for GM and WM. In table 7.2 the results are shown for SPM, FSL and N4 unmasked combined with 6 different SFCM windows. Lower errors were recorded for both GM and WM with the W2 (isotropic 3x3) and W3 (isotropic 5x5) windows. With larger kernels (W5 - 7x7 and W6 - 9x9) the errors were increased (table 7.2). In figure 7.5 a representative GM slice is presented segmented with the evaluated techniques along with the associated error map based on the ground truth segmentations.

Table 7.2: MAPEs (%) for GM and WM for voxels belonging in the brain mask (not necessarily in the ground truth GM cluster) and for voxels belonging in the GM cluster based on the ground truth for all examined segmentation techniques.

MAPE	SPM	FSL	W1	W2	W3	W4	W5	W6
GM mask>0	46.49	41.62	26.96	23.31	23.56	23.54	24.12	24.57
GM GTGM>0	72.85	65.30	42.53	36.85	37.24	37.20	38.11	38.80
WM mask>0	18.26	16.12	16.07	13.43	13.37	13.51	13.48	13.54
WM GTWM>0	42.52	37.54	37.44	31.31	31.16	31.49	31.41	31.57

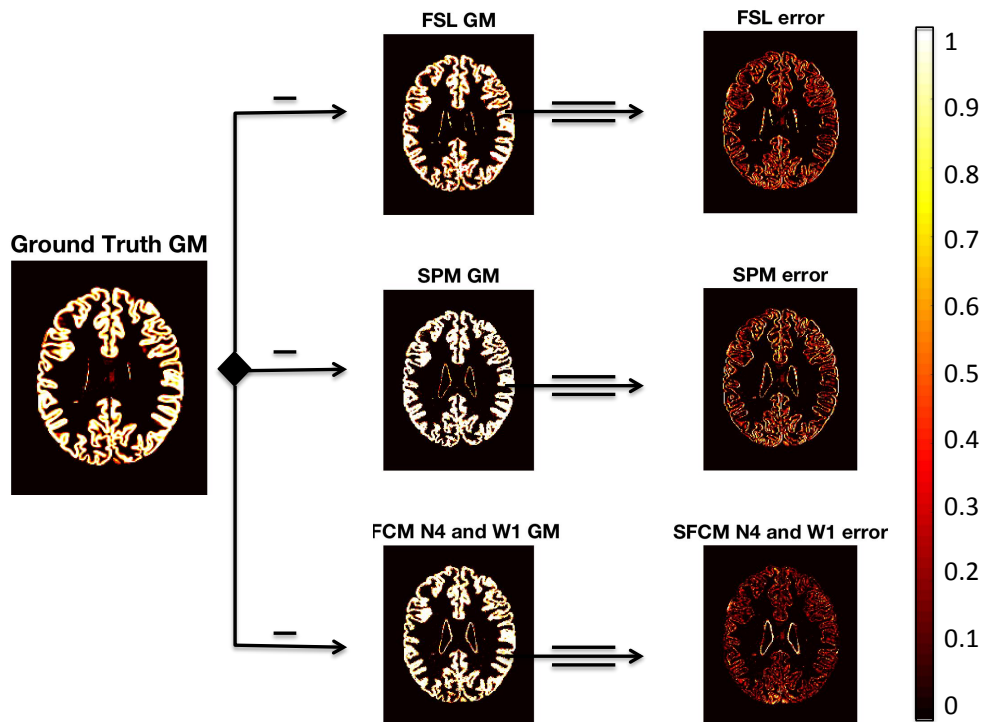


Figure 7.5: Segmentation results from a representative simulated slice. Generated GM maps along with their associated error maps are shown calculated based on the brainweb ground truth data.

7.2.2.3 Voxel base morphometry

Following F-tests (ANOVA) analysis the first contrast, designed to detect voxel-wise differences between HV and IGT did not reveal any significantly different clusters with both evaluated Gaussian smoothing kernels. The second contrast designed to detect changes between HV and T2DM patients with a p-value threshold of 0.05 and smoothing level of $\sigma = 3$, revealed that 8673 voxels were significantly different. With a smoothing level of $\sigma = 2$, the number of significantly different voxels was 7663 (figure 7.6).

T-test analysis unraveled that the differences are driven by higher values in the healthy volunteer group. The regions of difference as identified by using the labeled Harvard- Oxford cortical and subcortical atlases were:

- **subcortical regions identified with both $\sigma = 2$ and $\sigma = 3$:** Left cortical WM, left cerebral cortex, left lateral ventricle (LV), left caudate, left putamen, brain-stem, left hippocampus, left amygdala, left accumbens, right cortical WM, right cerebral cortex, right LV, right caudate, right thalamus, right putamen, right hippocampus, right pallidum, right

amygdala and right accumbens. **Left pallidum** was only identified with the $\sigma=3$ kernel.

- **cortical regions identified with both $\sigma = 2$ and $\sigma = 3$:** Frontal Pole, Insular Cortex, Temporal Pole, Superior Temporal Gyrus – anterior division, Middle Temporal Gyrus – anterior division, Inferior Temporal Gyrus – posterior division, Inferior Temporal Gyrus – temporooccipital part, Lateral Occipital Cortex – inferior division, Intracalcarine Cortex, Subcallosal Cortex, Cingulate Gyrus - posterior division, Precuneous Cortex, Cuneal Cortex, Frontal Orbital Cortex, Parahippocampal Gyrus - anterior division, Lingual Gyrus, Temporal Fusiform Cortex - anterior division, Temporal Fusiform Cortex - posterior division, Temporal Occipital Fusiform Cortex, Occipital Fusiform Gyrus, Planum Polare. The **Occipital Pole** was detected as a region of difference only with the $\sigma=3$ kernel.

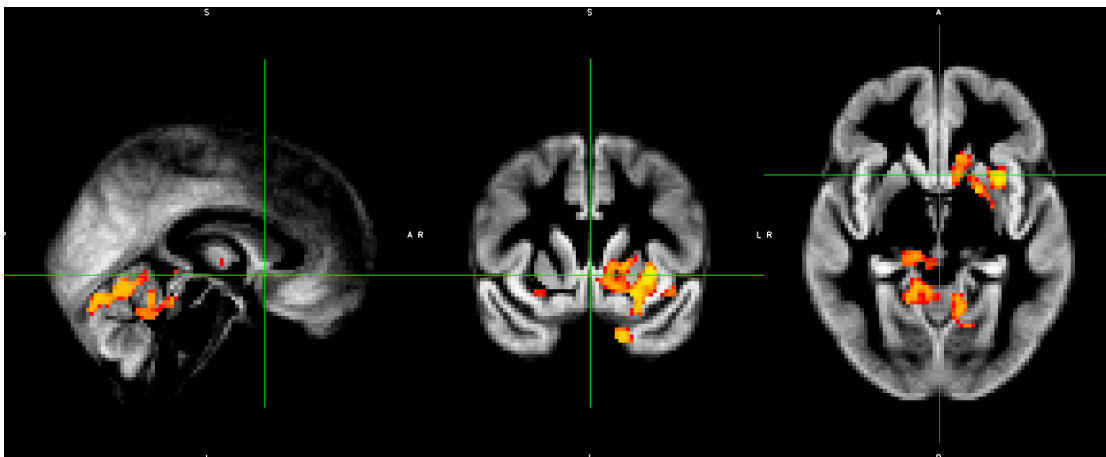


Figure 7.6: **VBM representative results with 2mm smoothing kernel.** The screenshot is taken from FSLeves.

The percentage of the volume for each of these structures differing between the groups was determined. Results are reported for structures for which more than 5% of their total volume differed between the groups:

- **$\sigma = 2$ kernel:, subcortical regions:** Left caudate (28.3%), left putamen (40.55%), brain-stem (5.3%), left hippocampus (10.9%), left amygdala (79.4%), left accumbens (78.7%), right putamen (28.4%), right hippocampus (12.1%), right caudate (9.0%) and right amygdala (36.9%).
- **$\sigma = 2$ kernel, cortical regions:** Insular cortex (5.6%), Temporal Pole (8.2%), Cingulate Gyrus-posterior division (5.9%), Frontal Orbital Cortex

(5.5%), Parahippocampal Gyrus - anterior division (37.1%), Lingual Gyrus (11.4%), Temporal Fusiform Cortex - posterior division (10.2%), Temporal Occipital Fusiform Cortex (11.8%) and Occipital Fusiform Gyrus (6.5%).

- **$\sigma = 3$ kernel, subcortical regions:** Left caudate (28.1%), left putamen (46.4%), brain-stem (7.0%), left hippocampus (15.2%), left amygdala (86.6%), left accumbens (78.7%), right caudate (7.8%), right putamen (21.1%), right hippocampus (9.6%) and right amygdala (39.3%).
- **$\sigma = 3$ kernel, cortical regions:** Insular Cortex (9.3%), Temporal Pole (11.3%), **Superior Temporal Gyrus –anterior division (6.5%), Middle Temporal Gyrus –anterior division (7.6%), Inferior Temporal Gyrus - posterior division (6.1%),** Cingulate Gyrus - posterior division (6.8%), Frontal Orbital Cortex (6.3%), Parahippocampal Gyrus - anterior division (41.1%), Lingual Gyrus (12.3%), Temporal Fusiform Cortex - posterior division (12.4%), Temporal Occipital Fusiform Cortex (11.2%), Occipital Fusiform Gyrus (6.3%) and **Planum Polare (5.3%)**.

Highlighted regions are the ones that appeared as significant only in one of the two examined kernels.

7.2.2.4 Tissue volume quantification

The reported results in this section are based on the N4 BFC and SFCM clustering combination for segmentation and are as in table 7.3, for our cohort.

Table 7.3: Tissue volume (normalized for total brain volume and non-normalized) for GM, WM and CSF calculated using N4 BFC and SFCM clustering.

	HV	IGT	T2DM
GM volume (cm³)	801.02±73.59	812.51±57.63	765.50±86.21
WM volume (cm³)	647.27±71.34	686.95±65.05	630.90±119.15
CSF volume (cm³)	280.10±84.01	295.18±56.4	300.84±97.11
Normalized GM	0.46±0.02	0.45±0.02	0.45±0.03
Normalized WM	0.37±0.03	0.38±0.03	0.37±0.04
Normalized CSF	0.16±0.04	0.16±0.03	0.18±0.05

None of the calculated values differed significantly between the groups.

7.2.2.5 Freesurfer analysis

The Freesurfer analysis results are presented in 3 tables (tables 7.4-7.6). In the first table, means for GM, WM, CSF, total intracranial (IV) and brain volume are shown for every group. In the second table, the volume of important subcortical structures is presented (additional results are tabulated in the Appendix2 – table A7.1), and in the final table, the cortical thickness values for the right and left hemisphere are reported.

Table 7.4: GM, WM, CSF, intracranial volume and total brain volumes calculated using Freesurfer.

	HV (cm³)	IGT (cm³)	T2DM (cm³)
Cortical GM	436.8±40.4	446.8±40.7	418.5±49.2
Subcortical GM	57.5±5.4	59.5±4.3	55.7±6.9
Cortical WM	448.1±52.1	471.6±52.7	428.9±84.2
CSF	0.9±0.2	1.1±0.3	1.0±0.3
IV volume	1344.8±178.3	1472.2±202.7	1380.3±280.4
Brain volume	1085.4±93.9	1139.7±99.1	1053.4±139.8

Table 7.5: Volume of subcortical structures of interest for the three groups under consideration.

	HV (cm³)	IGT (cm³)	T2DM (cm³)
Brainstem	20.8±2.2	21.3±2.1	19.5±2.7
Left hippocampus	4.1±0.5	4.0±0.3	3.9±0.4
Left lateral ventricles	7.9±4.1	13.0±7.2	14.1±10.6
Left pallidum	1.4±3.2	1.5±0.2	1.2±0.3
Left thalamus	7.4±1.0	7.4±0.8	7.4±1.2
Right hippocampus	4.2±0.4	4.3±0.4	4.0±0.5
Right lateral ventricles	7.3±3.2	10.5±4.1	12.7±7.9
Right pallidum	1.6±0.2	1.7±0.2	1.5±0.3
Right thalamus	6.4±0.8	6.7±0.6	6.2±1

The cortical thickness for the left and the right hemispheres for the considered groups, as calculated during the Freesurfer analysis was as follows:

Table 7.6: Cortical thickness for the left and the right hemisphere as calculated using Freesurfer

	HV	IGT	T2DM
Left hemisphere	2.37±0.08	2.33±0.08	2.33±0.13
Right hemisphere	2.37±0.09	2.34±0.08	2.32±0.12

When performing ANOVA analysis, the differences were significant for: right LV ($\chi^2(2) = 7.386$, $p = 0.03$), normalized right LV ($\chi^2(2) = 6.862$, $p = 0.03$) and left pallidum ($\chi^2(2) = 6.17$, $p = 0.05$). Following multiple comparison correction using FDR none of the differences remained significant.

7.2.2.6 Machine learning approach

The scans for every subject were registered to the MNI space using ITK-SNAP. Subsequently a universal brain mask was generated and applied to all scans. For every classification task, the voxels contributing towards optimal class differentiation were plotted using the following color coding: pink - voxels providing optimal classification performance, yellow – second best performance, green – third best performance and dark red all the different voxels – up to 500.

HV- T2DM comparison

The number of significantly different voxels for the high-resolution smoothed GM maps between the two groups was 39060 (total 265500 voxels). Following downsampling, the mean number of non-zero voxels was 4268 and the number of significantly different voxels was 851. Maximum classification accuracy was 90.6%, obtained with a minimum of 44 and a maximum of 75 voxels. Classification accuracy was consistently higher than 74% with an increasing number of voxels. Accuracy as a function of the number of voxels along with the voxels contributing towards optimal class differentiation is plotted in figure 7.7.

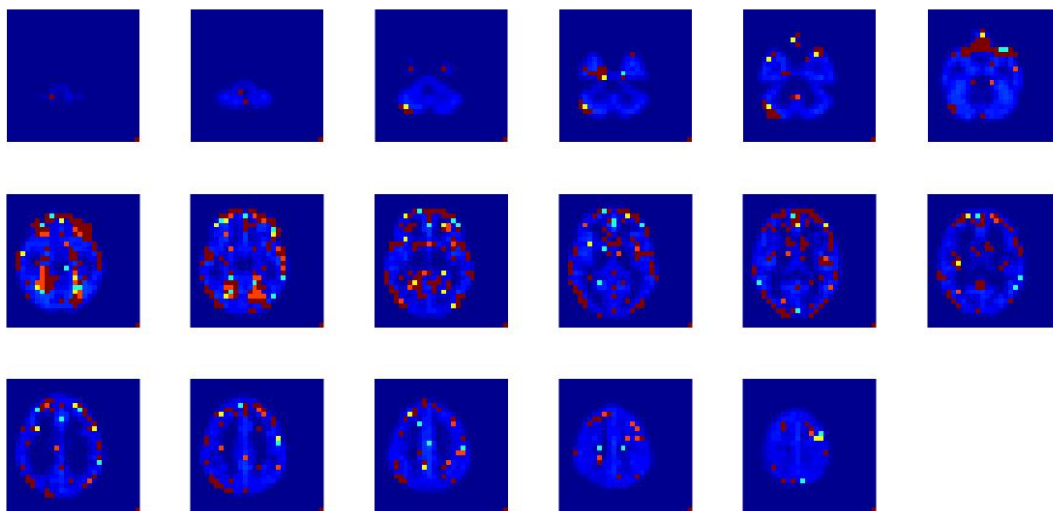
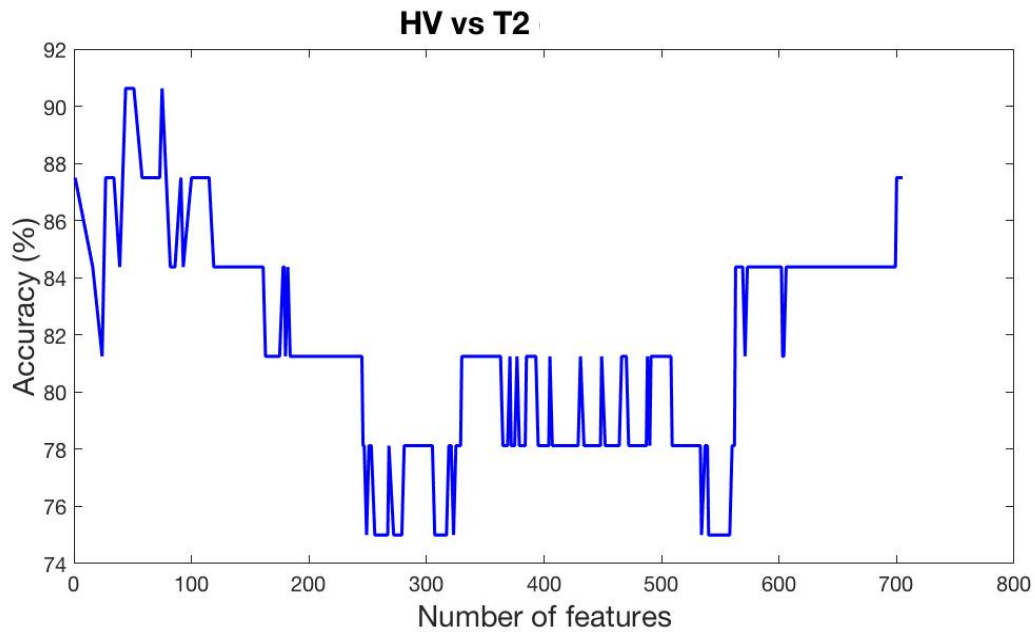


Figure 7.7: Classification accuracy for the HV vs T2DM task with an increasing number of features/ voxels accompanied with a figure showing the voxels contributing towards optimal class separation.

HV vs IGT

In the high-resolution scenario, 23271 voxels were significantly different. Following downsampling, 541 voxels differed. Maximum accuracy of 100% was achieved, with minimum 18 and maximum of 60 voxels. Results for the task are plotted in figure 7.8.

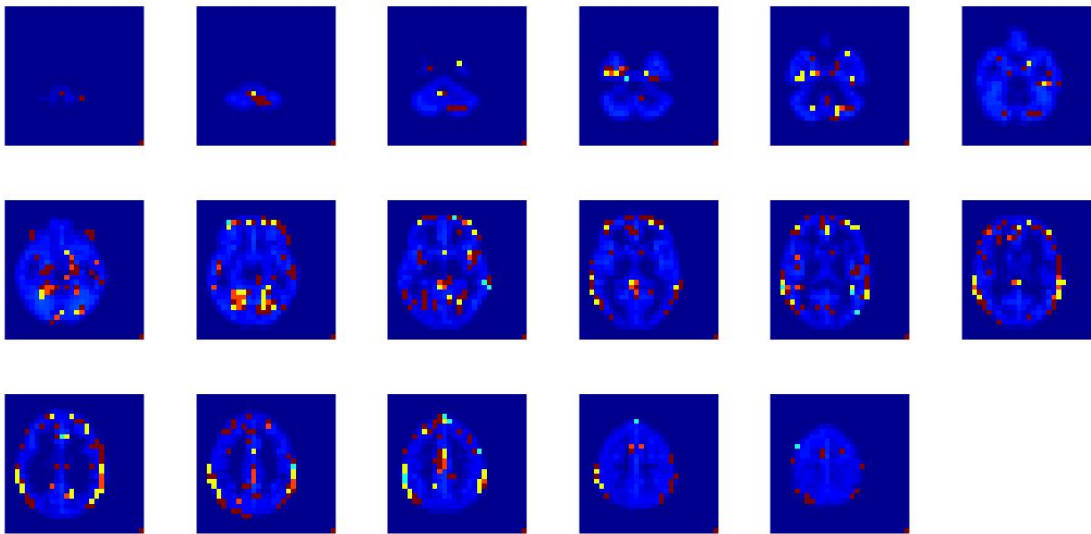
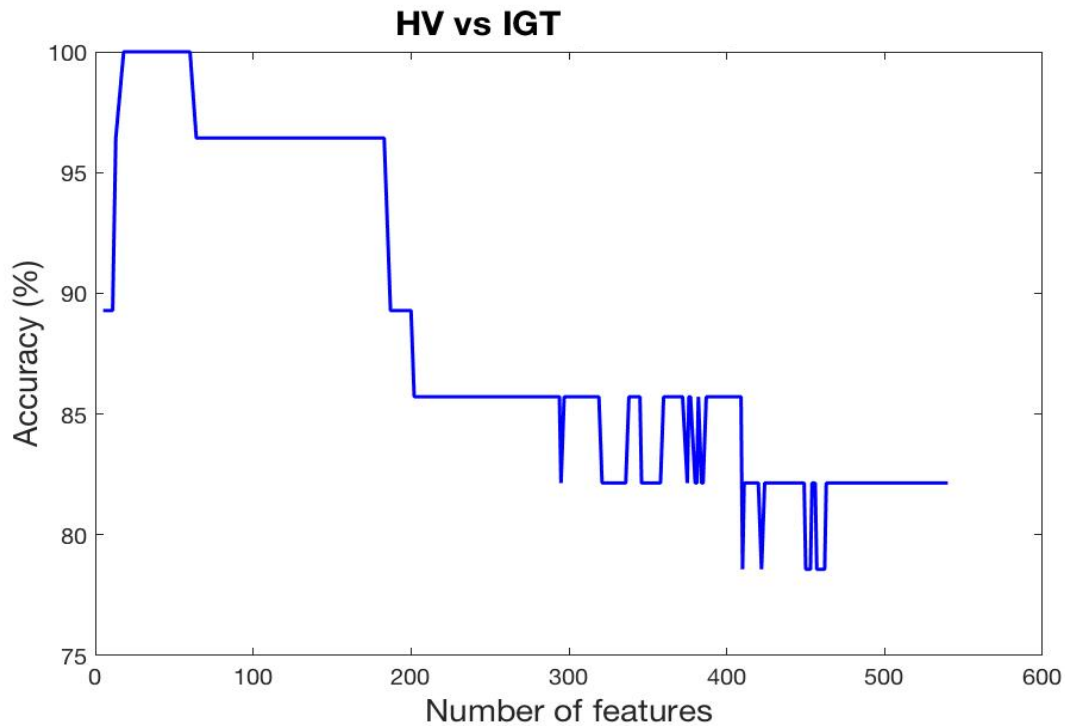


Figure 7.8: Classification accuracy for the HV vs IGT task with an increasing number of features/ voxels accompanied with a figure showing the voxels contributing towards optimal class separation.

IGT vs T2DM

In the high-resolution scenario, 11970 voxels were significantly different. Following downsampling, 184 voxels differed. Maximum performance of 100% was achieved with minimum 17 and maximum 50 voxels. Accuracy and voxels contributing towards optimal class differentiation are shown on figure 7.9.

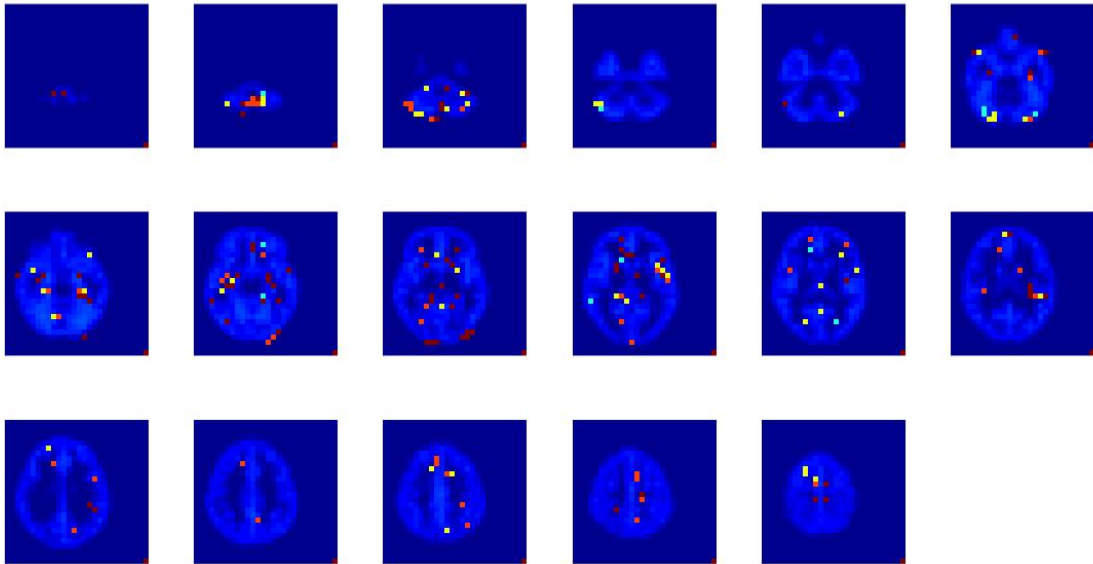
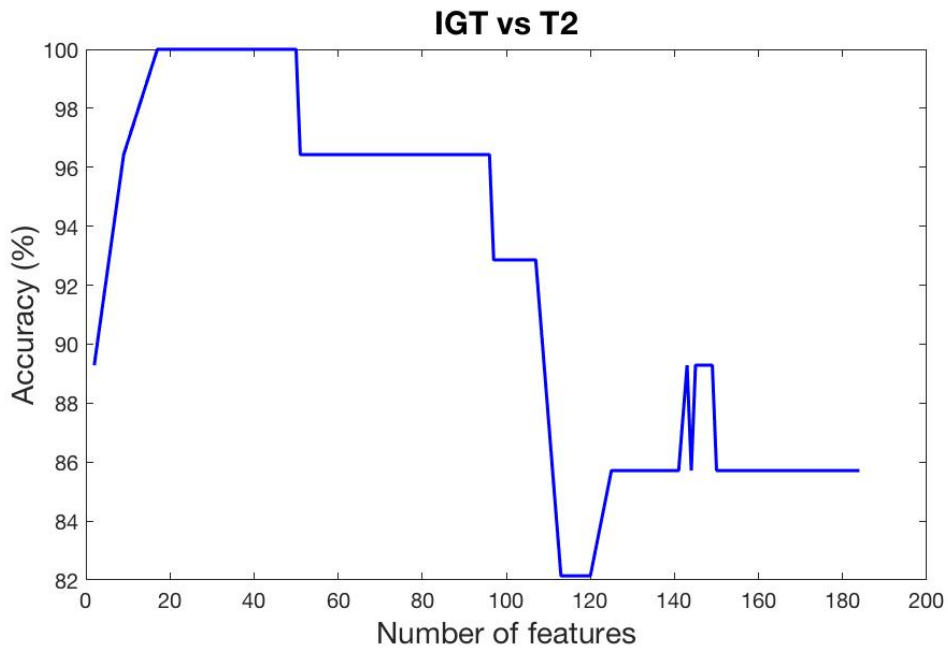


Figure 7.9: Classification accuracy for the T2DM vs IGT task with an increasing number of features/ voxels accompanied with a figure showing the voxels contributing towards optimal class separation.

7.2.3 Discussion

Optimal brain extraction, bias field correction and segmentation techniques were identified.

In this sub-chapter, processing of the acquired high-resolution T1-weighted scan included in this study was discussed. Initially, we investigated three of the most important pre-processing approaches; brain extraction, bias field correction and segmentation. It was shown that brain extraction using an automated tool, such as the evaluated BET algorithm, can fail when major abnormalities are present in the brain, for example very intense atrophy or extensive enlargement of the ventricles. The brain extraction result needs to be visually inspected every time to reassure that this pre-processing step succeeded before proceeding to further processing. Residual skull, or loss of tissue, can greatly distort the results when proceeding with further processing. Following extraction, the masked brain can subsequently be used for segmentation, bias field correction and potentially for partial volume correction. Failure at an early pre-processing step can propagate through the whole analysis and remain undetectable if it is not captured right after the brain extraction task. The scenario of an undetected brain extraction failure can be particularly troublesome when VBM or machine learning approaches performing voxel-wise comparisons are implemented, since the erroneous masked brains will be averaged and compared with error-free images.

The evaluated segmentation tools were those included in FSL and SPM and a method based on a combination of N4 BFC and SFCM clustering. The calculated MAPEs indicate that the combination introduced in this work outperformed every other. By examining the error maps, we can see that especially for the pixels at the edges of different tissue types SFCM outperforms the other methods. This finding is of particular importance since FSL and SPM are two of the most commonly used neuroimaging processing software tools. The comparison between them revealed that FSL has a better performance compared to SPM and both of them have an inferior performance compared to the introduced segmentation approach. The optimal weighting windows for the SFCM algorithm were the 3x3 and 5x5 isotropic ones leading to lower errors in both GM and WM. No weighting (simple FCM) resulted in higher

errors, whereas a higher degree of weighting (7x7 and 9x9 windows) was also connected with an increase in the MAPEs potentially due to the increased smoothing effect.

The segmentation methods were evaluated using a commonly used digital phantom (Brainweb) and the ground truth segmentation maps provided along with it. This phantom was based on healthy individuals and not on a disease population. In the future, these segmentation tools could be evaluated using disease phantoms as well. In the past, SFCM clustering has been compared with other clustering methods and FCM variants (325), however, there is no published study to our knowledge comparing it to typically used neuroimaging software segmentation algorithms. Its recorded performance combined with N4 BFC, especially when considering the fact that it is assumption-free, proves that the technique holds great potential and could be the method of choice for tissue segmentation.

Voxel-wise comparisons detected differences between HV and T2DM subjects.

Global and localized gray matter atrophies, a consistent finding in neuroimaging studies focused on type-2 diabetes (33, 38, 40) were not identified in this study when examining Freesurfer-derived volumes of structures of interest. The same finding was observed when tissue volume quantification was conducted with the optimal segmentation protocol described previously. Our findings are in line with (43, 54), as in these studies, no significant differences were found in WM, GM or subcortical structure volumes between T2DM and HV. Our findings agree partially with a study by Dale et al. (326), where when comparing cognitively normal T2DM patients with HV, no differences were found for the hippocampal volume, however lower cortical thickness was detected.

To investigate patterns of difference at a voxel-wise level without defining explicit ROIs, the FSL VBM analysis was utilised. The results indicate that significant differences exist only between the HV and T2DM groups. The analysis was run with two Gaussian smoothing kernels to investigate the effect of additional smoothing on the observed results. The applied kernels of $\sigma = 2$ and $\sigma = 3$ are typically used in Neuroimaging studies and recommended in the

FSL VBM guidelines. F-tests were used for the 3-group comparison and subsequent t-tests indicated that the identified differences between HV and T2DM were driven by lower values in the T2DM group pixel-wise intensities. To identify changes in structures of interest, the areas for which the percentage of the voxels differing between the groups was more than 5% were reported. Interestingly, a larger smoothing kernel identified an additional 2 structures as areas of difference between the groups, as opposed to a smaller kernel. Areas of difference identified with both kernels included the caudate (L-R), putamen (L-R), hippocampus (L-R), amygdala (L-R) and the left accumbens. When considering cortical regions, the temporal gyrus was identified as an area of difference only with the $\sigma=3$ kernel. This result is of particular importance, since it suggests that additional smoothing can imply that structures not differing are brought up as different due to additional smoothing. On the other hand, it could mean that a smaller kernel masks out differences since individual variations might prevail. Lack of standardization for these procedures is likely to yield these kind of results.

Studies using VBM in T2DM have found differences in numerous regions. Our results agreed partially (fusiform and cingulate gyri) with a study by Zhang et al. (38) where VBM with a larger smoothing kernel (8mm FWHM equivalent to a $\sigma = 3.5$) was used. The results are in agreement with (199), who found using SPM VBM differences in the caudate (L-R), putamen (L-R), left amygdala and left thalamus. A study by Moran et al. (40), with a big study population (350 T2DM patients, 363 HV), has shown reductions in GM, WM, hippocampal volume and GM loss in numerous areas of interest. The population though was not cognitively asymptomatic. In this latter study, SPM VBM and a cluster approach was used, as opposed to the utilised FSL VBM combined with TFCE analysis in the present study. Regions of agreement between our study and the Moran et al. study were the parahippocampal gyrus, left putamen, left caudate, cingulate gyrus and inferior temporal gyrus. Since our cohort was neurologically asymptomatic, these could be early changes occurring in diabetes, preceding cognitive decline.

For the machine learning approach, low-resolution maps were used in a machine learning context and demonstrated a good performance for every examined classification task. Optimal classification was achieved with only a

few voxels. When more voxels were used, the identified areas of difference between normoglycemic and hyperglycemic groups were at the periphery of the brain and around the ventricles; the pattern was similar for both the IGT and T2DM groups when compared with the HV cohort. A higher ventricular volume in the IGT and T2DM groups can explain why voxels around the ventricles are brought up as optimal. However, identification of voxels at the periphery of the cortex could imply two things; either group-differences are driven by changes at the edges of the cortex, or mis-registration of the scans led to identification of these particular voxels. To resolve this, a larger cohort needs to be examined with the available method and more robust non-linear registration methods should be applied. Only a few voxels differed between the IGT and T2DM groups, however, they were sufficient to provide good classification. The classification accuracy was 100% for the HV vs IGT task and 91% for the HV vs T2DM task.

The utilized sample-size in the present study is small but could provide useful insight on changes occurring in the examined groups if interpreted with caution. The observed results and areas of difference could be attributed to the sample idiosyncrasies or to other factors (e.g. age) and existing co-morbidities which were not accounted for. Several of our findings are in line with existing literature. Other findings will have to be validated using a larger study population. Especially the machine learning approach, as despite the utilization of a technique optimal for small datasets, there could still be overfitting. Processing of this small cohort unveiled several structural differences between the groups which is a promising observation. However, we will refrain from drawing conclusions about structural alteration occurring in IGT and T2DM and suggest that these initial findings can serve as a basis for further exploration.

Overall, in this sub-chapter, optimal techniques for brain extraction, bias field correction and segmentation were described. When analysing the structural scans of the available cohort using an ROI-based volumetric analysis, no regions emerged as differing significantly between the groups. However, detailed voxel-wise comparisons not confined to specific ROIs revealed differences between the HV and T2DM cohorts (VBM, machine learning approach) and the HV- IGT groups (machine learning approach).

These observations are potentially of great importance and the described approaches and analysis methods can form the basis for a detailed analysis in larger cohorts.

7.3 T2-weighted (FLAIR) processing

7.3.1 Methods

7.3.1.1 *White matter hyper-intensity detection*

Non-physiological hyper-intense regions in WM described as white matter hyper-intensities (WMH) or leukoaraiosis are a common finding in elderly subjects and subjects with cardiovascular risk factors and are connected with an increased risk of stroke and dementia (327). In T2DM, findings have been inconsistent since not every study has found a direct correlation between WMH and diabetes (33). The hyper-intense regions in WM are connected with increased water content in the tissue and myelin destruction and are thought to result from prolonged hypo-perfusion (237). Evaluation of the WMH burden can be conducted either by using visual assessment, based on scales such as the Fazekas scale (328), or by using automated tools to quantify the hyper-intensity volume. WMH segmentation is a challenging task since the performance of the existing algorithms greatly varies, depending on the examined disease, the utilised scanner type and the applied sequence variants (237).

Tested techniques for automated WMH segmentation were: a) the Wisconsin White Matter Hyperintensities Segmentation toolbox (329); b) a technique based on FCM clustering (232), similar to the one described previously for tissue segmentation in the MPRAGE image; and c) the Lesion segmentation toolbox in both its implementations (238).

The first two approaches had a suboptimal performance, resulting in extensive regions being selected as hyper-intense, so we proceeded with our analysis using the lesion segmentation toolbox. The toolbox by Schmidt et al (238) has two implementations; one based solely on the FLAIR scan (lesion prediction algorithm - LPA) and one based on a combination of FLAIR and a T1-weighted scan (lesion growth algorithm – LGA). The LPA relies on a binary classifier based on logistic regression, which has been trained on 53 MS patients and is applied at a voxel-wise level. The LPA was found to perform

better than the LGA for our dataset, so for the analysis of our cohort LPA was used.

7.3.1.2 FLAIR textural analysis

Due to the high in-plane resolution and sensitivity to WMHs, FLAIR images have the potential to provide rich textural information. This information can be extracted from ROIs and the whole brain. For the present analysis, the image was divided into sub-regions, having as a central point the centre of every slice. The ROIs were as in figure 7.10.

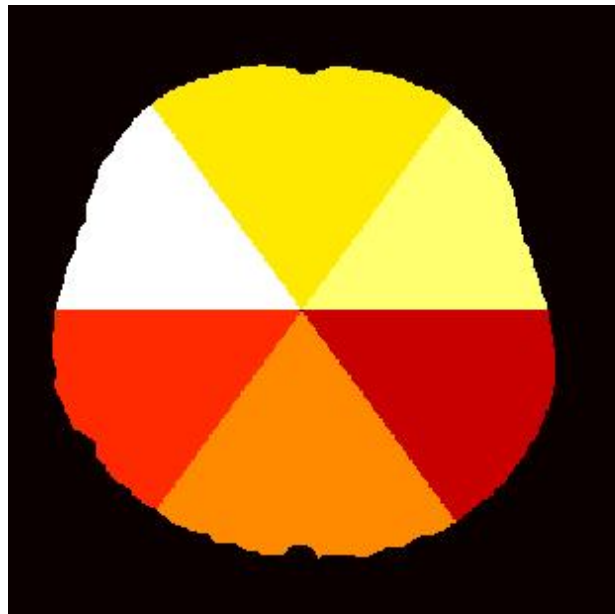


Figure 7.10: Definition of the ROIs used for textural analysis.

From these 6 ROIs, Gabor textural features (330) and features derived from the gray-level co-occurrence matrix (253) were determined, these were: energy, homogeneity, correlation and contrast. Additionally, the mean, standard deviation, kurtosis and skewness from the defined ROIs were quantified. Overall 70 rotationally invariant Gabor features were built (255, 269) in 7 wavelengths ($2\sqrt{2}$, 4, $4\sqrt{2}$, 6, $6\sqrt{2}$, 8, $8\sqrt{2}$) and 7 orientations (0,30, 60, 90, 120, 150, 180) with a spatial aspect ratio of 0.5. Each FLAIR image was subsequently filtered with every unique Gabor filter (49 overall) separately and the magnitude and phase images were derived.

Gabor features can be made shift and rotationally invariant, which are both desirable properties when conducting textural analysis. To achieve this, we

followed the steps suggested by Riaz et al. (331). Mean and standard deviation of the magnitude images were calculated and subsequently the mean and standard deviation vectors were reshaped to 7x7 matrices reflecting the 7 orientations and 7 wavelengths. A new 14x7 matrix was formed having at the top the means and at the bottom the standard deviations. The FFT of every row of the matrix was calculated and the 5 first coefficients were retained (330). The maximum number of unique frequency coefficients following FFT is given by the formula: orientations / 2 + 1, so in our case the number was 5. These features are shift and rotation invariant due to the properties of the discrete Fourier transform (331).

For all extracted statistical and textural features, comparisons between pairs of groups were conducted using t-tests. Due to the large number of comparisons, multiple comparison correction was implemented by estimating the FDR methodology. Finally, we evaluated these features in a machine learning context, similar to the one described in Chapter 6. The maximum accuracy of the classifier, along with the number of features contributing to this performance were recorded.

This procedure was investigated for 12 HV (4 scans not acquired), 11 IGT (1 discarded due to poor image quality) and 17 T2DM patients.

7.3.2 Results

Results for the examined cohort are shown in table 7.7.

Table 7.7: Number and volume of leukoaraiosis in the examined cohort.

	HV	IGT	T2DM
Age (years)	55.0±7.5	54.5±5.7	55.6±12.5
number	9.5±4.4	11.1±4.9	19.5±11.3
Volume (ml)	1.0±1.2	1.2±1.1	7.9±12.3
Hypertension (number of subjects)	4	9	8

The number of WMH was normally distributed, but the equal variance assumption was violated, so to compare the number and volume of WMH the non-parametric equivalent of one-way ANOVA, the Kruskal-Wallis test was used. Both the number of WMH and their volume differed between the groups ($\chi^2(2) = 8.3$, $p = 0.016$ and $\chi^2(2) = 7.8$, $p = 0.02$ respectively). Comparisons were also conducted for the number and volume of WMH using, as a grouping variable, the hypertensive status. The differences were not significant.

T2 FLAIR textural analysis

An overall of 474 textural features were calculated from 6 ROIs, these comprised: 70 Gabor textural features, 5 features from the gray level co-occurrence matrix and 4 statistical features. Following t-tests, 57 features were significantly different for the HV vs T2DM comparison, 12 for the HV vs IGT and 21 for IGT vs T2DM. Following correction for multiple comparisons, no feature was significantly different between the groups based on the adjusted p-values. However, we proceeded to machine-learning based analysis. For HV vs T2DM, maximum accuracy was achieved by one feature and it was 68.97%. Maximum accuracy for HV vs IGT was 65.2%, achieved with 3 features. For the IGT vs T2DM comparison maximum accuracy was 71.4% achieved with 6 features. Overall, the performance for every task was low based on the extracted textural features.

7.3.3 Discussion

A higher WMH burden was observed in T2DM compared to the healthy participants. WMHs were also detected in the HV and IGT groups; however, their volume was significantly lower compared to the T2DM participants. An increased WMH burden has been found in the past in several neuroimaging studies (35, 332), however, it is not a consistent finding (33). Hypertension is a condition connected with increased leukoaraiosis extent, hence we conducted additional statistical tests to investigate if the number and volume of WMH differed significantly between subjects with and without hypertension. The analysis identified non-significant differences, implying that the observed effect

is not attributed to hypertension, but more likely, to diabetes or other existing comorbidities in our cohort, which were not accounted for in this study.

The FLAIR image was also analysed using textural features to unravel potential textural differences between the examined groups. This modality was chosen for textural analysis due to the increased contrast between WMH and other tissues with a view to detecting potential subtle patterns of difference. Some features differed between the groups; however, multiple comparison correction left no significant differences. Correction for false positives is known to give rise to true negatives, so we proceeded to a machine learning-based analysis to examine whether the significantly different features between the groups provided good class differentiation. The accuracy of the classifier was low for all classification tasks indicating that textural analysis of the FLAIR image alone is not sufficient for optimal class differentiation.

7.4 Phase Contrast – Magnetic Resonance Angiography (PC-MRA) analysis

7.4.1 Methods

When carotid flow measurements are acquired, their typical processing involves using built-in scanner tools (in our case, tools provided as part of the Philips workstation) for manual segmentation of the carotids, or any other vessel of interest, and velocity, vessel area and flow quantification. This procedure can be time-consuming, user-dependent and potentially non-reproducible. The requirement from the user is to manually select the area of interest in the available image. For this to be done optimally, the user might have to adjust the contrast for accurate delineation of the vessel limits. In this procedure, it is rather common to miss small parts, or include parts outside the vasculature, in an effort to select manually the optimal region. Another obstacle when using the Philips workstation (as was the case in this study) is that it requires direct access to the scanner, which might not be available. Hence, a software tool based on Matlab was built to address these limitations and to quantify flow and velocity in an automated and reproducible way.

The developed algorithm works as follows: The .REC folder is separated into three parts, a magnitude image, a phase difference image and a complex

difference image from where velocity measurements are extracted. For each of these parts, 40 acquisitions reflecting 40 time-points were recorded. For every part, the mean is calculated. Subsequently, the mean phase and complex difference images are multiplied. Only the positive values are kept to retain the signal arising from the arterial supply. The resulting image is normalised by dividing by the maximum intensity value. Subsequently, a threshold is used (tested values: 0.2, 0.3, 0.4, 0.5, 0.6). The threshold reflects the intensity of the voxels that were left out in the thresholding step. Hence, a threshold of 0.2, means that voxels with intensity less than 20% of the image's maximum were thresholded out. As a result, voxels without any information from the vasculature are excluded.

The optimal threshold was found to be 0.3, which was adopted for the subsequent analysis. Following this step, the retained voxels are overlaid onto the magnitude image to manually select an area surrounding the vessel of interest. The area of the manually picked ROI does not influence the final result, since the manual selection is introduced as a means of choosing an already segmented vessel of interest, rendering this approach user-independent. The only control the user has is to choose the optimal threshold and to select the vessel of interest. The followed steps and the images resulting from every stage are depicted in figure 7.11.

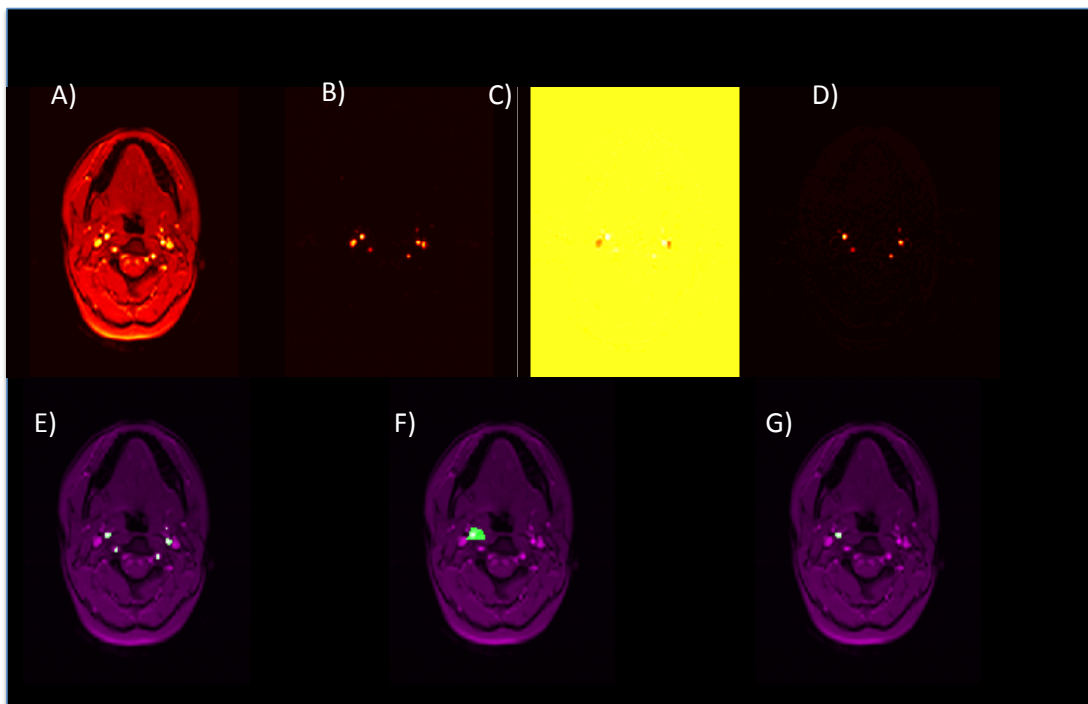


Figure 7.11: PC-MRA processing steps. A) mean magnitude image, B) mean phase image, C) mean velocity image, D) phase multiplied with velocity image (information from the veins is zeroed), E) arterial input overlaid on the magnitude image, F) hand drawn ROI, G) selected vessel overlaid on the velocity image.

The mean, maximum and minimum velocities were calculated from each vessel of interest at each time point and the final reported value was the mean of each of them within the vessel. Flow was calculated as the product of the mean velocity and the area of the vessel.

The areas of the vessel varied slightly for every individual and this could result in flow, min velocity and mean velocity differences due to the size of the vessel area. To account for that, the 10 voxels having maximum intensity inside the vessel of interest were retained, in order for the velocities to be compared with the same reference vessel area. This approach was run for the whole brain, the left and the right hemispheres separately. The retained voxels were the ones reflecting laminar flow, since they were situated at the center of the vessel. Additionally, to get a clearer picture of the inflowing blood flow pattern, results for all arterial input voxels exceeding the defined threshold were recorded.

Of primary interest in the analysis of the PC-MRA data was the inflowing velocity pattern, the area of the supplying voxels and the overall inflowing flow.

During the acquisition, every possible effort was made for the same region to be selected for every individual, however that was not always the case. Small deviations were noticed. For this reason, we focused more on the velocity pattern.

Two PC-MRA scans were acquired for every individual proximal to the right carotid, one at baseline and one following ACZ injection. The acquisition was optimized for the right carotid; however, measurements were also extracted from the left carotid and from all vessels surviving the thresholding procedure. CVR was evaluated as the percentage change in the flow values following administration of the vasodilating stimulus.

Mean and standard deviations for all subjects were calculated and initial comparisons took place with t-tests when data were normally distributed and with Wilcoxon rank sum test when they were not normally distributed. To compare the values between the three groups one-way ANOVA was used and when its assumptions were violated, the Kruskal-Wallis test was applied to detect potential differences. FDR was used to correct for multiple comparisons. The analysis was run for 15 HV (1 discarded due to poor image quality), 12 IGT subjects and 16 T2DM patients (1 discarded due to poor localization of the carotid).

7.4.2 Results

Overall, 46 variables were calculated from the PC-MRA scans. The mean area covered by feeding vessels for every group when a threshold = 0.3 was used is reported in number of voxels in table 7.8.

Table 7.8: Mean vessel area (mean \pm standard deviation) measured in number of voxels for the examined groups.

	HV	IGT	T2DM
Age (years)	48.4 \pm 13.6	54.8 \pm 5.3	54.4 \pm 11.9
All pre-ACZ	55.73 \pm 13.51	63.75 \pm 19.58	61.63 \pm 23.91
All post-ACZ	65.80 \pm 13.98	69.42 \pm 23.10	61.31 \pm 19.25
Right pre-ACZ	18.13 \pm 2.29	20.33 \pm 4.03	22.69 \pm 8.01
Right post-ACZ	23.20 \pm 6.05	24.00 \pm 4.86	25.38 \pm 10.27

Left pre-ACZ	19.60±3.36	19.42±5.47	21.13±8.86
Left post-ACZ	25.07±6.30	23.83±8.24	21.94±7.67

Differences between the areas covered by the examined vessels were not significant when examined using t-tests. Changes in the vessel diameter were significant only for the HV group for the right ($z = 2.877$, $p < 0.01$), left ($z = 2.749$, $p = 0.01$) and all identified arterial input ($z = 2.700$, $p = 0.01$). Age was not significantly different between the groups after the exclusion of the 3 noisy scans.

7.4.2.1 Flow evaluation

Flow was calculated for the whole area of the chosen vessel (left and right carotids), for the 10 more intense voxels within this vessel (left10, right10) and for all the arterial vessels exceeding the selected threshold. Results for the baseline and post-ACZ flow are shown in figure 7.12 and for CVR in table. 7.9 (CVR).

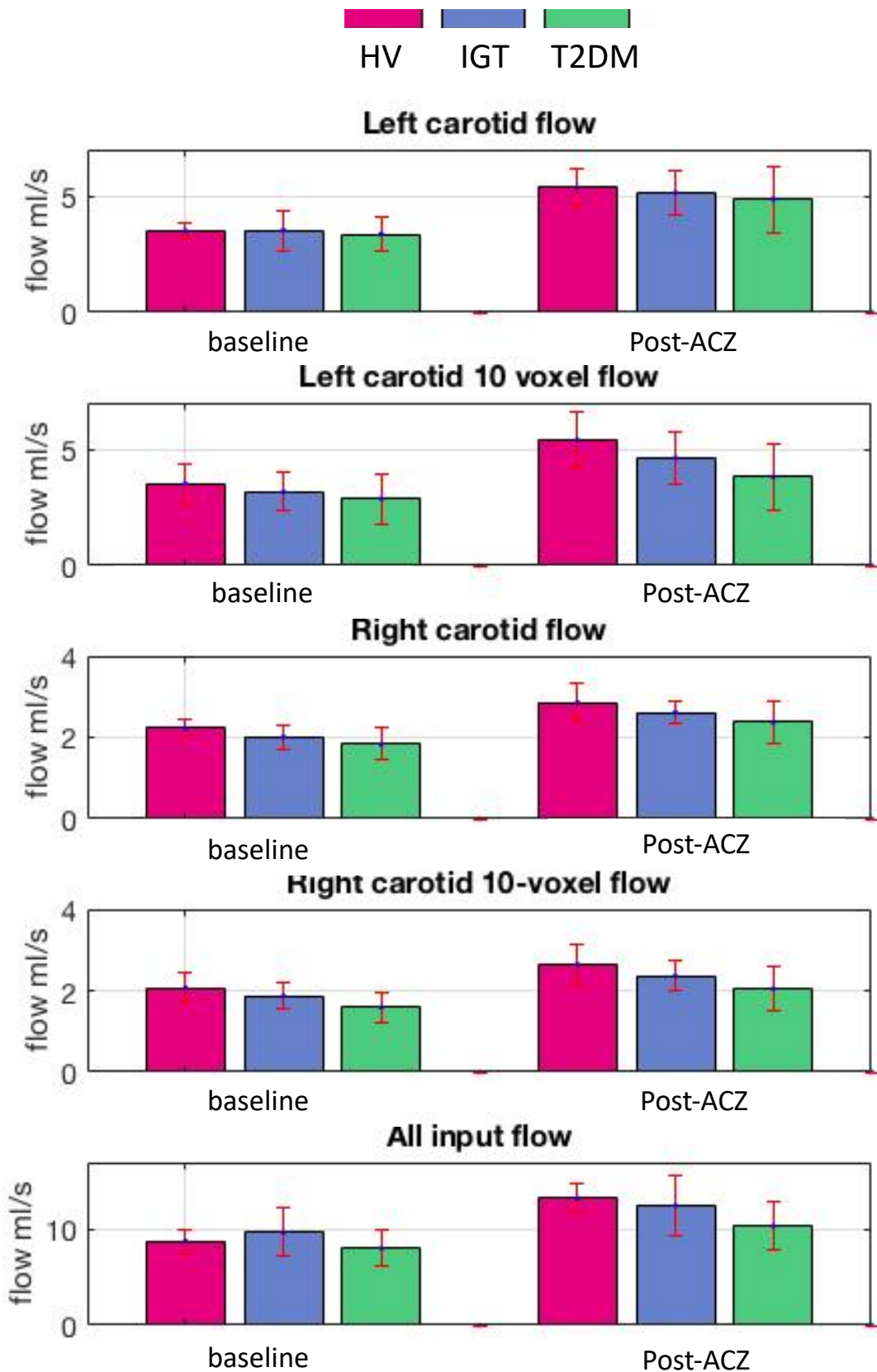


Figure 7.12: **Baseline and post-ACZ flow for the different ROIs.** Shown are the mean values per group accompanied with the standard deviation.

Differences were significant at baseline between HV-T2DM for the following: right10 ($z = -3.042$, $p = 0.01$), left10 ($t(26) = -2.691$, $p = 0.01$). Post-

ACZ differences were significant between HV-T2DM for the following: right ($z = -2.115$, $p = 0.03$), right10 ($z = -2.233$, $p = 0.03$), left ($t(26) = -3.066$, $p < 0.01$), left10 ($t(26) = -2.393$, $p = 0.02$) and all ($t(26) = -3.879$, $p < 0.01$).

Table 7.9: CVR for the 3 groups and examined areas evaluated as the % change between pre and post ACZ flow measurements.

	right (ml/s)	left(ml/s)	right10(ml/s)	left10(ml/s)	All (ml/s)
HV	54.24±20.47	55.85±26.73	29.49±23.19	29.65±23.91	51.50±11.87
IGT	49.94±36.54	49.68±37.42	31.5±18.91	27.53±13.71	30.74±19.5
T2DM	45.43±28.77	38.38±38.48	30.7±18.31	27.84±20.16	34.76±40.00

Differences in CVR were significant between HV and T2DM for: all vessels ($z = -2.273$, $p = 0.02$), and between HV and IGT for: right ($z = -1.976$, $p = 0.05$) and all ($z = -2.659$, $p = 0.01$).

7.4.2.2 Velocity measurements

Baseline and post-ACZ velocity values are analysed for the following velocities: mean maximum and minimum. Results are shown in figure 7.13 for the left and right carotid and the whole arterial input. Additional results for the 10-voxel area can be found in the appendix2 (tables A7.2-A7.7).

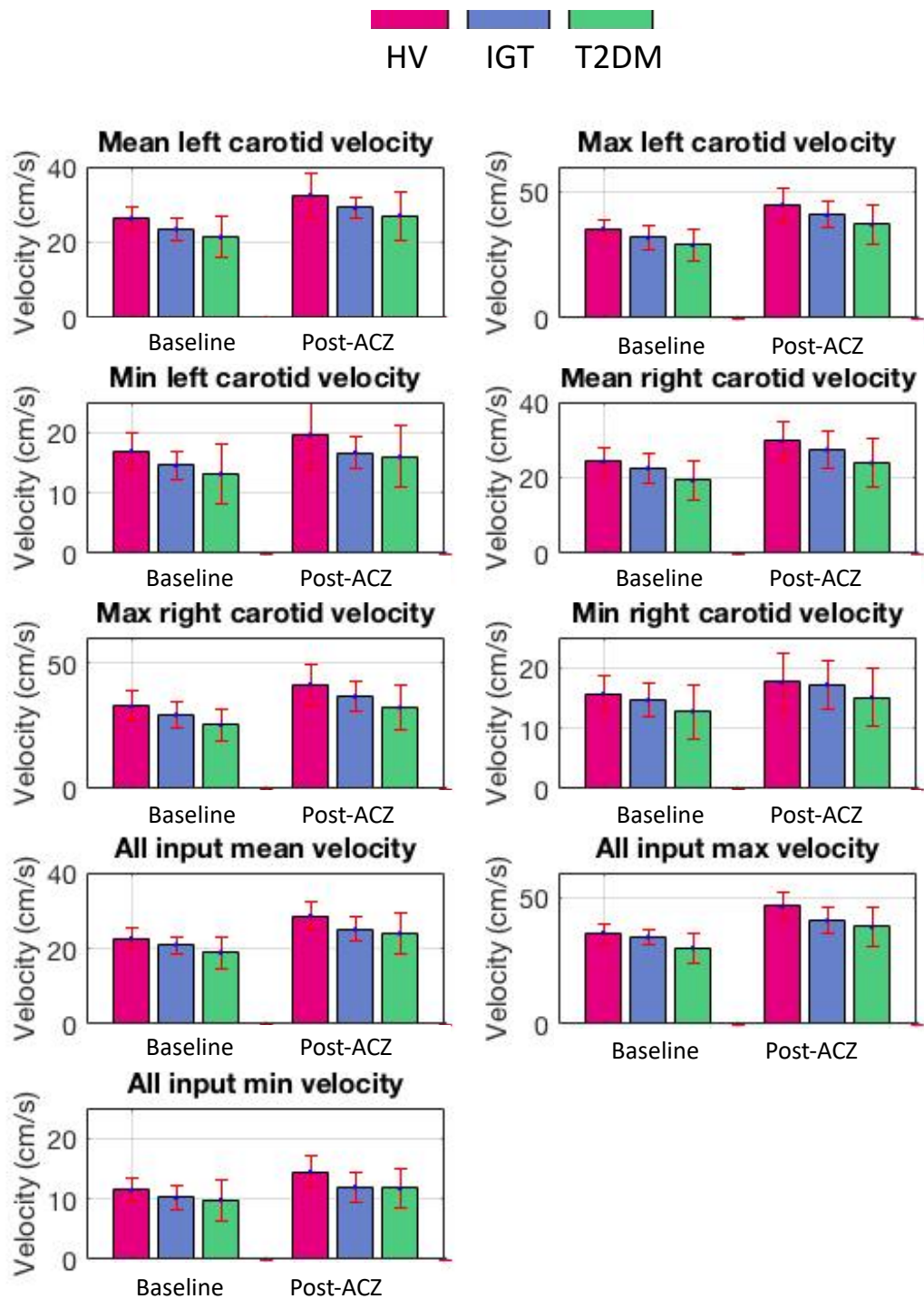


Figure 7.13: Mean, maximum and minimum velocities for the left and right carotids and all arterial input for the three considered group

Significant differences between the groups when using t-tests were identified for the following metrics:

- Mean baseline velocity

- HV - T2DM: right ($t(26) = -3.161$, $p < 0.01$), right10 ($t(26) = -3.409$, $p < 0.01$), left ($t(26) = -3.008$, $p = 0.01$), left10 ($t(26) = -3.257$, $p < 0.01$) and all ($t(26) = -2.895$, $p = 0.01$).
 - HV and IGT: right ($t(26) = -2.557$, $p = 0.02$) and right10 ($t(26) = -2.240$, $p = 0.03$).
- **Maximum baseline velocity**
 - HV - T2DM: right ($t(26) = -3.523$, $p < 0.01$), right10 ($t(26) = -3.529$, $p < 0.01$), left ($t(26) = -3.332$, $p < 0.01$), left10 ($t(26) = -3.333$, $p < 0.01$) and all ($t(26) = -3.097$, $p < 0.01$).
 - HV – IGT: right ($t(26) = -2.215$, $p = 0.04$) and right10 ($t(26) = -2.215$, $p = 0.04$).
 - IGT - T2DM: all arterial input ($t(26) = -3.420$, $p < 0.01$).
 - **Minimum baseline velocity**
 - HV - T2DM: right ($t(26) = -2.565$, $p = 0.02$), right10 ($t(26) = -3.169$, $p < 0.01$), left ($t(26) = -2.097$, $p = 0.04$) and left10 ($t(26) = -3.088$, $p < 0.01$) and all ($t(26) = -3.420$, $p < 0.01$).
 - IGT - T2DM: right ($t(26) = -2.215$, $p = 0.04$) and right10 ($t(26) = -2.318$, $p = 0.03$).
 - **Mean post-ACZ velocity**
 - HV-T2DM: right ($z = -2.154$, $p = 0.03$), right10 ($z = -2.431$, $p = 0.02$), left ($t(26) = -2.757$, $p = 0.01$), left10 ($t(26) = -3.125$, $p < 0.01$) and all ($z = -2.194$, $p = 0.03$).
 - HV-IGT: right ($z = -2.22$, $p = 0.03$), right10 ($z = -2.318$, $p = 0.02$) and all ($z = 2.611$, $p = 0.01$).
 - **Maximum post-ACZ velocity**
 - HV-T2DM: right ($z = -2.471$, $p = 0.01$), right10 ($z = -2.471$, $p = 0.01$), left ($t(26) = -3.029$, $p = 0.01$), left10 ($t(26) = -3.027$, $p = 0.01$) and all ($z = -2.866$, $p < 0.01$).
 - HV-IGT: right ($z = -2.123$, $p = 0.03$), right10 ($z = -2.123$, $p = 0.03$) all ($z = -2.757$, $p = 0.01$).

- **Minimum post-ACZ velocity**

- HV-T2DM: right10 ($z = -2.471$, $p = 0.01$), left10 ($z = -3.407$, $p < 0.01$) and all ($t(26) = -2.620$, $p = 0.01$).
- HV-IGT: right10 ($z = -2.123$, $p = 0.03$) and all ($z = -2.542$, $p = 0.02$) c) IGT-T2: left10 ($z = -2.288$, $p = 0.03$).

Result summary

Overall the differences between the three groups were significant for the following metrics:

Baseline:

- **Right carotid:** mean velocity ($\chi^2(2) = 9.5$, $p = 0.01$), max velocity ($\chi^2(2) = 8.433$, $p = 0.02$), min velocity ($\chi^2(2) = 6.935$, $p = 0.03$), 10-voxel flow ($\chi^2(2) = 8.726$, $p = 0.01$), 10-voxel mean velocity ($\chi^2(2) = 8.726$, $p = 0.01$), 10-voxel max velocity ($\chi^2(2) = 8.433$, $p = 0.02$), 10-voxel min velocity ($\chi^2(2) = 6.911$, $p = 0.03$).
- **Left carotid:** max velocity ($F(2,40) = 6.042$, $p = 0.01$), 10-voxel flow ($F(2,40) = 6.875$, $p < 0.01$), 10-voxel mean velocity ($F(2,40) = 5.792$, $p = 0.01$), 10-voxel max velocity ($F(2,40) = 6.046$, $p = 0.01$), 10-voxel min velocity ($F(2,40) = 5.45$, $p = 0.01$),
- **All:** mean baseline velocity ($\chi^2(2) = 7.088$, $p = 0.03$), max baseline velocity ($\chi^2(2) = 8.668$, $p = 0.01$).

Post-ACZ:

- **Right carotid:** mean velocity ($F(2,40) = 3.795$, $p = 0.03$), max velocity ($\chi^2(2) = 8.373$, $p = 0.02$), 10-voxel flow ($\chi^2(2) = 9.065$, $p = 0.01$), 10-voxel mean velocity ($\chi^2(2) = 9.065$, $p = 0.01$), 10-voxel min velocity ($\chi^2(2) = 9.214$, $p = 0.01$), 10-voxel max velocity ($\chi^2(2) = 8.433$, $p = 0.02$).
- **Left carotid:** flow ($F(2,40) = 5.749$, $p = 0.01$), mean velocity ($F(2,40) = 4.222$, $p = 0.02$), max velocity ($F(2,40) = 5.262$, $p = 0.01$), 10-voxel flow ($F(2,40) = 5.788$, $p = 0.01$), 10-voxel mean velocity ($F(2,40) = 5.671$, $p = 0.01$), 10-voxel max velocity ($F(2,40) = 5.257$, $p = 0.01$), 10-voxel min velocity ($F(2,40) = 6.921$, $p = 0.01$).

- **All:** flow ($\chi^2(2) = 9.217$, $p = 0.01$), mean velocity ($\chi^2(2) = 7.918$, $p = 0.02$), max velocity ($\chi^2(2) = 11.298$, $p < 0.01$), min velocity ($F(2,40) = 4.412$, $p = 0.02$).

CVR as calculated using the PC-MRA data differed significantly between the groups for all arterial input ($\chi^2(2) = 8.23$, $p = 0.02$). All the identified metrics remained significant following correction for multiple comparisons using FDR.

7.4.3 Discussion

Typical processing of a PC-MRA scan involves manual selection of the vessel of interest and quantification of several metrics from the chosen region. Commonly the flow values are reported. A new Matlab-based tool for carotid velocity and flow quantification was presented in this chapter. The method for arterial selection is user-independent and highly reproducible (unless users disagree on which vessel is the carotid). The tool's novelty relies on a shift in the focus from carotid flow to the actual acquired velocity pattern, which can be examined in its entirety.

When processing the PC-MRA scans, focus was put on the vessel for which the acquisition was optimised (right carotid) but also on the left part by keeping in mind that the acquisition might not have been perpendicular to the left side. The whole vessel was chosen in a user-independent manner. Additionally, a fixed area of 10 voxels inside the vessel of interest was selected to detect differences in the laminar velocity pattern, by considering a region of the same size for every subject. The analysis identified that the blood velocity was significantly different between the groups for both a set area of 10 voxels and the whole vessel region. Three velocities were evaluated, the maximum, minimum and mean. The flow value (multiplication between mean velocity and the area of the vessel) was also calculated and was found to differ between the groups.

A finding of interest is that the area of the arterial supply was higher at baseline (not significantly) in the T2DM group and following ACZ injection there was no big increase indicating that the vessel did not dilate in response to the stimulus. This finding was not significant; however, it shows a tendency for the hyperglycemic groups to have more dilated carotids at baseline. Both the IGT and T2DM groups showed a stabilisation of the vessel diameter pre- and post-

ACZ with only minor changes. On the contrary, the increase in the vessel diameter for the HV groups was significant for both left and right carotid and for all identified arterial supply. This finding could point towards a maximum vasodilation at baseline in the IGT and T2DM groups, associated with the presence of a potential compensatory mechanism due to impaired oxygen and nutrient delivery to the brain tissue.

In terms of the evaluated velocities, the HV group demonstrated higher mean, min and max velocities compared to the IGT and T2DM groups. IGT subjects had values in between HV and T2DM subjects. Flow differed between HV and T2DM in the 10-voxel areas for the right and left carotids at baseline. For the same groups post-ACZ flow differed for all examined ROIs. CVR at the level of the carotids was decreased for the T2DM group in all the examined arterial input; in IGT the difference when compared to HV was significant for the right carotid and all arterial input. In terms of differences in the velocity pattern, for the 10-voxel regions, all examined velocities differed between the three groups pre- and post-ACZ, implying a distinct laminar flow pattern. When examining the whole vessel areas, differences were recorded at baseline for the mean (R, all), min (R) and max (L, R, all) velocities. Post-ACZ the patterns of difference were identified for: mean (L, R, all), min (all) and max (L, R, all) velocities. These findings were mainly driven by differences between HV and T2DM, with differences between HV and IGT mainly detected for the right carotid for which the acquisition was optimised.

These findings ought to be discussed in light of the existing literature whereby a detailed velocity pattern analysis is not usually conducted. Only a few studies have looked into the carotid flow pattern using either TCD or PC-MRA in diabetes. Typically, the reported metrics are flow, velocity and metrics such as pulsatility index (53). A study using PC-MRA and ACZ as a vasodilator found no differences in baseline flow and a decrease in CVR in T2DM; the findings were non-significant (333). A study using TCD has reported reduced mean flow velocity in T2DM (42), a finding in line with our velocity findings. In the same study, CVR was assessed using CO₂ inhalation and was found to be significantly reduced in the diabetic cohort. Tiehuis et al. (44) did not find significant differences after correcting for brain volume. In their study, despite using PC-MRA, they focused on the calculation of CBF based on the velocity

information after correcting for the total brain volume. A study by Brundel et al. (193) showed that CBF, calculated by PC-MRA, was reduced in patients with T2DM. In the aforementioned study, CVR was assessed using TCD and was found to be increased; the significance of the findings though was not reported.

To summarise the findings reported in the literature, CVR, when using velocity-based quantification strategies, has generally been found to be decreased in diabetes. Baseline flow tends to be similar between the groups, whereas baseline velocity is decreased.

The present analysis is the first one of its kind focusing on a detailed analysis of the velocity pattern between the groups and findings suggest the existence of significant differences. We proposed that a detailed velocity and area analysis along with carotid flow calculation can have an additive diagnostic value since the observed flow pattern can be attributed either to a large vessel area or to a high blood velocity. Such an analysis can disentangle the cause of the observed flow differences and shed light on the inflowing velocity pattern. Based on the described findings, we suggest that the velocity of the inflowing blood is decreased in both IGT and T2DM and there is a non-significant increase in the area of the vessels, pointing towards dilation at baseline. Following pharmacologically induced vasodilation, we see a lower response with regards to vessel dilation, flow and velocity changes in the IGT and T2DM groups.

7.5 Time-of-flight – Magnetic Resonance Angiography (TOF-MRA) analysis

7.5.1 Methods

Three methods were tested for angiogram segmentation. Methods 1 and 3 were applied directly to the 2D coronal maximum intensity projection (MIP). Method 2 applied angiogram segmentation in two stages; an initial segmentation was performed in the 3D stack of axial slices of the angiogram. Subsequently the initial segmentation was projected (MIP) and a second segmentation was applied in the 2D projection. For method assessment two, subjects were used, one HV with a normal looking scan and one T2DM patient with high degree of collateral circulation.

Method 1

The first method involved using an adaptive threshold calculated locally in areas of $N \times N$ pixels. The evaluated window sizes (N) were: 15x15, 25x25, 45x45, 65x65, 85x85 and sensitivity levels of 0.2, 0.3, 0.4, 0.5. The utilised algorithm was Matlab's `adaptthresh` (334), which calculates a threshold based on the calculated mean inside a sliding window. A higher sensitivity level allows more pixels to be included in the generated mask.

Method 2

The second evaluated approach was as follows: the image was initially filtered with a wiener filter (5x5) (335). K-means clustering was used to classify the voxels into three separate clusters and remove background along with voxels with intensity values close to background. A square mask in the area (150:350, 150:350) was created to separate each 2D slice into two regions, a central and a peripheral. The peripheral region incorporated mainly background and branches emerging from the external carotid. Furthermore, the 222 slices were separated into three groups. The first group involved the region from the base of the neck until the point where the main carotids start converging, the second region was defined from the point where the convergence of carotids starts until the upper part of the circle of Willis and the third involved the slices from that point to the upper slice. These six groupings gave rise to distinct groups, each having its own threshold (the values were normalized). Multiple thresholds were tested for every individual and every region.

Method 3

One of the most popular algorithms for vessel segmentation especially for retinal images is Frangi's vesselness filter (336). The method enhances the vascular structures by filtering the image to improve vasculature segmentation. The filter detects tubular structures by exploiting the eigenvalues of the image's Hessian (336). The Hessian matrix of an image comprises the second order partial derivatives. Second order derivatives of a continuous function can be used to detect local maxima and minima in a signal/image. These are the points where the derivative has a value of zero and the nature of maxima/minima can be determined by whether the second order derivative is negative (maximum)

or positive (minimum). Hence, the idea behind the Frangi filter is that, following smoothing by convolution with a Gaussian, the eigenvalues of the Hessian matrix are determined and a high 'vessel response' is said to exist when the eigenvalues fulfill set criteria (thresholding). For more details on the operating principles of the filter, the reader is referred to the original publication (336). The evaluated Frangi filters had standard deviation values of $\sigma = 1, 3$ and 5 . A Matlab function built by D.-J. Kroon (282) was used for the implementation of the Frangi filter.

Performance evaluation and calculated metrics

The MIP of the coronal plane was used to visually evaluate the success of the segmentation methods. Metrics were extracted to evaluate potential differences in the area covered by vessels (indicative of vascular deficits) or the number of different branches (indicative of the presence of collateral circulation or loss of vasculature) for every individual. To proceed to vasculature-descriptive metric extraction, the number of non-zero pixels was counted in the designated area of interest. Subsequently, the resulting vasculature segmentation was 'skeletonized' using the `bwmorph` Matlab function with "thin" as an argument and 10 iterations and the resulting length of the vascular tree was calculated (MATLAB and Image Processing Toolbox 2016a, The MathWorks Inc., Natick, Massachusetts, USA). The number of branching points was also recorded, again using `bwmorph`.

Metrics regarding the vessel density, centerlines (vessel length without density information) and number of branching points were recorded for vessels arising from the MCA territory. The image region including the MCA was manually chosen. To achieve optimal segmentation we used both the developed 2nd method and also segmentation based on simple Otsu thresholding (287).

7.5.2 Results

In figures 7.14 & 7.15, results for the 1st developed method are depicted with varying values for the adaptive window and threshold level. Visual assessment of the segmentation results suggests that optimal segmentation was obtained with a window of 45x45 and a sensitivity level of 0.3. These

values were used for subsequent comparison of the segmentation result using methods 2 and 3.

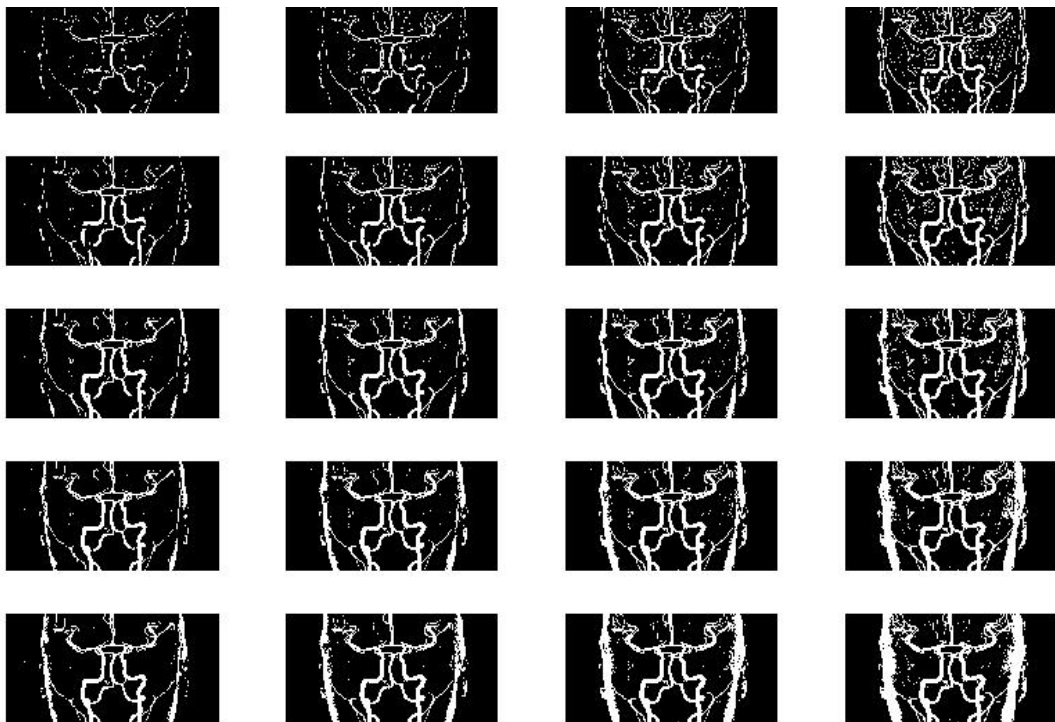
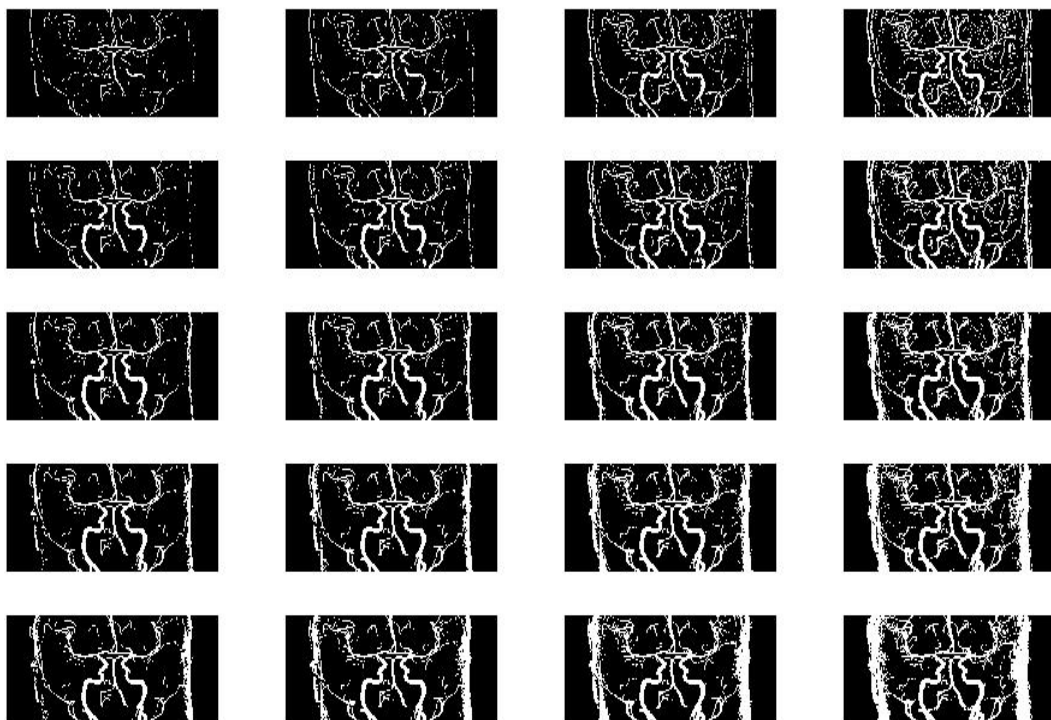


Figure 7.14: 1st method for angiogram segmentation for one HV. Every row corresponds to a different window size (15x15, 25x25, **45x45**, 65x65, 85x85) and every column to a different threshold (0.2, **0.3**, 0.4, 0.5).



*Figure 7.15: Segmented MIP for one T2DM subject using the first method. Every row corresponds to a different window size (15x15, 25x25, **45x45**, 65x65, 85x85) and every column to a different threshold (0.2, **0.3**, 0.4, 0.5).*

For the second method, with 6 distinct ROIs each having a tailor-made threshold, angiographic segmentation results are shown in figure 7.16.

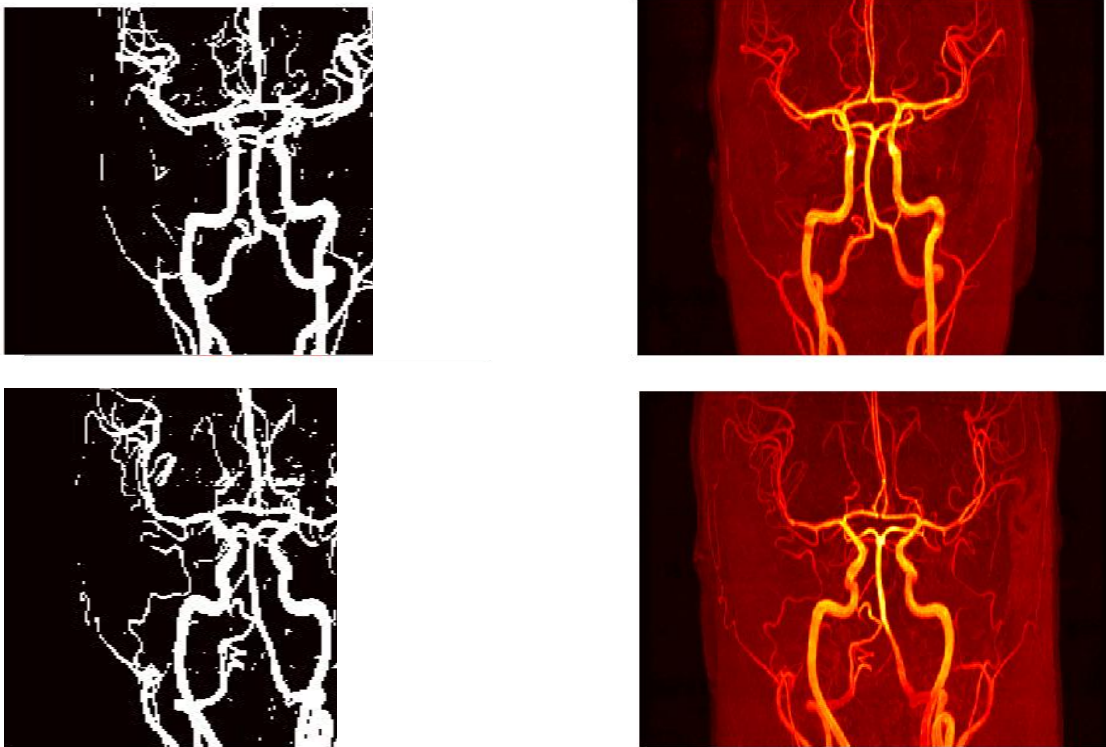


Figure 7.16: Segmentation with the 2nd method for one HV (top) and one T2DM patient (bottom)

Segmentation results for method 3 (Frangi's vesselness filter) are shown in figures 7.17 & 7.18.

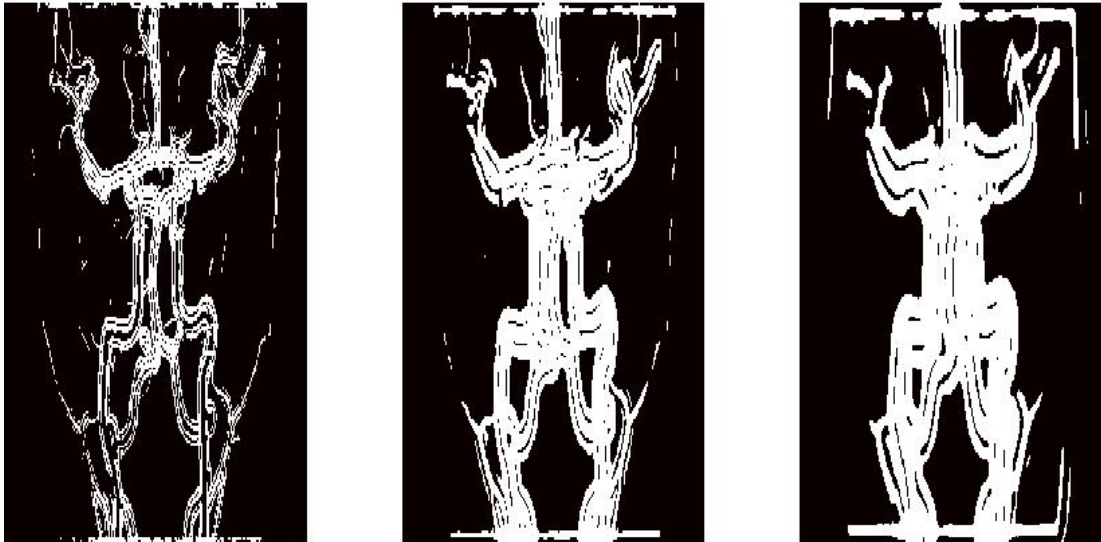


Figure 7.17: MIP segmentation using Frangi filter with 3 different standard deviations (from left to right, $\sigma = 1, 3$ and 5) for one healthy subject.

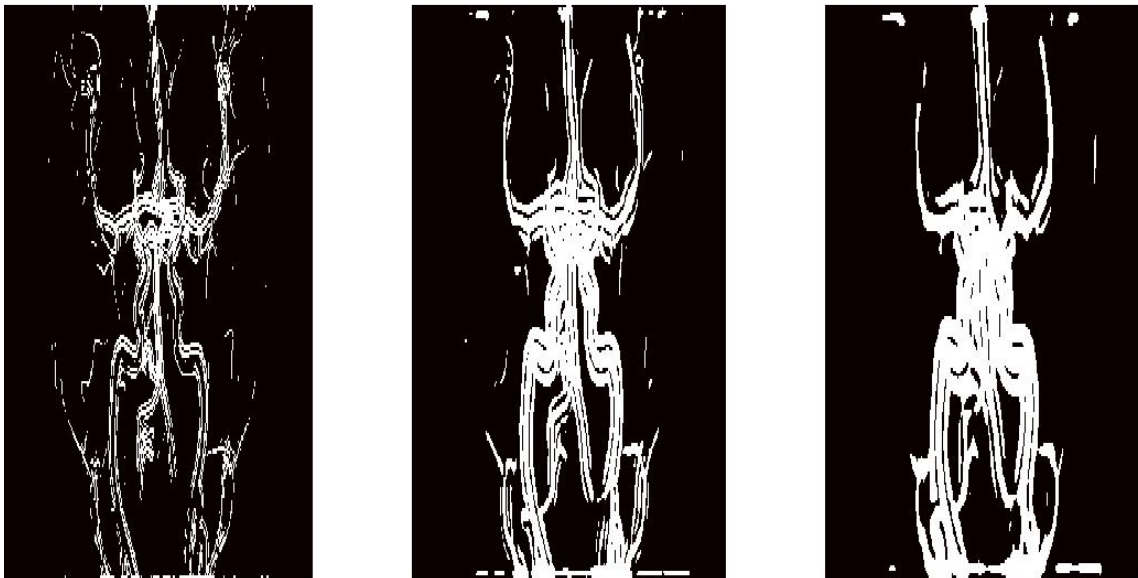


Figure 7.18: MIP segmentation using Frangi filter with 3 standard deviations (from left to right, $\sigma = 1, 3$ and 5) for one T2DM patient.

The implemented Frangi vessel segmentation resulted in missing some of the smaller vessels at the anterior part of the brain, which were successfully identified with the developed methodology due to the various thresholds chosen carefully for every individual. This came at the expense of allowing several noisy pixels inside the segmented angiogram. For this particular study the region encompassing the MCA and ACA territories is of particular interest, since it is the region on which the perfusion ASL measurements were conducted,

hence it is important to identify the underlying vascular structure. A comparison of all three methods side by side for two subjects is shown in figure 7.19.

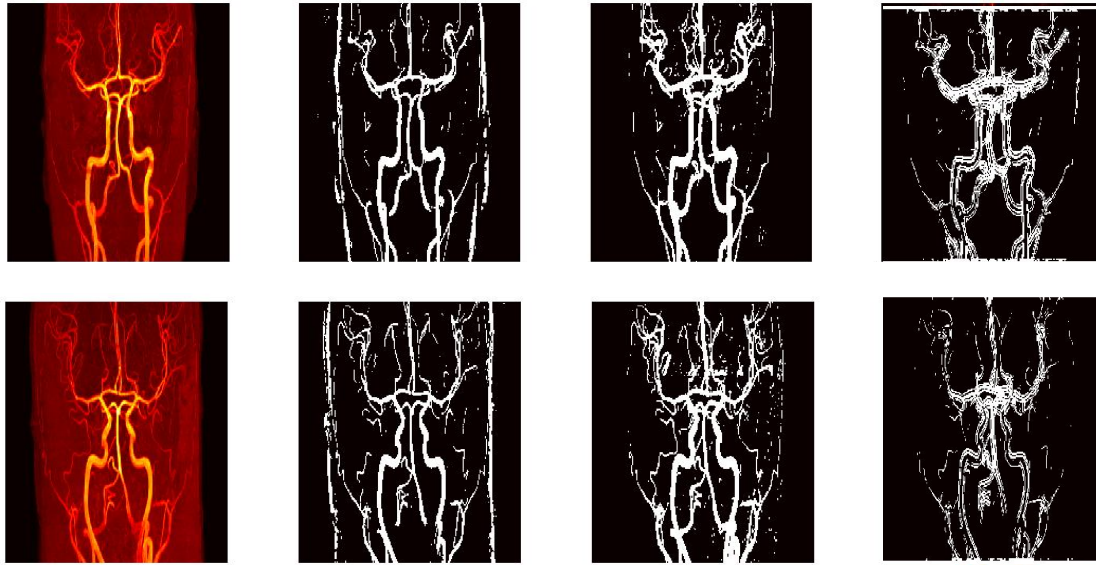


Figure 7.19: Comparison of the MIP segmentation obtained with the 3 evaluated methods. From left to right: MIP, angiogram segmentation with the 1st, 2nd and 3rd method.

Angiographic segmentation is a challenging task, and even after the introduced development, noisy regions were not efficiently masked out in several scans. As mentioned earlier, segmentation of the MCA territory is of particular interest, so results were evaluated for the MCA separately for the best performing methods (1 & 2). Results are shown in figure 7.20.

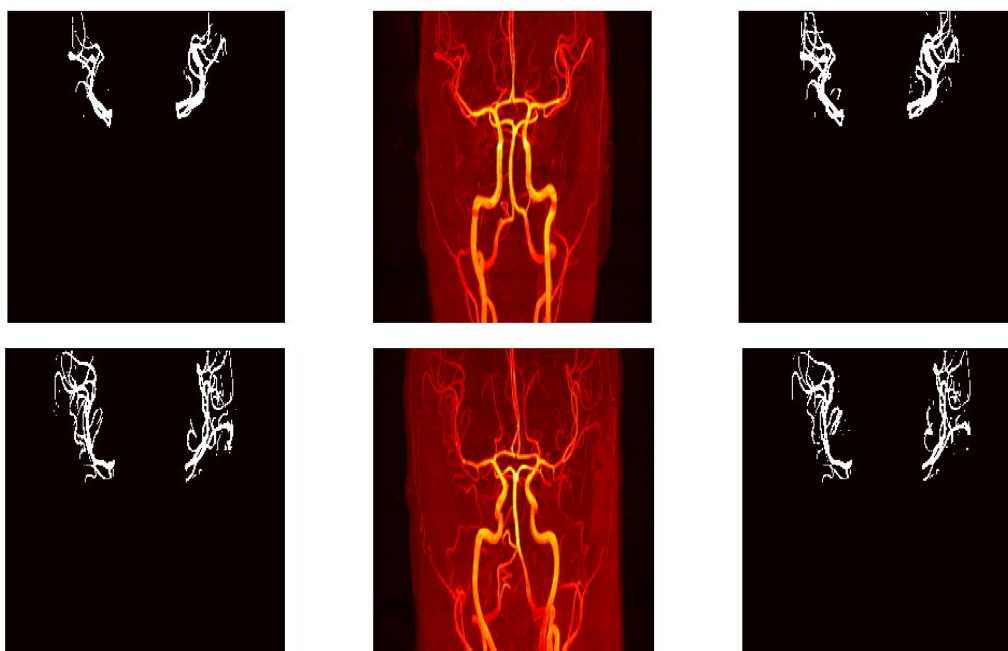


Figure 7.20: **MCA territory segmentation.** From left to right: Segmentation based on Otsu, MIP and segmentation with the 2nd angiogram segmentation method.

Optimal segmentation results were obtained for the second method, as assessed by visual evaluation of the resulting maps, so it was used for the subsequent analysis of the segmented MCA vasculature. Results for the evaluated vasculature-descriptive metrics are shown in table 7.10.

Table 7.10: **Vasculature-descriptive metrics extracted from the MCA territory for the 3 groups.**

	HV	IGT	T2DM
Vessel density	4385.5±804.8	4146.7±894.7	3712.5±1134.0
Vessel length	1396.9±209.3	1363.5±251.7	1208.5±336.3
Branch points	149.9±28.5	138.0±31.6	110.7±40.9

The differences were significant between HV and T2DM for the number of branching points ($z = -3.103$, $p < 0.01$). The number of branching points also differed between IGT and T2DM patients ($z = -2.237$, $p = 0.03$). Vessel length ($p = 0.058$) and density ($p = 0.054$) did not differ between HV and T2DM; an underlying tendency was noticed though for a lower vessel length and density in the T2DM group.

7.5.3 Discussion

Angiogram segmentation is a cumbersome task and constitutes a vivid research area where neural networks have come into play to assist (316). Currently, there is no gold standard for this procedure; several tools have been developed but are at an experimental stage (337, 338). Here, we presented a semi-automated method, which requires the user to evaluate different thresholds in six regions in order to achieve optimal segmentation. The algorithm initially partitions the scan into two regions, a peripheral and a central one and subsequently to three additional sub-regions in the head-foot axis.

The results for the developed approach were promising and demonstrated a good performance compared to alternative techniques evaluated for vascular segmentation. Our goal was not to successfully segment only the large vessels, but to extract accurately the anatomy and vasculature of the smaller arterioles. When the popular Frangi filter was used, even with the least degree of smoothing, detail (especially small vessels) was lost. A second evaluated approach based on a local adaptive threshold resulted in accurate vascular segmentation, although several noisy background voxels were included in the segmented mask. However, when this approach was used, the vascular anatomy was preserved in greater detail (especially small arterioles) and was better separated from the background. Hence, the subsequent quantitative analysis was facilitated.

The main drawback of the introduced technique is that it is semi-automated, requiring the user to test multiple thresholds. Additionally, it requires a subjective visual evaluation of the segmentation result based on the MIP.

The angiogram analysis revealed significant group differences, although large variability existed within the groups. There was no distinct pattern that all diabetic patients followed, for some of them an increased collateral blood supply was noticed, whereas for others the collateral circulation was totally missing. When focusing on the MCA territory, following vasculature analysis, the number of branching points was significantly lower in the T2DM cohort compared to HV and a tendency for reduced vessel length and density was noticed, indicating that the overall tendency was for a reduction in the number of vessels. Another possible explanation is that due to slower flow in the

diabetes group the moving spins inside smaller vessels were saturated along with stationary spins resulting in signal loss.

Regardless of the cause for this reduced number of vessels, these findings are of great importance, since they highlight that the vasculature of the examined T2DM cohort is influenced even in the absence of neurological complications. A decrease in the number of blood vessels or a slower blood flow could result from the build-up of atherosclerotic plaques and especially in the case of a slower flow, it could be connected with the increased ATT times observed in the cohort in the previous chapter. These findings are not surprising based on the diabetic symptomatology since diabetic subjects are in a higher risk of ischemic stroke and are likely to develop small vessel disease. Another interesting observation is that the IGT cohort was highly similar to the HV cohort suggesting that alterations in the vascular anatomy have not yet occurred in this pre-diabetic group.

However, quantification of vasculature-descriptive metrics from the MCA angiograms which could lead to useful disease biomarkers is not typically conducted. A PubMed search with the terms “MRA”, “diabetes” and “brain” conducted in October 2018, returned 44 articles from which only one was relevant. This study by Yashiro et al. (192) reported findings similar to ours with regards to the number of branches / branching points. In their study, they focused on the same area (MCA) as we did in the present study. Their analysis involved additional metrics such as stems and vessel tortuosity, which were all extracted based on line tracing in the final MIP.

Quantitative angiogram analysis, typically not conducted due to the complex processing and the requirement for vessel segmentation, holds great promise for detecting subtle disease patterns. Our study along with the study by Yashiro et al. (192) are the only ones to our knowledge that have looked into analysing TOF-MRA images from a T2DM cohort in a quantitative way and resulted in similar findings. Angiograms hold great potential for extraction of vasculature-descriptive metrics and in the long run a detailed fully-automated analysis could provide important biomarkers. Being currently a field attracting increasing interest due to the segmentation challenges, TOF-MRA images could be used in the future for quantification of multiple metrics when their

processing is more standardised and the obstacles created by imperfect segmentation are surpassed.

7.6. Diffusion Weighted Image analysis

7.6.1 Methods

DWI scans were acquired at 2 b-values ($b = 0$ and $1000 \text{ s} / \text{mm}^2$) and in three orthogonal gradient directions. This DWI acquisition allows solely for the quantification of the ADC map, which is useful in order to identify how isotropic the diffusion pattern is. The higher b-value sensitizes the water molecules to motion and the three applied directions determine the directionality of this sensitization, whereas $b=0$ gives a T2-weighted image which allows for quantification. The ADC was calculated for every individual for $b = 1000$ using the following equation: $\text{ADC} = \log(S / S_0) / b$, whereby S_0 is the signal for $b = 0$ and S the signal for $b = 1000$. The signals were calculated for every b as the geometrical mean from signals emerging from all the directions. A further interesting extension to this study would be to apply more b-values and utilize a larger number of directions (e.g. 64) to sensitize the acquisition to more directions and hence determine other quantities of interest such as fractional anisotropy and radial diffusivity. A more detailed DTI acquisition would also allow for analysis of the white matter tracts and structural connectivity which was not possible in the present study.

Images were normalized to the MNI space using ANTs registration to generate an affine transformation. ADC values were extracted for structures of interest using the cortical and subcortical Harvard-Oxford maps from the following regions (left and right): amygdala, thalamus, hippocampus, caudate, putamen, pallidum, WM, CC, lateral ventricles, brainstem and accumbens. Additionally, ADC values were compared for the temporal, parietal, occipital and frontal lobes, the insula and thalamus. Overall data from 11 HV (aged 55.9 ± 7.1), 12 IGT (aged 54.8 ± 5.3) and 16 T2DM (aged 54.5 ± 11.8) patients were available.

7.6.2 Results

The ADC values for the different lobes and structures of interest are shown in tables 7.11 & 7.12. Example images for one subject are as in figure 7.21.

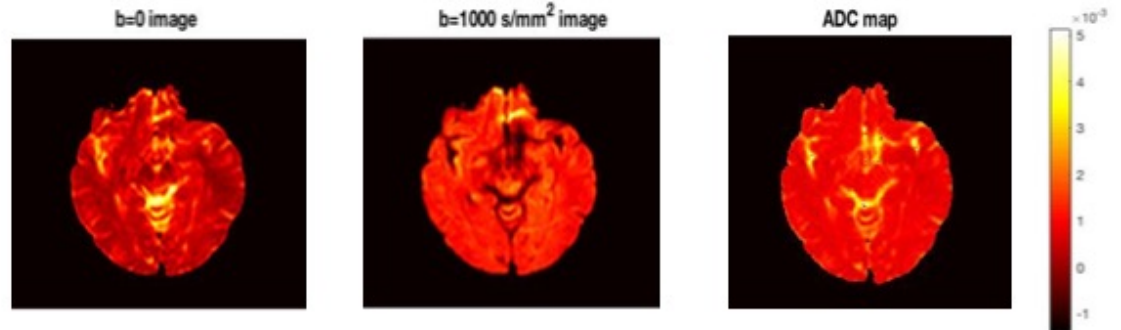


Figure 7.21: Example images for one subject for $b=0$, $b=1000 \text{ s/mm}^2$ and the associated ADC map.

Table 7.11: ADC values for the main lobes, insula and thalamus for the examined groups.

	HV ($\times 10^{-3}$) mm^2/s	IGT ($\times 10^{-3}$) mm^2/s	T2DM ($\times 10^{-3}$) mm^2/s
Frontal lobes	0.99 \pm 0.14	0.98 \pm 0.10	1.02 \pm 0.16
Temporal lobes	0.82 \pm 0.08	0.83 \pm 0.06	0.85 \pm 0.10
Parietal lobes	0.98 \pm 0.14	0.95 \pm 0.11	0.99 \pm 0.12
Occipital lobes	0.84 \pm 0.09	0.84 \pm 0.06	0.85 \pm 0.09
Insula	0.94 \pm 0.12	0.94 \pm 0.08	1.03 \pm 0.20
Thalamus	0.93 \pm 0.11	0.94 \pm 0.16	1.12 \pm 0.35

Table 7.12: ADC values in structures of interest for the examined groups.

	HV ($\times 10^{-3}$) mm^2/s	IGT ($\times 10^{-3}$) mm^2/s	T2DM ($\times 10^{-3}$) mm^2/s
Brainstem	1.10 \pm 0.15	1.15 \pm 0.16	1.27 \pm 0.21
Left accumbens	0.69 \pm 0.05	0.73 \pm 0.11	0.81 \pm 0.32
Left amygdala	0.84 \pm 0.13	0.97 \pm 0.09	0.99 \pm 0.18
Left caudate	1.06 \pm 0.23	1.15 \pm 0.47	1.44 \pm 0.65
Left CC	1.00 \pm 0.12	0.99 \pm 0.09	1.02 \pm 0.13
Left hippocampus	0.99 \pm 0.09	1.04 \pm 0.09	1.15 \pm 0.19
Left LV	2.23 \pm 0.38	2.41 \pm 0.45	2.44 \pm 0.46
Left pallidum	0.75 \pm 0.12	0.69 \pm 0.13	0.69 \pm 0.14
Left putamen	0.71 \pm 0.07	0.69 \pm 0.05	0.71 \pm 0.06
Left thalamus	1.07 \pm 0.15	1.07 \pm 0.20	1.26 \pm 0.41

Left WM	0.80±0.05	0.83±0.06	0.90±0.20
Right	0.71±0.06	0.70±0.07	0.88±0.27
accumbens			
Right amigdala	0.87±0.11	0.98±0.06	0.99±0.15
Right caudate	1.15±0.29	1.29±0.40	1.59±0.59
Right CC	1.02±0.14	1.01±0.09	1.04±0.13
Right	1.01±0.08	1.05±0.13	1.10±0.19
hippocampus			
Right LV	2.15±0.44	2.28±0.39	2.38±0.40
Right pallidum	0.61±0.11	0.57±0.19	0.62±0.16
Right putamen	0.66±0.07	0.64±0.11	0.67±0.10
Right thalamus	1.03±0.21	1.06±0.20	1.21±0.38
Right WM	0.79±0.05	0.81±0.04	0.89±0.17

Differences between the HV and the T2DM group were recorded for the following structures: brainstem ($t(26) = 2.309$, $p = 0.03$), left amygdala ($t(26) = 2.339$, $p = 0.03$), left hippocampus ($t(26) = 2.506$, $p = 0.02$), right accumbens ($z = 2.097$, $p = 0.04$), right amygdala ($t(26) = 2.146$, $p = 0.04$) and right caudate ($t(26) = 2.352$, $p = 0.03$). HV and IGT differed in the following regions: left and right amygdala ($t(26) = 2.953$, $p = 0.02$ and $t(26) = 2.898$, $p = 0.01$), and for IGT-T2DM for the right accumbens ($z = 2.344$, $p = 0.02$). Following FDR correction for multiple comparisons, none of the differences remained significant. However a tendency was noticed for the ADC values in the regions of difference identified prior to FDR correction to be higher in T2DM and IGT compared to HV indicating that the molecular diffusion is higher.

For the 3-group comparisons and the structures identified as significantly different in the binary comparisons the results were as follows: brainstem ($F(2,36) = 6.293$, $p = 0.04$), left amygdala ($\chi^2(2) = 8.467$, $p = 0.01$), left hippocampus ($\chi^2(2) = 7.146$, $p = 0.03$), right accumbens ($\chi^2(2) = 7.311$, $p = 0.03$) and right amygdala ($\chi^2(2) = 6.284$, $p = 0.04$). Following multiple comparison correction with FDR none of the differences remained significant between the groups.

7.6.3 Discussion

The diffusion pattern in the available cohort was investigated using DWI. The acquisition with three directions and two b-values allowed only for the calculation of ADC maps and not for a detailed diffusion analysis as would be the case with a DTI acquisition. Several significant differences were initially identified using statistical comparisons, however, significance was lost following multiple comparison correction. The ADC values in T2DM demonstrated a tendency to be higher in the amygdala, caudate, hippocampus, accumbens and the brainstem; in IGT the ADC was higher in the amygdala. These findings might indicate that there is a trend of increased water diffusivity, potentially connected to the endothelial dysfunction and BBB disruption observed in T2DM (10). Hence, the amygdala could potentially be one of the first areas with impaired (increased) water diffusivity in hyperglycemia, since it is the single structure brought up in the binary comparisons between hyperglycemia and normoglycemia.

Studies of diffusion patterns in T2DM have found global and local increases in ADC values (mean diffusivity) in line with our findings (339, 340). The majority of studies have used more advanced multi-directional techniques, such as DTI, to examine microstructural changes in WM, so more focus is put on non-isotropic/directional metrics such as fractional anisotropy (199). A more detailed analysis of the diffusion pattern would be of interest for the present cohort; however, the DWI acquisition means that this isn't possible. In the future, DTI or diffusion kurtosis imaging sequences could be incorporated into protocols investigating WM changes in T2DM and IGT.

7.7 Summary

In this chapter a multitude of MRI modalities were processed and processing solutions were discussed. These modalities involved high-resolution T1-weighted, T2 FLAIR, PC-MRA, DWI and MRA scans. The MPRAGE (T1 scan) was processed using multiple methods that have been extensively validated previously for group-wise comparisons. The burden of WMH was quantified from the FLAIR scan using existing software. The PC-MRA scan was analysed using a newly developed Matlab-based approach. DWI images were processed by implementing in Matlab the theoretical equations for quantification

of the ADC. Finally, the angiograms were also segmented using a newly developed method and vasculature specific metrics were derived. After proving the efficiency of the developed approaches, they were implemented to the available dataset.

For the **MPRAGE** processing: the brain was extracted based on SPM and minor dilation, erosion and filling operations were implemented when the results were suboptimal. Segmentation using SFCM with a 5x5 window was implemented following BFC with N4. Additionally, MPRAGE images were processed using VBM with FSL, Freesurfer, for cortical parcellation and structure volume determination and a machine learning-based approach based on feature reduction and classification. Key findings from this modality regarding the T2DM group (when compared to HV) involved differences in areas such as the hippocampi, amygdala and thalami identified using VBM. Interestingly there were no differences between HV and IGT subjects. The machine learning approach unraveled that high classification performance was achieved when considering voxels in the periphery of the cortex and around the ventricles.

For the **T2-FLAIR** scan, the brain lesion segmentation toolbox was used. A significantly higher number and volume of WMH in T2DM was recorded. Results for the IGT groups were similar to the HV group. When using textural analysis to identify potential subtle textural changes, the achieved classification performance was poor for all examined binary tasks.

The **PC-MRA** scan was processed using a developed Matlab tool, quantifying the velocity pattern at the level of the carotids. The average min, mean and max velocities were calculated for the whole arterial input, the left and right carotid. These velocities were quantified for the whole vessel area and for fixed regions of 10-voxels demonstrating the highest intensity. Key findings involved larger vessel area at baseline (non-significant) in the IGT and T2DM groups and lower velocity patterns at baseline and following ACZ injection compared to the HV group for both hyperglycemic groups.

The acquired **TOF-MRA** images were analysed using a developed semi-automated method. Results indicate that the diabetic group had a lower number of branching points.

Finally, for the analysis of the **DWI** a developed Matlab script was utilised. Findings following multiple comparison correction were not significant, however a tendency was noticed for increased ADC locally in IGT (amygdala) and T2DM (hippocampus, amygdala, accumbens, brainstem and caudate).

Five MRI modalities were processed after having presented a proof of concept for the adopted processing approaches. The purpose was to present a preliminary analysis of functional and structural changes occurring in the examined groups that can be considered along with the extended hemodynamic analysis presented in Chapter 6. Further processing optimization of the examined techniques could be evaluated in the future.

An optimal segmentation approach for the acquired MPRAGE scan was suggested and implemented. PC-MRA and TOF-MRA data were processed with newly developed a semi-automated methods and multiple metrics were extracted. These metrics, not typically quantified in neuroimaging studies differed significantly between the groups. Voxel-wise comparison for the structural scan using machine learning was implemented and high accuracy was achieved in the classification tasks. Image analysis unraveled structural and functional differences between HV and T2DM. A lower number of differences was recorded for IGT compared to both HV and T2DM. Regional differences in cortical and subcortical structures of interest (VBM), increased WMH burden (FLAIR), lower carotid flow velocity, non-significant carotid dilation at baseline (PC-MRA) and a reduction in the number of branching points in the MCA vascular territory (TOF-MRA) were the main findings for the T2DM group. Interestingly, IGT or else pre-diabetes was structurally similar to the HV group (MPRAGE, FLAIR, TOF-MRA). Functionally, differences were identified in the velocity pattern at the level of the carotids for IGT. Hence, IGT demonstrates a similar structural profile to HV, however, functionally the IGT profile bears similarities to the T2DM group.

The identified differences are of great importance; some of them were identified for the first time (velocity pattern, vasculature characteristics) and a larger cohort will be needed to assess reproducibility and provide further validation.

CHAPTER 8:

MRI-derived biomarkers for hyperglycemia unraveled

In the previous three chapters, findings emerging from every examined MRI modality were presented and discussed separately, without drawing any connections. In Chapter 6 hemodynamic metrics were extracted from the QUASAR ASL sequence and were subsequently processed using a developed pipeline described in Chapter 5. The data were analysed using two approaches. The first was based on conventional QUASAR processing whereby CBF, ATT and aBV metrics were of primary interest. The second approach was based on the implementation of an extended hemodynamic analysis whereby numerous perfusion-related metrics were extracted from the acquired hemodynamic signals. In Chapter 7, T1- and T2-weighted structural, TOF-MRA, PC-MRA and DWI scans were processed and metrics of interest were quantified. Thus, the aim of this final chapter is to combine metrics extracted from all modalities under one umbrella, to unravel potential structural, functional and physiological interactions.

Before examining such interactions, it is worth coming back to figure 4.1, introduced in chapter 4 and reproduced as figure 8.1 below, demonstrating the approximate spatial coverage of the utilised MRI techniques.

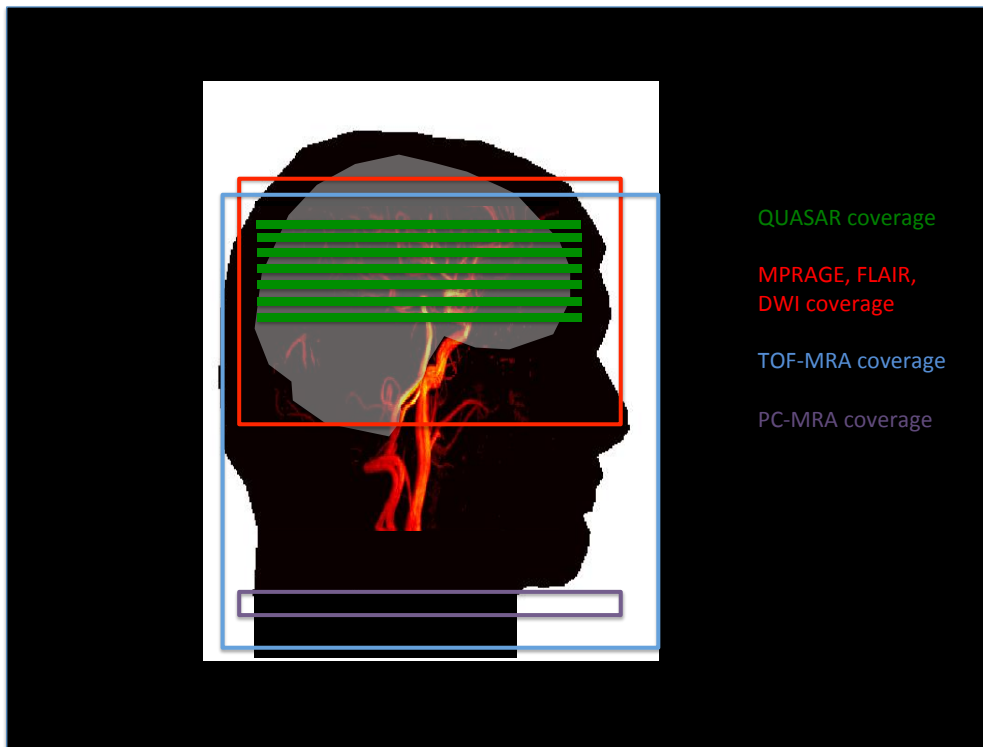


Figure 8.1: Spatial coverage of the utilised MR protocol.

In particular, the PC-MRA scan was acquired at the level of the carotids, with every effort being made by the radiographers to perform the scan at the same anatomical position for every subject. The metrics obtained from PC-MRA related to blood velocity and carotid diameter, and these were combined to provide flow measurements. The acquisition was optimized for the right carotid; however, velocity and flow measurements were also extracted from the left carotid and additional smaller arterial input sources.

Connections between QUASAR and PC-MRA

Considering the QUASAR ASL acquisition in tandem with the PC-MRA, we expect that, for the temporal length of the bolus ($\tau = 0.65\text{s}$), the underlying carotid flow pattern (both influenced by velocity and vessel cross-sectional area) will impact on the number of protons inverted by the ASL labeling pulses. As a result, the effect of both the velocity pattern and the number of labeled protons will be reflected in the calculated CBF values. Due to the utilisation of saturation pulses before and after the control and the labeled phases, the temporal length of the bolus is expected to be a well-defined 0.65s for all groups (155). If the labeling was continuous, the amount of labeled spins would

be proportional to the velocity of the inflowing spins and to the area covered by the feeding vessel. Utilisation of a pulsed labeling scheme with pre- and post-saturation pulses is nearly instantaneous which means that the amount of labeled spins at a given time in the labeling slab depends on the number of spins present at the time (connected to the area). Conversely, the amount of labeled spins surviving the post-saturation Q2-TIPS scheme (157) will depend on the velocity of the spins. These remarks are useful to consider when examining the flow pattern at the carotids and relating it to the perfusion parameters at the level of the cerebrum.

Processing of the PC-MRA data established that carotid flow at baseline was lower for T2DM subjects compared to IGT and HV. The post-ACZ carotid flow was higher in HV, lower in IGT and even lower for the T2DM subjects. The mean velocities for the left and right carotids were higher for the HV group both at baseline and post-ACZ compared to the other groups, whereas the feeding vessel cross-sectional area was larger for the T2DM group at baseline (not significant); this pattern was reversed post-ACZ.

Increased baseline CBF could be explained by increased carotid dilation.

Perfusion-related metrics were extracted from the QUASAR ASL arterial, residual and tissue signals at a voxel-wise level along with CBF, aBV and ATT measurements. Normally, a finding indicative of increased velocity and carotid flow would be expected to co-exist with increased CBF (as is the case for the HV group) and a similar connection (decreased carotid flow – decreased CBF) would be anticipated for the T2DM group. However, the recorded results at baseline point towards an increased CBF for the T2DM group.

The ASL signal is based on hydrogen protons in water molecules. Thus, tissue perfusion, as measured with ASL, relates to the amount of water being exchanged at the time of imaging. Even when considering this, a finding of increased baseline CBF would normally be connected to a finding of increased flow at the level of the carotids. However, as already mentioned, our findings in T2DM point towards increased baseline CBF at the cerebrum co-existing with reduced carotid blood velocity and increased carotid diameter. This increased vessel diameter might explain partially the increased baseline CBF finding in T2DM, especially when considering the applied pre- and post- saturation

pulses, implemented for a clear bolus definition. The idea behind Q2-TIPS is that the saturation pulses are applied at a time-point where the trailing edge of the labeled bolus leaves the labeling area. The amount of label that is saturated by the pulse depends on the velocity of the label and is therefore non-quantifiable. If the blood velocity was sufficient for the trailing edge of the bolus to leave the labeling region in time, then this finding could be explained by increased vessel dilation.

Increased carotid dilation and CBF at baseline in T2DM might suggest the existence of a compensatory mechanism.

Following ACZ injection, an increase was noticed for all parameters in the HV group. The increase was lower for the IGT and T2DM groups for metrics emerging from both the QUASAR and PC-MRA scans. High flow-related baseline values and lower than expected increases in parameters following ACZ injection in the hyperglycemic groups might indicate the presence of a compensatory mechanism for impaired oxygen retention at rest, leading to vasodilation, especially in the T2DM group. In T2DM studies, it has been suggested that due to the shift in the oxygen dissociation curve of glycated hemoglobin, tissue hypoxia occurs and an increased baseline flow can be observed as a compensatory mechanism (302). This interpretation could potentially explain our results as well.

The overall tendency for T2DM subjects, when examining their cerebral vasculature using TOF-MRA, was a reduction in the number of branching points. A tendency towards reduced vessel length and density was also noticed for the MCA (not significant). This finding could also result from the slower velocity of the moving blood inside the vasculature of T2DM patients, which can influence the depicted vasculature if the velocity is slow enough for the spins inside the vessels to be saturated.

In chapters 6 and 7, it was found that type-2 diabetes is associated with lower CVR, increased baseline CBF, prolonged TTP, HWL and FW values for hemodynamic signals, lower velocity at the level of the carotids and increased number of WMH. A trend towards increased ADC values, lower cortical thickness and increased CSF volume was uncovered. Based on VBM analysis, we have identified areas of differences between the groups mainly centered in

the caudate, putamen, amygdala, brainstem, hippocampus and thalamus. The IGT groups demonstrated a distinct functional pattern, with similarities at baseline to the HV groups and post-ACZ to the T2DM group when considering the QUASAR scan. Structurally, IGT demonstrated more similarities with the HV group. A slightly larger carotid diameter was discovered at baseline for IGT and T2DM. Baseline CBF was higher in T2DM compared to HV for the examined vascular territories, a pattern which was not present post-ACZ. The T2DM group also demonstrated a higher number of WMH and a smaller number of branching points compared to HV. A pictorial summary for quantified measures of interest is presented for the three groups in figure 8.2. The mean value is shown for the baseline and post-ACZ scans for the following metrics quantified in chapters 6 and 7: carotid diameter, carotid velocity (mean, min, max left and right), ACA, MCA, PCA, GM and WM CBF, number and volume of white matter hyperintensities (shown for convenience in the post-ACZ scan) and density, length and number of branching points.

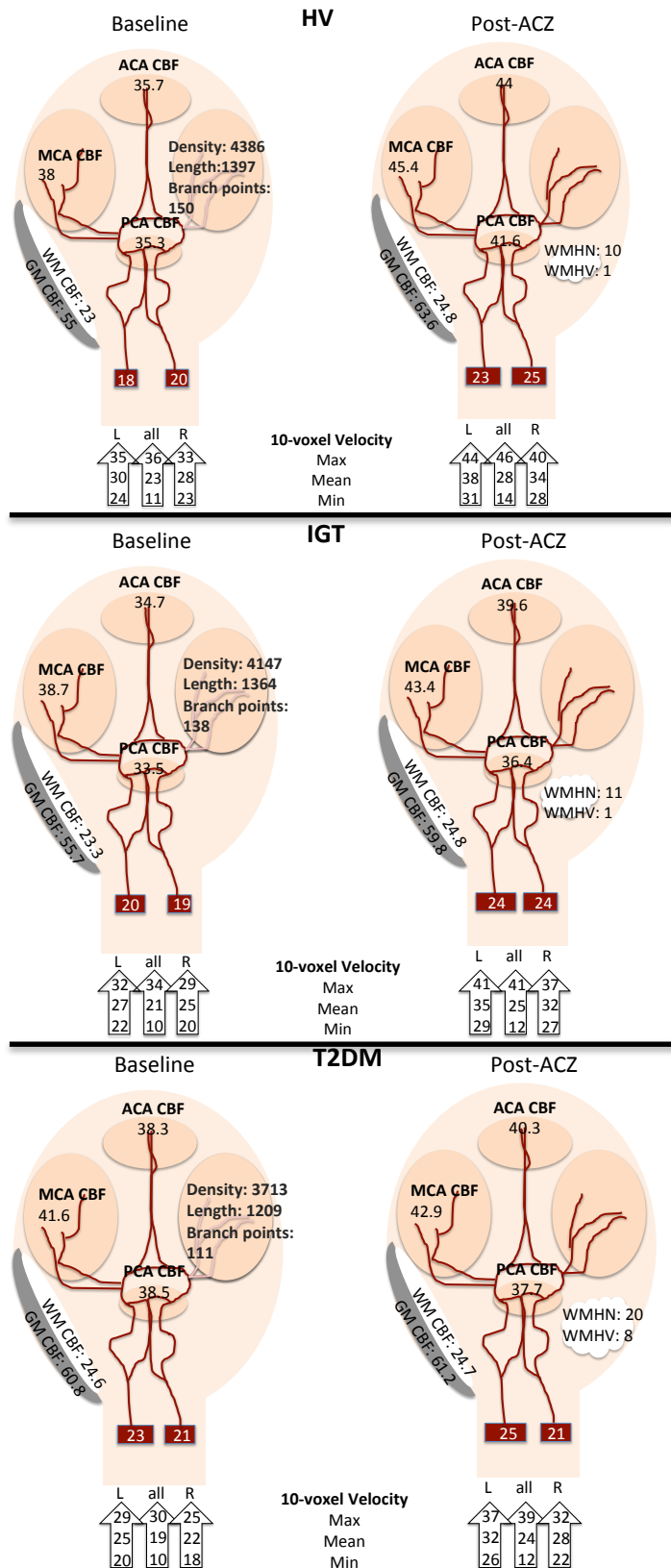


Figure 8.2: Summary figure for the three examined groups and metrics of interest. Values for carotid velocity, CBF in the examined vascular territories, carotid diameter, number of WMH and GM and WM CBF are shown.

8.1 Determination of the feature combination leading to optimal class-differentiation

The idea, in this sub-chapter, is to detect the feature combination that leads to optimal group-differentiation, by taking into account features derived from every considered modality using a multi-variate processing approach. To achieve this, measures from each MRI technique, based on findings from chapters 6 and 7, were chosen in a supervised manner and were incorporated into the feature vector under consideration. The resulting vector was analysed using a machine learning approach to identify the optimal feature combination based on all techniques (figure 8.3). Two models were considered, the first one comprised all modalities and the second comprised MPRAGE, TOF-MRA, PC-MRA and QUASAR scans. This choice was made since FLAIR and DWI scans were not acquired for all HV.

The selected features from the QUASAR acquisition were the ones comprising model 5 which demonstrated one of the highest performances when examined in Chapter 6 (243 features). The included MPRAGE features were cortical and subcortical GM volumes, WM volume, ventricular volume (normalised), the volume of the hippocampi, brainstem, thalami, amygdala, putamen, accumbens and the left and right cortical thickness (18 features). The ADC values from the same structures along with the ADC from the occipital and temporal lobes were included only in the first model from the DWI scan (19 features).

The number and volume of WMH was included only in the first model. Mean, max and min velocities from the 10-voxel regions in the left and right carotids examined in Chapter 7 and all the arterial input were included from the PC-MRA scan (24 features). The number of branching points, vessel density and length were included from the TOF-MRA scan. Additionally, age and sex were added into the feature vector.

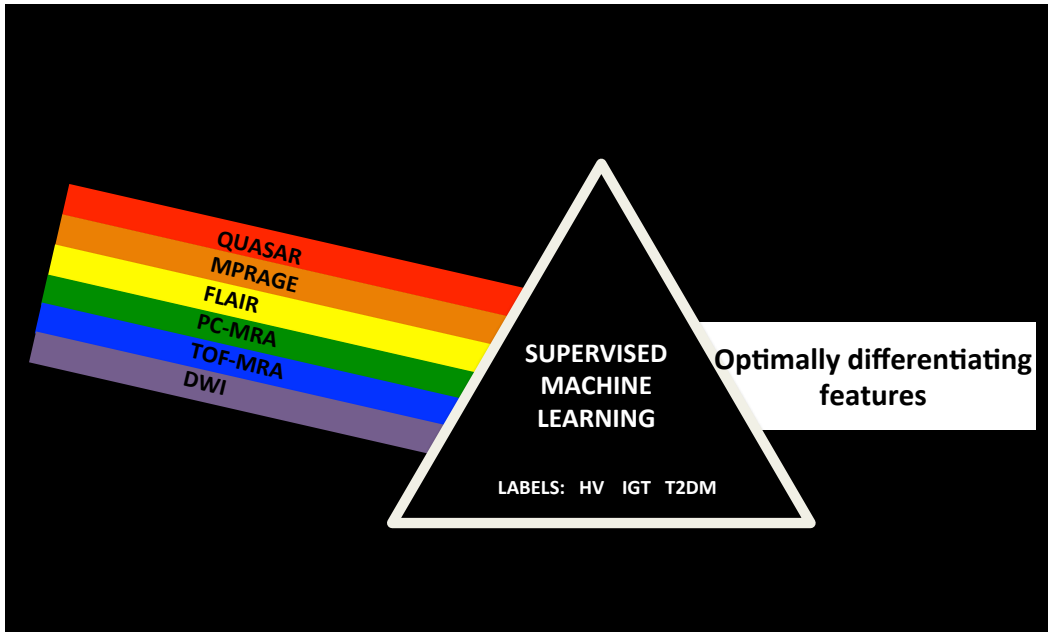


Figure 8.3: A pictorial representation of the machine learning analysis, combining metrics from all modalities.

For the first model, 34 subjects were analysed (11 HV, 8 IGT, 15 T2DM). These numbers per group were formed due to the absence of 5 scans from the HV group: 3 FLAIR/DWI were not acquired, subjects with one noisy MPRAGE and 1 noisy PC-MRA scan were excluded, subjects with 2 noisy QUASAR and 2 noisy FLAIR scans were omitted from the IGT group and subjects with 1 noisy QUASAR and 1 noisy MPRAGE scan from the T2DM group. Overall, the considered features numbered 311. Results for every task can be found in table 8.1.

Table 8.1: Accuracy (Acc) sensitivity (Sens) specificity (Spec) features and number of features (Nf) for every task and the first model. The number in brackets accompanying the number of features indicates that they were identified in the top-M features. With BOLD the non-QUASAR features are underlined>.

Task	Acc(%)	Sens(%)	Spec(%)	Features	Nf
HV vs T2DM	96.2	93.3	100	CVR (26), <u>ACA</u> <u>HWL</u> <u>AIFSH</u> post-ACZ (25), <u>ACA</u> <u>TTP</u> <u>AIFSH</u> post-ACZ (25), number of branching points (23), <u>W SKEW</u> <u>AIFSH</u> post-ACZ (15), <u>W KURT</u> <u>AIFSH</u> baseline (6), <u>PCA</u> <u>HWR</u> <u>TIS</u> post-ACZ (6), <u>WB</u> <u>HWL</u> <u>AIFSH</u> post-ACZ (2), <u>ACA</u>	10 (5)

HV vs IGT& T2DM	85.3	87.0	81.8	SKEW AIFSH post-ACZ (1), ACA TTP TIS post-ACZ (1) Not shown	68 (49)
HV vs IGT	89.5	75.0	100	PCA HLW AIFSH post-ACZ (18) PCA TTP COMB post-ACZ (1)	2 (1)
IGT vs T2DM	87.0	93.3	75.0	ACA HWL AIFSH post-ACZ (10), CVR (9), ACA TTP COMB post-ACZ (3), MCA SKEW COMB post-ACZ (1)	4 (1)

For the second model, data from 14 HV, 10 IGT patients and 15 patients with T2DM were retained and overall 289 features comprised the considered feature vector. These numbers resulted from exclusion of subjects with 1 noisy MPRAGE and one noisy PC-MRA scan for the HV group, 2 noisy QUASAR scans for the IGT group and one noisy QUASAR and one noisy MPRAGE from the T2DM group. Results for every task can be found in table 8.2.

Table 8.2: Accuracy (Acc) sensitivity (Sens) specificity (Spec) features and number of features (Nf) for every task and the second model. The number in brackets accompanying the number of features indicates that they were identified in the top-M features. Bold is used for the non-QUASAR features.

Task	Acc(%)	Sens(%)	Spec(%)	Features	Nf
HV vs T2DM	96.6	93.3	100	CVR (19), ACA HWL AIF _{SH} post-ACZ (15), ACA TTP AIF _{SH} post-ACZ (11), PCA HWR ΔM_{cr} post-ACZ (7), number of branching points (3), GM CBF baseline (2), ACA SKEW AIF _{SH} baseline (1)	7 (2)
HV vs IGT& T2DM	87.2	92.0	78.6	CVR (26), ACA HWL AIF _{SH} post-ACZ (5), PCA HWR ΔM_{cr} post-ACZ (3), W KURT ΔM_{ncr} baseline (3), W KURT AIF _{SH} baseline (2)	5 (1)
HV vs IGT	100	100	100	PCA HWL AIF _{SH} post-ACZ (24), PCA TTP AIF _{SH} post-ACZ (21), PCA HWL ΔM_{ncr} post-ACZ (2), W KURT ΔM_{cr} post-ACZ (1)	4 (2)
IGT vs T2DM	68.0	80.0	50.0	CVR (9), GM CBF baseline (9), W	5 (1)

	HWR ΔM_{cr} baseline (3), ACA	
	KURT ΔM_{ncr} post-ACZ (3), MCA	
	HWL AIF _{SH} baseline (1)	

The combined analysis of all modalities indicated that QUASAR ASL is the main modality contributing information leading towards optimal class-separation. The only feature not derived from the QUASAR sequence brought up as optimal with a high occurrence for the HV vs T2DM task was the number of branching points, a feature extracted from the TOF-MRA image. The considered analysis, based on features from all modalities combined into a single model, emphasizes the importance of incorporating into a study protocol a perfusion imaging modality such as QUASAR for pathology detection. The number of branching points, which was part of the optimally-differentiating pattern for HV versus T2DM, was quantified based on processing of the TOF-MRA scan, which is not typically conducted, since angiogram evaluation mainly involves visual assessment and is aimed at detecting gross changes.

The dominance of QUASAR features in the final pattern could also be attributed to the fact that the number of features from every technique was not balanced (249). The approach of concatenating all features into a single vector is very common; however, other feature fusion strategies have been suggested. An approach, for creating a balanced feature vector, is based on applying classification approaches in every technique separately to reduce the features emerging from each one and subsequently combining the resulting optimal features into a single model (341). Such an approach was adopted to provide reassurance that the optimal pattern is not dominated by QUASAR features due to their very high number.

Model 1 – balanced number of features

A balanced number of features was considered for the two models and the HV vs T2DM and HV vs IGT tasks.

For the HV vs T2DM task classification solely with the QUASAR features was run and the optimal performance was achieved with 44 features (88.5%).

The second highest performance was recorded for 14 features and was 84.6%¹. These 14 features were retained. Subsequently, classification was run for all non-QUASAR features separately and the maximum achieved performance was recorded with three features: the number of branching points (occurrence of 23 in the top-1 of the SVM-RFE matrix), maximum velocity in the left carotid pre (occurrence of 2 in the top-1) and post-ACZ (occurrence of 1) and was 65.4%. When the 11 significantly different features from all non-QUASAR modalities were combined with the 14 QUASAR features, maximum performance was **92.3%** achieved with 5 features (top-2): number of branching points (occurrence of 2 in the top-M of the SVM-RFE matrix), ACA TTP AIF_{SH} post-ACZ (occurrence of 3), W SKEW AIF_{SH} post-ACZ (occurrence of 2), ACA HWL AIF_{SH} post-ACZ (occurrence of 24) and CVR (occurrence of 21). Hence, even when using a balanced feature vector, the dominating features emerged from QUASAR ASL and were based on the time delays in the delivery of the bolus to the tissue post-ACZ and CVR. The only non-QUASAR feature part of the optimal pattern, which also dominated the non-QUASAR classification task, was the number of branching points.

For the HV vs IGT task, when only QUASAR features were used, maximum performance of 89.5% was achieved with 2 features: PCA HWL AIF_{SH} post-ACZ (18), PCA TTP ΔM_{ncr} post-ACZ (1). When non-QUASAR features were used, 2 features differed significantly and maximum performance was 63.2% achieved with a single feature the ADC of the right amygdala. When all features were combined, maximum performance of 89.5% was achieved with the QUASAR features. These QUASAR features were both extracted from post-ACZ curves and in particular from the PCA vascular territory.

Model 2 – balanced number of features

When examining the HV vs T2DM task and the QUASAR derived features, 56 differed significantly and a maximum performance of 86.2% was achieved with 29 features. Second best performance was 82.8% with 10 features, which were kept for the subsequent analysis. When examining the

¹ Please note that differences in performance compared to chapter 6 are explained by the different subjects used for analysis in this section due to absence of DWI and FLAIR acquisitions for several subjects

non-QUASAR features, 14 differed (out of the 45) and a maximum performance of 79.3% was achieved with 9 features. When combined, maximum performance of 96.6% was achieved with 10 features identified to the top-5 of the SVM-RFE matrix. These included the number of branching points (29) from non-QUASAR features and the other 9 were all derived from QUASAR: PCA HWR ΔM_{cr} post-ACZ (occurrence in the top-M: 22), W KURT ΔM_{cr} baseline (2), ACA TTP AIF_{SH} post-ACZ (26), ACA SKEW AIF_{SH} baseline (1), W KURT AIF_{SH} baseline (1), MCA PEAK AIF_{SH} baseline (1), ACA HWL AIF_{SH} post-ACZ (27), GM CBF baseline (7) and CVR (29).

For the HV vs IGT task, 93 features derived from the QUASAR sequence were significantly different. Maximum performance of 100% was achieved with 4 features. When the non-QUASAR features were examined, only one differed significantly between the groups and maximum performance was 66.7%; this feature was the volume of cortical GM. When combined, maximum performance of 100% was achieved solely with the QUASAR features identified in the top-2 of the SVM-RFE matrix, which were: W KURT ΔM_{cr} post-ACZ (occurrence of 1), PCA TTP AIF_{SH} post-ACZ (21), PCA HWL AIF_{SH} post-ACZ (24), PCA HWL ΔM_{ncr} post-ACZ (2).

Hence, feature fusion to create balanced vectors changed the observed results and performance for the first model and the HV vs T2DM task for which a lower performance was achieved. The QUASAR feature dominance in the optimally differentiating feature pattern is not attributed to the fact that the technique contributes the majority of features, but rather to their high discriminatory power. For the HV vs T2DM task, an equally strong feature was the number of branching points. Similarities in performance, with and without a balanced feature vector, could also be attributed to the usage of a dimensionality reduction technique retaining only significantly different features, which greatly reduces the number of utilised features.

The reader is reminded that accuracy of 96.9% was achieved with 27 features (Chapter 6.3.2) for the HV vs T2DM task. Model 2 in the present chapter achieved a performance of 96.6% with only 7 features emerging mainly from the ACA, PCA territories and from GM. The achieved accuracy was the same as in chapter 6.3.2 for the HV vs IGT task with features emerging from the post-ACZ curves and the PCA territory and watershed areas.

Overall in this subchapter features from all examined modalities were combined into a single model. It was shown that optimal feature combinations for the examined tasks emerge mainly from the QUASAR sequence. The only non-QUASAR feature contributing to optimal separation between HV and T2DM emerged from the cerebral angiogram. Accuracy for this task was the same when solely QUASAR and features from all techniques were considered. However, inclusion of the number of branching points (TOF-MRA) led to a smaller optimal pattern, which is desirable.

8.2 Overall thesis discussion

The goal of the work presented in this thesis was to gain a deep insight into the brain of subjects with impaired glucose tolerance and type-2 diabetes, being particularly focused in cerebral perfusion. To achieve this, MRI modalities capturing different aspects of structure and function were analysed using state-of-the-art processing techniques to capture group-differences and detect cerebral areas and MR-derived metrics contributing towards optimal group-separation.

The detailed analysis and described methodologies established that the volumetric changes were subtle between the groups especially when focusing on specific ROIs; more differences were detected when the image was analysed at a voxel-wise level. The number and volume of white matter hyperintensities was significantly higher in the T2DM groups compared to HV. Processing of the cerebral vasculature was focused on the MCA territory and identified that the number of branching points differed. Carotid flow velocity analysis unraveled several differences in the velocity pattern between T2DM patients and HV, both at baseline and following ACZ injection. Both laminar and whole vessel velocity was decreased in both T2DM and IGT. At the level of the cerebrum, perfusion analysis conducted using QUASAR ASL and newly developed processing tools, identified a multitude of hemodynamic metrics differing between all considered groups, suggesting the existence of a distinct hemodynamic pattern.

Structural alterations were focused on several cortical and subcortical regions, WM and cerebral vasculature.

Global and localized atrophies have been consistently reported in diabetic cohorts (33). When analysing the available cohort though, only the ventricular volume differed between the groups; a finding which did not remain significant following multiple comparison correction. This finding is of great importance, since it could potentially mean that the considered diabetic group was captured at a disease stage where prominent structural abnormalities associated with volume reduction have not yet occurred. Significant structural alterations involved WMH and changes in the vasculature. The number of WMH was higher in T2DM, a finding not consistently reported in T2DM studies. The IGT group had a similar volume and number of WMH to the HV group. The number of branching points in the MCA territory was significantly reduced in T2DM. The results from the DWI analysis uncovered several areas where the water diffusivity was impaired, such as the amygdala, hippocampi, brainstem and caudate. The amygdala (left and right) was the only region differing between HV and IGT, suggesting that early changes in the diffusivity of water molecules might occur there. However, it needs to be emphasised that the DWI findings were not significant following multiple comparison correction, hence they are suggestive of the existence of a certain pattern regarding water diffusivity which warrants further investigation.

VBM analysis identified several regions of difference between the groups. VBM differs from ROI specific approaches, since it focuses on the GM PV maps at a voxel-wise level. Hence, it is capable of detecting more dispersed patterns of difference between the groups. Structures that differed between IGT and T2DM involved the amygdala, thalami, hippocampi and accumbens. The IGT group did not differ from the HV group.

The fact that the cohort was cognitively asymptomatic and without prominent atrophy patterns, highlights the importance of conducting a detailed functional (in our case hemodynamic) analysis to shed light on potential functional alterations that could lead, if prolonged, to structural changes observed consistently in T2DM patients.

Functional analysis identified the existence of a potential compensatory mechanism

Functional characteristics were explored using PC-MRA, capturing the blood velocity pattern at the level of the carotids and QUASAR ASL, capturing the CBF pattern at the level of the cerebrum. Starting from the carotid level, the velocity of the blood was reduced and vessels appeared more dilated in T2DM and IGT (not a significant finding). Following ACZ injection, the increase in the carotid diameter was significant only for the HV group indicating the ability for vasodilation. The carotid diameter was relatively static in both IGT and T2DM following induced vasodilation. These findings, together, point towards increased dilation at baseline for the hyperglycemic groups with reduced ability to respond to increased needs for oxygen and nutrients, when presented with a task requiring dilation to meet energy demands.

A detailed hemodynamic analysis, conducted using ASL at the level of the cerebrum, focused on the vascular territories of the internal carotid and watershed areas, identified a delayed, more dispersed, delivery of the labeling bolus in the T2DM groups. Interestingly, the results for IGT at baseline were more similar to the HV groups and post-ACZ to the T2DM group, indicating that functional alterations are also occurring in pre-diabetes. More importantly, classification of HV and IGT was perfect and driven by features capturing delayed and dispersed bolus delivery post-ACZ, while no structural differences were observed between the HV and IGT groups. This finding indicates that a potential analysis targeted at unraveling early biomarkers for diabetes, focused on subjects with pre-diabetes, might miss early functional changes if it investigates only structural changes or functional alterations occurring at rest.

The finding of increased baseline CBF was an unexpected finding for the cohort. We were expecting decreased CBF both at baseline and post-ACZ and a decreased CVR based on previous reports for the T2DM group (33). The two latter findings were verified, the former one was not. These findings are of particular interest, since increased CBF has only been reported in a few studies (46, 47). It might be connected with early stages of tissue hypoxia, whereby the oxygen is not sufficiently retained due to hyperglycemia and a compensatory mechanism leading to baseline hyper-perfusion is established to meet the tissue energy demands (302).

This mechanism has also been observed in the early stages of Alzheimer's, when mild cognitive impairment has been detected (342). However, this compensatory mechanism fails after a certain point leading to structural alterations, hypo-perfusion and cognitive changes. The cohort under consideration was neurologically asymptomatic; hence, we might have captured this cohort at a stage where the compensatory mechanism built to account for tissue hypoxia, has not yet failed. This would potentially explain both the finding of increased baseline CBF, increased vessel dilation and reduced CVR. For this to be validated, a follow-up scan and detailed cognitive evaluation should take place. Potential cognitive changes and failure of the detected compensatory mechanism leading to hypo-perfusion would provide a clearer picture of how the cascade of alterations occurs in diabetes.

Features that could be evaluated as potential disease biomarkers were identified using a machine learning framework

Currently, there are no MR-derived features connected exclusively with T2DM. Global and local atrophy patterns, typically detected in diabetic subjects, are also present in other conditions such as Alzheimer's (343). WMHs, occasionally present in T2DM, are also connected with all major cardiovascular risk factors, such as hypertension, and are not a consistent finding (327). Altered patterns in mean diffusivity, carotid flow, velocity and cerebral blood flow are not exclusively connected with diabetes and also occur in other diseases such as Alzheimer's (343, 344). Hence, using a framework examining feature combinations and identifying the optimal-ones for the classification task in question might have the potential to capture disease-specific patterns of pathophysiology.

The results, especially those based on arterial spin labeling, are extremely promising regarding the ability of the technique to capture subtle hemodynamic patterns. Optimal classification was achieved with only a few QUASAR-derived features that could be evaluated as disease biomarkers (Chapter 6). The achieved classification accuracy for the HV versus T2DM task reached 96.6% and for the HV versus IGT task 100%, when considering solely QUASAR hemodynamic features. These findings suggest that inclusion of a perfusion imaging acquisition in clinical protocols, especially in its dynamic

form, could be beneficial and of clinical value. Features that were identified as highly discriminant for both the HV vs T2DM and HV vs IGT tasks could be evaluated as potential biomarkers for hyperglycemia and diabetes. Such features capture the pattern of delivery of the labeled bolus to the tissue (how delayed and dispersed the pattern is) and were extracted from all acquired hemodynamic curves. Also, the majority of optimal features were extracted from the post-ACZ scan, emphasizing the importance of incorporating into the protocol a vasodilating stimulus to evaluate the ability of the neurovascular unit to adapt to higher energy demands.

In this final chapter, all the techniques were brought together and analysed using a machine-learning framework to identify optimally differentiating feature combinations. Two methods were applied to detect the feature combination leading to high classification performance. The first method utilised all QUASAR features and a selection of features from all the other MRI modalities, which were significantly different or were expected to differ between healthy individuals and diabetic patients. In the second model, a small number of highly discriminant features from QUASAR was used along with the same selection of features from the other MRI modalities to create a balanced pattern. The QUASAR features for both methods, dominated the classification tasks leading to optimal class separation, suggesting that the QUASAR-extracted hemodynamic metrics are particularly strong features in accurately classifying normoglycemia versus hyperglycemia. The only feature emerging from another technique was the number of branching points, calculated based on the TOF-MRA scan, which was one of the top features for HV vs T2DM classification. The accuracy was 96.6%, achieved with only 7 features, as opposed to 96.9% with 27 features, when utilising only QUASAR features. This suggests that the number of branching points is a strong feature leading to a smaller optimal pattern of features. Overall, the QUASAR metric dominance when the multi-modal features were combined into one single model, emphasized even more the strength of the considered QUASAR-derived features and their sensitivity in separating the groups under consideration.

The protocol utilised in this study was extensive, capturing different aspects of function and structure. However, further information could be acquired. Of interest would be, instead of using DWI, to acquire DTI images.

DTI images can shed light on the complex diffusion patterns in the brain and are not confined to the calculation of a single parameter (ADC). Diffusion tractography could be applied, along with graph analysis, to examine structural connectivity (345). Additionally, MRS data could be acquired and information regarding the concentration of different metabolites quantified (346). Finally, resting-state fMRI could shed light into changes in functional connectivity of areas of interest (347). This would allow the identification of optimally discriminative features based on an even larger collection of MRI features, using an approach similar to the one used earlier on this chapter, where features from different modalities were combined in a supervised manner.

In this study, only a small cohort was available and this poses limitations for the generalisability of the observations, since we could be modeling cohort idiosyncrasies. A larger cohort needs to be recruited, in order to examine if the findings of this thesis can be replicated. An interesting extension would be to compare QUASAR ASL with time-encoded ASL, which offers high SNR and examine them in the same study to see if the same pattern can be captured using alternative multi time-point ASL techniques.

The extracted optimal features from the classification tasks hold great potential to be examined as disease biomarkers and are directly connected to underlying physiological processes, coupled with the mechanism of water delivery to the tissue. Hence, it would be of interest to examine, in a future study with a larger cohort, the associated hemodynamic curves. Another interesting extension to this study would be to recruit a cohort comprised of healthy volunteers, IGT and T2DM subjects with and without cognitive impairment to evaluate whether the detected compensatory mechanism fails when cognitive decline emerges.

References

1. Ghosh SK. Human cadaveric dissection: a historical account from ancient Greece to the modern era. *Anat Cell Biol.* 2015;48(3):153-69.
2. Zimmerman C. The Anatomical Renaissance. Young Historians Conference 2011.
3. Mansfield P, Garroway AN, Grannell PK. Image formation in NMR by a selective irradiative process. *J Phys C.* 1974;7:457-62.
4. Lauterbur P. Image Formation by Induced Local Interactions: Examples Employing Nuclear Magnetic Resonance. *Nature.* 1973;242:190-1.
5. Miller KL, Alfaro-Almagro F, Bangerter NK, Thomas DL, Yacoub E, Xu J, et al. Multimodal population brain imaging in the UK Biobank prospective epidemiological study. *Nat Neurosci.* 2016;19(11):1523-36.
6. DiabetesUK. Diabetes: Facts and Stats. 2015.
7. Ramachandran VS. The tell-tale brain: A neuroscientist's quest for what makes us human. New York, NY, US: W W Norton & Co; 2011.
8. Zlokovic BV. The blood-brain barrier in health and chronic neurodegenerative disorders. *Neuron.* 2008;57(2):178-201.
9. Daneman R, Prat A. The blood-brain barrier. *Cold Spring Harb Perspect Biol.* 2015;7(1):a020412.
10. Prasad S, Sajja RK, Naik P, Cucullo L. Diabetes Mellitus and Blood-Brain Barrier Dysfunction: An Overview. *J Pharmacovigil.* 2014;2(2):125.
11. Harder DR, Zhang, C., Gebremedhin, D. Astrocytes Function in Matching Blood Flow to Metabolic Activity. *News Physiol Sci.* 2002;16.
12. Zlokovic BV. Neurovascular pathways to neurodegeneration in Alzheimer's disease and other disorders. *Nat Rev Neurosci.* 2011;12(12):723-38.
13. Muoio V, Persson PB, Sendeski MM. The neurovascular unit - concept review. *Acta Physiol (Oxf).* 2014;210(4):790-8.
14. Girouard H, Iadecola C. Neurovascular coupling in the normal brain and in hypertension, stroke, and Alzheimer disease. *J Appl Physiol* (1985). 2006;100(1):328-35.
15. Duarte JV, Pereira JM, Quendera B, Raimundo M, Moreno C, Gomes L, et al. Early disrupted neurovascular coupling and changed event level hemodynamic response function in type 2 diabetes: an fMRI study. *J Cereb Blood Flow Metab.* 2015;35(10):1671-80.
16. Moore CI, Cao R. The hemo-neural hypothesis: on the role of blood flow in information processing. *J Neurophysiol.* 2008;99(5):2035-47.
17. Duncombe J, Kitamura A, Hase Y, Ihara M, Kalaria RN, Horsburgh K. Chronic cerebral hypoperfusion: a key mechanism leading to vascular cognitive impairment and dementia. Closing the translational gap between rodent models and human vascular cognitive impairment and dementia. *Clin Sci (Lond).* 2017;131(19):2451-68.
18. Phillips AA, Chan FH, Zheng MM, Krassioukov AV, Ainslie PN. Neurovascular coupling in humans: Physiology, methodological advances and clinical implications. *J Cereb Blood Flow Metab.* 2016;36(4):647-64.
19. Chandra A, LI W, Stone C, Geng X, Ding Y. The cerebral circulation and cerebrovascular disease I: Anatomy. *Brain Circ.* 2017;3:45-56.

20. Perutz MF. THE HEMOGLOBIN MOLECULE. *Scientific American*. 1964;211(5):64-79.
21. Lawther BK, Kumar S, Krovvidi H. Blood-brain barrier. *Continuing Education in Anaesthesia Critical Care & Pain*. 2011;11(4):128-32.
22. de la Monte S, Tong M. Insulin Resistance and Metabolic Failure Underlie Alzheimer Disease 1. In: Farooqui A, Farooqui T, editors. *Metabolic Syndrome and Neurological Disorders*: Wiley-Blackwell; 2013.
23. DeFronzo RA. Pathogenesis of type 2 diabetes mellitus. *Medical Clinics of North America*. 2004;88(4):787-835.
24. Tuomilehto J, Lindström J, Eriksson JG, Valle TT, Hämäläinen H, Ilanne-Parikka P, et al. Prevention of Type 2 Diabetes Mellitus by Changes in Lifestyle among Subjects with Impaired Glucose Tolerance. *New England Journal of Medicine*. 2001;344(18):1343-50.
25. Investigators TDT. Effect of rosiglitazone on the frequency of diabetes in patients with impaired glucose tolerance or impaired fasting glucose: a randomised controlled trial. *The Lancet*. 2006;368(9541):1096-105.
26. Nathan DM, Davidson MB, DeFronzo RA, Heine RJ, Henry RR, Pratley R, et al. Impaired fasting glucose and impaired glucose tolerance: implications for care. *Diabetes Care*. 2007;30(3):753-9.
27. Cheung N, Mitchell P, Wong TY. Diabetic retinopathy. *The Lancet*. 2010;376(9735):124--36.
28. Muthuppalaniappan VM, Sheaff M, Yaqoob MM. Diabetic nephropathy. *Medicine*. 2015;43(9):520--5.
29. Tesfaye S. Neuropathy in diabetes. *Medicine*. 2010;38(12):649--55.
30. Yamagishi S. Cardiovascular disease in recent onset diabetes mellitus. *Journal of cardiology*. 2011;57(3):257-62.
31. WHO. Definition and diagnosis of diabetes mellitus and intermediate hyperglycaemia 2006.
32. Pu LJ, Shen Y, Lu L, Zhang RY, Zhang Q, Shen WF. Increased blood glycohemoglobin A1c levels lead to overestimation of arterial oxygen saturation by pulse oximetry in patients with type 2 diabetes. *Cardiovascular Diabetology*. 2012;11(110).
33. Brundel M, Kappelle LJ, Biessels GJ. Brain imaging in type 2 diabetes. *European Neuropsychopharmacology*. 2014;24:1967--81.
34. van Bussel FCG, Backes WH, Hofman PAM, van Oostenbrugge RJ, van Boxtel MPJ, Verhey FRJ, et al. Cerebral Pathology and Cognition in Diabetes: The Merits of Multiparametric Neuroimaging. *Front Neurosci*. 2017;11:188.
35. Manschot SM, Brands AMA, van der Grond J, Kessels RPC, Algra A, Kappelle LJ, et al. Brain magnetic resonance imaging correlates of impaired cognition in patients with type 2 diabetes. *Diabetes*. 2006;55(4):1106-13.
36. Last D, Alsop DC, Abduljalil AM, Marquis RP, de Bazelaire C, Hu K, et al. Global and regional effects of type 2 diabetes on brain tissue volumes and cerebral vasoreactivity. *Diabetes Care*. 2007;30(5):1193-9.
37. Espeland MA, Bryan RN, Goveas JS, Robinson JG, Siddiqui MS, Liu S, et al. Influence of Type 2 Diabetes on Brain Volumes and Changes in Brain Volumes Results from the Women's Health Initiative Magnetic Resonance Imaging Studies. *Diabetes Care*. 2013;36(1):90-7.

38. Zhang Y, Zhang X, Zhang J, Liu C, Yuan Q, Yin X, et al. Gray matter volume abnormalities in type 2 diabetes mellitus with and without mild cognitive impairment. *Neuroscience Letters*. 2014;562:1-6.
39. Roberts RO, Knopman DS, Przybelski SA, Mielke MM, Kantarci K, Preboske GM, et al. Association of type 2 diabetes with brain atrophy and cognitive impairment. *Neurology*. 2014;82(13):1132-41.
40. Moran C, Phan TG, Chen J, Blizzard L, Beare R, Venn A, et al. Brain Atrophy in Type 2 Diabetes. *Diabetes Care*. 2013;36(12):4036-42.
41. Umemura T, Kawamura T, Umegaki H, Mashita S, Kanai A, Sakakibara T, et al. Endothelial and inflammatory markers in relation to progression of ischaemic cerebral small-vessel disease and cognitive impairment: a 6-year longitudinal study in patients with type 2 diabetes mellitus. *J Neurol Neurosurg Psychiatry*. 2011;82(11):1186-94.
42. Novak V, Last D, Alsop DC, Abduljalil AM, Hu K, Lepicovsky L, et al. Cerebral blood flow velocity and periventricular white matter hyperintensities in type 2 diabetes. *Diabetes Care*. 2006;29(7):1529-34.
43. Cui Y, Liang X, Gu H, Hu Y, Zhao Z, Yang XY, et al. Cerebral perfusion alterations in type 2 diabetes and its relation to insulin resistance and cognitive dysfunction. *Brain Imaging Behav*. 2017;11(5):1248-57.
44. Tiehuis AM, Vincken KL, van den Berg E, Hendrikse J, Manschot SM, Mali WP, et al. Cerebral perfusion in relation to cognitive function and type 2 diabetes. *Diabetologia*. 2008;51(7):1321-6.
45. Rusinek H, Ha J, Yau PL, Storey P, Tirsi A, Tsui WH, et al. Cerebral perfusion in insulin resistance and type 2 diabetes. *J Cereb Blood Flow Metab*. 2015;35(1):95-102.
46. van Bussel FC, Backes WH, Hofman PA, van Oostenbrugge RJ, Kessels AG, van Boxtel MP, et al. On the Interplay of the microvasculature, Parenchyma and Memory in T2DM. *Diabetes Care*. 2015;38:875-82.
47. Grill V, Gutniak M, Bjorkman O, Lindqvist M, Stone-Elander S, Seitz RJ, et al. Cerebral blood flow and substrate utilization in insulin-treated diabetic subjects. *American Journal of Physiology Endocrinology and Metabolism*. 1990;258(5).
48. Naylor LH, Green DJ, Jones TW, Kalic RJ, Suriano KL, Shah M, et al. Endothelial Function and Carotid Intima-Medial Thickness in Adolescents with Type 2 Diabetes Mellitus. *Journal of Pediatrics*. 2011;159(6):971-4.
49. Makimattila S, Yki-Jarvinen H. Endothelial dysfunction in human disease. *Current diabetes reports*. 2002;2(1):26--36.
50. Kim J-a, Montagnani M, Koh KK, Quon M. Reciprocal Relationships Between Insulin Resistance and Endothelial Dysfunction: Molecular and Pathophysiological Mechanisms. *Circulation*. 2006;113(15):1888--904.
51. Avogaro A, Albiero M, Menegazzo L, de Kreutzenberg S, Fadini GP. Endothelial dysfunction in diabetes: the role of reparatory mechanisms. *Diabetes Care*. 2011;34 Suppl 2:S285-90.
52. Levy BI, Schiffrin EL, Mourad JJ, Agostini D, Vicaut E, Safar ME, et al. Impaired tissue perfusion: a pathology common to hypertension, obesity, and diabetes mellitus. *Circulation*. 2008;118(9):968-76.
53. Selvarajah D, Hughes T, Reeves J, Boland E, Marques J, Gandhi R, et al. A preliminary study of brain macrovascular reactivity in impaired glucose tolerance and type-2 diabetes: Quantitative internal carotid artery blood flow using magnetic resonance phase contrast angiography. *Diab Vasc Dis Res*. 2016;13(5):367-72.

54. Xia W, Rao H, Spaeth AM, Huang R, Tian S, Cai R, et al. Blood Pressure is Associated With Cerebral Blood Flow Alterations in Patients With T2DM as Revealed by Perfusion Functional MRI. *Medicine*. 2015;94(48):e2231.
55. Watanabe K, Hirano S, Kojima K, Nagashima K, Mukai H, Sato T, et al. Altered cerebral blood flow in the anterior cingulate cortex is associated with neuropathic pain. *J Neurol Neurosurg Psychiatry*. 2018;89(10):1082-7.
56. Xu RS. Pathogenesis of diabetic cerebral vascular disease complication. *World J Diabetes*. 2015;6(1):54-66.
57. Sena CM, Pereira AM, Seica R. Endothelial dysfunction - A major mediator of diabetic vascular disease. *Biochimica Et Biophysica Acta-Molecular Basis of Disease*. 2013;1832(12):2216-31.
58. Sumpio BE, Riley T, Dardik A. Cells in focus: Endothelial cell. *International Journal of Biochemistry and Cell Biology*. 2002;34(12):1508--12.
59. Hahn C, Schwartz MA. Mechanotransduction in vascular physiology and atherogenesis. *Nature Reviews Molecular Cell Biology*. 2009;10(1):53--62.
60. Phelps ME, Hoffman EJ, Mullani NA, Higgins CS, Ter-Pogossian MM. Design considerations for a positron emission transaxial tomography (PET III). *IEEE Nucl Sci* 1976;23:516-22.
61. Hounsfield GN. Computerized transverse axial scanning (tomography): I. Description of system. *Br J Radiol*. 1973;46:1016-22.
62. Guy C, Ffytche D. *An Introduction to the principles of Medical Imaging*. London: Imperial College Press; 2005.
63. Constantinides C. *Introduction to Magnetic Resonance Imaging (MRI): The Basics*. Florida: CRC Press; 2014.
64. Haacke EM, Brown RW, Thompson MR, Venkatesan R. *Magnetic Resonance Imaging: Physical Principles and Sequence Design*. Hoboken, MJ, USA: John Wiley & Sons; 1999.
65. Lipton M. *Introducing MRI*: Albert Einstein College of Medicine; 2014.
66. Hidalgo-Tobon SS. Theory of gradient coil design methods for magnetic resonance imaging. *Concepts in Magnetic Resonance Part A*. 2010;36A(4):223-42.
67. Mezrich R. A perspective on k-space. *Radiology*. 1995;195:297-315.
68. Mansfield P. Multi-planar image formation using NMR spin echoes. *J Phys C*. 1977;10:L55-L8.
69. Schmitt F, Stehling MK, Turner R. *Echo Planar Imaging: Theory Technique and Application*. Berlin: Springer; 1998.
70. Hennig J, Nauerth A, Friedburg H. RARE imaging: a fast method for clinical MR. *Magn Reson Med*. 1986;3:823-33.
71. Feinberg DA, Oshio K. GRASE (gradient- and spin-echo) MR imaging: a new fast clinical imaging technique. *Radiology*. 1991;181(2):597-602.
72. Wright KL, Hamilton JI, Griswold MA, Gulani V, Seiberlich N. Non-Cartesian parallel imaging reconstruction. *J Magn Reson Imaging*. 2014;40(5):1022-40.
73. Paschal CB, Morris HD. K-space in the clinic. *J Magn Reson Imaging*. 2004;19(2):145-59.
74. Fischer H, Ladebeck R. *Echo-Planar Imaging Image Artifacts*. *Echo Planar Imaging: Theory Technique and Application*. Berlin, Heidelberg: Springer; 1998.
75. Horger W, Kiefer B. *Fat Suppression Techniques- a Short Overview*: Siemens Healthcare; 2011 [Available from: <http://www.siemens.com/magnetom-world>].

76. Le Bihan D, Poupon C, Amadon A, Lethimonnier F. Artifacts and pitfalls in diffusion MRI. *J Magn Reson Imaging*. 2006;24(3):478-88.
77. Kim S-G. Perfusion MR imaging: Evolution from initial development to functional studies. *Neuroimage*. 2012;62(2):672-5.
78. van Golen LW, Kuijter JP, Huisman MC, RG IJ, Barkhof F, Diamant M, et al. Quantification of cerebral blood flow in healthy volunteers and type 1 diabetic patients: comparison of MRI arterial spin labeling and [(15)O]H₂O positron emission tomography (PET). *J Magn Reson Imaging*. 2014;40(6):1300-9.
79. Jaszczak RJ, Coleman RE, Lim C. SPECT: Single photon emission computer tomography. *IEEE Trans Nucl Sci NS*. 1980;27:1137-53.
80. Aaslid R, Markwalder T, Nornes H. Noninvasive transcranial Doppler ultrasound recording of flow velocity in basal cerebral arteries. *J Neurosurg*. 1982;57:769-74.
81. Villringer A, Rosen BR, Belliveau JW. Dynamic imaging with lanthanide chelates in normal brain: contrast due to magnetic susceptibility effects. *Magn Reson Med*. 1988;6:164-74.
82. Williams DS, Detre JA, Leigh JS, Koretsky AP. Magnetic resonance imaging of perfusion using spin inversion of arterial water. *Proc Natl Acad Sci USA*. 1992;89:212-6.
83. Le Bihan D, Breton E, Lallemand D, Aubin M-L, Vignaud J, Laval-Jeantet M. Separation of Diffusion and Perfusion in Intravoxel Incoherent Motion MR Imaging. *Radiology*. 1988;168:497-505.
84. Lu H, Golay X, Pekar JJ, Van Zijl PC. Functional magnetic resonance imaging based on changes in vascular space occupancy. *Magn Reson Med*. 2003;50(2):263-74.
85. Rao MR, Stewart NJ, Griffiths PD, Norquay G, Wild JM. Imaging Human Brain Perfusion with Inhaled Hyperpolarized (129)Xe MR Imaging. *Radiology*. 2017;286(2):659-65.
86. Ogawa S, Lee TM, Kay AR, Tank DW. Brain magnetic resonance imaging with contrast dependent on blood oxygenation. *Proceedings of the National Academy of Sciences of the United States of America*. 1990;87(24):9868-72.
87. Roher AE, Debbins JP, Malek-Ahmadi M, Chen K, Pipe JG, Maze S, et al. Cerebral blood flow in Alzheimer's disease. *Vasc Health Risk Manag*. 2012;8:599-611.
88. Silva AC, Kim S-G, Garwood M. Imaging Blood Flow in Brain Tumors Using Arterial Spin Labeling. *Magnetic Resonance in medicine*. 2000;44:169-73.
89. Detre JA, Alsop DC, Vives LR, Maccotta L, Teener JW, Raps EC. Noninvasive MRI evaluation of cerebral blood flow in cerebrovascular disease. *Neurology*. 1998;50(3):633-41.
90. Chen JJ. Cerebrovascular-Reactivity Mapping Using MRI: Considerations for Alzheimer's Disease. *Front Aging Neurosci*. 2018;10:170.
91. Nealon RS, Howe PR, Jansen L, Garg M, Wong RH. Impaired cerebrovascular responsiveness and cognitive performance in adults with type 2 diabetes. *J Diabetes Complications*. 2017;31(2):462-7.
92. Wilkinson ID, Griffiths PD, Hoggard N, Cleveland TJ, Gaines PA, Macdonald S, et al. Short-Term Changes in Cerebral Microhemodynamics after Carotid Stenting. *American Journal of Neuroradiology*. 2003;24:1501-7.

93. Fierstra J, Sobczyk O, Battisti-Charbonney A, Mandell DM, Poublanc J, Crawley AP, et al. Measuring cerebrovascular reactivity: what stimulus to use? *J Physiol*. 2013;591(23):5809-21.
94. Inao S, Tadokoro M, Nishino M, Mizutani N, Terada K, Bundo M, et al. Neural activation of the brain with hemodynamic insufficiency. *Journal of Cerebral Blood Flow and Metabolism*. 1998;18(9):960-7.
95. Yokota C, Hasegawa Y, Minematsu K, Yamaguchi T. Effect of acetazolamide reactivity and long-term outcome in patients with major cerebral artery occlusive diseases. *Stroke*. 1998;29(3):640-4.
96. Chaer RA, Shen J, Cho JS, Abu Hamad G, Makaroun MS. Cerebral reserve is decreased in elderly patients with carotid stenosis. *Journal of Vascular Surgery*. 2010;52(3):569-75.
97. Bokkers RPH, van Osch MJP, Klijn CJM, Kappelle LJ, Hendrikse J. Cerebrovascular reactivity within perfusion territories in patients with an internal carotid artery occlusion. *Journal of Neurology Neurosurgery and Psychiatry*. 2011;82(9):1011-6.
98. Okazawa H, Yamauchi H, Sugimoto K, Takahashi M. Differences in vasodilatory capacity and changes in cerebral blood flow induced by acetazolamide in patients with cerebrovascular disease. *Journal of Nuclear Medicine*. 2003;44(9):1371-8.
99. Okazawa H, Yamauchi H, Toyoda H, Sugimoto K, Fujibayashi Y, Yonekura Y. Relationship between vasodilatation and cerebral blood flow increase in impaired hemodynamics: A PET study with the acetazolamide test in cerebrovascular disease. *Journal of Nuclear Medicine*. 2003;44(12):1875-83.
100. Demolis P, Florence G, Thomas L, Dinh YRT, Giudicelli JF, Seylaz J. Is the acetazolamide test valid for quantitative assessment of maximal cerebral autoregulatory vasodilation? An experimental study. *Stroke*. 2000;31(2):508-14.
101. Zhou Y, Rodgers ZB, Kuo AH. Cerebrovascular reactivity measured with arterial spin labeling and blood oxygen level dependent techniques. *Magnetic Resonance Imaging*. 2015;33(5):566-76.
102. Brian JEJ. Carbon dioxide and the cerebral circulation. *Anesthesiology*. 1998;88:1365-86.
103. Danker JF, Duong TQ. Quantitative regional cerebral blood flow MRI of animal model of attention-deficit/hyperactivity disorder. *Brain Research*. 2007;1150:217-24.
104. Paiva FF, Tanns A, Silva AC. Measurement of cerebral perfusion territories using arterial spin labelling. *NMR in biomedicine*. 2007;20(7):633--42.
105. Donahue MJ, Strother MK, Hendrikse J. Novel MRI Approaches for Assessing Cerebral Hemodynamics in Ischemic Cerebrovascular Disease. *Stroke*. 2012;43(3):903-15.
106. Knutsson L, van Westen D, Petersen ET, Bloch KM, Holtas S, Stahlberg F, et al. Absolute quantification of cerebral blood flow: correlation between dynamic susceptibility contrast MRI and model-free arterial spin labeling. *Magnetic Resonance Imaging*. 2010;28(1):1-7.
107. Wolf RL, Detre JA. Clinical neuroimaging using arterial spin-labeled perfusion magnetic resonance imaging. *Neurotherapeutics*. 2007;4(3):346-59.
108. Alsop DC, Detre JA, Golay X, Gunther M, Hendrikse J, Hernandez-Garcia L, et al. Recommended implementation of arterial spin-labeled perfusion MRI for

- clinical applications: A consensus of the ISMRM perfusion study group and the European consortium for ASL in dementia. *Magn Reson Med*. 2015;73(1):102-16.
109. Petcharunpaisan S, Ramalho J, Castillo M. Arterial spin labeling in neuroimaging. *World J Radiol*. 2010;2(10):384--98.
 110. Oshio K, Feinberg DA. GRASE (gradient and spin-echo) imaging: A novel fast MRI technique. *Magn Reson Med*. 1991;20(2):344-9.
 111. Park S-H, Wang DJJ, Duong TQ. Balanced steady state free precession for arterial spin labeling MRI: Initial experience for blood flow mapping in human brain, retina, and kidney. *Magnetic Resonance Imaging*. 2013;31(7):1044-50.
 112. Golay X, Petersen ET, Zimine I, Lim TCC. Arterial Spin Labeling: a one-stop-shop for measurement of brain perfusion in the clinical settings. Conference proceedings : Annual International Conference of the IEEE Engineering in Medicine and Biology Society IEEE Engineering in Medicine and Biology Society Annual Conference. 2007;2007:4320-3.
 113. Borogovac A, Asllani I. Arterial Spin Labeling (ASL) fMRI: advantages, theoretical constrains, and experimental challenges in neurosciences. *Int J Biomed Imaging*. 2012;2012:818456.
 114. Schmid S, Ghariq E, Teeuwisse WM, Webb A, van Osch MJP. Acceleration-Selective Arterial Spin Labeling. *Magnetic Resonance in Medicine*. 2014;71(1):191-9.
 115. Ferré J-C, Bannier E, Raoult H, Mineur G, Carsin-Nicol B, Gauvrit J-Y. Arterial spin labeling (ASL) perfusion: Techniques and clinical use. *Diagnostic and interventional imaging*. 2013;94(12):1211-23.
 116. Edelman RR, Siewert B, Darby DG, Thangaraj V, Nobre AC, Mesulam MM, et al. Qualitative mapping of cerebral blood flow and functional localization with echo-planar MR imaging and signal targeting with alternating radio frequency. *Radiology*. 1994;192(2):513-20.
 117. Wong EC. An introduction to ASL labeling techniques. *J Magn Reson Imaging*. 2014;40(1):1-10.
 118. Wu WC, Fernandez-Seara M, Detre JA, Wehrli FW, Wang J. A theoretical and experimental investigation of the tagging efficiency of pseudo-continuous arterial spin labeling. *Magn Reson Med*. 2007;58(5):1020-7.
 119. Heijtel DFR, Mutsaerts HJMM, Bakker E, Schober P, Stevens MF, Petersen ET, et al. Accuracy and precision of pseudo-continuous arterial spin labeling perfusion during baseline and hypercapnia: A head-to-head comparison with O-15 H2O positron emission tomography. *Neuroimage*. 2014;92:182-92.
 120. Kilroy E, Apostolova L, Liu C, Yan L, Ringman J, Wang D. Reliability of two-dimensional and three-dimensional pseudo-continuous arterial spin labeling perfusion MRI in elderly populations: comparison with 15O-water positron emission tomography. *J Magn Reson Imaging*. 2014;39(4):931--9.
 121. Mutsaerts HJ, van Dalen JW, Heijtel DF, Groot PF, Majoie CB, Petersen ET, et al. Cerebral Perfusion Measurements in Elderly with Hypertension Using Arterial Spin Labeling. *PLoS One*. 2015;10(8):e0133717.
 122. Dai W, Fong T, Jones RN, Marcantonio E, Schmitt E, Inouye SK, et al. Effects of arterial transit delay on cerebral blood flow quantification using arterial spin labeling in an elderly cohort. *J Magn Reson Imaging*. 2017;45(2):472-81.
 123. Wang J, Alsop DC, Song HK, Maldjian JA, Tang K, Salvucci AE, et al. Arterial transit time imaging with flow encoding arterial spin tagging (FEAST). *Magn Reson Med*. 2003;50(3):599-607.

124. Wong EC, Cronin M, Wu WC, Inglis B, Frank LR, Liu TT. Velocity-selective arterial spin labeling. *Magn Reson Med.* 2006;55(6):1334-41.
125. van Osch MJ, Teeuwisse WM, Chen Z, Suzuki Y, Helle M, Schmid S. Advances in arterial spin labelling MRI methods for measuring perfusion and collateral flow. *J Cereb Blood Flow Metab.* 2017;38(9):1461-80.
126. Hernandez-Garcia L, Lahiri A, Schollenberger J. Recent progress in ASL. *Neuroimage.* 2018.
127. Jezzard P, Chappell MA, Okell TW. Arterial spin labeling for the measurement of cerebral perfusion and angiography. *J Cereb Blood Flow Metab.* 2018;38(4):603-26.
128. Detre JA, Rao H, Wang DJ, Chen YF, Wang Z. Applications of arterial spin labeled MRI in the brain. *J Magn Reson Imaging.* 2012;35(5):1026-37.
129. Robson PM, Madhuranthakam AJ, Smith MP, Sun MR, Dai W, Rofsky NM, et al. Volumetric Arterial Spin-labeled Perfusion Imaging of the Kidneys with a Three-dimensional Fast Spin Echo Acquisition. *Acad Radiol.* 2016;23(2):144-54.
130. Chouhan MD, Lythgoe MF, Mookerjee RP, Taylor SA. Vascular assessment of liver disease-towards a new frontier in MRI. *Br J Radiol.* 2016;89(1064):20150675.
131. Englund EK, Rodgers ZB, Langham MC, Mohler ER, 3rd, Floyd TF, Wehrli FW. Measurement of skeletal muscle perfusion dynamics with pseudo-continuous arterial spin labeling (pCASL): Assessment of relative labeling efficiency at rest and during hyperemia, and comparison to pulsed arterial spin labeling (PASL). *J Magn Reson Imaging.* 2016;44(4):929-39.
132. Xing D, Zha Y, Yan L, Wang K, Gong W, Lin H. Feasibility of ASL spinal bone marrow perfusion imaging with optimized inversion time. *J Magn Reson Imaging.* 2015;42(5):1314-20.
133. Zun Z, Zaharchuk G, Andescavage NN, Donofrio MT, Limperopoulos C. Non-Invasive Placental Perfusion Imaging in Pregnancies Complicated by Fetal Heart Disease Using Velocity-Selective Arterial Spin Labeled MRI. *Sci Rep.* 2017;7(1):16126.
134. Cox EF, Smith JK, Chowdhury AH, Lobo DN, Francis ST, Simpson J. Temporal assessment of pancreatic blood flow and perfusion following secretin stimulation using noninvasive MRI. *J Magn Reson Imaging.* 2015;42(5):1233-40.
135. Schraml C, Schwenzer NF, Martirosian P, Boss A, Schick F, Schafer S, et al. Non-invasive pulmonary perfusion assessment in young patients with cystic fibrosis using an arterial spin labeling MR technique at 1.5 T. *MAGMA.* 2012;25(2):155-62.
136. Wang DJ, Bi X, Avants BB, Meng T, Zuehlsdorff S, Detre JA. Estimation of perfusion and arterial transit time in myocardium using free-breathing myocardial arterial spin labeling with navigator-echo. *Magn Reson Med.* 2010;64(5):1289-95.
137. Kim J, Whyte J, Patel S, Avants B, Europa E, Wang J, et al. Resting cerebral blood flow alterations in chronic traumatic brain injury: an arterial spin labeling perfusion fMRI study. *J Neurotrauma.* 2010;27(8):1399-411.
138. Ota M, Ishikawa M, Sato N, Okazaki M, Maikusa N, Hori H, et al. Pseudo-continuous arterial spin labeling MRI study of schizophrenic patients. *Schizophr Res.* 2014;154(1-3):113-8.
139. Duhameau B, Ferre JC, Jannin P, Gauvrit JY, Verin M, Millet B, et al. Chronic and treatment-resistant depression: a study using arterial spin labeling perfusion MRI at 3Tesla. *Psychiatry Res.* 2010;182(2):111-6.

140. Ma Y, Huang C, Dyke JP, Pan H, Alsop D, Feigin A, et al. Parkinson's disease spatial covariance pattern: noninvasive quantification with perfusion MRI. *J Cereb Blood Flow Metab.* 2010;30(3):505-9.
141. Yoshiura T, Hiwatashi A, Yamashita K, Ohyagi Y, Monji A, Takayama Y, et al. Simultaneous measurement of arterial transit time, arterial blood volume, and cerebral blood flow using arterial spin-labeling in patients with Alzheimer disease. *AJNR Am J Neuroradiol.* 2009;30(7):1388-93.
142. Biswal B, Kunwar P, Natelson BH. Cerebral blood flow is reduced in chronic fatigue syndrome as assessed by arterial spin labeling. *J Neurol Sci.* 2011;301(1-2):9-11.
143. Paling D, Thade Petersen E, Tozer DJ, Altmann DR, Wheeler-Kingshott CA, Kapoor R, et al. Cerebral arterial bolus arrival time is prolonged in multiple sclerosis and associated with disability. *J Cereb Blood Flow Metab.* 2014;34(1):34-42.
144. Gevers S, Nederveen AJ, Fijnvandraat K, van den Berg SM, van Ooij P, Heijtel DF, et al. Arterial spin labeling measurement of cerebral perfusion in children with sickle cell disease. *J Magn Reson Imaging.* 2012;35(4):779-87.
145. Grade M, Hernandez Tamames JA, Pizzini FB, Achten E, Golay X, Smits M. A neuroradiologist's guide to arterial spin labeling MRI in clinical practice. *Neuroradiology.* 2015;57(12):1181-202.
146. Look DC, Locker DR. Time saving in measurement of NMR and EPR relaxation times. *Rev Sci Instrum.* 1970;41:250-1.
147. Gunther M, Bock M, Schad LR. Arterial spin labeling in combination with a look-locker sampling strategy: Inflow turbo-sampling EPI-FAIR (ITS-FAIR). *Magnetic Resonance in Medicine.* 2001;46(5):974-84.
148. Gunther M. Efficient visualization of vascular territories in the human brain by cycled arterial spin labeling MRI. *Magn Reson Med.* 2006;56(3):671-5.
149. Dai W, Shankaranarayanan A, Alsop DC. Volumetric measurement of perfusion and arterial transit delay using hadamard encoded continuous arterial spin labeling. *Magn Reson Med.* 2013;69(4):1014-22.
150. Teeuwisse WM, Schmid S, Ghariq E, Veer IM, van Osch MJ. Time-encoded pseudocontinuous arterial spin labeling: basic properties and timing strategies for human applications. *Magn Reson Med.* 2014;72(6):1712-22.
151. Zierler KL. Equations for Measuring Blood Flow by External Monitoring of Radio isotopes. *Circulation Research.* 1965;16:309-21.
152. Ostergaard L, Weisskoff RM, Chesler DA, Gyldensted C, Rosen BR. High Resolution Measurement of Cerebral Blood Flow using Intravascular Tracer Bolus Passages. Part I: Mathematical Approach and Statistical Analysis. *Magn Reson Med.* 1996;36(5):715-25.
153. Calamante F. Arterial input function in perfusion MRI: a comprehensive review. *Prog Nucl Magn Reson Spectrosc.* 2013;74:1-32.
154. Chappell MA, Woolrich MW, Petersen ET, Golay X, Payne SJ. Comparing Model-Based and Model-Free Analysis Methods for QUASAR Arterial Spin Labeling Perfusion Quantification. *Magnetic Resonance in Medicine.* 2013;69(5):1466-75.
155. Petersen ET, Lim T, Golay X. Model-free arterial spin labeling quantification approach for perfusion MRI. *Magnetic Resonance in Medicine.* 2006;55(2):219-32.
156. Golay X, Petersen ET, Hui F. Pulsed star labeling of arterial regions (PULSAR): A robust regional perfusion technique for high field imaging. *Magnetic Resonance in Medicine.* 2005;53(1):15-21.

157. Wong EC, Buxton RB, Frank LR. Quantitative Imaging of Perfusion Using a Single Subtraction (QUIPSS and QUIPSS II). *Magn Reson Med*. 1998;39(5):702-8.
158. Buxton RB, Frank LR, Wong EC, Siewert B, Warach S, Edelman RR. A general kinetic model for quantitative perfusion imaging with arterial spin labeling. *Magnetic Resonance in Medicine*. 1998;40(3):383-96.
159. Varela M, Petersen ET, Golay X, Hajnal JV. Cerebral blood flow measurements in infants using look-locker arterial spin labeling. *Journal of Magnetic Resonance Imaging*. 2015;41(6):1591-600.
160. Petersen ET, Zimine I, Ho Y-CL, Golay X, editors. An Improved QUASAR sequence for User-Independent Quantitative and Reproducible Perfusion Measurements. *Intl Soc Magn, Reson Med*; 2007.
161. Petersen ET, Mouridsen K, Golay X, Study QT-r. The QUASAR reproducibility study, Part II: Results from a multi-center Arterial Spin Labeling test-retest study. *Neuroimage*. 2010;49(1):104-13.
162. Hendrikse J, Petersen ET, van Laar PJ, Golay X. Cerebral border zones between distal end branches of intracranial arteries: MR imaging. *Radiology*. 2008;246(2):572-80.
163. Knutsson L, Bloch KM, Holtas S, Wirestam R, Stahlberg F. Model-free arterial spin labelling for cerebral blood flow quantification: introduction of regional arterial input functions identified by factor analysis. *Magnetic Resonance Imaging*. 2008;26(4):554-9.
164. Chng SM, Petersen ET, Zimine I, Sitoh Y-Y, Lim CCT, Golay X. Territorial Arterial Spin Labeling in the Assessment of Collateral Circulation Comparison With Digital Subtraction Angiography. *Stroke*. 2008;39(12):3248-54.
165. Uchihashi Y, Hosoda K, Zimine I, Fujita A, Fujii M, Sugimura K, et al. Clinical application of arterial spin-labeling MR imaging in patients with carotid stenosis: quantitative comparative study with single-photon emission CT. *AJNR Am J Neuroradiol*. 2011;32(8):1545-51.
166. Kamagata K, Motoi Y, Hori M, Suzuki M, Nakanishi A, Shimoji K, et al. Posterior hypoperfusion in Parkinson's disease with and without dementia measured with arterial spin labeling MRI. *J Magn Reson Imaging*. 2011;33(4):803-7.
167. Hirai T, Kitajima M, Nakamura H, Okuda T, Sasao A, Shigematsu Y, et al. Quantitative blood flow measurements in gliomas using arterial spin-labeling at 3T: intermodality agreement and inter- and intraobserver reproducibility study. *AJNR Am J Neuroradiol*. 2011;32(11):2073-9.
168. van Westen D, Petersen ET, Wirestam R, Siemund R, Bloch KM, Stahlberg F, et al. Correlation between arterial blood volume obtained by arterial spin labelling and cerebral blood volume in intracranial tumours. *MAGMA*. 2011;24(4):211-23.
169. Henriksen OM, Hansen NL, Osler M, Mortensen EL, Hallam DM, Pedersen ET, et al. Sub-Clinical Cognitive Decline and Resting Cerebral Blood Flow in Middle Aged Men. *PLoS One*. 2017;12(1):e0169912.
170. Tatewaki Y, Higano S, Taki Y, Thyreau B, Murata T, Mugikura S, et al. Regional Reliability of Quantitative Signal Targeting with Alternating Radiofrequency (STAR) Labeling of Arterial Regions (QUASAR). *Journal of Neuroimaging*. 2014;24(6):554-61.
171. Heijtel DF, Petersen ET, Mutsaerts HJ, Bakker E, Schober P, Stevens MF, et al. Quantitative agreement between [(15)O]H₂O PET and model free QUASAR

- MRI-derived cerebral blood flow and arterial blood volume. *NMR Biomed.* 2016;29(4):519-26.
172. Fieselmann A, Kowarschik M, Ganguly A, Hornegger J, Fahrigr R. Deconvolution-Based CT and MR Brain Perfusion Measurement: Theoretical Model Revisited and Practical Implementation Details. *Int J Biomed Imaging.* 2011;2011:467563.
173. Grobner T. Gadolinium--a specific trigger for the development of nephrogenic fibrosing dermopathy and nephrogenic systemic fibrosis? *Nephrol Dial Transplant.* 2006;21(4):1104-8.
174. Rogosnitzky M, Branch S. Gadolinium-based contrast agent toxicity: a review of known and proposed mechanisms. *Biometals.* 2016;29(3):365-76.
175. Kanda T, Fukusato T, Matsuda M, Toyoda K, Oba H, Kotoku J, et al. Gadolinium-based Contrast Agent Accumulates in the Brain Even in Subjects without Severe Renal Dysfunction- Evaluation of Autopsy Brain Specimens with Inductively Coupled Plasma Mass Spectroscopy. *Neuroradiology.* 2015;276(1).
176. Williams S, Grimm H. Gadolinium Toxicity A Survey of the Chronic Effects of Retained Gadolinium from Contrast MRIs 2015 [Available from: <https://gdtoxicity.files.wordpress.com/2014/09/gd-symptom-survey.pdf>.
177. Lu H, Hua J, van Zijl PC. Noninvasive functional imaging of cerebral blood volume with vascular-space-occupancy (VASO) MRI. *NMR Biomed.* 2013;26(8):932-48.
178. Hua J, Qin Q, Donahue MJ, Zhou J, Pekar JJ, van Zijl PC. Inflow-based vascular-space-occupancy (iVASO) MRI. *Magn Reson Med.* 2011;66(1):40-56.
179. Donahue MJ, Sideso E, MacIntosh BJ, Kennedy J, Handa A, Jezard P. Absolute arterial cerebral blood volume quantification using inflow vascular-space-occupancy with dynamic subtraction magnetic resonance imaging. *J Cereb Blood Flow Metab.* 2010;30(7):1329-42.
180. Bihan DL, Turner R. The capillary network: a link between ivim and classical perfusion. *Magnetic Resonance in Medicine.* 1992;27(1):171-8.
181. Federau C, O'Brien K, Meuli R, Hagmann P, Maeder P. Measuring brain perfusion with intravoxel incoherent motion (IVIM): Initial clinical experience. *Journal of Magnetic Resonance Imaging.* 2014;39(3):624-32.
182. Stieb S, Boss A, Wurnig MC, Ozbay PS, Weiss T, Guckenberger M, et al. Non-parametric intravoxel incoherent motion analysis in patients with intracranial lesions: Test-retest reliability and correlation with arterial spin labeling. *Neuroimage Clin.* 2016;11:780-8.
183. Shen N, Zhao L, Jiang J, Jiang R, Su C, Zhang S, et al. Intravoxel incoherent motion diffusion-weighted imaging analysis of diffusion and microperfusion in grading gliomas and comparison with arterial spin labeling for evaluation of tumor perfusion. *J Magn Reson Imaging.* 2016;44(3):620-32.
184. Zhang X, Ingo C, Teeuwisse WM, Chen Z, van Osch MJP. Comparison of perfusion signal acquired by arterial spin labeling-prepared intravoxel incoherent motion (IVIM) MRI and conventional IVIM MRI to unravel the origin of the IVIM signal. *Magn Reson Med.* 2018;79(2):723-9.
185. Brant-Zawadzki M, Gillan GD, Nitz WR. MP RAGE: A Three-dimensional, T1-weighted, Gradient-Echo Sequence - Initial Experience in the Brain. *Radiology.* 1992;182:769-75.

186. Hajnal JV, De Coene B, Lewis PD, Baudouin CJ, Cowan FM, Pennock JM, et al. High signal regions in normal white matter shown by heavily T2-weighted CSF nulled IR sequences. *J Comput Assist Tomogr.* 1992;16(4):506-13.
187. Bakshi R, Ariyaratana S, Benedict RB, Jacobs L. Fluid-attenuated inversion recovery magnetic resonance imaging detects cortical and juxtacortical multiple sclerosis lesions. *Archives of Neurology.* 2001;58(5):742-8.
188. van Harten B, de Leeuw F-E, Weinstein HC, Scheltens P, Biessels GJ. Brain imaging in patients with diabetes - A systematic review. *Diabetes Care.* 2006;29(11):2539-48.
189. Saloner D. An Introduction to MR Angiography. *radiographics.* 1995;15:453-65.
190. Okell TW, Schmitt P, Bi X, Chappell MA, Tijssen RH, Sheerin F, et al. Optimization of 4D vessel-selective arterial spin labeling angiography using balanced steady-state free precession and vessel-encoding. *NMR Biomed.* 2016;29(6):776-86.
191. Nayak KS, Nielsen JF, Bernstein MA, Markl M, P DG, R MB, et al. Cardiovascular magnetic resonance phase contrast imaging. *J Cardiovasc Magn Reson.* 2015;17:71.
192. Yashiro S, Kameda H, Chida A, Todate Y, Hasegawa Y, Nagasawa K, et al. Evaluation of Lenticulostriate Arteries Changes by 7 T Magnetic Resonance Angiography in Type 2 Diabetes. *J Atheroscler Thromb.* 2018;25(10):1067-75.
193. Brundel M, van den Berg E, Reijmer YD, de Bresser J, Kappelle LJ, Biessels GJ, et al. Cerebral haemodynamics, cognition and brain volumes in patients with type 2 diabetes. *J Diabetes Complications.* 2012;26(3):205-9.
194. Stejskal EO, Tanner JE. Spin Diffusion Measurements: Spin Echoes in the Presence of a Time - Dependent Field Gradient. *The Journal of Chemical Physics.* 1965;42(1):288-92.
195. Hagmann P, Jonasson L, Maeder P, Thiran J-P, Wedeen VJ, Meuli R. Understanding Diffusion MR Imaging Techniques- From Scalar Diffusion-weighted Imaging to Diffusion Tensor Imaging and Beyond. *RadioGraphics.* 2006;26:205-23.
196. Jensen JH, Helpert JA, Ramani A, Lu H, Kaczynski K. Diffusional kurtosis imaging: the quantification of non-gaussian water diffusion by means of magnetic resonance imaging. *Magn Reson Med.* 2005;53(6):1432-40.
197. Glenn GR, Kuo LW, Chao YP, Lee CY, Helpert JA, Jensen JH. Mapping the Orientation of White Matter Fiber Bundles: A Comparative Study of Diffusion Tensor Imaging, Diffusional Kurtosis Imaging, and Diffusion Spectrum Imaging. *AJNR Am J Neuroradiol.* 2016;37(7):1216-22.
198. Wang Z, Lu Z, Li J, Pan C, Jia Z, Chen H, et al. Evaluation of apparent diffusion coefficient measurements of brain injury in type 2 diabetics with retinopathy by diffusion-weighted MRI at 3.0 T. *NeuroReport.* 2017;28(2):69-74.
199. Nouwen A, Chambers A, Chechlacz M, Higgs S, Blissett J, Barrett TG, et al. Microstructural abnormalities in white and gray matter in obese adolescents with and without type 2 diabetes. *NeuroImage: Clinical.* 2017;16:43-51.
200. Zheng G, Zhang LJ, Zhong J, Wang Z, Qi R, Shi D, et al. Cerebral blood flow measured by arterial-spin labeling MRI: A useful biomarker for characterization of minimal hepatic encephalopathy in patients with cirrhosis. *European Journal of Radiology.* 2013;82(11):1981-8.

201. Friston KJ. Introduction: Experimental design and Statistical Parametric Mapping. In: Frackowiak RSJ, editor. *Human Brain Function*: Academic Press; 2004.
202. Smith SM, Jenkinson M, Woolrich MW, Beckmann CF, Behrens TEJ, Johansen-Berg H, et al. Advances in functional and structural MR image analysis and implementation as FSL. *Neuroimage*. 2004;23:S208-S19.
203. Fischl B. FreeSurfer. *NeuroImage*. 2012;62(2):774--81.
204. Cox RW. AFNI: Software for analysis and visualization of functional magnetic resonance neuroimages. *Computers and Biomedical Research*. 1996;29:162-73.
205. Belaroussi B, Milles J, Carme S, Zhu YM, Benoit-Cattin H. Intensity non-uniformity correction in MRI: existing methods and their validation. *Med Image Anal*. 2006;10(2):234-46.
206. Vovk U, Pernus F, Likar B. A review of methods for correction of intensity inhomogeneity in MRI. *IEEE Trans Med Imaging*. 2007;26(3):405-21.
207. Song S, Zheng Y, He Y. A Review of Methods for Bias Correction in Medical Images. *Biomedical Engineering Review*. 2017;1(1).
208. Tustison NJ, Avants BB, Cook PA, Zheng Y, Egan A, Yushkevich PA, et al. N4ITK: improved N3 bias correction. *IEEE Trans Med Imaging*. 2010;29(6):1310-20.
209. Sled JG, Zijdenbos AP, Evans AC. A Nonparametric Method for Automatic Correction of Intensity Nonuniformity in MRI Data. *IEEE Transactions on Medical Imaging*. 1998;17(1).
210. Larsen CT, Iglesias JE, Van Leemput K, editors. *N3 Bias Field Correction Explained as a Bayesian Modeling Method*. Bayesian and graphical Models for Biomedical Imaging; 2014 2014//; Cham: Springer International Publishing.
211. Kalavathi P, Prasath VB. Methods on Skull Stripping of MRI Head Scan Images-a Review. *J Digit Imaging*. 2016;29(3):365-79.
212. Kleesiek J, Urban G, Hubert A, Schwarz D, Maier-Hein K, Bendszus M, et al. Deep MRI brain extraction: A 3D convolutional neural network for skull stripping. *Neuroimage*. 2016;129:460-9.
213. Smith SM. Fast robust automated brain extraction. *Hum Brain Mapp*. 2002;17(3):143-55.
214. Ashburner J, Friston K. Image Segmentation. In: Frackowiak RSJ, Friston KJ, Frith C, Dolan R, Price CJ, Zeki S, et al., editors. *Human Brain Function*. 2nd ed: Academic Press; 2003.
215. Segonne F, Dale AM, Busa E, Glessner M, Salat D, Hahn HK, et al. A hybrid approach to the skull stripping problem in MRI. *Neuroimage*. 2004;22(3):1060-75.
216. Solomon C, Breckon T. *Fundamentals of digital image processing: A practical approach with examples in Matlab*. Chichester: Wiley-Blackwell; 2011.
217. Klein A, Andersson J, Ardekani BA, Ashburner J, Avants B, Chiang MC, et al. Evaluation of 14 nonlinear deformation algorithms applied to human brain MRI registration. *Neuroimage*. 2009;46(3):786-802.
218. Avants BB, Epstein CL, Grossman M, Gee JC. Symmetric Diffeomorphic Image Registration with CrossCorrelation- Evaluating Automated Labeling of Elderly and Neurodegenerative Brain. *Medical Image Analysis*. 2008;12(1).
219. Ardekani BA, Braun M, Hutton BF, Kanno I, Iida H. A fully automatic multimodality image registration algorithm. *Journal of Comput Assist Tomogr*. 1995;19(4).

220. Ashburner J. A fast diffeomorphic image registration algorithm. *Neuroimage*. 2007;38(1):95-113.
221. Mazziotta JC, Toga AW, Evans A, Fox P, Lancaster J. A Probabilistic Atlas of the Human Brain: Theory and Rationale for Its Development: The International Consortium for Brain Mapping (ICBM). *NeuroImage*. 1995;2(2, Part A):89-101.
222. Talairach J, Tournoux P. Co-planar stereotaxic atlas of the human brain. 3-Dimensional proportional system: an approach to cerebral imaging; Thieme; 1988.
223. Dora L, Agrawal S, Panda R, Abraham A. State-of-the-Art Methods for Brain Tissue Segmentation: A Review. *IEEE Rev Biomed Eng*. 2017;10:235-49.
224. van Opbroek A, van der Lijn F, de Bruijne M. Automated Brain-Tissue Segmentation by Multi-Feature SVM Classification. *The MIDAS Journal*. 2013.
225. Akkus Z, Galimzianova A, Hoogi A, Rubin DL, Erickson BJ. Deep Learning for Brain MRI Segmentation: State of the Art and Future Directions. *J Digit Imaging*. 2017;30(4):449-59.
226. Vrooman HA, Cocosco CA, van der Lijn F, Stokking R, Ikram MA, Vernooij MW, et al. Multi-spectral brain tissue segmentation using automatically trained k-Nearest-Neighbor classification. *Neuroimage*. 2007;37(1):71-81.
227. MacQueen JB, editor *Some Methods for classification and Analysis of Multivariate Observations* 1967; Berkeley: University of California Press.
228. Bezdek JC, Ehrlich R, Full W. FCM: The fuzzy c-means clustering algorithm. *Computers & Geosciences*. 1984;10:191-203.
229. Dunn JC. A Fuzzy Relative of the ISODATA Process and Its Use in Detecting Compact Well-Separated Clusters. *Cybernetics and Systems*. 1973;3(3):32-57.
230. Zadeh LA. Fuzzy Sets. *Information and Control*. 1965;8:338-53.
231. Brandt ME, Bohan TP, Kramer LA, Fletcher JM. Estimation of CSF, White and Gray Matter volumes in hydrocephalic children using fuzzy clustering of MR images. *Computerized Medical Imaging and Graphics*. 1994;18(1):25-34.
232. Chuang KS, Tzeng HL, Chen S, Wu J, Chen TJ. Fuzzy c-means clustering with spatial information for image segmentation. *Comput Med Imaging Graph*. 2006;30(1):9-15.
233. Ahmed MN, Yamany SM, Mohamed N, Farag AA, Moriarty T. A Modified Fuzzy C-Means Algorithm for Bias Field Estimation and Segmentation of MRI Data. *IEEE Transactions on Medical Imaging*. 2002;21(3).
234. Salem WS, Ali HF, Seddik AF, editors. *Spatial Fuzzy C-Means Algorithm for Bias Correction and Segmentation of Brain MRI Data* International Conf Biomedical Engineering and Science; 2015.
235. Ji Z, Liu J, Cao G, Sun Q, Chen Q. Robust spatially constrained fuzzy c-means algorithm for brain MR image segmentation. *Pattern Recognition*. 2014;47(7):2454-66.
236. Choudhry MS, Kapoor R. Performance Analysis of Fuzzy C-Means Clustering Methods for MRI Image Segmentation. *Procedia Computer Science*. 2016;89:749-58.
237. Caligiuri ME, Perrotta P, Augimeri A, Rocca F, Quattrone A, Cherubini A. Automatic Detection of White Matter Hyperintensities in Healthy Aging and Pathology Using Magnetic Resonance Imaging: A Review. *Neuroinformatics*. 2015;13(3):261-76.
238. Schmidt P, Gaser C, Arsic M, Buck D, Forschler A, Berthele A, et al. An automated tool for detection of FLAIR-hyperintense white-matter lesions in Multiple Sclerosis. *Neuroimage*. 2012;59(4):3774-83.

239. Griffanti L, Zamboni G, Khan A, Li L, Bonifacio G, Sundaresan V, et al. BIANCA (Brain Intensity AbNormality Classification Algorithm): A new tool for automated segmentation of white matter hyperintensities. *Neuroimage*. 2016;141:191-205.
240. Asllani I, Borogovac A, Brown TR. Regression algorithm correcting for partial volume effects in arterial spin labeling MRI. *Magn Reson Med*. 2008;60(6):1362-71.
241. Chappell MA, Groves AR, MacIntosh BJ, Donahue MJ, Jezzard P, Woolrich MW. Partial volume correction of multiple inversion time arterial spin labeling MRI data. *Magn Reson Med*. 2011;65(4):1173-83.
242. Zhao MY, Mezue M, Segerdahl AR, Okell TW, Tracey I, Xiao Y, et al. A systematic study of the sensitivity of partial volume correction methods for the quantification of perfusion from pseudo-continuous arterial spin labeling MRI. *Neuroimage*. 2017;162:384-97.
243. Ahlgren A, Wirestam R, Petersen ET, Stahlberg F, Knutsson L. Partial volume correction of brain perfusion estimates using the inherent signal data of time-resolved arterial spin labeling. *NMR Biomed*. 2014;27(9):1112-22.
244. Shin W, Geng X, Gu H, Zhan W, Zou Q, Yang Y. Automated brain tissue segmentation based on fractional signal mapping from inversion recovery Look-Locker acquisition. *Neuroimage*. 2010;52(4):1347-54.
245. Ashburner J, Friston KJ. Voxel-based morphometry: the methods. *Neuroimage*. 2000;11(6):805-21.
246. Davatzikos C, Fan Y, Wu X, Shen D, Resnick SM. Detection of prodromal Alzheimer's disease via pattern classification of magnetic resonance imaging. *Neurobiology of Aging*. 2008;29(4):514-23.
247. Gaonkar B, Pohl K, Davatzikos C. Pattern Based Morphometry. *Medical image computing and computer-assisted intervention : MICCAI International Conference on Medical Image Computing and Computer-Assisted Intervention*. 2011;14(0 2):459-66.
248. Varol E, Sotiras A, Davatzikos C. MIDAS: Regionally linear multivariate discriminative statistical mapping. *Neuroimage*. 2018;174:111-26.
249. Rathore S, Habes M, Iftikhar MA, Shacklett A, Davatzikos C. A review on neuroimaging-based classification studies and associated feature extraction methods for Alzheimer's disease and its prodromal stages. *Neuroimage*. 2017;155:530-48.
250. Vemuri P, Gunter JL, Senjem ML, Whitwell JL, Kantarci K, Knopman DS, et al. Alzheimer's disease diagnosis in individual subjects using structural MR images: Validation studies. *Neuroimage*. 2008;39(3):1186-97.
251. Fan Y, Batmanghelich N, Clark CM, Davatzikos C, Alzheimers Dis Neuroimaging I. Spatial patterns of brain atrophy in MCI patients, identified via high-dimensional pattern classification, predict subsequent cognitive decline. *Neuroimage*. 2008;39(4):1731-43.
252. Kassner A, Thornhill RE. Texture analysis: a review of neurologic MR imaging applications. *AJNR Am J Neuroradiol*. 2010;31(5):809-16.
253. Haralick RM, Shanmugam K, Dinstein I. Textural Features for Image Classification. *IEEE Transactions on Systems, Man, and Cybernetics*. 1973;SMC-3(6):610-21.
254. Materka A, Strzelecki M. *Texture Analysis Methods – A Review.pdf*. Brussels: Technical University of Lodz, Institute of Electronics, 1998.

255. Tan TN. Rotation Invariant Texture Features and Their Use in Automatic Script Identification. *IEEE transactions of pattern analysis and machine intelligence*. 1998;20(7).
256. Hira ZM, Gillies DF. A Review of Feature Selection and Feature Extraction Methods Applied on Microarray Data. *Adv Bioinformatics*. 2015;2015:198363.
257. Guyon I, Weston J, Barnhill S, Vapnik V. Gene Selection for Cancer Classification using Support Vector Machines. *Machine Learning*. 2002;46(1-3):389-422.
258. Rakotomamonjy A. Variable Selection Using SVM-based Criteria. *Journal of Machine Learning Research*. 2003;3:1357-70.
259. Theodoridis S, Pikrakis A, Koutroumbas K, Cavouras D. *Introduction to Pattern Recognition: A Matlab Approach*: Academic Press, Inc.; 2010. 240 p.
260. Cortes C, Vapnik V. Support-vector networks. *Machine Learning*. 1995;20(3):273-97.
261. Winston P. 16. *Learning: Support Vector Machines*: Massachusetts Institute of Technology: MIT OpenCourseWare; 2010.
262. Smith BT. Lagrange Multipliers Tutorial in the Context of Support Vector Machines. Memorial University of Newfoundland, 2004.
263. Singh A. *Support Vector Machines*: Carnegie Mellon University; 2011.
264. Berwick R. *An Idiot's guide to Support vector machines*: Massachusetts Institute of Technology; 2003.
265. Steorts RC. *Resampling Methods: Cross Validation*. STA 325 Data Mining and Machine Learning: Duke University; 2017.
266. Kohavi R. A study of cross-validation and bootstrap for accuracy estimation and model selection. *Proceedings of the 14th international joint conference on Artificial intelligence - Volume 2*; Montreal, Quebec, Canada. 1643047: Morgan Kaufmann Publishers Inc.; 1995. p. 1137-43.
267. Rao RB, Fung G, Rosales R, editors. *On the dangers of cross-validation. An experimental evaluation*. *Proceedings of the 2008 SIAM International Conference on Data Mining*; 2008: SIAM.
268. Cuingnet R, Gerardin E, Tessieras J, Auzias G, Lehericy S, Habert MO, et al. Automatic classification of patients with Alzheimer's disease from structural MRI: a comparison of ten methods using the ADNI database. *Neuroimage*. 2011;56(2):766-81.
269. Zacharaki EI, Wang S, Chawla S, Soo Yoo D, Wolf R, Melhem ER, et al. Classification of brain tumor type and grade using MRI texture and shape in a machine learning scheme. *Magn Reson Med*. 2009;62(6):1609-18.
270. Peng B, Wang S, Zhou Z, Liu Y, Tong B, Zhang T, et al. A multilevel-ROI-features-based machine learning method for detection of morphometric biomarkers in Parkinson's disease. *Neurosci Lett*. 2017;651:88-94.
271. Schnack HG, Nieuwenhuis M, van Haren NE, Abramovic L, Scheewe TW, Brouwer RM, et al. Can structural MRI aid in clinical classification? A machine learning study in two independent samples of patients with schizophrenia, bipolar disorder and healthy subjects. *Neuroimage*. 2014;84:299-306.
272. Lui YW, Xue Y, Kenul D, Ge Y, Grossman RI, Wang Y. Classification algorithms using multiple MRI features in mild traumatic brain injury. *Neurology*. 2014;83(14):1235-40.

273. Bron EE, Steketee RM, Houston GC, Oliver RA, Achterberg HC, Loog M, et al. Diagnostic classification of arterial spin labeling and structural MRI in presenile early stage dementia. *Hum Brain Mapp.* 2014;35(9):4916-31.
274. Bron EE, Smits M, Papma JM, Steketee RME, Meijboom R, de Groot M, et al. Multiparametric computer-aided differential diagnosis of Alzheimer's disease and frontotemporal dementia using structural and advanced MRI. *Eur Radiol.* 2017;27(8):3372-82.
275. Orru G, Pettersson-Yeo W, Marquand AF, Sartori G, Mechelli A. Using Support Vector Machine to identify imaging biomarkers of neurological and psychiatric disease: a critical review. *Neurosci Biobehav Rev.* 2012;36(4):1140-52.
276. FMRIB. FSLVBM / User Guide Oxford: FSL; 2015 [Available from: <https://fsl.fmrib.ox.ac.uk/fsl/fslwiki/FSLVBM/UserGuide>].
277. Jenkinson M, Beckmann CF, Behrens TEJ, Woolrich MW, Smith SM. FSL. *NeuroImage.* 2012;62(2):782-90.
278. Chang C-C, Lin C-J. LIBSVM: A library for support vector machines. *ACM Trans Intell Syst Technol.* 2011;2(3):1-27.
279. Li BN, Chui CK, Chang S, Ong SH. Integrating spatial fuzzy clustering with level set methods for automated medical image segmentation. *Computers in Biology and Medicine.* 2011;41(1):1-10.
280. Yan K, Zhang D. Feature selection and analysis on correlated gas sensor data with recursive feature elimination. *Sensors and Actuators B: Chemical.* 2015;212:353-63.
281. Kroon D-J. B-spline Grid, Image and Point based Registration. Mathworks; File Exchange: Mathworks; 2008.
282. Kroon D-J. Hessian based Frangi Vesselness filter. Mathworks File Exchange 2009.
283. Yushkevich PA, Piven J, Hazlett HC, Smith RG, Ho S, Gee JC, et al. User-guided 3D active contour segmentation of anatomical structures: significantly improved efficiency and reliability. *Neuroimage.* 2006;31(3):1116-28.
284. Dai W, Garcia D, de Bazelaire C, Alsop DC. Continuous flow-driven inversion for arterial spin labeling using pulsed radio frequency and gradient fields. *Magn Reson Med.* 2008;60(6):1488-97.
285. Gunther M. Highly efficient accelerated acquisition of perfusion inflow series by cycled arterial spin labeling. ISMRM; Berlin, Germany 2006.
286. Zipfel GJ, Fox DJ, River DJ. Moyamoya Disease in Adults: The Role of Cerebral Revascularization. *Skull Base.* 2005;15(1):27-41.
287. Otsu N. A Threshold Selection Method from Gray-Level Histograms. *IEEE Transactions on Systems, Man, and Cybernetics.* 1979;9(1):62-6.
288. Canny JA. A computational approach to edge detection. *IEEE Trans Pattern Anal Machine Intel.* 1986;8:679-98.
289. Ho Y-CL, Petersen ET, Golay X. Measuring arterial and tissue responses to functional challenges using arterial spin labeling. *Neuroimage.* 2010;49(1):478-87.
290. Bonekamp D, Degaonkar M, Barker PB. Quantitative Cerebral Blood Flow in Dynamic Susceptibility Contrast MRI Using Total Cerebral Flow from Phase Contrast Magnetic Resonance Angiography. *Magnetic Resonance in Medicine.* 2011;66(1):57--66.
291. Ahlgren A, Wirestam R, Petersen ET, Stahlberg F, Knutsson L. Perfusion quantification by model-free arterial spin labeling using nonlinear stochastic regularization deconvolution. *Magn Reson Med.* 2013;70(5):1470-80.

292. Wu O, Ostergaard L, Weisskoff RM, Benner T, Rosen BR, Sorensen AG. Tracer arrival timing-insensitive technique for estimating flow in MR perfusion-weighted imaging using singular value decomposition with a block-circulant deconvolution matrix. *Magn Reson Med.* 2003;50(1):164-74.
293. Gander W. The Singular Value Decomposition Zurich2008 [Available from: https://www2.math.ethz.ch/education/bachelor/lectures/hs2014/other/linalg_I/NFK/svdneu.pdf].
294. Petr J, Schramm G, Hofheinz F, Langner J, van den Hoff J. Partial volume correction in arterial spin labeling using a Look-Locker sequence. *Magn Reson Med.* 2013;70(6):1535-43.
295. Barata JCA, Hussein MS. The Moore–Penrose Pseudoinverse: A Tutorial Review of the Theory. *Brazilian Journal of Physics.* 2012;42(1):146-65.
296. Castellaro M, Peruzzo D, Mehndiratta A, Pillonetto G, Petersen ET, Golay X, et al. Estimation of arterial arrival time and cerebral blood flow from QUASAR arterial spin labeling using stable spline. *Magn Reson Med.* 2015;74(6):1758-67.
297. Rorden C, Brett M. Stereotaxic display of brain lesions. *Behavioural Neurology.* 2000;12(4):191-200.
298. Petersen ET, De Vis JB, van den Berg CAT, Hendrikse J, editors. Turbo-QUASAR: a signal-to-noise optimal arterial spin labeling and sampling strategy. *ISMRM;* 2013.
299. Logothetis NK. The Underpinnings of the BOLD Functional Magnetic Resonance Imaging Signal. *The Journal of Neuroscience.* 2003;23(10):3963-71.
300. Kavakiotis I, Tsave O, Salifoglou A, Maglaveras N, Vlahavas I, Chouvarda I. Machine Learning and Data Mining Methods in Diabetes Research. *Comput Struct Biotechnol J.* 2017;15:104-16.
301. Ahlgren A. Perfusion MRI: Non-Linear Stochastic Regularization for Deconvolution of Model-Free Arterial Spin Labelling Data: Lund University; 2011.
302. Ditzel J, Standl E. THE PROBLEM OF TISSUE OXYGENATION IN DIABETES MELLITUS Its relation to the early functional changes in the microcirculation of diabetic subjects. *Journal of Internal Medicine.* 1975;197(S578):49-58.
303. Ditzel J. Affinity hypoxia as a pathogenetic factor of microangiopathy with particular reference to diabetic retinopathy. *Acta endocrinologica Supplementum.* 1980;238:39-55.
304. van Bussel FCG, Backes WH, van Veenendaal TM, Hofman PAM, van Boxtel MPJ, Schram MT, et al. Functional Brain Networks Are Altered in Type 2 Diabetes and Prediabetes- Signs for Compensation of Cognitive Decrements? The Maastricht Study. *Diabetes.* 2016;65(8):2404-13.
305. Fan AP, Guo J, Khalighi Mohammad M, Gulaka Praveen K, Shen B, Park Jun H, et al. Long-Delay Arterial Spin Labeling Provides More Accurate Cerebral Blood Flow Measurements in Moyamoya Patients. *Stroke.* 2017;48(9):2441-9.
306. Lu H, Clingman C, Golay X, van Zijl PC. Determining the longitudinal relaxation time (T1) of blood at 3.0 Tesla. *Magn Reson Med.* 2004;52(3):679-82.
307. Irace C, Carallo C, Scavelli F, De Franceschi MS, Esposito T, Gnasso A. Blood viscosity in subjects with normoglycemia and prediabetes. *Diabetes Care.* 2014;37(2):488-92.
308. Cheng G, Huang C, Deng H, Wang H. Diabetes as a risk factor for dementia and mild cognitive impairment: a meta-analysis of longitudinal studies. *Intern Med J.* 2012;42(5):484-91.

309. Imamine R, Kawamura T, Umemura T, Umegaki H, Kawano N, Hotta M, et al. Does cerebral small vessel disease predict future decline of cognitive function in elderly people with type 2 diabetes? *Diabetes Res Clin Pract.* 2011;94(1):91-9.
310. Williamson JD, Miller ME, Bryan RN, Lazar RM, Coker LH, Johnson J, et al. The Action to Control Cardiovascular Risk in Diabetes Memory in Diabetes Study (ACCORD-MIND): rationale, design, and methods. *Am J Cardiol.* 2007;99(12A):112i-22i.
311. Erus G, Battapady H, Zhang T, Lovato J, Miller ME, Williamson JD, et al. Spatial patterns of structural brain changes in type 2 diabetic patients and their longitudinal progression with intensive control of blood glucose. *Diabetes care.* 2015;38(1):97-104.
312. Launer LJ, Miller ME, Williamson JD, Lazar RM, Gerstein HC, Murray AM, et al. Effects of intensive glucose lowering on brain structure and function in people with type 2 diabetes (ACCORD MIND): a randomised open-label substudy. *The Lancet Neurology.* 2011;10(11):969-77.
313. McIntosh C, Hamarneh G, editors. *Vessel Crawlers: 3D Physically-based Deformable Organisms for Vasculature Segmentation and Analysis.* IEEE Computer Science Conference on Computer Vision and Pattern Recognition; 2006.
314. Despotovic I, Goossens B, Philips W. MRI segmentation of the human brain: challenges, methods, and applications. *Comput Math Methods Med.* 2015;2015:450341.
315. Morey RA, Petty CM, Xu Y, Hayes JP, Wagner HR, 2nd, Lewis DV, et al. A comparison of automated segmentation and manual tracing for quantifying hippocampal and amygdala volumes. *Neuroimage.* 2009;45(3):855-66.
316. Chen L, Mossa-Basha M, Balu N, Canton G, Sun J, Pimentel K, et al. Development of a quantitative intracranial vascular features extraction tool on 3D MRA using semiautomated open-curve active contour vessel tracing. *Magn Reson Med.* 2018;79(6):3229-38.
317. Popescu V, Battaglini M, Hoogstrate WS, Verfaillie SC, Sluimer IC, van Schijndel RA, et al. Optimizing parameter choice for FSL-Brain Extraction Tool (BET) on 3D T1 images in multiple sclerosis. *Neuroimage.* 2012;61(4):1484-94.
318. Zhang Y, Brady M, Smith S. Segmentation of brain MR images through a hidden Markov random field model and the expectation-minimization algorithm. *IEEE Trans Med Imaging.* 2001;20(1):45-57.
319. Collins DL, Zijdenbos AP, Kollokian V, Sled JG, Kabani NJ, Holmes CJ, et al. Design and Construction of a Realistic Digital Brain Phantom. *IEEE Trans Med Imaging.* 1998;17(3).
320. FMRIB. GLM Oxford2016 [Available from: <https://fsl.fmrib.ox.ac.uk/fsl/fslwiki/GLM>].
321. Smith SM, Nichols TE. Threshold-free cluster enhancement: addressing problems of smoothing, threshold dependence and localisation in cluster inference. *Neuroimage.* 2009;44(1):83-98.
322. Dale AM, Fischl B, Sereno MI. Cortical Surface-Based Analysis I. Segmentation and Surface Reconstruction. *Neuroimage.* 1999;9(2):179-94.
323. Fischl B, Salat DH, Busa E, Albert M, Dieterich M, Haselgrove C, et al. Whole Brain Segmentation: Automated Labeling of Neuroanatomical Structures in the Human Brain. *Neuron.* 2002;33(3):341-55.

324. Benjamini Y, Hochberg Y. Controlling the False Discovery Rate: A Practical and Powerful Approach to Multiple Testing. *Journal of the Royal Statistical Society Series B (Methodological)*. 1995;57(1):289-300.
325. Deng WQ, LI XM, Gao X, Zhang CM. A modified fuzzy c-means algorithm for brain MR image segmentation and bias field correction. *Journal of Computer Science and Technology*. 2016;31(3):501-11.
326. Moran C, Beare R, Phan TG, Bruce DG, Callisaya ML, Srikanth V. Type 2 diabetes mellitus and biomarkers of neurodegeneration. *Neurology*. 2015;85(13):1123.
327. Debette S, Markus HS. The clinical importance of white matter hyperintensities on brain magnetic resonance imaging: systematic review and meta-analysis. *BMJ*. 2010;341:c3666.
328. Fazekas F, Chawluk JB, Alavi A, Hurtig HI, Zimmerman RA. MR signal abnormalities at 1.5 T in Alzheimer's dementia and normal aging. *American Journal of Roentgenology*. 1987;149(2):351-6.
329. Ithapu V, Singh V, Lindner C, Austin BP, Hinrichs C, Carlsson CM, et al. Extracting and summarizing white matter hyperintensities using supervised segmentation methods in Alzheimer's disease risk and aging studies. *Hum Brain Mapp*. 2014;35(8):4219-35.
330. Bianconi F, Fernandez A, Mancini A, editors. Assessment of rotation-invariant texture classification through Gabor filters and discrete Fourier transform. 20th International Congress on Graphical Engineering; 2008; Valencia, Spain.
331. Riaz F, Hassan A, Rehman S, Qamar U. Texture Classification Using Rotation- and Scale-Invariant Gabor Texture Features. *IEEE Signal Processing Letters*. 2013;20(6):607-10.
332. Novak V, Zhao P, Manor B, Sejdic E, Alsop D, Abduljalil A, et al. Adhesion molecules, altered vasoreactivity, and brain atrophy in type 2 diabetes. *Diabetes Care*. 2011;34(11):2438-41.
333. Kario K, Ishikawa J, Hoshida S, Matsui Y, Morinari M, Eguchi K, et al. Diabetic brain damage in hypertension: role of renin-angiotensin system. *Hypertension*. 2005;45(5):887-93.
334. Bradley D, Roth G. Adapting Thresholding Using the Integral Image. *Journal of Graphics Tools*. 2007;12(2):13-21.
335. Wiener N. *Extrapolation, Interpolation, and Smoothing of Stationary Time Series*: The MIT Press; 1964.
336. Frangi AF, Niessen WJ, Vincken KL, Viergever MA, editors. *Multiscale vessel enhancement filtering* 1998; Berlin, Heidelberg: Springer Berlin Heidelberg.
337. El-Baz A, Elnakib A, Khalifa F, El-Ghar MA, McClure P, Soliman A, et al. Precise segmentation of 3-D magnetic resonance angiography. *IEEE Trans Biomed Eng*. 2012;59(7):2019-29.
338. Bullitt E, Gerig G, Pizer SM, Weili L, Aylward SR. Measuring tortuosity of the intracerebral vasculature from MRA images. *IEEE Transactions on Medical Imaging*. 2003;22(9):1163-71.
339. Reijmer YD, Brundel M, de Bresser J, Kappelle LJ, Leemans A, Biessels GJ, et al. Microstructural white matter abnormalities and cognitive functioning in type 2 diabetes: a diffusion tensor imaging study. *Diabetes care*. 2013;36(1):137-44.

340. Xiong Y, Sui Y, Zhang S, Zhou XJ, Yang S, Fan Y, et al. Brain microstructural alterations in type 2 diabetes: diffusion kurtosis imaging provides added value to diffusion tensor imaging. *European Radiology*. 2018.
341. Dai Z, Yan C, Wang Z, Wang J, Xia M, Li K, et al. Discriminative analysis of early Alzheimer's disease using multi-modal imaging and multi-level characterization with multi-classifier (M3). *NeuroImage*. 2012;59(3):2187-95.
342. Ding B, Ling HW, Zhang Y, Huang J, Zhang H, Wang T, et al. Pattern of cerebral hyperperfusion in Alzheimer's disease and amnesic mild cognitive impairment using voxel-based analysis of 3D arterial spin-labeling imaging: initial experience. *Clin Interv Aging*. 2014;9:493-500.
343. Mak E, Gabel S, Mirette H, Su L, Williams GB, Waldman A, et al. Structural neuroimaging in preclinical dementia: From microstructural deficits and grey matter atrophy to macroscale connectomic changes. *Ageing Res Rev*. 2017;35:250-64.
344. Leijenaar JF, van Maurik IS, Kuijter JPA, van der Flier WM, Scheltens P, Barkhof F, et al. Lower cerebral blood flow in subjects with Alzheimer's dementia, mild cognitive impairment, and subjective cognitive decline using two-dimensional phase-contrast magnetic resonance imaging. *Alzheimer's & dementia (Amsterdam, Netherlands)*. 2017;9:76-83.
345. Chung MK, Hanson JL, Adluru N, Alexander AL, Davidson RJ, Pollak SD. Integrative Structural Brain Network Analysis in Diffusion Tensor Imaging. *Brain connectivity*. 2017;7(6):331-46.
346. Tognarelli JM, Dawood M, Shariff MI, Grover VP, Crossey MM, Cox IJ, et al. Magnetic Resonance Spectroscopy: Principles and Techniques: Lessons for Clinicians. *J Clin Exp Hepatol*. 2015;5(4):320-8.
347. Vemuri P, Jones DT, Jack CR, Jr. Resting state functional MRI in Alzheimer's Disease. *Alzheimer's research & therapy*. 2012;4(1):2-.

Appendix

Appendix1

Chapter 6

Table A6.1: Summary of classification accuracy and number of features for every task and model. Models in bold are the ones for which optimal performance was achieved.

Model	Number of features	Significant features	Accuracy (%)	Top-M features (M)
Healthy volunteers vs type-2 diabetes				
1	211	59	96.9	27 (12)
2	211	71	84.4	7(3)
3	351	116	93.8	9(3)
4	34	3	81.3	1(1)
5	244	62	90.6	6(3)
6	244	74	93.8	3(2)
7	384	119	84.4	3(1)
Healthy volunteers vs type-2 diabetes & impaired glucose tolerance				
1	211	85	92.9	14(4)
2	211	85	83.3	5(1)
3	351	153	88.1	42(19)
4	34	7	81	4(3)
5	244	92	92.9	11(3)
6	244	92	83.3	23(13)
7	384	160	88.1	22(7)
Healthy volunteers vs impaired glucose tolerance				
1	211	85	100	5(3)
2	211	86	92.3	7(3)
3	351	148	92.3	2(1)
4	34	6	73.1	6(3)
5	244	91	100	5(3)
6	244	92	92.3	6(3)
7	384	154	92.3	2(1)
Impaired glucose tolerance vs type-2 diabetes				
1	211	6	65.4	4(1)

2	211	10	69	5(1)
3	351	15	69.2	11(4)
4	34	4	73.1	4(1)
5	244	10	80.7	7(1)
6	244	14	65.4	11(5)
7	384	19	80.7	6(1)

Table A6.2: Details for the two best performing models for every task. The accuracy (Acc), sensitivity (Sens) and specificity (Spec) for every model are shown. Along with these the number of significantly different features (NF1) and the number of features providing optimal class differentiation (NF2) are provided. Finally, in the last column, the top scoring features (maximum 5) are shown accompanied by a number indicating their occurrence. The maximum possible number in the brackets would be for task 1: 32, task 2: 42, task 3: 26 and task 4: 26.

Task	Model	NF1	Acc. (%)	Sens. (%)	Spec. (%)	NF2	Feature combination providing optimal accuracy (max 5 shown)
HV vs T2DM	1	59	96.9	100	93.8	27	PCA HWR ΔM_{cr} post-ACZ (32), PCA FW ΔM_{cr} post-ACZ (32), ACA TTP AIF _{SH} post-ACZ (32), ACA SKEW AIF _{SH} baseline (32), ACA HWL AIF _{SH} post-ACZ (32)
HV vs T2DM	6	74	93.8	93.8	93.8	3	WB HWL Res post-ACZ (31), WB TTP Res post-ACZ (26), CVR (7)
HV vs IGT&T2DM	1	85	92.9	96.2	87.5	14	PCA HWR ΔM_{cr} post-ACZ (40), MCA SKEW ΔM_{cr} post-ACZ (35), ACA SKEW ΔM_{cr} post-ACZ (18), W KURT ΔM_{cr} baseline (18), ACA KURT AIF _{SH} baseline (17)
HV vs IGT&T2DM	5	92	92.9	96.2	87.5	11	CVR (36), MCA SKEW ΔM_{cr} post-ACZ (31), ACA HWL AIF _{SH} post-ACZ (23), PCA HWR ΔM_{cr} post-ACZ (21), ACA SKEW AIF _{SH} baseline (7)
HV vs IGT	1	85	100	100	100	5	PCA HWL AIF _{SH} post-ACZ (26), PCA TTP AIF _{SH} post-ACZ (26), W KURT ΔM_{cr} post-ACZ (17), PCA HWL ΔM_{ncr} post-ACZ (8), ACA TTP ΔM_{ncr} post-ACZ (1)
HV vs IGT	5	91	100	100	100	5	
IGT vs T2DM	5	10	80.7	87.5	70	7	GM CBF baseline (10), CVR (9), ACA aBV baseline (2), PCA HWL ΔM_{ncr} post-ACZ (2), MCA KURT ΔM_{ncr} post-ACZ (1)
IGT vs T2DM	7	19	80.7	81.3	80	6	MCA HWL R baseline (1), PCA HWL ΔM_{ncr} post-ACZ

(2), GM CBF baseline (17),
CVR (4), ACA aBV baseline
(4)

Appendix 2

Chapter 7

A7.1

	HV (cm ³)	IGT (cm ³)	T2DM (cm ³)
Left accumbens	0.6±0.2	0.7±0.2	0.6±0.1
Left amygdala	1.7±0.3	1.7±0.2	1.6±0.2
Left caudate	3.4±0.4	3.7±0.4	3.7±0.9
Left putamen	5.6±0.7	5.9±0.7	5.5±1.0
Right accumbens	0.6±0.2	0.7±0.2	0.6±0.1
Right amygdala	2.2±0.4	2.2±0.3	2.0±0.3
Right caudate	3.6±0.5	3.7±0.6	3.7±0.8
Right putamen	5.7±0.6	5.9±0.6	5.3±0.7

Chapter 7.4

Qflow tables with the mean and standard deviation for the calculated velocities

Table A7.2: Baseline mean velocity for the 3 groups and areas of interest.

	right (ml/s)	left(ml/s)	right10(ml/s)	left10(ml/s)	All (ml/s)
HV	26.36±2.77	24.28±3.78	30.19±2.68	28.09±4.99	22.59±2.77
IGT	23.54±2.94	22.53±3.78	27.30±4.03	25.31±4.46	20.97±2.22
T2DM	21.41±5.44	19.32±5.23	24.86±5.45	21.80±5.35	18.89±4.16

Table A7.3: Baseline max velocity for the 3 groups and areas of interest.

	right (ml/s)	left(ml/s)	right10(ml/s)	left10(ml/s)	All (ml/s)
HV	35.38±3.42	32.69±5.97	35.38±3.42	32.69±5.97	36.22±3.77
IGT	31.96±4.61	29.30±5.22	31.96±4.62	29.30±5.22	34.48±2.78
T2DM	28.96±6.24	25.31±6.34	28.93±6.25	25.30±6.24	30.18±5.78

Table A7.4: Baseline min velocity for the 3 groups and 5 areas of interest.

	right (ml/s)	left(ml/s)	right10(ml/s)	left10(ml/s)	All (ml/s)
HV	16.89±3.02	15.67±2.99	24.23±2.32	22.77±4.29	11.47±1.88
IGT	14.54±2.32	14.66±2.93	21.70±3.37	20.23±3.36	10.21±1.90
T2DM	13.15±4.83	12.78±4.48	19.96±4.72	17.72±4.78	9.82±3.35

Table A7.5: Post-ACZ mean velocity for the examined cohort and the areas of interest.

	right (ml/s)	left(ml/s)	right10(ml/s)	left10(ml/s)	All (ml/s)
HV	32.10±6.33	28.50±6.61	38.32±6.45	34.45±8.26	27.96±4.65
IGT	29.17±2.93	27.37±4.81	35.39±3.93	32.02±5.07	25.02±3.15
T2DM	27.11±6.40	23.92±6.20	32.14±6.98	27.82±7.36	23.97±5.62

Table A7.6: Post-ACZ max velocity for the examined cohort and the areas of interest.

	right (ml/s)	left(ml/s)	right10(ml/s)	left10(ml/s)	All (ml/s)
HV	44.43±6.89	39.84±9.36	44.42±6.92	39.82±9.38	46.22±6.13
IGT	40.85±5.14	33.38±5.56	40.85±5.14	36.53±6.16	41.05±4.90
T2DM	37.16±7.97	30.77±7.95	37.11±8.00	32.16±8.71	38.60±7.83

Table A7.7: Post-ACZ min velocity for the examined cohort and the areas of interest

	right (ml/s)	left(ml/s)	right10(ml/s)	left10(ml/s)	All (ml/s)
HV	19.25±6.26	16.71±5.47	30.89±6.50	28.29±7.41	14.10±3.24
IGT	16.66±2.60	17.20±4.03	28.78±2.94	26.95±4.18	11.96±2.43
T2DM	15.96±5.14	15.09±4.84	25.94±6.13	22.32±5.99	11.73±3.24